



Eleventh meeting on
Visual & Physiological
Optics - Antwerp '23

Book of abstracts



Edited by Jos J. Rozema

Scientific committee

Ray Applegate (USA)
Pablo Artal (Spain)
Magdalena Asejczyk (Poland)
David Atchison (Australia)
Neil Charman (UK)
Tanya Evans (South Africa)
Harilaos Ginis (Greece)
José Ramón Jiménez (Spain)
Sabine Kling (Switzerland)
Linda Lundström (Sweden)
Vasyl Molebny (Ukraine)
Rafael Navarro (Spain)
Barbara Pierscionek (UK)
Jos Rozema (Belgium)
Juan Tabernero (Spain)
Tom van den Berg (Netherlands)
Maria Viñas Peña (Spain)
Brian Vohnsen (Ireland)

Organizing committee

Jos Rozema
Arezoo Farzanfar
Sharon Francis
Hosna Ghaderi

With the kind support from



University
of Antwerp

OPTICA | Formerly
Advancing Optics and Photonics Worldwide
OSA

Invited speakers



Alejandra Consejo

[The hidden secrets of corneal tomography](#)

Alejandra Consejo, MSc, PhD, is an assistant professor and researcher at the Department of Applied Physics at the University of Zaragoza (Spain). She applies data science to eye research. Her research interests include contact lens wear, corneoscleral characterization, and the early detection of eye disease.



Sasha Goncharov

[Crystalline Lens Models of Today and Tomorrow](#)

and

[The ideas that shaped the design of the Extremely Large Telescope \(ELT\)](#)

Alexander Goncharov is a lecturer in Physics at the University of Galway, Ireland, doing research in astronomical and ophthalmic optics at the Applied Optics group. He is a Senior Member of Optica.



Kirill Larin

[Dynamic optical coherence elastography \(OCE\) and Brillouin spectroscopy for ocular biomechanics](#)

Kirill Larin is a Cullen College of Engineering Distinguished Professor of Biomedical Engineering at the University of Houston. He received his first M.S. in Laser Physics and Mathematics from the Saratov State University, Russia, in 1995, his second M.S. in Cellular Physiology and Molecular Biophysics in 2001, and his Ph.D. in Biomedical Engineering in 2002 from the University of Texas Medical Branch. Larin is widely recognized for his research contributions in the fields of Biomedical Optics and Biophotonics, where he has developed and applied various optical methods for non-invasive and non-destructive imaging and diagnostics of tissues and cells.



Cynthia Roberts

[Evolving stress distribution in keratoconus and prediction of progression from a single tomographic map](#)

Professor Cynthia J Roberts, PhD, is the Martha G. and Milton Staub Chair for Research in Ophthalmology at The Ohio State University. She has spent more than 30 years studying clinical ocular biomechanics for applications including keratoconus, glaucoma, Intraocular pressure measurement error, and response to refractive surgery. Professor Roberts has over 170 papers in the peer reviewed literature, has given over 240 National and International Invited Lectures, as well as over 200 lectures in medical education courses.

Conference programme

Sunday 27/8/2023

08:30 – 09:00 Registration

Session 1: Opening					Moderator: Jos Rozema		
09:00	09:05	5	Jos Rozema University of Antwerp (Belgium)	Welcome			
09:05	09:30	25	Carina Koppen University of Antwerp (Belgium)	20 years of crosslinking for keratoconus: ongoing quest for a valid diagnosis of cone progression			
Session 2: Crystalline lens optics I					Moderator: Rafael Navarro		
09:30	10:00	30	Sasha Goncharov University of Galway (Ireland)	Crystalline lens models of today and tomorrow			
10:00	10:15	15	Conor Flynn University of Galway (Ireland)	Calculation of the paraxial parameters of a GRIN lens with analytical ray-tracing			
10:15	10:30	15	Veronica Lockett Ruiz CSIC (Spain)	Effect of crystalline lens geometry on the intracapsular accommodation mechanism			
10:30	10:45	15	Rafael Navarro CSIC (Spain)	Effect of the inner curvature gradient on crystalline lens performance			
10:45	11:00	15	Discussion				
11:00	11:30	30	Coffee break				
Session 3: Crystalline lens optics II					Moderator: Tanya Evans		
11:30	11:45	15	Tanya Evans Uni. Johannesburg (S. Africa)	Astigmatic power of the crystalline lens derived from ocular biometry (Part 1)			
11:45	12:00	15	Sarah Hershko University of Antwerp (Belgium)	Influence of straylight on driving performance in young adults			
12:00	12:15	15	Maria Mechó García University of Minho (Portugal)	Spherical aberration and accommodative lag in young adults.			
12:15	12:30	15	Ebrahim Safarian CSIC (Spain)	Variability in wavefront changes during sustained reading and recovery in presbyopic eyes			
12:30	12:45	15	Discussion				
12:45	13:45	60	Lunch break				
Session 4: Optical coherence elastography					Moderator: Jorge Grasa		
13:45	14:15	30	Kirill Larin University of Houston (USA)	Dynamic optical coherence elastography (OCE) and Brillouin spectroscopy for ocular biomechanics			
14:15	14:30	15	Matteo Frigelli University of Bern (Switzerland)	Optical coherence elastography assessment of mechanical and refractive changes induced by different corneal cross-linking protocols			
14:30	14:45	15	Sabine Kling ETHZ/ Univ. of Bern (Switzerland)	High-resolution optical coherence elastography of the human lens <i>in vivo</i>			
14:45	15:00	15	Vahoura Tahsini University of Bern (Switzerland)	Characterization of the mechanical contribution of the capsule of crystalline lenses using optical coherence elastography			
15:00	15:15	15	Discussion				
15:15	15:45	30	Coffee break				

Session 5: IOL optics					Moderator: David Atchison
15:45	16:00	15	David Atchison Queensland Univ of Tech (Australia)	Change in refractive errors with changes in IOL parameters	
16:00	16:15	15	Jasmien Rens Antwerp Univ. Hospital (Belgium)	Novel OCT-based estimation of postoperative IOL position	
16:15	16:30	15	Haris Ginis Diestia Systems (Greece)	Measuring the optics of eyes with diffractive intraocular lenses	
16:30	16:45	15	Michael Simpson Simpson Optics LLC (USA)	Intraocular lens tilt, the pupil, and simple eye models	
16:45	17:00	15	Discussion		

Session 6: Posters					
17:00	18:00	60	Jorge Ares University of Zaragoza (Spain)	RGP contact lens fluorogram visualization with 3D printed sclero-corneal surfaces	
			Diana Gargallo University of Zaragoza (Spain)	A comparison between measurements of actual lens position with two optical biometers: Lenstar LS 900 and Anterior	
			Diana Gargallo University of Zaragoza (Spain)	Effect of rotation and axial shift of toric intraocular lenses analyzed by means of numerical ray tracing	
			Pilar Casado University of Zaragoza (Spain)	Visual motion perception in a young university population	
			Tanya Evans Uni. Johannesburg (S. Africa)	Astigmatic power of the crystalline lens surfaces derived from ocular biometry (Part 2)	
			Cristina Rovira Gay Polytech Univ Catalunya (Spain)	Objective assessment of the effects of a vision therapy protocol on adults with typical binocular vision	
			Valdeflors Vinuela Navarro Polytech Univ Catalunya (Spain)	Immersive virtual reality intervention for post-COVID-19 condition: An eye movement pilot study	
			Saeed Zahabi WUST (Poland)	An optomechanical model of the human eye for deducting the properties of the biological tissues	

Monday 28/8/2023

Session 7: OBERON hackathon pitches					Moderator: Jos Rozema
08:00	08:15	15	OBERON group A	Pitch	
08:15	08:30	15	OBERON group B	Pitch	
08:30	08:45	15	OBERON group C	Pitch	
08:45	09:00	15	OBERON group D	Pitch	

Session 8: Corneal biomechanics					Moderator: Magdalena Asejczyk
09:00	09:30	30	Cynthia Roberts The Ohio State University (USA)	Evolving stress distribution in keratoconus and prediction of progression from a single tomographic map	
09:30	09:45	15	Magdalena Asejczyk WUST (Poland)	Corneal dynamic analysis and its correlation with blood pulsation	
09:45	10:00	15	Benedetta Fantaci University of Zaragoza (Spain)	Computational optics for finite-element corneal modelling	
10:00	10:15	15	Elena Redaelli University of Zaragoza (Spain)	Analysis of the influence of keratoconus mechanical properties, dimension and position on the outputs of Corvis	
10:15	10:30	15	Discussion		

10:30	11:00	30	Coffee break	
-------	-------	----	--------------	--

Session 9: Crystalline lens and IOL biomechanics					Moderator: Barbara Pierscionek
11:00	11:15	15	Ali Dahaghin WUST (Poland)	Opto-mechanical simulations of crystalline lens wobbling during gaze change in accommodated eyes	
11:15	11:30	15	Liying Feng Johnson & Johnson (NL)	Modelling the sensitivity of the accommodative amplitude to the orientation of zonular fibres	
11:30	11:45	15	Kehao Wang Beihang University (China)	Influence of zonular fibres on lens accommodation assessed by a pre-stressed eye model	
11:45	12:00	15	Lin Ye Anglia Ruskin University (UK)	The effect of lens shape, zonular insertion and finite element model on simulated stretching of the lens	
12:00	12:00	15	Discussion		

12:15	13:00	45	Lunch break	
-------	-------	----	-------------	--

Session 10: Corneal optics					Moderator: Alejandra Consejo
13:00	13:30	30	Alejandra Consejo University of Zaragoza (Spain)	The hidden secrets of corneal tomography	
13:30	13:45	15	Iñaki Blanco University of Minho (Portugal)	Linear fitting of biconic surfaces for corneal modelling	
13:45	14:00	15	Diana Gargallo University of Zaragoza (Spain)	Measuring contact lens base curve radius using a clinical OCT: an in-vitro study	
14:00	14:15	15	Sharon Francis University of Antwerp (Belgium)	Contact lens mask to block the most aberrated pupillary regions in keratoconic eyes	
14:15	14:30	15	Masoud Mehrjoo - SCHWIND eye-tech solutions (Germany)	Automatic segmentation of corneal cuts in OCT images	
14:30	14:45	15	Discussion		

14:45	15:15	30	Coffee break	
-------	-------	----	--------------	--

Session 11: Modern digital methods					Moderator: José Manuel González-Méijome
15:15	15:30	15	José Manuel González-Méijome University of Minho (Portugal)	Algorithm-assisted refraction: preliminary perspectives from different clinical application paradigms.	
15:30	15:45	15	Mateusz Jaskulski University of Murcia (Spain)	Mobile app for tele-monitoring potential changes in myopia and presbyopia	
15:45	16:00	15	Norberto López Gil University of Murcia (Spain)	Mobile app for detecting early cataract	
16:00	16:15	15	Aina Turull Mallofré Polytech Univ Catalunya (Spain)	Prediction of the spherical subjective refraction from accommodation data	
16:15	16:30	15	Discussion		

Session 12: Visual function					Moderator: José Manuel González-Méijome
16:30	16:45	15	Pilar Casado University of Zaragoza (Spain)	The effect of stimulus background luminance on temporal contrast sensitivity	
16:45	17:00	15	Jorge Lasarte Sanz Tech University Dublin (Ireland)	Design of a holographic stereoaquity test	
17:00	17:15	15	Joan Goset Maldonado Polytech Univ Catalunya (Spain)	Cognitive impairment in patients with post-COVID condition: correlations between eye movements metrics and the Stroop Color and Word neuropsychological test	
17:15	17:30	15	Discussion		

18:00	19:30	Social programme: City walk
19:30	22:00	Social programme: Congress dinner (Universiteitsclub, Prinsstraat 13B, 1 st floor, M. Mayerzaal)

Tuesday 29/8/2023

Session 13: Refractive error and wavefronts					Moderator: Mateusz Jaskulski
09:00	09:15	15	Jorge Ares University of Zaragoza (Spain)	A study about the relation between virtual subjective refraction, objective refraction, and real subjective refraction	
09:15	09:30	15	Jan-Willem Beenakker Leiden UMC (Netherlands)	ZOSPy, a Python package for optical simulations	
09:30	09:45	15	Diana Gargallo University of Zaragoza (Spain)	A study about Jackson cross cylinder test reliability by means of retinal image simulation	
09:45	10:00	15	José Manuel González-Méijome University of Minho (Portugal)	Bridging physiological optics and visual physiology in myopia control research	
10:00	10:15	15	Mateusz Jaskulski Indiana University (USA)	Optical characterisation of two novel myopia control spectacle lenses	
10:15	10:30	15	Discussion		
10:30	11:00	30	Coffee break		
Session 14: Eye modelling					Moderator: Norberto López Gil
11:00	11:15	15	Fabian Debowy Anglia Ruskin University (UK)	How the source of the refractive error can influence image quality	
11:15	11:30	15	Arezoo Farzanfar University of Antwerp (Belgium)	Estimating the biometric contributions to variations in refractive error in premature and full-term children	
11:30	11:45	15	Hosna Ghaderi University of Antwerp (Belgium)	SyntEyes OBM: higher order statistical model for biomechanical analyses	
11:45	12:00	15	Jos Rozema University of Antwerp (Belgium)	How similar are male and female eyes?	
12:00	12:15	15	Discussion		
Session 15: Closing					Moderator: Jos Rozema
12:15	12:45	30	Sasha Goncharov University of Galway (Ireland)	The ideas that shaped the design of the Extremely Large Telescope (ELT)	
12:45	12:50	5	Jos Rozema University of Antwerp (Belgium)	Closing	
12:50	12:55	5	Magdalena Asejczyk WUST (Poland)	VPO 2024 - Wroclaw (Poland)	

Abstracts

(in order of presentation)

Calculation of the paraxial parameters of a GRIN lens with analytical ray-tracing

Conor Flynn^{1*} and Alexander V. Goncharov¹

¹ Applied Optics Group, Physics Unit, School of Natural Sciences, University of Galway, Galway, Ireland

* Corresponding author: c.flynn24@nuigalway.ie

Purpose

The purpose of this research is to find the effective focal length (EFL) of a gradient refractive index (GRIN) lens. GRIN lenses represented by a quadratic GRIN profile were tested and compared to a GRIN5 surface type in Zemax OpticStudios. This work is done to test the methods so they can be used on a schematic eye model such as one proposed by Liou and Brennan. This will offer an analytic method to find the equivalent power of an eye model where the crystalline lens is represented by a GRIN lens.

Methods

An analytic solution is proposed to a differential equation derived from the paraxial ray-tracing equations. This solution, defined as $h(z)$ and represented by Legendre polynomials, shows the vertical change in the trajectory of light rays along the optical axis, within the lens. This expression for $h(z)$ can be used to calculate the EFL and back focal distance of a GRIN lens, and can thus be used to locate the principal point along the optical axis. This work is done with focus on quadratic GRIN profiles used to describe a crystalline lens. The nature of the GRIN profile will be that of:

$$n(z, h(z)) = n_0 - n_1 h(z)^2 + n_3 z - n_4 z^2,$$

where n_0 is the refractive index on the surface of the lens and n_i , with $i \in \{1,3,4\}$, are the GRIN lens coefficients. This expression describes the geometry of the iso-indicial contours of the GRIN medium which are applied as the initial conditions for the equation mapping the trajectory of the light ray.

The EFL of a GRIN lens is calculated using the formula: $EFL = \frac{-h(z_0)}{n_0 h'(z_1)}$, where $h(z)$, is the derived expression based on Legendre polynomials, $h'(z)$ is the derivative with respect to z , z_0 is where light enters the lens and z_1 is the point at which the light emerges from the lens. z_0 is obtained from the initial conditions and z_1 is calculated from equating an expression for $h(z)$ to the back surface of the lens, derived from the power law equation above.

Results

The quadratic GRIN profile $n(z, h(z)) = 1.37 - 0.01 h(z)^2 + 0.04z - 0.01z^2$, represents a spherical lens of radius 2 mm, leading to a surface radius of curvature and semi-diameter equal to the radius, and a thickness equal to the diameter. The surface and core refractive indices are 1.37 and 1.41 respectively. When the lens is placed in a medium equal to the refractive index at the surface, the calculated EFL by Zemax OpticStudios is 12.9885 mm. The difference between the numerical estimate of the EFL in Zemax and the EFL calculated by the analytical method presented here is less than 3 nm.

Conclusion

The methods developed here will allow for analytical ray-tracing through a quadratic GRIN without the need of ray-tracing software.

Keywords: *GRIN lenses, Gradient-index Optics, Refractive index, Ray-tracing, Zemax, Eye model*

Effect of crystalline lens geometry on the intracapsular accommodation mechanism

Veronica Lockett-Ruiz,^{1*} Rafael Navarro,¹ and Norberto López-Gil²

¹ INMA-CSIC and Universidad de Zaragoza, Zaragoza, Spain

² Instituto Universitario de Investigación en Envejecimiento, Universidad de Murcia, Murcia, Spain

* Corresponding author: vlockett@unizar.es

Gullstrand's intracapsular accommodation mechanism (IAM) suggests that the lens equivalent refractive index must increase to fully explain the boost in lens power during accommodation. We evaluate the presence of an IAM by fitting a GRINCU lens model to observed changes in the lens's external and internal geometry during accommodation. We computed the paraxial lens power and equivalent refractive index at each accommodative step for all datasets and found an increasing equivalent refractive index, corresponding to a positive IAM. These results suggest a strong dependence of the lens equivalent refractive index on the inner curvature gradient.

Keywords: GRIN; accommodation; intracapsular accommodation mechanism, Gullstrand

Introduction

According to the intracapsular accommodation mechanism (IAM), first proposed by Gullstrand [1], an increase in the effective refractive index is required to account for the rise in lens power during accommodation.

Here we analyse the presence of an IAM during accommodation by computing the power increase and the equivalent refractive index of a GRINCU [2] accommodative lens model. To do so, we use two studies in the literature [3, 4] that include in-vivo experimental data for the internal and external lens geometry changes with accommodation.

Methods

To compute the lens power change and equivalent refractive index, a GRINCU accommodative lens model was fitted to published data in the literature that includes geometrical changes in the lens during accommodation. The first dataset corresponds to the Scheimpflug video of a 16-year-old lens disaccommodating [3], from which we extracted the anterior and posterior nucleus and external surface radii of curvature, conic constants, and thicknesses for accommodation stages depicted in 25 successive frames. The second dataset was based on a Scheimpflug imaging accommodation and age-dependent study [4]. Lens geometrical parameters were calculated for ages 18, 29, and 45 years with an accommodation interval 0D to 9D using the equations provided by the authors [5, 6, 7].

The GRINCU model was fitted to the obtained parameters, and the paraxial power was computed using the analytical ray transfer method [8] for each accommodative stage of the four lenses considered. Using our calculated GRINCU lens power, we found the equivalent refractive index, n_{eq} , at each accommodation state. We later used the unaccommodated value of n_{eq} to find the refractive power at each accommodative state for an equivalent two-surface homogeneous lens.

Results

The nucleus and external surface anterior and posterior radii of curvature, the cortex and nucleus thicknesses, and the net radius of curvature gradient were calculated at each accommodative stage of the two studies (four ages) considered. For the first dataset (video), we were also able to find the external surface conic constants. The external surface radii of curvature change the most, while the cortex thickness remains roughly constant during accommodation. These two factors cause a steepening of the lens's net radius of curvature gradient, further enhancing the paraxial lens power and increasing the equivalent refractive index during accommodation, showing a positive IAM.

The refractive power increases monotonically, displaying a nearly quadratic trend with accommodation for all datasets (see Fig. 1). The equivalent refractive index increased monotonically for most datasets, suggesting a positive IAM. The youngest lens in the age-dependent study data showed an almost constant equivalent refractive index and a very small IAM (see Fig. 2).

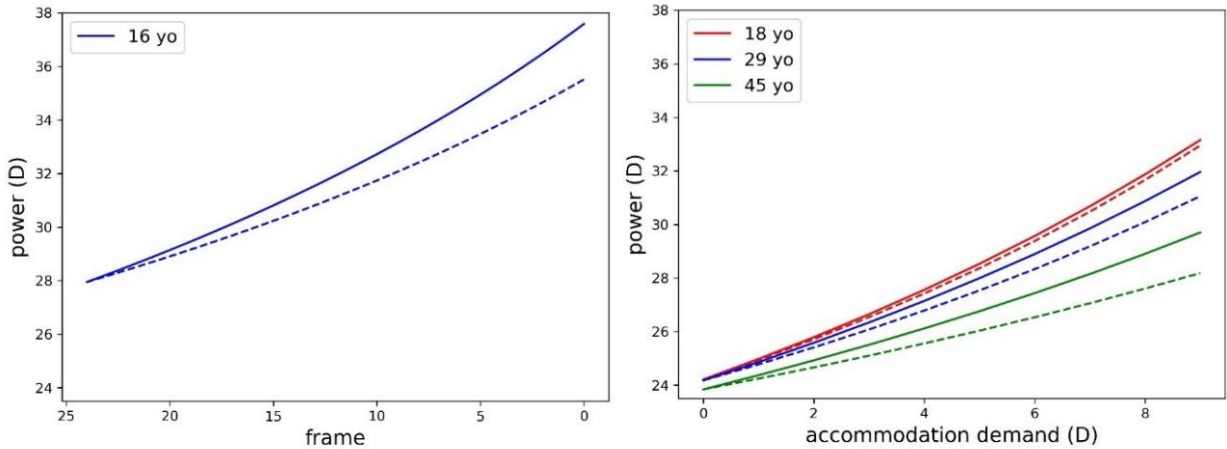


Figure 1. Accommodative lens power for each age considered. The solid line is the GRINCU lens power, calculated with the ray transfer matrix; the dashed line is the equivalent power of a two-surface homogeneous lens, calculated with the unaccommodated equivalent refractive index. On the left, results for the in-vivo video, and on the right, results for the age-dependent study data.

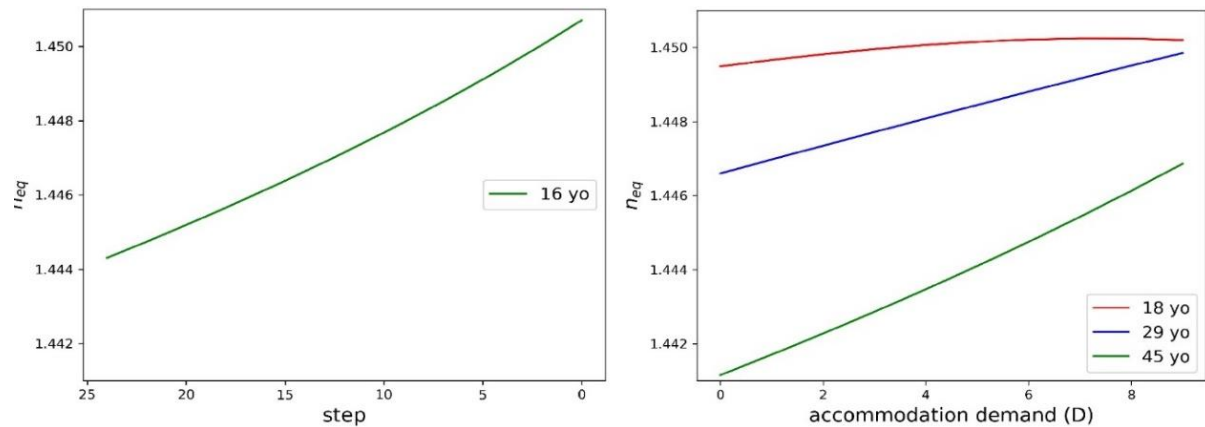


Figure 2. Equivalent refractive index as a function of accommodation. On the left, results for the in-vivo video, and on the right, results for the age-dependent study data.

Conclusion

The paraxial lens power and equivalent refractive index strongly depend on the lens's internal and external geometry. In the four cases studied, the positive IAM found is linked to the deformation of the iso-indicial surfaces, which augment the net curvature gradient inside the lens during accommodation. The equivalent refractive index increase, and subsequent IAM, becomes more prominent with age.

References

- [1] Gullstrand, A. How I found the mechanism of intracapsular accommodation. Nobel Lectures, Physiology or Medicine. 1921; 414.
- [2] Navarro, R., Baquedano, S., & Sánchez-Cano, A. I. (2021). GRINCU lens with conicoid iso-indicial surfaces: application for modeling the crystalline lens. *Optics Express*, 29(20), 30998-31009.
- [3] Hermans, E., Dubbelman, M., van der Heijde, R., & Heethaar, R. (2007). The shape of the human lens nucleus with accommodation. *Journal of Vision*, 7(10), 16-16.
- [4] Koretz, J. F., Kaufman, P. L., Neider, M. W., & Goeckner, P. A. (1989). Accommodation and presbyopia in the human eye—aging of the anterior segment. *Vision Research*, 29(12), 1685-1692.
- [5] Koretz, J. F., Cook, C. A., & Kaufman, P. L. (1997). Accommodation and presbyopia in the human eye. Changes in the anterior segment and crystalline lens with focus. *Investigative Ophthalmology & Visual Science*, 38(3), 569-578.
- [6] Koretz, J. F., Cook, C. A., & Kaufman, P. L. (2001). Aging of the human lens: changes in lens shape at zero-diopter accommodation. *JOSA A*, 18(2), 265-272.
- [7] Koretz, J. F., Cook, C. A., & Kaufman, P. L. (2002). Aging of the human lens: changes in lens shape upon accommodation and with accommodative loss. *JOSA A*, 19(1), 144-151.
- [8] Navarro, R., Lockett-Ruiz, V., & López, J. L. (2022). Analytical ray transfer matrix for the crystalline lens. *Biomedical Optics Express*, 13(11), 5836-5848.

Effect of the inner curvature gradient on crystalline lens performance

Rafael Navarro*, Veronica Lockett-Ruiz

INMA, CSIC & Universidad de Zaragoza, Zaragoza, Spain

* Corresponding author: rafaelnb@unizar.es

A novel GRINCU model of the human lens is formulated and implemented. The predicted optical performance (power, aberrations, etc.) is evaluated through both paraxial and finite ray tracing. This allows us to evaluate the effect of external (radii and conic constants) and internal (curvature gradient) geometry on lens power, spherical aberration, lens astigmatism, chromatic aberration, and off-axis aberrations.

Keywords: GRIN; crystalline lens; optical performance; lens aberrations

Introduction

The human lens has an onion-type shell structure. In optical terms, it can be realized as a high number of cemented thin meniscus lenses (shells) around a central core. The optical performance of each meniscus is mainly determined by its refractive index n and radius of curvature R . Both n and R change across the lens: n increases from the surfaces (n_s) towards the center (n_c), whereas R decreases in magnitude. This means that we have two gradients: of n and R . Our goal is to better understand the effects of this double gradient on the power and optical performance of the human lens. It is expected to have a sort of multiplicative effect [1] since the shell contribution to the power is proportional to $\Delta n R$.

Methods

The great majority of previous models considered concentric shells. The new formulation of the GRINCU lens model is based on a generalization to non-concentric shells. This is accomplished by introducing a curvature gradient parameter G [2]. This GRINCU lens model is then implemented as a cemented doublet made of its anterior and posterior parts (see Figure 1). It is based on simple assumptions which consider (non-revolution) conicoid shell surfaces and a constant gradient of R inside each part. The model is polychromatic and is not restricted to the rotationally symmetric case, and hence it can include lens astigmatism. Ray transfer matrix is used for paraxial computations, whereas both paraxial en finite ray tracing are implemented in ZEMAX. A 4-surface (homogeneous cortex and nucleus) was also impleted for comparison purposes.

Results

We computed the effect of several parameters of the model on optical performance. In particular, we study the combined effect of the conic constants (Q) and the curvature gradient (G) on lens power and spherical aberration Figure 2 compares the lens power computed by the matrix method (Matrix) and Zemax (GRINCU & 4-surfaces). The computed longitudinal spherical aberration is shown in Figure 3. Lens astigmatism, longitudinal chromatic aberration, and off-axis aberrations are computed as well.

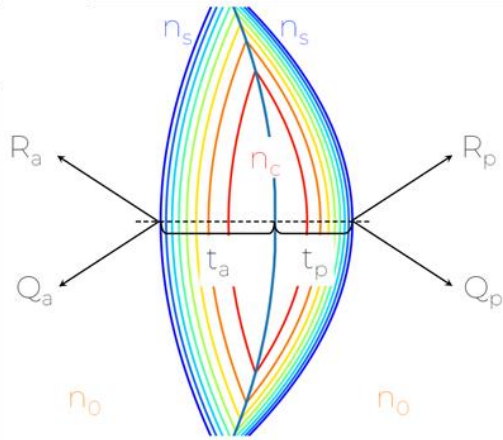


Figure 1. GRINCU lens model

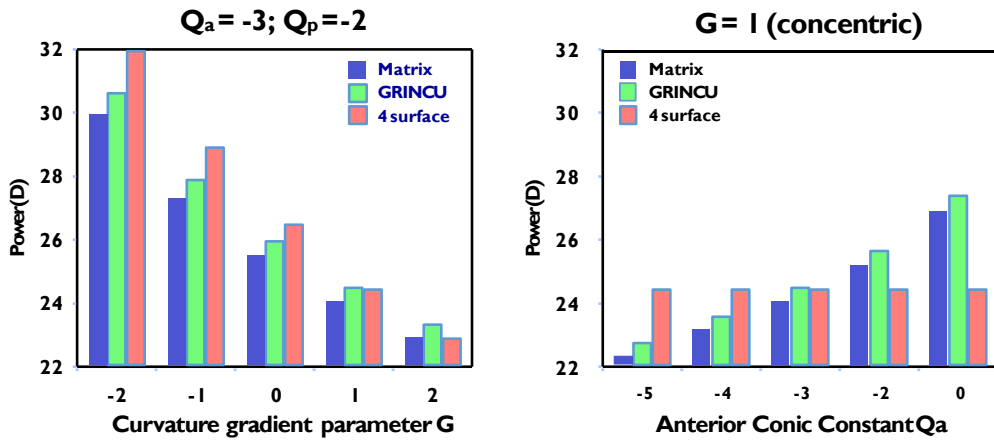


Figure 2. GRINCU lens power for different Q and G values.

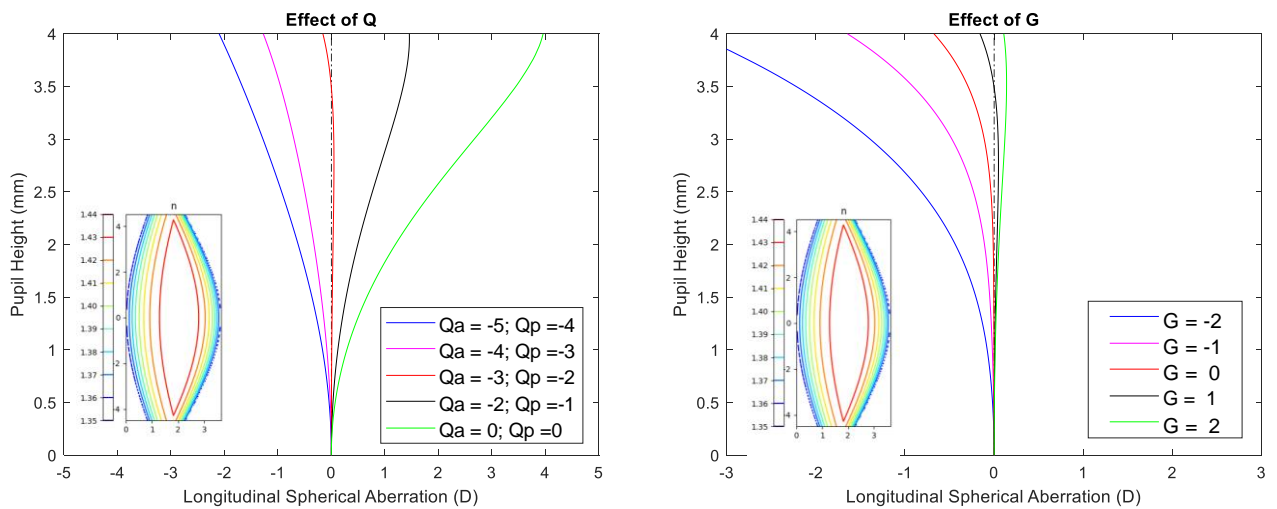


Figure 3. Longitudinal spherical aberration for different Q and G values.

Conclusion

The optical performance of the GRINCU lens is strongly dependent on both external shape and internal curvature gradient. The paraxial power decreases with G and increases with the conic constants. The spherical aberration is strongly affected by Q . The optimal values nearly correcting spherical aberrations are $Q_a = -3$ and $Q_p = -2$ (for G positive).

References

- [1] Navarro, R. and López-Gil, N. (2017). "Impact of internal curvature gradient on the power and accommodation of the crystalline lens," *Optica* 4(3), 334–340.
- [2] Navarro, R., Baquedano, S., & Sánchez-Cano, A. I. (2021). GRINCU lens with conicoid iso-indicial surfaces: application for modeling the crystalline lens. *Optics Express*, 29(20), 30998-31009.

Astigmatic power of the crystalline lens derived from ocular biometry

Tanya Evans^{1*} and Jos J Rozema²

¹ Department of Optometry, University of Johannesburg, Johannesburg, South Africa

² Visual Optics Lab Antwerp (VOLANTIS), Faculty of Medicine and Health Sciences,

University of Antwerp, Antwerp Belgium

* Corresponding author: tevans@uj.ac.za

Ocular biometry provides us with corneal surface powers and depths or thicknesses of the cornea, anterior chamber, lens, and axial length. This paper uses linear optics to obtain the equivalent power of the crystalline lens, as well as the power of the eye. An example is given based on biometry measurements taken of a real eye.

Keywords: Astigmatism; Crystalline lens power; Ocular biometry, Linear optics

Introduction

Eye modelling has been used in vision sciences for many reasons, such as to understand the optics of the eye, analyse optical phenomena or changes to ocular biometry, and to calculate the power of an intraocular lens [1]. Models range in complexity from the simplest single-surface reduced eye to multiple-surface and GRIN models, each with its own purpose.

Ocular biometry is able to provide front- and back-surface powers for the cornea (K1 and K2), as well as the depths and thicknesses for the cornea (k), anterior chamber depth (q), lens thickness (t) and axial length. Although it is possible to measure the lens surface curvatures using phakometry, this is not typically provided by commercially available ocular biometry instruments. The power of the crystalline lens, therefore, needs to be obtained through modelling methods.

This study aims to estimate the astigmatic power of the crystalline lens as well as the power of the eye using linear optics [2]. Linear optics is a paraxial method able to comprehensively model astigmatism based on a ray transfer matrix or *transference* [2].

Methods

Bennett [3] proposed a method to approximate the equivalent spherical power of the crystalline lens by ray tracing from the eye's far point to the retina, and subsequently estimate the powers of the lens surfaces for specific positions of the lenticular principal planes. This method was later reformulated and validated [4].

The proposed method obtains the equivalent power of the lens through calculation and generalizes this for astigmatic systems. Although Bennett used the far point of the eye, creating a conjugate system [2], this would not work in an astigmatic system as the far point is split into two line foci, separated by the interval of Sturm. To address the two line foci, a thin toric lens of power F_0 , described by a 2×2 symmetric dioptric power matrix [5], was placed at the spectacle plane to correct the eye for distance. This emmetropizes system S_{OE} , comprising of correction F_0 and the eye, making the incident vergence onto system S_{OE} null. Definitions of the system and its subsystems are provided in Figure 1.

One of the strengths of linear optics, which uses a 4×4 transference matrix to represent the fundamental paraxial optical properties of a system and determine how rays traverse the optical system, is its ability to account for elements that are astigmatic [2]. The transference is given as $\mathbf{S} = \begin{pmatrix} \mathbf{A} & \mathbf{B} \\ \mathbf{C} & \mathbf{D} \end{pmatrix}$, where the 2×2 submatrices \mathbf{A} and \mathbf{D} are unitless, \mathbf{B} is in units of length and \mathbf{C} in inverse length, usually dioptres (D) [2]. For a detailed explanation of linear optics, please see [6]. The transference of S_{0Ae1} is obtained from the known biometric parameters and comprises the transferences of the elementary systems, multiplied in reverse such that $S_{0Ae1} = S_{e1} S_q S_{K2} S_k S_{K1} S_x S_{F0}$. The lenticular principal plane positions T_{P1} and T_{P2} are estimated using the customised Bennett constants [4], which allows estimating vergence $L_{P1} = C_{0Ae1} A_{0Ae1}^{-1}$ at T_{P1} [7]. Next, the transference $S_{e2v} = S_v S_{e2}$ is obtained, as well as the vergence $L_{P2} = B_{e2v}^{-1} A_{e2v} = n_v(z_v - e_2)^{-1} I$ needed at T_{P2} to focus light on the retina at T_R (I is the identity matrix). L_{P1} and L_{P2} are symmetric 2×2 vergence matrices and L_{P2} is, of necessity, a scalar matrix [5, 7]. The equivalent power of the lens is then obtained from Gauss's relationship $F_{eq} = L_{P2} - L_{P1}$, with F_{eq} a symmetric, 2×2 dioptric power matrix [2, 5, 7]. The power of the eye is obtained from the transference of the eye, without F_0 : $S_E = (S_v)(S_{e2} S_{Leq} S_{e1})(S_q S_{K2} S_k S_{K1}) = S_v S_L S_A$, where the whole-eye power $F_E = -C_E$ [2]. The method is first tested on the Gullstrand-Emsley eye and results compared to Bennett's method and the actual power of the lens. Next, the method is applied to the left eye of a 63-year-old man with a large internal astigmatism, recruited during Project Gullstrand [8] for which the biometry is provided in Table 1.

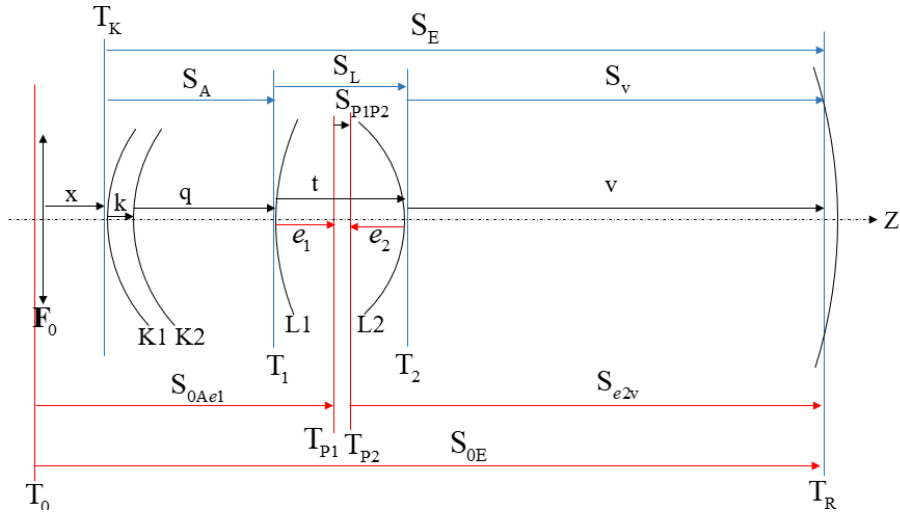


Figure 1: Two systems superimposed in one diagram, indicated by red and blue lines. The optical system of the eye S_E (blue) has a longitudinal axis Z and is bound by the entrance plane T_K , immediately in front of the cornea, and the posterior plane T_R , immediately in front of the retina. Transverse planes T_1 and T_2 define the subsystem of the (thick) lens S_L , effectively dividing the eye into three subsystems, anterior S_A , lens S_L and posterior S_v . The corrected system S_{OE} (red) includes spectacle refractive compensation F_0 from T_0 to T_R . T_{P1} and T_{P2} are the principal planes of the crystalline lens. S_{OE} comprises subsystems S_{0Ae1} (from T_0 to T_{P1}), the equivalent lens at S_{P1P2} and S_{e2v} (from T_{P2} to T_R).

Results

The calculated results from the above method were compared to Bennett's results, based on the emmetropic Gullstrand-Emsley eye [3]. The same parameters for the eye and constants to estimate principal plane positions of the lens as Bennett [3] were used. Only the spherical component was traced, that is, $(M \ 0 \ 0)^T$. Bennett gives the lens power as 21.76 D and we obtained 21.79 D, using transferences. Similarly, the power of the eye is 60.49 D compared to 60.50 D obtained using transferences and the estimated lens power. Both the lens- and eye powers compare well to Bennett's results. The accuracy of the lens, and consequently eye-powers, depends on the estimated positions of

the lens principal planes, determined by the distribution of the lens surface-powers.

The method was then applied to the real eye of a 63-year-old man with refractive error of $2.25/-4.25 \times 82$ (or $\mathbf{f}_0 = (0.13 \ -2.09 \ 0.37)^T$). The ocular biometry in Table 1 corresponds with a lens power of $(27.97 \ -0.55) \text{ D}$ (or $\mathbf{f} = (24.76 \ 3.22 \ -0.55)^T \text{ D}$ or $28.02/-6.53 \times 175.1^\circ$). The transference of the eye is $\mathbf{S}_E = \begin{pmatrix} -0.0310 & 0.0061 & 0.0162 \text{ m} & 0.0000 \text{ m} \\ 0.0061 & 0.0381 & 0.0000 \text{ m} & 0.0166 \text{ m} \\ -63.3021 \text{ D} & 0.4534 \text{ D} & 0.8800 & 0.0024 \\ 0.4535 \text{ D} & -58.1378 \text{ D} & 0.0024 & 0.9080 \end{pmatrix}$ and, from the relationship $\mathbf{F} = -\mathbf{C}$, the power of the eye is $(63.30 \ -0.45) \text{ D}$ (or $\mathbf{f} = (60.72 \ 2.58 \ -0.45)^T \text{ D}$ or $63.34/-5.24 \times 175.0^\circ$).

Table 1. Ocular biometry of an eye

Parameter	Powers $(M \ J_0 \ J_{45})^T$	Gaps	Refractive indices
Anterior cornea (K1)	$\mathbf{f}_{K1} = (46.07 \ 0.02 \ 0.05)^T$		
Cornea (k)		498 μm	1.376
Posterior cornea (K2)	$\mathbf{f}_{K2} = (-5.80 \ -0.09 \ -0.05)^T$		
Anterior chamber / aqueous (q)		2.71 mm	1.336
Lens (t)		4.60 mm	1.436
Axial length (AL)/ vitreous (v)		24.08 mm	1.336

Conclusion

Linear optics provides a simple method to obtain the equivalent astigmatic power of the crystalline lens in an eye where the ocular biometry is known. Consequently, the transference and astigmatic power of the eye itself are available for a real eye as opposed to a model eye. Whilst linear optics is limited to paraxial optics, its strength lies in its ability to account for astigmatism of all surfaces. This opens the door for understanding the astigmatic contribution of the crystalline lens as well as the quantitative analysis of eyes [8].

References

- [1] Atchison DA and Thibos LN. Optical models of the human eye. *Clin Exp Optom.* 2016. 99: 99-106.
- [2] Harris WF. A unified paraxial approach to astigmatic optics. *Optom Vis Sci.* 1999. 76: 480-499.
- [3] Bennett AG. A method of determining the equivalent powers of the eye and its crystalline lens without resorting to phakometry. *Ophthal Physiol Opt.* 1988. 8: 53-59.
- [4] Rozema JJ, Atchison DA and Tassignon MJ. Comparing methods to estimate the human lens power. *Invest Ophthalmol Vis Sci.* 2011. 52: 7937-7942.
- [5] Rubin A, Evans T and Hasrod N. Dioptric power and refractive behaviour: a review of methods and applications. *BMJ Open Ophth.* 2022. 7: e00929.).
- [6] Evans T and Rubin A. Linear optics of the eye and optical systems: a review of methods and applications. *BMJ Open Ophthalmol.* 2022; 7: e000932.
- [7] Harris WF. Wavefronts and their propagation in astigmatic optical systems. *Optom Vis Sci.* 1996. 73: 605-612.
- [8] Rozema J, Hershko S and Tassignon M. The components of adult astigmatism and their age-related changes. *Ophthal Physiol Opt.* 2019. 39: 183-193.

Influence of straylight on simulated driving performance in young adults

Sarah Hershko,^{1,2,*} Tom Brijs,³ Karel Van den Bergh,³ Wim Ectors,³
Carina Koppen,^{1,2} Jos Rozema,^{1,2} Veerle Ross³

¹ Antwerp University Hospital, Department of Ophthalmology, Edegem, Belgium

² University of Antwerp, Department of Medicine and Health Sciences, Wilrijk, Belgium

³ UHasselt, School of Transportation Sciences, Transportation Research Institute (IMOB), Hasselt, Belgium

* Corresponding author: sarah.hershko@uantwerpen.be

This study investigates how an increase in straylight (SL) affects the driving capability of young, healthy volunteers in various real-life driving circumstances using a driving simulator. Participants were asked to (virtually) drive along a certain course in four conditions: a regular drive (baseline), a drive in the presence of a glare source and a drive in the presence of a glare source while wearing two types of straylight filters (SLF1 and SLF2). The drives included six scenarios (e.g. pedestrian crosses the road). The van den Berg straylight meter (C-Quant) was used to quantify the glare experienced by participants. A total of 21 Participants between the ages of 19 and 38 years were included in the study. Overall, driving performance was significantly influenced by increased straylight. The analysis of different driving scenarios brought a better in depth understanding of the effect of glare on driving performance.

Keywords: Straylight, glare, driving safety, driving simulator

Introduction

Glare is common phenomenon in which an observer is confronted with a bright light source within a relatively dim background, such as when looking at the headlights of oncoming cars at night. This causes a considerable loss in contrast and an instinctive need to divert the gaze away from the source, which is often experienced as highly unpleasant. The phenomenon is caused by straylight (SL), the scattering of light by microscopic imperfections in the ocular media that produce a luminous veil over the retinal image. Straylight does not correlate well with visual acuity [1], and both contribute about equally to quality of vision [2]. This suggests that straylight represents an aspect of visual function that should be considered separately from visual acuity. Currently in Belgium, visual acuity in bright and dim conditions, as well as the visual field are considered the primary parameters for the visual assessment of drivers [3]. While important, a focus on visual acuity and visual field alone can be problematic as these are not affected much by increased straylight [4],[5]. If straylight would be considered, however, a clear and unacceptable risk becomes apparent, as confirmed by the Belgian traffic accident statistics. These show that 1 accident every 2 days and 3% of all traffic fatalities may be associated with glare [6]. To this end, a recent paper on visual standards for safe driving advised including glare sensitivity standards, but no legislative efforts to that effect have been made thus far. To highlight the importance of glare in traffic, this study determines how increased straylight affects the driving capability of young, healthy volunteers in a driving simulator under real-life circumstances.

Methods

Participants were active drivers recruited from the personnel and students at the Hasselt University. The data collected consisted of a general questionnaire on biographical data, such as age, sex, driving

experience (i.e., period since obtaining licence) and exposure (i.e., driven distance/week). In addition, the straylight test using the van den Berg straylight meter (Oculus C-Quant) [7], as well as the self-administered VFQ-25/NL questionnaire to assess the visual function. This was supplemented by a clinical measurement of the subject's habitual correction, visual acuity, and straylight. Finally, participants were asked to drive along a certain course in a driving simulator (Figure 1) under four conditions: a baseline ride, a ride with a bright glare source (*R*), and two rides with the glare source while wearing a light scattering filter simulating mild cataract (*SLF1*) and moderate levels of cataract (*SLF2*). Each ride included 6 events (e.g., pedestrian crossing the road, dark stationary motorcycle, etc.). This yielded 37 parameters for analysis, including mean speed, stopping distance, and position of the road. One such parameter is the time to collision (*TTC*), the time required for two vehicles to collide if they continue at their present speed and on the same path. *TTC* is calculated at moment of release of the gas pedal (*TTC-detection time, TTCdt*) and when the participant pushed the break (*TTC-reaction time, TTCr*). The minimum *TTC* (*min TTC*) was calculated as the distance between the hazard and the driver, divided by speed. This is an indicator for the severity of an encounter, where lower *min TTC* corresponds with a higher risk of collision [8].

Results

Twenty-one participants aged 19 to 38 years were included (see Table 1 for demographic variables). There were significant differences in straylight between *R*, *SLF1* and *SLF2* measurements (1.09 ± 0.05 , 1.34 ± 0.04 and 1.49 ± 0.02 log straylight units, respectively. ANOVA, $p < 0.001$).

The analysis of the scenarios demonstrated that the most significant effects of increased straylight on driving was detected when the critical event occurred closest to the glare source (e.g., stationary motorcycle in the middle of the road). Table 2 shows the driving parameters and their p-values for the scenarios with the stationary motorcycle and the crossing of the pedestrian, when compared between the different driving conditions.

Detection time and reaction time in the scenario with the stationary motorcycle significantly increased as glare hindrance increased ($p < 0.001$, ANOVA). This was not the case for the crossing pedestrian, where reaction time was significantly lower for *SLF2* (1.386 ± 0.122 s) compared to both *R* (1.746 ± 0.077 s, $p = 0.013$, ANOVA) and *SLF1* (1.869 ± 0.058 s, $p = 0.001$, ANOVA). In the scenario with the stationary motorcycle *TTCdt*, *TTCr* and *min TTC* all significantly decreased with added glare hinder ($p < 0.001$, ANOVA for *TTCdt*; $p < 0.001$, Friedman for *TTCr* and *min TTC*). Meanwhile, in the scenario with the crossing pedestrian *TTCr* was significantly higher for *SLF2* (1.659 ± 0.121 s) compared to *R* (1.203 ± 0.067 s, $p = 0.013$, ANOVA) and to *SLF1* (0.993 ± 0.043 s, $p = 0.001$, ANOVA). *TTCr* for *SLF1* was significantly lower compared to the *TTCr* of *R* ($p = 0.029$, ANOVA).

In the 250 m road segment between events, where participants drove straight ahead without obstacles, both mean and minimum driving speed decreased significantly with the light source and the scatter filters (ANOVA, $p < 0.001$). The maximum speed showed only a significant decrease in speed for *SLF2*.



Figure 1: Fixed-base driving simulator

Table 1: Demographics

Total participants	21
Male: Female	11:10
Mean age	26.33 ± 1.44 years
Age range	19 - 38 years
Average driving experience	6.81 ± 1.29 years
Driving experience range	< 1 year - 19 years

Table 2: Changes in driving parameters

Parameter	Baseline	Light source	SLF1	SLF2	ANOVA / Friedmann
Stationary motorcycle					
Detection time (s)	0.713	3.808	6.554	7.213	< 0.001
Reaction time (s)	1.875	5.500	7.146	8.634	< 0.001
TTC Detection time (s)	6.903	4.543	2.044	2.353	< 0.001
TTC Reaction time (s)	6.013	3.058	1.476	0.986	< 0.001
Min TTC (s)	5.268	2.834	0.940	0.431	< 0.001
Stop distance to motor (m)	21.596	13.892	5.772	3.272	< 0.001
Mean speed M10 (kph)	71.064	65.441	61.497	59.183	< 0.001
Mean Speed M250 (kph)	20.068	19.531	27.383	36.314	< 0.001
Speed change (kph)	50.996	45.910	34.114	22.869	< 0.001
Pedestrian crosses road					
Detection time (s)	2.097	2.376	0.976	2.785	0.509
Reaction time (s)	1.746	1.302	1.869	1.386	0.041
TTC Detection time (s)	1.628	0.318	1.187	2.554	---
TTC Reaction time (s)	1.203	1.601	0.993	1.659	0.026
Min TTC (s)	0.745	1.516	0.662	1.370	0.145
Speed change (kph)	24.996	22.847	20.609	21.876	0.182

TTC: time to collision, M10: the first 10m in a 250m zone before the hazard location M250: the last 10m in a 250m zone before the hazard location

Conclusion

These results clearly demonstrate that an increase in straylight (SL) affects the driving performance of young, healthy volunteers in the scenarios considered. These were intentionally chosen to best assess the effect of the glare source. The effect is stronger in scenarios where the critical event occurred closer to the source, such as for the stationary motorcycle, while less effects are seen in scenarios such as the crossing pedestrian, which focused on events farther away from the glare source. The outcomes are best seen in the detection time, reaction time, *TTCdt*, *TTCrt* and *min TTC*.

Overall, increased straylight significantly leads drivers to have slower response times, longer stopping distances and slower driving speeds, which could have important consequences for traffic safety.

References

- [1] T. J. T. P. Van Den Berg et al., "Straylight Effects with Aging and Lens Extraction," *Am. J. Ophthalmol.*, vol. 144, no. 3, 2007, doi: 10.1016/j.ajo.2007.05.037.
- [2] I. J. E. van der Meulen et al., "Straylight measurements as an indication for cataract surgery," *J. Cataract Refract. Surg.*, vol. 38, no. 5, pp. 840–848, 2012.
- [3] Vias, "De online Referentie van de wegcode," , 1998. <https://www.wegcode.be/nl> (accessed 28/3/2023).
- [4] I. Adamsons, G. S. Rubin, S. Vitale, H. R. Taylor, and W. J. Stark, "The effect of early cataracts on glare and contrast sensitivity: a pilot study," *Arch. Ophthalmol.*, vol. 110, no. 8, pp. 1081–1086, 1992.
- [5] D. B. Elliott and P. Situ, "Visual acuity versus letter contrast sensitivity in early cataract," *Vision Res.*, vol. 38, no. 13, pp. 2047–2052, 1998.
- [6] Ville de Hannut, "Conducteurs éblouis par le soleil: 1 accident tous les 2 jours en Wallonie," 2018, [Online]. Available: <http://bitly.ws/Pro5>.
- [7] I. J. E. Van Der Meulen et al., "Straylight measurements as an indication for cataract surgery," *J. Cataract Refract. Surg.*, vol. 38, no. 5, pp. 840–848, 2012, doi: 10.1016/j.jcrs.2011.11.048.
- [8] M. M. Minderhoud and P. H. L. Bovy, "Extended time-to-collision measures for road traffic safety assessment," *Accid. Anal. Prev.*, vol. 33, no. 1, pp. 89–97, 2001.

Spherical aberration and accommodative lag in young adults

María Mechó-García^{1*}, Vicente Fernández-Sánchez², Norberto López-Gil²
and José Manuel González-Méijome¹

¹ Clinical & Experimental Optometry Research Lab, Center of Physics (Optometry),
School of Sciences, University of Minho, Braga, Portugal.

² Clínica Universitaria de Visión Integral (CUVI), University of Murcia, Murcia, Spain

* Corresponding author: mmechogarcia@fisica.uminho.pt

The aim of this study was to evaluate the relationship between primary and secondary spherical aberration, on the subject's accommodative response measured with dynamic retinoscopy (MEM), and on the amplitude of accommodation measured with two different subjective methods (Minus lens and Push-up method). In the 88 eyes evaluated (24.14 ± 3.24 years of age, range: 20-35 years) there was no relationship between accommodative lag and age. No statistically significant correlations were found between the three methods used to assess accommodative response and accommodative amplitude with the different Zernike coefficients C40 and C60, and Pearson's coefficients show values of negligible correlation. Coefficients measured for far vision did not explain the variability in accommodative response and/or accommodation amplitude. However, there was a trend for higher positive spherical aberration in eyes with larger values of accommodative lag.

Keywords: Zernike coefficients; amplitude of accommodation; accommodative response, accommodative lag.

Introduction

The assessment of the accommodative response (AR) to a near target is an important component of any routine eye examination. Accommodation produces changes in the subjects' wavefront, which are of different magnitudes in different subjects [1-2]. The AR to the same vergence is also variable among subjects with most subjects showing a reduced response (accommodative lag) as measured with clinical methods. The aim of the study is to analyse if spherical aberration is related to the variability in accommodative lag.

Methods

Fifty healthy subjects without a history of ocular abnormality participated in this study. A total of 88 eyes were included in the analysis. All subjects were between 20 and 35 years old, with a mean age of 24.14 ± 3.24 years. The mean visual acuity measured monocularly was -0.09 ± 0.54 logMAR measured using a Bailey-Lovie high-contrast test at 6 m. The objective mean sphere was -0.94 ± 1.92 D and the mean cylinder was -0.49 ± 0.49 D, measured with the auto-refractometer. The subjective mean sphere was -0.79 ± 2.04 D and the mean cylinder was -0.38 ± 0.49 D. Wavefront was measured with an aberrometer based on the Hartmann-Shack principle (IRX3, Imagine Eyes, Orsay, France) focusing on a distant point using the internal Badal system of the instrument, under monocular conditions. Then, the stimulus vergence was increased from 0 to 5 D (near vision) in steps of 0.5 D. The AR for each Zernike coefficient was calculated as the difference between the value at 5.0 D and the value at 0 D.

The results obtained by the IRX3 were exported with a maximum pupil and then rescaled for 4.0 mm

pupil sizes based on the formulas described by Jim Schwiegerling (2002) [3]. An analysis was performed comparing the Zernike coefficients with radial symmetry C40 and C60 with Lag, push-up method and minus lens. To determine a relationship between the Zernike coefficients and the method used, bivariate correlations to determine Spearman's correlation coefficient for not parametric sample was performed.

The accommodative amplitude (AA) was subjectively assessed using the minus lens and push-up method. The accommodative Lag was assessed with the dynamic retinoscopy monocular estimated method (MEM) in both eyes.

Results

Figure 1 shows the AA as a function of age (A) and the accommodative Lag as a function of age (B). It can be seen that although the AA decreases with increasing age, there is no relationship between the accommodative Lag and age. Furthermore, can be observed that the AA presents higher values when measured with the push-up method (Figure 1. A).

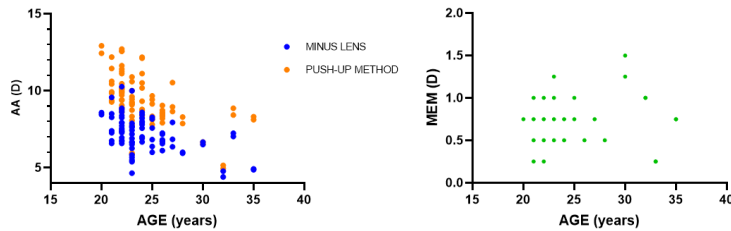


Figure 1. Variation of the AA (measured with minus lens and push-up Method) (A) and MEM (B) as a function of age.

The distribution of the data obtained from the MEM as a function of the Zernike coefficients C40 (A) and C60 (B) is presented in Figure 2. No statistically significant correlations were observed between MEM and C40 ($\text{Rho}=-0.007, p = 0.946$) nor between MEM and C60 ($\text{Rho}=-0.101, p = 0.351$) both of them suggest a negligible correlation. Despite this, the distribution of the C40 coefficient was between 0 μm and 0.05 μm for MEM values $\leq +0.50 \text{ D}$, for higher values of the MEM the C40 was distributed between -0.04 μm and 0.08 μm (Figure 3. A). C60 presents values between 0.003 μm and -0.005 μm for MEM values $\leq +0.50 \text{ D}$, for higher values of MEM, the C60 presents values between -0.04 μm and -0.006 μm (Figure 3. B).

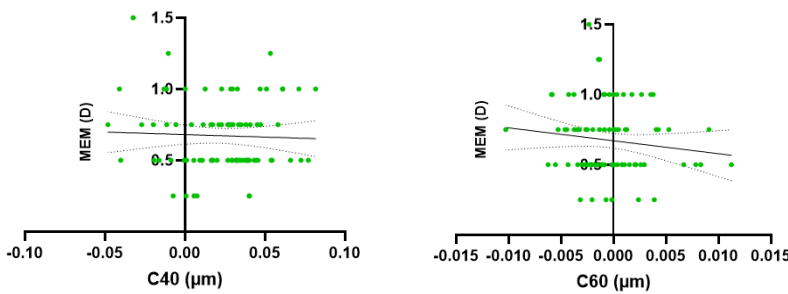


Figure 2. Variation of the Zernike coefficient corresponding to the C40(A) and C60 (B) as a function of the accommodative Lag measured with the MEM method.

The Mann-Whitney U Test was performed for independent samples for C40 and C60, between two groups (MEM values $\leq 0.50 \text{ D}$ and MEM values $\geq 0.75 \text{ D}$). No statistically significant differences were found for any of the Zernike coefficients evaluated in C40 ($p = 0.773$) and C60 ($p = 0.789$) (Figure 3). No statistically significant correlations were observed between Minus lens and C40 ($\text{Rho}=0.219, p = 0.040$) nor between Minus lens and C60 ($\text{Rho}=-0.123, p = 0.253$) both of them suggest a weak correlation.

The AA of accommodation measured with the subjective method minus lens, presents values between 6.0 D and 9.0 D for the C40, and in a smaller range for C60, between 6.0 D and 8.0 D.

In contrast to the Minus lens method, the AA measured from the push-up method shows higher values between 8.0 D and 12.0 D, in both Zernike Coefficients analysed C40 and C60.

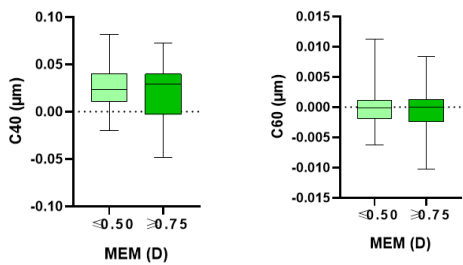


Figure 3. Box-plot of the values C40 and C60 as a function of the MEM divided into two groups (≤ 0.50 D and ≥ 0.75 D). The black line represents the mean of each of the groups.

No statistically significant correlations were observed between Push-up method and C40 ($\text{Rho}=0.187$, $p=0.082$) nor between Push-up method and C60 ($\text{Rho}=-0.065$, $p=0.549$) both of them suggest a weak correlation. There was no clear trend in the difference between the Zernike coefficients at 0D and 5.0 D with respect to the MEM values (Figure 4). C40 values of the difference between the two accommodative demands studied are in the range of 0 μm to -0.1 μm . However, the values of the difference of C60 are between -0.01 μm and 0.01 μm .

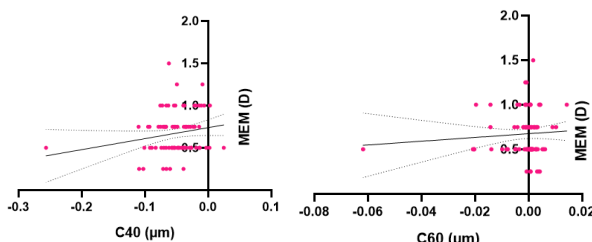


Figure 4. Representation of the C40 (A) and C60 (B) calculated between the difference in the accommodated and unaccommodated stage of the eye as a function of the accommodative lag.

Conclusions

Push-up method results had an apparently higher AA (Figure 1. A), compared to the minus lens methods. Many clinicians observed higher AA with the push-up method [4-5]. No clear trends were found when comparing the Zernike coefficients C40 and C60, measured in far-distance vision, with the different objective (MEM dynamic retinoscopy) and subjective (Push-up method and minus lens) measurements. No clear trends were shown in the C40 and C60 calculated differences from the values of the accommodated eye (0 D) and the unaccommodated eye (5.0 D), in reference to the accommodative lag values obtained. Fourth and sixth-order spherical aberration do not explain the differences in Lag accommodation in this sample of young adult healthy eyes. However, there was found a trend for eyes with a higher lag of accommodation to present a positive spherical aberration coefficient that deserves further investigation.

Acknowledgment

This project has received funding from: the European Union's Horizon 2020 research and innovation programme under the Marie Skłodowska-Curie grant agreement No 956720.

References

- [1] López-Alcón D, et al. Optical factors influencing the amplitude of accommodation. *Vision Res.* 2017;141:16-22.
- [2] López-Gil N, Fernández-Sánchez V. The change of spherical aberration during accommodation and its effect on the accommodation response. *J Vis.* 2010;10(13):12.
- [3] Schwiegerling J. Scaling Zernike expansion coefficients to different pupil sizes. *J Opt Soc Am A Opt Image Sci Vis.* 2002;19(10):1937-1945.
- [4] Ostrin LA, Glasser A. Accommodation measurements in a presbyopic and presbyopic population. *J Cataract Refract Surg.* 2004;30:1435-44.
- [5] Rosenfield M, Cohen AS. Repeatability of clinical measurements of the amplitude of accommodation. *Ophthalmic Physiol Opt.* 1996; 16:247-9.

Variability in wavefront changes during sustained reading and recovery in presbyopic eyes

Ebrahim Safarian Baloujeh^{1*}, José M. González-Méijome²

¹ INMA, Consejo Superior de Investigaciones Científicas & Universidad de Zaragoza, Zaragoza, Spain

² Department and Center of Physics – Optometry and Vision Science, School of Science Braga, Portugal

* Corresponding author: esafarian@unizar.es

This study aimed to evaluate the impact of sustained reading on temporal changes of the wavefront error. A near vision reading experiment was conducted, and the wavefront aberration of the eyes was recorded using an IRX3 Shack-Hartmann aberrometer before and at 3 moments after the task. The results showed that small changes in Zernike coefficients can be detected after a sustained visual task under different lighting conditions, demonstrating some predominant patterns. Total RMS of higher order aberrations increased immediately after the reading task and then decreased in subsequent measurements. HOA RMS which includes comatic (3rd order) and spherical-like aberrations (4th and 6th order) showed a similar trend of changes. The dynamic changes in HOA reported here might be associated to the biomechanical properties and changes in decentration of crystalline lens after sustained near vision tasks in the presbyopic subjects.

Keywords: ocular wavefront; Zernike coefficients; aberrometry; comatic aberration

Introduction

Accommodation is the ability of the eye to adjust the focusing power of the lens in order to see objects clearly [1]. Eye loses this ability gradually due to aging which is called presbyopia [2]. However, small changes are possible in lens position and geometry in response to accommodative stimuli in presbyopic eyes [3]. Lens cortex may keep some elasticity [4] and some level of accommodation ability during visual tasks such as reading a book. The small deformation of the lens cortex in presbyopes may contribute to changes in higher order aberrations (HOA). These changes can be studied using aberrometry technique [5]. The crystalline lens of young people reshapes back to the relaxed state immediately after doing a visual task, but this happens with some delay in partially presbyopic lenses [6].

The purpose of this study was to evaluate the impact of sustained reading on temporal changes of the wavefront error in presbyopic subjects after sustained reading activity.

Methods

Thirteen healthy volunteers with ages ranging from 44 to 57 years, were asked to perform a near vision reading task under two lighting conditions: first, ambient light was maximum (255.81 lux, high lighting condition), and the brightness of the reading device was set to the highest value (where pointing luminance-meter to a white circle and a black circle yielded 362.54 cd/m² and 2.23 cd/m² respectively. Michelson contrast equals 0.987). Second, the ambient light was dimmed (0.97 lux, low lighting condition), and brightness of the device was set to the lowest value (luminance of a white circle and a black circle were 5.46 cd/m² and 0.02 cd/m² respectively. Michelson contrast equals 0.992).

A laptop (Microsoft Surface Book 2, Microsoft.) with a screen size of 3000 x 2000 pixels was used for

performing this reading task. Baseline aberrometry was always performed by the same observer upon arrival of the participant before starting the reading. Participants rested their chin and forehead on a head movement stability tool at a distance ranging from 20 cm to 45 cm away from the reading device. This distance was chosen in a way that made the subject's eye have maximum accommodating effort where the text to read started to blur. The subjects were asked to read a text for 20 minutes in the above-mentioned high and low lighting conditions. Aberrometry measurements were performed using an IRX3 Shack-Hartmann aberrometer (Imagine Eyes, Orsay, France) before the reading activity, right after doing the activity, 5 minutes, and 10 minutes after finishing the activity. Measurements were made in triplicated at each time point and then averaged for subsequent analysis. Aberrometric data of each eye was rescaled to the smallest value of maximum round pupil as recorded during each measurement.

Results

The results of the near vision reading experiment show that defocus aberration (C_2^0 coefficient) in high lighting condition increases right after performing visual tasks and recovers to the baseline value in the subsequent measurements in 42% of eyes. This percentage for low lighting condition reported as 54% .

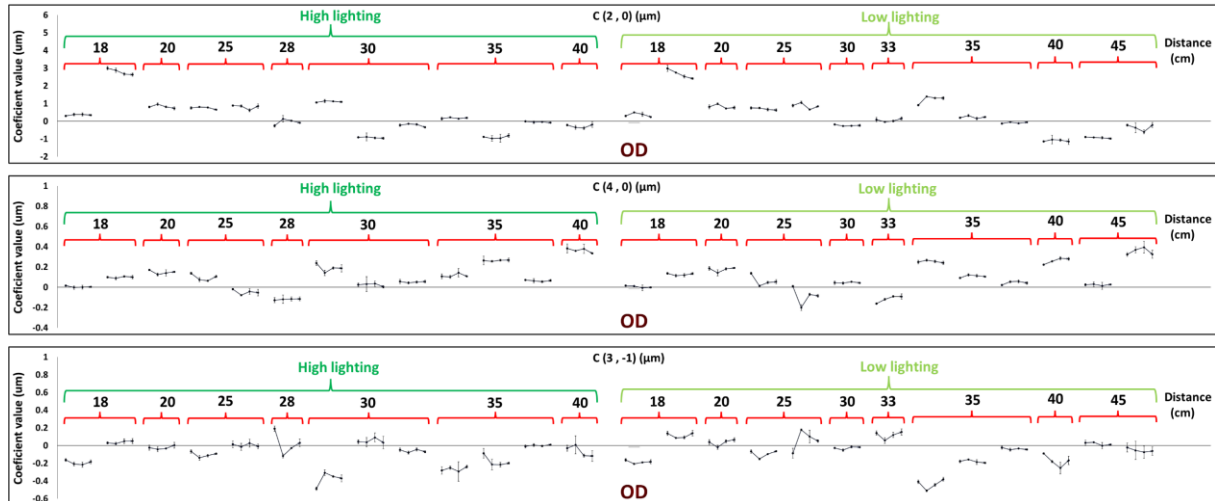


Figure 1. C_2^0 , C_4^0 , and C_3^{-1} coefficients values of right eyes of subjects, before, right after, after 5 minutes, and after 10 minutes of near vision task, respectively, for high and low lighting conditions, with respect to distance to the stimulus. Each pattern is for one subject.

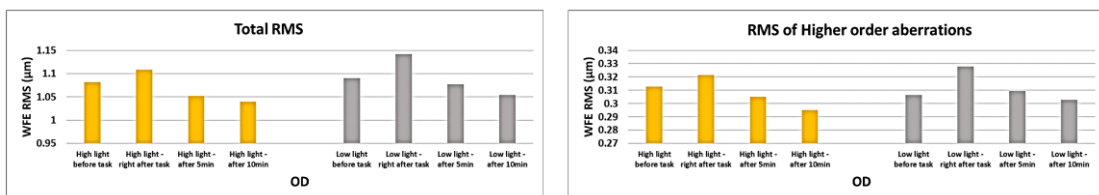


Figure 2. Average of total RMS and RMS of higher order aberrations for right eyes in high and low lighting conditions, before, right after, after 5, and after 10 minutes of near vision task.

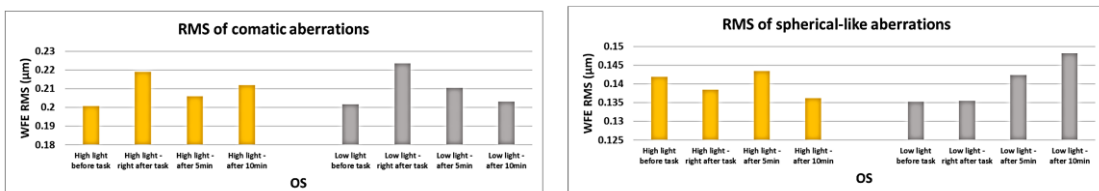


Figure 3. Average RMS of comatic and spherical-like aberrations of left eyes in high and low lighting conditions, before, right after, after 5, and after 10 minutes of near vision task.

The C_4^0 coefficient which represents primary spherical aberration undergoes a decrease right after the task and then increases in 46% of eyes, in high lighting condition. This trend was also observed for C_4^0 coefficient in 27% of eyes in low lighting condition. For vertical coma, we see a decrease and then increase trend in 42% of eyes in high lighting condition. In low lighting, the same trend appeared in 73% of eyes for C_3^{-1} coefficient. Results of changes in vertical coma showed meaningful increase in low lighting condition, but not other coefficients. Confirming it with more subjects is beneficial.

Total RMS of aberrations increased after finishing the reading task and then decreased in subsequent measurements. RMS of higher order aberrations which include comatic and spherical-like aberrations showed a similar trend of changes. However, RMS of spherical-like aberrations (high lighting) decreased after task and recovered in 5- and 10-minutes aberrometric measurements. As expected, measuring HOA right after near vision task show more increase in low lighting condition due to pupil enlargement than high lighting, when we see a similar trend.

Conclusions

It was found that after a sustained visual task under different lighting conditions the total RMS of aberrations and RMS of higher order aberrations increased immediately after finishing the near vision reading task, and then decreased while crystalline lens reshaped to its relaxed condition [7]. RMS of comatic aberrations shows a similar trend of changes but RMS of spherical-like aberrations demonstrated an opposite trend. Moreover, small changes in some of Zernike coefficients could be detected, demonstrating some predominant patterns that deserve further investigation. The potential explanation for this phenomenon is that the crystalline lens drops downward during accommodation due to gravity which leads to change in higher order aberrations. Additionally, the morphological deformation during sustained accommodation might have some inertia after the reading task stops. During the recovery period after the task, it is expected that the crystalline lens reshapes back to the relaxed state with different delays in partially presbyopic subjects due to the changing biomechanical properties of the lens. Therefore, it is observed that different eyes might show different relaxation times to recover and aberrometry might be able to measure those differences.

Acknowledgement

The EU's Horizon 2020 research and innovation programme under the Marie-Curie grant agreement No 956720.

References

- [1] von Helmholtz H. Über der Akkommodation des Auges. Archiv Ophthalmol. 1855; 1:1-89.
- [2] Weale R. Presbyopia toward the end of the 20th century. Surv Ophthalmol. 1989; 34(1):15-30.
- [3] He L, Donnelly WJ 3rd, Stevenson SB, Glasser A. Saccadic lens instability increases with accommodative stimulus in presbyopes. J Vis. 2010; 10(4):14.1-16.
- [4] Heys KR, Cram SL, Truscott RJ. Massive increase in the stiffness of the human lens nucleus with age: the basis for presbyopia? Mol Vis. 2004; 10:956-63.
- [5] McLellan JS, Marcos S, Burns SA. Age-related changes in monochromatic wave aberrations of the human eye. Invest Ophthalmol Vis Sci. 2001; 42:1390-1395.
- [6] Orduna-Hospital E, Safarian Baloujeh E, Navarro R, Sanchez-Cano A. Optical and motor changes associated with lighting and near vision tasks in electronic devices. JEMR, 2023; 16(2). [7] Gomes JRM, Franco SMB. Near Vision Tasks and Optical Quality of the Eye. J Ophthalmic Vis Res. 2021;16(4):620-630.

Optical coherence elastography assessment of mechanical and refractive changes induced by different corneal cross-linking protocols

Matteo Frigelli¹, Philippe Büchler¹ and Sabine Kling^{1,2*}

¹ ARTORG Center for Biomedical Engineering Research, University of Bern, Bern, Switzerland

² Institute for Biomedical Engineering, ITET department, ETH Zürich, Zürich, Switzerland

* Corresponding author: sabine.kling@unibe.ch

Biomechanical properties play an important role in the diagnosis and treatment of corneal ectasia. By increasing tissue stiffness, corneal cross-linking (CXL) stops the progression of keratoconus, yet the relation between mechanical and optical changes remains poorly understood. Here, we apply optical coherence elastography (OCE) to quantify the refractive and mechanical effects of patterned CXL. Three treatment protocols were investigated: standard Dresden CXL (fluence of 5.4 J/cm²), accelerated CXL (fluence of 5.4 J/cm²), and high-intensity CXL (fluence of 16.2 J/cm²). The axial strain distribution in the stroma induced by ocular inflation ($\Delta p=30$ mmHg) was quantified, and maps of the anterior sagittal curvature were constructed. We show that comparable amounts of stiffening and refractive changes are induced 30 minutes after Dresden CXL and accelerated CXL, while high-intensity CXL induced the highest response in terms of axial strain ($6.7 \pm 4.1\%$) and refractive correction (3.4 ± 0.9 D). OCE demonstrates that refractive changes are related to the modification of corneal biomechanics.

Keywords: Optical Coherence Elastography; Corneal Cross-linking; Optomechanical changes

Introduction

Corneal cross-linking (CXL) is a technique that aims to photochemically stiffen the cornea by creating cross-links in the extracellular matrix. The clinical interest in CXL as a treatment for refractive correction is growing, due to the minimally invasive nature of this procedure. Originally, the treatment involved the application of UVA light at an intensity of 3 mW/cm^2 for 30 minutes [1]. However, over time, alternative protocols have been developed to accelerate the procedure by increasing the amount of energy delivered in a shorter amount of time. Shortening the CXL protocol is expected to increase patient comfort by reducing the risk of infection and minimizing hospital waiting time [2]. In an effort to develop a more refined and predictable protocol for refractive correction by CXL, a better understanding of the relationship between irradiation energy, degree of tissue stiffening, and resulting refractive change is required. In recent years, optical coherence tomography (OCT) emerged as a promising tool to investigate both the biomechanical properties and refractive changes of the cornea. OCT elastography (OCE) has recently demonstrated its ability to assess altered strain distribution in ex vivo rat eyes after CXL [3], and to show that this effect is limited to regions exposed to UV irradiation. In the present study, we quantify for the first time using OCE the degree of stiffening as well as the magnitude of the resulting refractive changes induced in the cornea by the CXL treatment at different UV fluences.

Methods

Nine freshly enucleated porcine corneas were obtained from the local slaughterhouse and subjected to

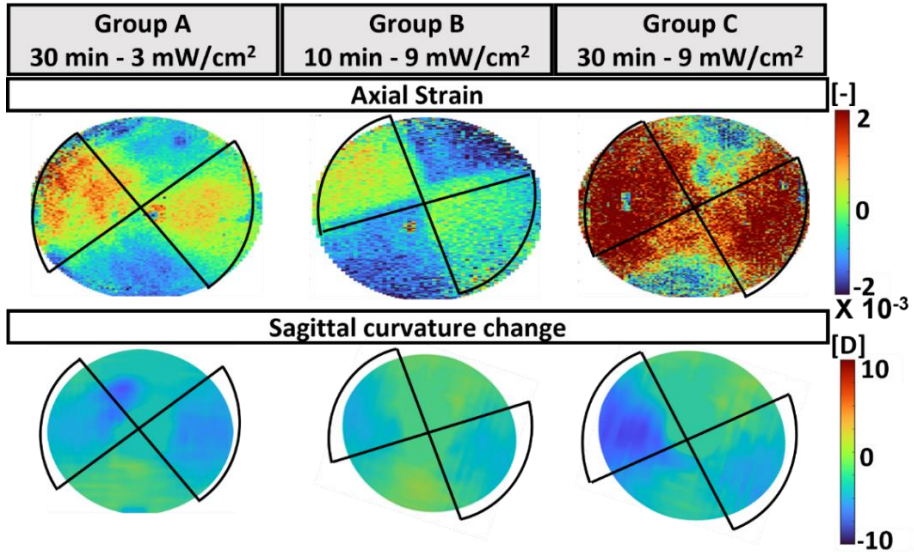


Figure 1. Localized optomechanical changes induced by different CXL protocols.

CXL treatment within 2 to 12 hours from collection. Each eye was subjected to a bowtie patterned CXL protocol, in which UV irradiation was restricted to a specific area of the cornea using a steel mask. The samples were divided into three subgroups, each with a sample size of $n = 3$. Group A was underwent a standard Dresden protocol treatment (365 nm , 3 mW/cm^2 for 30 min , corresponding to a fluence of 5.4 J/cm^2) [1]; group B underwent an accelerated CXL protocol (10 min irradiation with an irradiance of 9 mW/cm^2 , corresponding to a fluence of 5.4 J/cm^2); the eyes in group C were irradiated for 30 min with 9 mW/cm^2 (fluence of 16.2 J/cm^2). The biomechanical and refractive assessments were performed with an OCE setup based on ambient pressure modulation described previously [3]. The pig eye was placed inside a pressure chamber and inflated by applying an external vacuum using a syringe. OCE measurements were acquired before and after applying a Δp of -30 mmHg . Each measurement provided a volumetric scan of the cornea (consisting of a stack of 100 2D-images , with axial and lateral resolution of $4.7\text{ }\mu\text{m}$ (in air) and $12\text{ }\mu\text{m}$, respectively). The entire measurement took approximately 1 minute. Two OCE measurements were acquired on each sample: the first after instillation of riboflavin and the second 30 minutes after patterned UV irradiation. The pixel-wise enface axial strain and sagittal curvature maps were derived from the OCT datasets. OCE-derived axial strains were computed using a phase-sensitive algorithm described previously [4]. To obtain the corneal geometry, each $2D$ image was segmented using an in-house MATLAB script (Massachusetts: The MathWorks Inc., 2019). The anterior surface was then extracted and the sagittal curvature K_s [D] was computed as:

$$K_s = \frac{(n-1)}{R_a}, \quad (1)$$

where $n=1.3375$ and R_a is the local sagittal radius of the anterior surface.

Results

Thirty minutes after CXL, we report a shift toward positive strain in the anterior stroma and an overall flattening of the corneal surface in the regions treated with CXL (Figure 1). As shown in Figure 2, axial strain was higher in group C ($6.7 \pm 4.1\%$) than in other two groups ($2.1 \pm 1.1\%$ and $1.3 \pm 0.7\%$ for groups A and B, respectively). Similarly, the high-fluence CXL group exhibited a tendency for a greater reduction in sagittal curvature within the treated region ($3.4 \pm 0.9\text{ D}$), compared to groups A and B ($2.1 \pm 0.8\text{ D}$ and $2.3 \pm 0.6\text{ D}$, respectively). Groups A and B showed a comparable increase in axial strain and decrease in sagittal curvature.

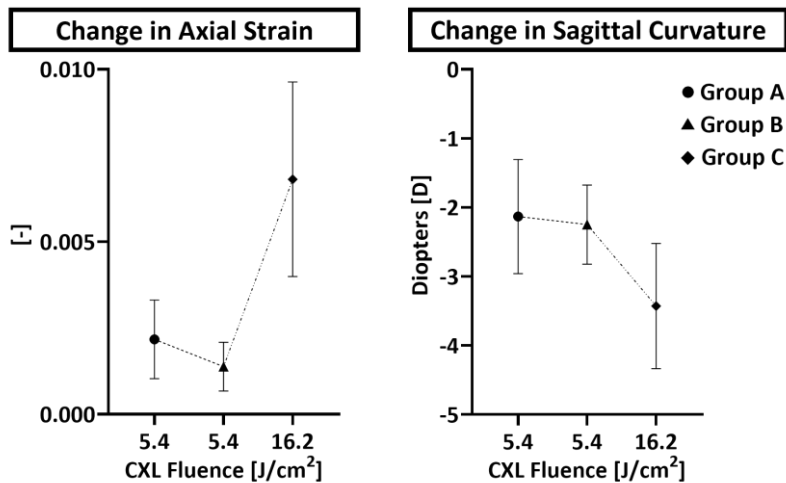


Figure 2. Axial strain and sagittal curvature change induced by three different CXL protocols in the irradiated area.

Conclusions

OCE allows high-resolution visualization and quantification of the optomechanical effects of CXL in the anterior stroma. Our results showed that mechanical stiffening is accompanied by geometric and thus refractive changes in the cornea, and these two effects are proportional to the energy delivered to the tissue: a tripling of the energy delivered during CXL increases the induced refractive correction by 1.5-fold. Moreover, we found that not only the mechanical but also the refractive correction induced by accelerated CXL and the Dresden protocol (both at 5.4 J/cm^2) were similar (Figure 1). These findings are in agreement with clinical data reporting the equivalence of these two protocols in terms of both induced stiffening [5] and refractive correction [6].

Acknowledgements

This work received funding from the European Union's HORIZON 2020 research and innovation programme under grant agreement No 956720 and from the AMBIZIONE grant PZ00P2_174113 from the Swiss National Science Foundation.

References

- [1] Wollensak G, Spoerl E, Seiler T. Riboflavin/ultraviolet-A-induced collagen crosslinking for the treatment of keratoconus. *Am J Ophthalmol*. 2003; 135(5):620–7.
- [2] Wernli J, Schumacher S, Spoerl E, Mrochen M. The efficacy of corneal cross-linking shows a sudden decrease with very high intensity UV light and short treatment time. *Investig Ophthalmol Vis Sci*. 2013; 54(2):1176–80.
- [3] Kling S. Optical coherence elastography by ambient pressure modulation for high-resolution strain mapping applied to patterned cross-linking. *J R Soc Interface*. 2020; 17(162).
- [4] Kling S, Khodadadi H, Goksel O. Optical Coherence Elastography-Based Corneal Strain Imaging During Low-Amplitude Intraocular Pressure Modulation. *Front Bioeng Biotechnol*. 2020; 7(January):1–13.
- [5] Mazzotta C, Raiskup F, Hafezi F, Torres-Netto EA, Armia Balamoun A, Giannaccare G, et al. Long term results of accelerated 9 mW corneal crosslinking for early progressive keratoconus: the Siena Eye-Cross Study 2. *Eye Vis*. 2021; 8(1):1–12.
- [6] Lang PZ, Hafezi NL, Khandelwal SS, Torres-netto EA, Hafezi F, Randleman JB. Comparative Functional Outcomes After Corneal Crosslinking Using Standard, Accelerated, and Accelerated With Higher Total Fluence Protocols. *Cornea*. 2019; 38(4):433–41.

High-resolution optical coherence elastography of the human lens in vivo

Sabine Kling^{1,2}, Matteo Frigelli², M. Enes Aydemir³, Vahoora Tahsini²,
Leonard Kollros³, Emilio A. Torres-Netto^{3,4}, Farhad Hafezi^{3,4}

¹ Institute for Biomedical Engineering, ITET department, ETH Zurich, Switzerland

² ARTORG Center for Biomedical Engineering Research, University of Bern, Switzerland

³ ELZA Institute AG, Dietikon, Switzerland

⁴ CABMM, University of Zurich, Switzerland

* Corresponding author: kling.sabine@gmail.com

As a key element of ocular accommodation, the deformability of the crystalline lens determines its optical functionality. Quantifying the deformation characteristics and stiffness distribution in the lens can improve the diagnosis and follow-up of lenticular disorders and guide refractive interventions in the future. Here, we present a novel type of optical coherence elastography able to examine the mechanical characteristics of the human crystalline lens in vivo. The concept is demonstrated through lens displacement and strain measurements in an age-mixed group of human subjects in response to an external and an intrinsic mechanical deformation stimulus. There was an excellent agreement between the high-resolution strain map retrieved during steady-state micro-fluctuations and earlier reports on lens stiffness in the cortex and nucleus suggesting a 1.6 to 2.8 times stiffer cortex than the nucleus in young lenses and a 1.7 to 9.8 times stiffer nucleus than the cortex in the old lenses.

Keywords: optical coherence tomography; elastography; crystalline lens; biomechanics

Introduction

Accommodation is the process of the crystalline lens changing its shape to adjust the eye's focus to a closer distance. Mechanical properties determine the deformability of a material and thus play an essential role to which extent the lens can change its focal length, especially during the onset of presbyopia. Presbyopia is an age-related condition culminating in the complete loss of accommodation above the age of 60 years. It originates most likely from a stiffening of the lens nucleus [1] (lenticular sclerosis [2]), yet up to date, only indirect evidence has been collected [3].

So far, our understanding of accommodation and presbyopia is based on lens biometry and correspondingly on observations of lens thickness [4], curvature and ciliary body diameter [5] and their changes during stimulated accommodation. A challenge in assessing internal lens deformations and displacements is the high transparency of the tissue resulting in a poor signal-to-noise ratio in structural imaging, including optical techniques, MRI [6] and ultrasound [7, 8]. So far, most analyses are limited to analyzing anterior and posterior lenticular surface deformations, which inherently have the highest contrast.

In the current study, we evaluate both, an external ambient pressure change and the naturally occurring steady-state micro-fluctuations of accommodation, as two distinct mechanical stimuli for their suitability to be used in combination with optical coherence elastography in the in vivo human crystalline lens.

Methods

Measurements were conducted in four eyes of four subjects between 31 and 72 years using a spectral-domain commercial anterior segment optical coherence tomography (OCT) device (ANTERION, Heidelberg Engineering, Germany). The OCT system with an axial and lateral resolution of 9.5 (in air) and $30 \mu\text{m}$, respectively, was synchronized with an external pressure modulation unit as described earlier [9]. The protocol for *in vivo* OCT elastography was revised and approved by the cantonal ethics committee Zurich (number 2021-02275). The study was conducted in accordance with the Declaration of Helsinki. Briefly, each person was asked to wear a set of customized swimming goggles for the examination. Then, 128 subsequent OCT B-scans were recorded, while the participant was looking at a visual fixation target integrated in the ANTERION device. At approx. 1/3 of the recording time period, the pressure within the goggle chamber was suddenly reduced by 10 mmHg inducing an expansion of the eye globe. At the same time, micro-fluctuations of accommodation were simultaneously recorded over the total measurement duration of ~2s.

Phase-sensitive axial displacement and strain tracking was applied on the complex dispersion-corrected OCT signal following a vector-based summation approach described earlier [10, 11] in order to assess the internal lens deformation.

Results

Ambient pressure change

When positioning the lens with its centre at the origin of the coordinate system, a similar displacement behaviour was observed in all lenses, with a maximal amplitude at -1.5 mm distance from the lens centre (towards the anterior surface). Considering that the young lens had a smaller thickness, there was a pronounced forward movement in the anterior 20% ($p = 0.032$) and a subtle backward movement between 32 to 100% ($p = 0.024$) of the lens thickness. The corresponding axial strain, or derivative of the displacement indicates the anterior cortex gets compressed and the nuclear region expands axially in response to the ambient pressure change. This deformation pattern is in agreement with accommodation.

Micro-fluctuation of accommodation

Throughout the repeated B-scan acquisition duration of ~2.6s, we also observed physiologic steady state micro-fluctuations of accommodation independent of the external pressure application. Figure 1 shows a representative image of the strain distribution at maximal amplitude during micro-accommodation and micro-dis-accommodation and the strain profiles for different ages. As can be recognized, in younger participants, the nucleus deforms strongest and the lens cortex least. The situation changes in the two oldest participants, where the deformation is more concentrated on the lens cortex and the overall strain amplitude decreases dramatically.

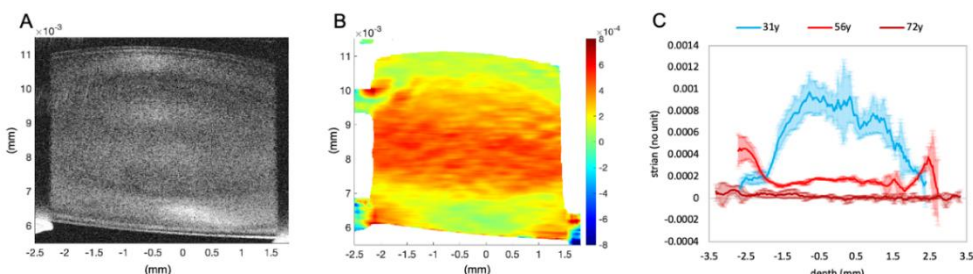


Figure 1. Micro-fluctuation of accommodation. Representative structural (A) and elastographic (B) OCT scan in a 31-year-old subject. (C) Axial strain profile for lenses of different age.

Conclusions

Optical coherence elastography permits to experimentally quantify the internal lens deformation pattern *in vivo*, and for the first time directly and with high spatial resolution without the need of any modelling assumptions. The observed age-related changes in the axial strain distribution during steady state micro-fluctuations are in agreement with earlier literature. The lens tends to accommodate in response to the application of a negative pressure gradient between the aqueous and vitreous humour. Having a method to assess the biological age of an individual patient's lens will permit a more fact-based decision of which type of refractive surgery would most suitable for pre-presbyopic people within an age range of 45 to 55 years. Furthermore, lens elastography opens a new way to advance lenticular refractive surgery (lentotomy [12]) and could permit an earlier detection of lenticular abnormalities [13] including cataracts.

Acknowledgements

This work received funding from the European Union's HORIZON 2020 research and innovation programme under grant agreement No 956720 and from the AMBIZIONE grant PZ00P2_174113 from the Swiss National Science Foundation. The authors thank Heidelberg Engineering for providing an Anterior OCT device to conduct this research.

References

- [1] Heys KR, Cram SL, Truscott RJ. Massive increase in the stiffness of the human lens nucleus with age: the basis for presbyopia?
- [2] Fisher R. The mechanics of accommodation in relation to presbyopia. *Eye* 1988; 2: 646–649.
- [3] Lanchares E, Navarro R, Calvo B. Hyperelastic modelling of the crystalline lens: Accommodation and presbyopia. *Journal of Optometry* 2012; 5: 110–120.
- [4] Baikoff G, Lutun E, Wei J, et al. Anterior chamber optical coherence tomography study of human natural accommodation in a 19-year-old albino. *Journal of Cataract & Refractive Surgery* 2004; 30: 696–701.
- [5] Strenk SA, Strenk LM, Koretz JF. The mechanism of presbyopia. *Progress in retinal and eye research* 2005; 24: 379–393.
- [6] Sheppard AL, Evans CJ, Singh KD, et al. Three-dimensional magnetic resonance imaging of the phakic crystalline lens during accommodation. *Investigative ophthalmology & visual science* 2011; 52: 3689–3697.
- [7] Storey J, Rabie E. Ultrasound—a research tool in the study of accommodation. *Ophthalmic and Physiological Optics* 1983; 3: 315–320.
- [8] Yoon S, Agyamov S, Karpiouk A, et al. A high pulse repetition frequency ultrasound system for the *ex vivo* measurement of mechanical properties of crystalline lenses with laser-induced microbubbles interrogated by acoustic radiation force. *Physics in Medicine & Biology* 2012; 57: 4871.
- [9] Kling S. In-Vivo Measurement of Ocular Deformation In Response to Ambient Pressure Modulation. *Front Bioeng Biotechnol* 2021; 1113.
- [10] Kling S, Khodadadi H, Goksel O. Optical Coherence Elastography-Based Corneal Strain Imaging During Low-Amplitude Intraocular Pressure Modulation. *Frontiers in bioengineering and biotechnology* 2020; 7.
- [11] Zaitsev VY, Matveyev AL, Matveev LA, et al. Optimized phase gradient measurements and phase-amplitude interplay in optical coherence elastography. *Journal of Biomedical Optics* 2016; 21: 116005.
- [12] Ripken T, Oberheide U, Fromm M, et al. fs-Laser induced elasticity changes to improve presbyopic lens accommodation. *Graefe's archive for clinical and experimental ophthalmology* 2008; 246: 897–906.
- [13] Wright KW. Lens abnormalities. *Pediatric ophthalmology and strabismus* 2003; 450–480.

Characterization of the mechanical contribution of the capsule of crystalline lenses using optical coherence elastography

Vahoura Tahsini^{1*}, Philippe Büchler¹ and Sabine Kling^{1,2}

¹ARTORG Center for Biomedical Engineering Research, University of Bern, Switzerland.

²Institute of Biomedical Engineering, ETH Zurich, Switzerland.

* Corresponding author: sabine.kling@unibe.ch

To date, the biomechanical processes involved in the accommodation of the crystalline lens and the development of presbyopia are not fully understood. In particular, the mechanical role of the lens capsule needs further clarification. Here, we apply optical coherence elastography to quantify the axial compression induced by sinusoidal compression and to characterize the dynamic mechanical behavior of both intact and decapsulated fresh lenses. We show that the axial strain amplitude in the cortex increased by a factor of 1.08 after decapsulation and the strain amplitude in the nucleus decreased by a factor of 1.11. The ratio of cortical to nuclear strain was 1.22 in the intact lens and 1.45 in the decapsulated lens. Fresh lenses also showed a greater viscoelastic time delay than decapsulated lenses. These results highlight the biomechanical importance of the lens capsule.

Keywords: Optical Coherence Tomography; Elastography; Compression

Introduction

Accommodation is a dynamic process in which the focal point of the eye changes by up to 14 diopters in young people due to the deformation of the crystalline lens [1]. The biomechanical properties of the lens are key parameters that determine its deformability and thus its refractive power. With age, the lens becomes stiffer and the accommodative response decreases. However, the underlying mechanical mechanism of the age-related decrease in lens deformation, and in particular the role of the capsule on the overall lens stiffness are not fully understood yet.

Optical coherence elastography (OCE) is a new technique for noninvasive characterization of tissue mechanics. In the past, air-cushion-based OCE has shown promising results in detecting differences in lens stiffness with varying intraocular pressure [2] and with increasing age [3]. Recently, phase sensitive OCE was shown to provide high-resolution, localized tissue stiffening after photochemical cross-linking during modulation of ambient pressure [4]. In this study, the methodology is applied to the evaluation of the ocular lens.

Material and method

Thirty-three (33) freshly enucleated porcine eyes were obtained from a local slaughterhouse. The crystalline lens was carefully removed from all eyes. For the intact condition, $N = 12$ lenses were used without additional modifications, but lenses from the decapsulated group ($N = 21$) were carefully incised at the lens equator, and the capsule was peeled off. Each sample was compressed between two glass lamellae over a piezoelectric actuator and a force sensor. The distance between the lamellae was 5.4 mm for intact lenses and 4.4 mm for decapsulated lenses to achieve a similar relative compression, before the sinusoidal oscillation was applied. The initial compression force by upper lamella after 10s

(short relaxation, $N = 17$) or 30 min (long relaxation, $N = 16$) after relaxation were recorded.

Then, without further modifying the lamellae distance, the optical coherence tomography device (OCT) was synchronized with the piezoelectric actuator. A sinusoidal oscillation with an amplitude of $36 \mu\text{m}$ and a frequency of 0.2 Hz was applied, while OCT scans were recorded simultaneously. Internal tissue deformation was determined by calculating the phase difference between two consecutive B-scans using a complex-valued vector summation approach [5]. The induced strain amplitude in cortex and nucleus was quantified. The time delay between nucleus and cortex (where a positive value indicates that the oscillation of the nucleus advances that of the cortex) was used as a measure of viscoelasticity. Statistical analysis was performed using SPSS.

Results

The initial pre-compression corresponded to a strain of 27% in the intact and 34% in the decapsulated lenses, for which a force of 5.42 and 5.35 gf was necessary ($p = 0.518$). There was no significant difference ($p = 0.069$) in force relaxation between the intact and decapsulated lenses (4.24 vs 3.84 gf). Figure 1 shows representative strain maps in cross-section for both conditions. According to Y-axis of the Figure 1 a and b, the decapsulated lenses show a greater difference between the cortical and nuclear regions compared to the intact lenses.

When comparing the amplitude of the strain oscillation, there was a significant decrease in the amplitude of the strain peaks between nuclei after decapsulation (12.6 versus 11.4%, $p < 0.001$). Cortex strain amplitude tended to increase after decapsulation (15.4 vs. 16.6%, $p = 0.056$). Under both conditions, the nucleus exhibited a smaller strain amplitude than the cortex, indicating higher stiffness. The viscoelastic time delay between the nucleus and cortex decreased significantly ($p = 0.002$) after decapsulation (31.3 vs. 10.9 s).

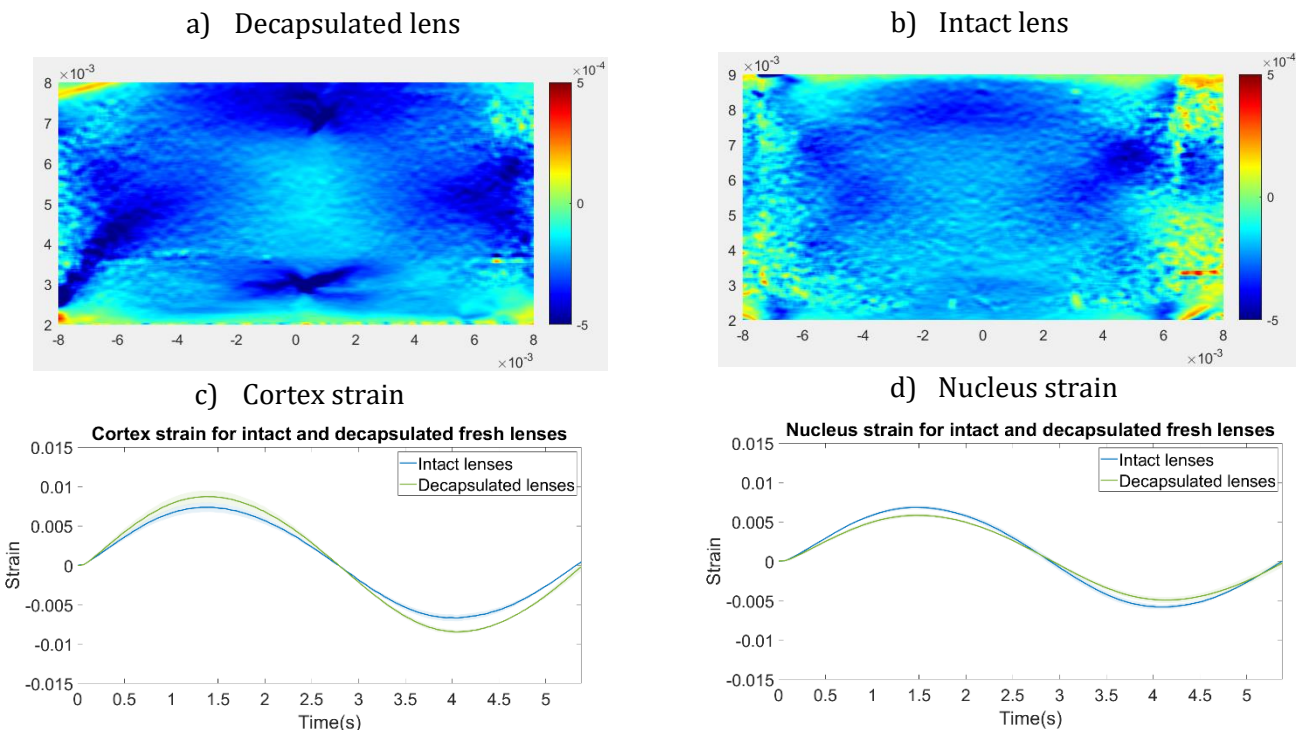


Figure 1. Cross-sectional image and strain plot in the (a) decapsulated and (b) intact fresh lens. The corresponding average temporal strain profile in the (c) cortex and (d) nucleus. Error bars represent standard deviation.

Table 1. Statistical analysis – Peak to peak strain values

Parameter	Decapsulated lens	Intact lens	p-value
Thickness (mm)	6.67 ± 0.58	7.43 ± 0.28	<0.001
Max Force (gf)	5.35 ± 3.12	5.42 ± 0.43	0.518
Min Force (gf)	3.84 ± 3.13	4.24 ± 3.14	0.069
Cortex Amplitude (%)	16.6 ± 1.86	15.4 ± 1.18	0.056
Nucleus Amplitude (%)	11.4 ± 0.97	12.6 ± 0.51	<0.001
Time delay between Cortex and Nucleus (ms)	10.9 ± 10.0	31.3 ± 19.3	0.002

Conclusion

The proposed technique based on compression tests and OCE allowed a viscoelastic characterization of the crystalline lens. Due to the high spatial resolution, the strain distribution within the sample became accessible, allowing different regions within the sample to be analyzed separately. Quantification of strain amplitude in the cortex and nucleus suggests that the porcine nucleus is 1.22 times stiffer than the cortex in intact lenses and 1.46 times stiffer in decapsulated lenses. This observation may explain why porcine lenses do not accommodate. In addition, the decrease in viscoelasticity after decapsulation suggests that the lens capsule plays an important role in lens deformability.

Acknowledgment

This project has received funding from: the European Union's Horizon 2020 research and innovation programme under the Marie Skłodowska-Curie grant agreement No 956720.

References

- [1] Gerometta R, Zamudio AC, Escobar DP, Candia OA. Volume change of the ocular lens during accommodation. *American Journal of Physiology-Cell Physiology*. 2007;293(2):C797-C804.
- [2] Wu C, Aglyamov SR, Han Z, Singh M, Liu CH, Larin KV. Assessing the biomechanical properties of the porcine crystalline lens as a function of intraocular pressure with optical coherence elastography. *Biomed Opt Express, BOE*. 2018;9(12):6455-6466.
- [3] Zhang H, Singh M, Zvietcovich F, Larin K, Aglyamov S. Age-related changes in the viscoelasticity of rabbit lens characterised by surface wave dispersion analysis. *Quantum Electron*. 2022;52(1):42-47.
- [4] Kling S. Optical coherence elastography by ambient pressure modulation for high-resolution strain mapping applied to patterned cross-linking. *J R Soc Interface*. 2020;17(162):20190786. doi:10.1098/rsif.2019.0786
- [5] Kling S, Khodadadi H, Goksel O. Optical Coherence Elastography-Based Corneal Strain Imaging During Low-Amplitude Intraocular Pressure Modulation. *Front Bioeng Biotechnol*. 2020;7:453.

Change in refractive errors with changes in IOL parameters

David A. Atchison^{1*} and David L. Cooke²

¹ School of Optometry and Vision Sciences, Queensland University of Technology, Brisbane, Australia

² Great Lakes Eye Care, Saint Joseph, Michigan, USA

* Corresponding author: d.atchison@qut.edu.au

Tilt or longitudinal displacement of intraocular lenses (IOLs) can cause considerable errors of refraction. We addressed the issue of how refraction will change if a thin IOL is positioned differently with regards to tilt or position or is replaced by another IOL with different fitting characteristics. Raytracing was done through a correcting lens of a particular refraction through to the image side of an IOL, transferred to the position of a second thin IOL, and then traced backwards to determine a second refraction. Examples are presented showing effects of changing tilt and changing lens power.

Keywords: IOL power; lens tilt; raytracing

Introduction

Sometimes intraocular lenses (IOLs) do not fit as intended, with particular problems being unwanted tilt or longitudinal displacement that can result in considerable errors of refraction [1]. It would be helpful for Ophthalmologists to know how critical is the placement of an IOL in the eye and how replacing one IOL by a better fitting one might affect the residual refraction. This is posed as the question: given a refraction with a particular IOL in the eye, what will be the refraction if the IOL is positioned differently with regards to tilt or position or is replaced by another IOL with different fitting characteristics?

Methods

A method for determining refractive errors is developed here for thin IOLs using equations developed for tilting of thin spherocylinder lenses about any axis [2]. The approach can be given simplistically as

$$\text{Refraction1} + \text{IOL1} = \text{Refraction2} + \text{IOL2}$$

Here the subscript “1” is used for parameters associated with forwards raytracing (into-the-eye), and the subscript “2” is used for backwards raytracing (out-of-the-eye). In more detail (Figure 1), light is traced through a correcting lens of power Refraction1 to the cornea, refracted at the cornea, transferred to IOL1, refracted at IOL1, and transferred to the position of IOL2 (which may be the same IOL as IOL1 but with a different position and/or tilt). Then, it is refracted backwards through IOL2, transferred to the cornea and refracted out of the eye to give the new correcting lens of power Refraction2.

If a refracting element and the corresponding reduced object vergence do not have the same principal meridians, vector refraction is required for a forwards raytrace [3, 4]. Similarly, if a refracting element and the corresponding reduced image vergence do not have the same principal meridians, vector refraction is required for a backwards raytrace.

Required parameters with IOL₁ include: lens correction (sphere, cylinder and axis); vertex distance of the lens; corneal powers along the principal meridians and a corneal cylinder axis; anterior chamber depth (distance from cornea to lens); IOL sphere, cylinder and axis; IOL refractive index, angle of tilt, and the axis about which this occurs. Required parameters with IOL₂ are any parameters that are different from those of IOL₁, except obviously for the new lens correction that is to be determined. Changing parameters may include the anterior chamber depth, lens power, lens tilt and axis about which it occurs. Refractive index of the aqueous and vitreous are assumed to be 1.336.

The procedure assumes that the corneal power and anterior chamber depth are accurately determined. The axial length is not needed, although it would have been used to choose the power of the IOL to be placed in the eye. The cornea is treated as a thin lens, which is reasonable as its principal planes are located about 0.05 mm in front of the anterior cornea. The anterior chamber is taken as the distance from the anterior cornea to a thin IOL, which can be placed at the centre of the actual IOL.

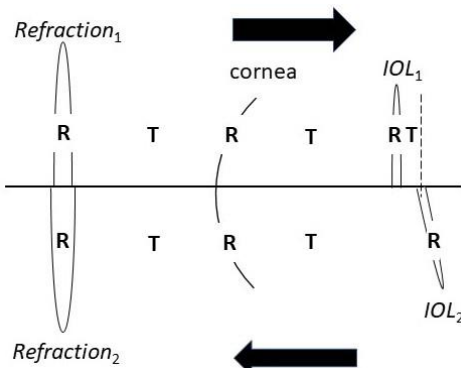


Figure 1. Raytracing schema showing (top) forwards raytracing to the position of IOL₂, and (bottom) backwards raytracing from IOL₂. **R** and **T** indicate refraction and transfer, respectively.

Results

Table 1 shows some examples and Figure 2 shows the tilt of the initial IOL in Example 3. For Example 1, a 20.00/-2.79 x 90 power IOL was tilted incorrectly by 20° about an axis of 35°, with refraction of -0.67/-2.00 x 31.3; removing the tilt gives a Plano refraction. Example 2 shows the same initial IOL; as part of the calculations the IOL power (17.94/-2.64 x 66.3) can be determined for the same fitting conditions that gives a plano refraction.

Example 3 is a case study in which a 23D IOL had a tilt of 12 degrees about an axis of approximately 145 degrees. The anterior chamber depth was 4.4 mm, which was estimated to be too close to the cornea by 0.3 mm. The refraction was -1.25/-0.75 x 155. It was estimated that if the IOL was removed and replaced by one without the tilt and at the correct position, that the refraction would become +0.33/-0.19 x 21. This was a close match to the 1 week post-operative refraction of *plano*/−0.25 x 17.

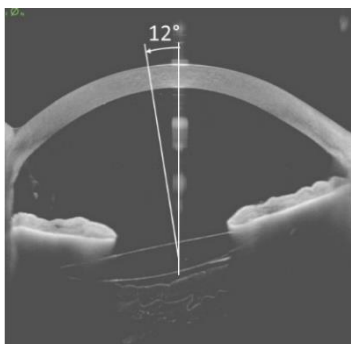


Figure 2. OCT image of an IOL along the 55° meridian. Angle of tilt relative to the visual axis is 12°.

Table 1: Example showing changes in refraction with change in IOL related parameters

Initial parameters	Example 1	Example 2	Example 3
vertex distance (mm)	0		12
corneal sphere power (D)	40		43.33
corneal cylinder power (D)	2		0
corneal cylinder axis	90		90
anterior chamber depth (mm)	5		4.4
IOL spherical power (D)	20	As for Example 1	23
IOL cylinder power (D)	-2.79		0
IOL cylinder axis	90		90
IOL index	1.5		1.554
angle of tilt (deg.)	20		12
axis about which tilt occurs (deg.)	35		145
correction - sphere (D)	-0.67		-1.25
correction - cylinder (D)	-2.00		-0.75
correction - axis (deg.)	31.3		155
Final parameters (if changed)			
anterior chamber depth (mm)			4.7
IOL spherical power (D)		17.94	22
IOL cylinder power (D)		-2.64	
IOL cylinder axis		66.3	
Angle of tilt (deg.)`	0	20	0
axis about which tilt occurs (deg.)	35	35	0
correction - sphere (D)	0.00	0.00	0.33
correction - cylinder (D)	0.00	0.00	-0.19
correction - axis (deg.)	180	180	31

Conclusion

A procedure has been developed to show how replacing one IOL by the same or a different one at a different tilt and/or position will affect the residual refraction. The case study presented indicates that the procedure works well.

References

- [1] Atchison DA. Refractive errors induced by displacement of intraocular lenses within the pseudophakic eye. Optom. Vis. Sci. 1989; 66:146-152.
- [2] Harris WF. Effect of tilt on the tilted power vector of a thin lens. Optom. Vis. Sci. 2006; 83:E693-E696.
- [3] Thibos LN, Wheeler W, Horner D. Power vectors: an application of Fourier analysis to the description and statistical analysis of refractive error. Optom. Vis. Sci. 1997; 74:367-375.
- [4] Atchison DA, Smith G. Optics of the Human Eye. 2nd edition. 2023. CRC press., 104-107.

Novel OCT-based estimation of postoperative IOL position

Jasmien Rens^{1,2*} and Jos Rozema^{1,2}

¹ Department of Ophthalmology, Antwerp University Hospital, Edegem, Belgium

² Faculty of Medicine and Health sciences, University of Antwerp, Belgium

* Corresponding author: jasmien.rens@uza.be

Purpose

Cataract is a leading cause of low vision worldwide. The surgical treatment is to remove the opaque lens and replace it by an artificial intraocular lens (IOL). The power of this IOL is preoperatively calculated based on patient's biometric parameters to achieve the preferred refractive outcome. Different generations of formulas are available to estimate the postoperative effective lens position (*ELP*), which remains the most important cause of error since it cannot be measured preoperatively. The purpose of this study is to enhance the accuracy of the estimated *ELP* by utilizing preoperative anterior segment optical coherence tomography (AS-OCT).

Methods

In this study, we enrolled patients planned for cataract surgery with the 'bag-in-the-lens' technique to undergo a preoperative AS-OCT examination, as well as 5-weeks postoperatively. The following parameters were assessed: axial length, lens radius of curvature (front and back), lens equatorial position (distance between anterior cornea and the widest edge of the lens), lens diameter and postoperative anterior chamber depth (distance from the anterior cornea to anterior IOL surface). The estimation of the new IOL power calculation formula was performed using stepwise multiple linear regression, a process in which initially all predicting parameters are considered and the least significant term is iteratively removed until all remaining terms are significant at a level of $p < 0.05$.

Results

The best estimator of the *ELP* found was based on axial length, posterior lens radius of curvature and lens equatorial position, and had a coefficient of determination (r^2) of 0.71 compared to the *ELP* measured by AS-OCT. For reference, the corresponding coefficients of determination frequently used formulas (SRK/T, Haigis, and Olsen) resulted in values of 0.32, 0.49 and 0.51, respectively.

Conclusion

The new estimator of the effective lens position using AS-OCT shows great promise and has potential to enhance the precision of IOL power calculations.

Keywords: biometry; intraocular lens implantation; optical coherence tomography

Measuring the optics of eyes with diffractive intraocular lenses

Harilaos Ginis^{*1}, Alex Pennos¹, Spyridon Tsoukalas¹, Dimitrios Christaras¹

¹ Diestia systems, Athens, Greece

* Corresponding author: harilaos@diestia.com

Purpose

Diffractive intraocular lenses (IOLs) split the incoming light to (usually) three foci assigned to far, intermediate and near vision. Despite being static, this correction offers a functional depth of focus to the patient, presumably sufficient for vision without spectacles. This depth of focus (additional foci) is obtained at the expense of image quality at any of the foci. Image quality with diffractive lenses can be quantified in-vitro bench tests or by psychophysical testing of patients. Diffractive lenses are designed to operate in the visible spectrum. Wavefront sensing devices operating in the infrared will not measure correctly (or at all) the diffracted orders.

Methods

We present a new instrument for the in-vivo measurement of the through-focus image quality in the human eye that is moreover capable of measuring eyes with diffractive IOLs. The instrument, developed at Diestia systems (Athens, Greece) features electrically driven tuneable lenses and scanning infrared (780 nm) and visible (530 nm) lasers to generate a spot on the area of the fovea. The aerial image of that spot reveals the double-pass point spread function (*PSF*) of the eye for any given refractive state addressed by the tuneable lenses. The focus of the first and the second pass are controlled independently.

Results

The instrument completes a through-focus scan of ($5D$) in less than 300 ms , presumably before the onset of the pupillary reflex. Analysis of the *PSF* reveals the through-focus curve (expressed as the *VSOTF* as a function of defocus) from which the far, intermediate and near refraction can be obtained as well as the balance of far/near correction, the astigmatism. Analysis of the *PSF* at the best far focus can reveal the glare associated with the diffracted light at the rings as well as other sources of straylight in the eye.

Conclusion

We present the principles of operation, the proof of concept and indicative measurements with a novel instrument to measure the through-focus *PSF* of pseudophakic eyes with diffractive lenses. Such an instrument may help understand the actual refractive state of these eyes as well as the optical phenomena associated with the subjective phenomena (such as glare) reported by patients.

Keywords: *PSF; pseudophakic; refraction; IOL; diffractive; diagnostic instrument*

Intraocular lens tilt, the pupil, and simple eye models

Michael J. Simpson ¹

¹ Simpson Optics LLC, Arlington TX, USA

* Corresponding author: mjs1@outlook.com

Modern instrumentation measures parameters that can be used for a simple eye model, where on average the cornea, the pupil, and the lens, are approximately aligned along an optical axis. The instruments themselves make measurements along an approximate visual axis, which can lead to descriptions of an intraocular lens (IOL) being tilted by 5°, rather than the eye being rotated (angle alpha). One fundamental limitation is that corneal keratometry and topography do not appear to be routinely evaluated along the optical axis, potentially leading to a displaced corneal surface in the model. Also, the pupil location has complexities that affect its evaluation, with the iris moving forwards as a person ages, and then backwards following cataract surgery. The magnitudes of these changes are evaluated for cataract patients.

Keywords: Intraocular lens tilt; Angle alpha; Angle kappa; Pupil diameter

Introduction

Eye models often assume circular symmetry when fundamental properties are being evaluated, yet it is also known that the foveola is not on the optical axis, leading to an average rotation of the eye away from the nose of 5° (angle alpha). Intraocular lenses (IOLs) simplify an eye model because the refractive index of the lens material is constant, rather than having a gradient refractive index like the crystalline lens, and also it is possible for their optical design to be known because they are manmade lenses (though manufacturers are not often forthcoming with the design details). Ophthalmic measurement equipment has progressed rapidly in recent years, and a general concept has been implemented where there is an underlying assumption that the cornea, the pupil, and the lens lie generally along a single optical axis. However, the eye is usually oriented to have retroreflection at the cornea, at the same time as the eye is sighting along the instrument axis [1]. This leads to the iris and the internal lens appearing tilted when looking at the eye along the instrument axis, even if there was perfect symmetry.

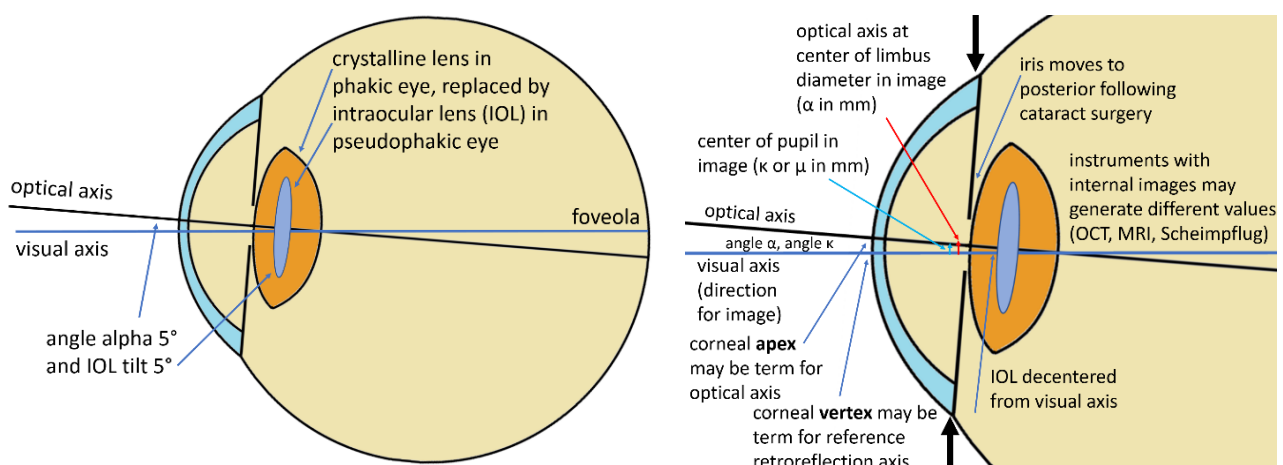


Figure 1. Simplified model of average eye. Angles may be in degrees or mm. Right eye from above.

This description for the eye is not always summarized very clearly, and it also has a fundamental discrepancy because corneal keratometry and topography measurements are made along the instrument axis rather than the optical axis. Published parameters were used to evaluate this broad topic, and OCT images were used to evaluate the pupil.

Methods

Publications were reviewed that had parameters like IOL tilt, IOL decentration, angle alpha, angle kappa, and chord mu. OCT images for preop and postop cataract patients covering the full axial length range [2] were also re-evaluated, and the apparent magnification of the pupil was estimated for each eye using the paraxial equation: $Pupil Magnification = n_{\text{fluid}} / (n_{\text{fluid}} - z_p * K_{\text{adj}} / 1000)$ [3], with $n_{\text{fluid}} = 1.336$, K_{adj} the best estimate for corneal power, and z_p the axial depth of the limiting iris diameter, with the depth increasing following cataract surgery.

Results

Angle alpha is the most straightforward parameter, with several sources giving an average angle of about 5° rotating about a vertical axis outwards from the visual axis to the optical axis for both the actual angle in object space [3], and the tilt of both the iris and an IOL [4] (Figure 1). This is consistent with the eye being primarily a centred optical system, with the eye rotated because the foveola is not on the optical axis. The corneal information is less straightforward, with one definition for the “apex” being the location with the smallest radius of curvature [3], and one definition for the “vertex” being the location of the coaxially sighted corneal light reflex (CSCLR) [5]. These appear to be for the two axes of interest, yet corneal data are not recorded along what is thought to be the axis of symmetry.

Rather than measuring angles, equipment measurements are often based on an additional assumption about eye symmetry. The white region outside clear cornea (the limbus) can be easily identified in an image of the eye, and the centre of this is assumed to be the optical axis at the depth of that image plane. The pupil centre can also be found in the same manner. Lateral distances can be calculated in mm from the retroreflection reference point, though these might be labelled as angles (α, κ), with the pupil centre sometimes called chord mu (μ) rather than kappa. It is valuable to have the parameters readily available, and the pupil information is perhaps the most complex. The pupil centre can vary with illumination changes, but also the iris is pushed forwards with age as the crystalline lens grows, and then drops back following cataract surgery, leading to the variations in Figure 2 for cataract patients.

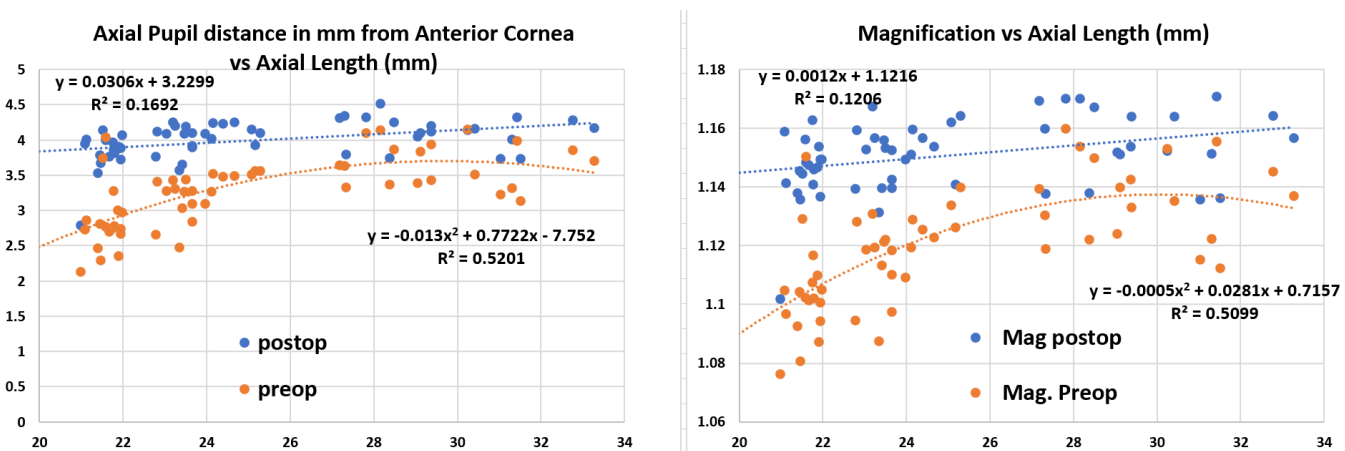


Figure 2. (left) Axial distance from corneal vertex to physical pupil. (right) Estimate of magnification of physical pupil in an image. Most eyes are in the 2nd grouping of axial lengths.

The pupil is often assumed to be decentred on average, yet mean angle Kappa values for younger phakic eyes of 3.9° [3] and 5.8° [5] suggest that the pupil is also generally centred on the optical axis. With chord mu (or kappa), instruments that use a visual image give the distance of the *apparent* pupil centre from the reference of about 0.3 mm , yet instruments with internal information, such as Scheimpflug and OCT, might give a value for the *actual* internal pupil of about 0.2 mm [6]. Mean kappa and alpha values elsewhere for phakic eyes of 0.35 mm [5] and 0.44 mm [7] hint at a decentred pupil because the values are not identical, but it is possible that effects due to magnification of the pupil are not specifically addressed. IOL decentration values are also given by some instruments, but typically as decentrations compared to the visual axis for a rotated eye, rather than from the optical axis.

Conclusions

There are many publications that provide values for rotations, tilts, and decentrations using different methods, both for the phakic eye and the pseudophakic eye, but rarely with enough information for a complete understanding. Taken together, the concept that both types of eyes are on average generally symmetrical about an optical axis, including a generally centred pupil, seems reasonable. This implies that an IOL is typically centred by the capsular bag (and if certain styles of IOL are slightly more variable in centration than others then measurements should show it). It would be useful if publications gave information relative to both the axes of interest. A “tilted and decentred IOL” sounds like a problem, but it seems likely that the average IOL is centred on the optical axis. The most important retinal location is the foveal centre, and that could be described using a field angle, relative to the optical axis. There are substantial variations in the parameters about the mean, and there are particular concerns about the centration of corneal procedures, and the centration of IOLs that are not monofocal. Improvements in characterizing the pupil location would be beneficial, as would additional information about the centration of corneal data (with the words *vertex* and *apex* being too similar for the description of two different points on the cornea).

Acknowledgement

Grateful thanks to Maria Muzyka-Woźniak for the OCT images.

References

- [1] Chang DH, Waring GO. The subject-fixated coaxially sighted corneal light reflex: A clinical marker for centration of refractive treatments and devices. *Am J Ophthalmol*. 2014;158(5):863–74.
- [2] Simpson MJ, Muzyka-Woźniak M. Iris characteristics affecting far peripheral vision and negative dysphotopsia. *J Cataract Refract Surg*. 2018;44(4):459–65.
- [3] Atchison DA, Smith G. *Optics of the Human Eye*. 2nd ed. CRC Press; 2023.
- [4] van Vught L, Luyten GPM, Beenakker J-WM. Distinct differences in anterior chamber configuration and peripheral aberrations in negative dysphotopsia. *J Cataract Refract Surg*. 2020;46:1007–15.
- [5] Reinstein DZ, Archer TJ, Rowe EL, Gobbe M, Vida RS. Distribution of pupil offset and angle kappa in a refractive surgery preoperative population of 750 myopic, emmetropic, and hyperopic eyes. *J Refract Surg*. 2021;37(1):49–62.
- [6] Holladay JT. Apparent chord mu and actual chord mu and their clinical value. *J Cataract Refract Surg* [Internet]. 2019;45(8):1198–9.
- [7] Mahr MA, Simpson MJ, Erie JC. Angle alpha orientation and magnitude distribution in a cataract surgery population. *J Cataract Refract Surg*. 2020;46:372–7.

RGP Contact lens Fluorogram visualization with 3D Printed sclero-corneal surfaces

Jorge Ares*, Nerea Tolón, Diana Gargallo, Francisco Ávila and

Applied physics, University of Zaragoza, Zaragoza, Spain

*fatxuxa@unizar.es

Rigid gas permeable contact lens (RGP-CL) fitting can be a complex and time-consuming process for both practitioner and patient. Recently, 3D printing technology was suggested as an alternative tool to reduce patient chair-time during RGP-CL fitting. The aim of this work was to research the scope of 3-D light-stereolithography technology to manufacture sclero-corneal surfaces suitable to pre-evaluate the fluorogram pattern of a particular RGP-CL fitting. To accomplish this, a series of symmetric astigmatic sclero-corneal surfaces were: modelled, 3-D printed with a commercial stereolithography 3D printer and, measured with a clinical 3-D Fourier profilometer. The accuracy of the proposal was successfully contrasted versus their corresponding numerical simulated fluorograms.

Keywords: Rigid gas permeable Contact lenses; fitting; fluorogram; 3D printing

Introduction

Rigid gas permeable contact lenses (RGP-CLs) are an important solution for correcting corneal irregularities, high levels of astigmatism and presbyopia. However, RGP-CLs may cause discomfort and require a more complex fitting processes than regular soft CLs. Currently, different methods for fitting RGP contact lenses are available, mainly based on topographic measurements to assess the corneal surface and evaluating fluorescein patterns with trial RGP-CLs. The incorporation of topography-based algorithms [1] have allowed to simulate fluorescein patterns and optimize the fitting process. These methods have been proven to reduce fitting time by the clinician, the number of required trial RGP-CLs, and the risk of corneal abrasion.

Following this line Zhao et al. [2,3] proposed the use of commercial Fused Deposition Modelling (FDM) 3D printing technology to evaluate RGP-CLs fitting without the patient intervention (excepting the measurement of its surface corneal geometry). The idea consisted in using 3-D printed cornea models to pre-evaluate the contact lens saving chair-time to the patient. In comparison with virtual fluorograms based on topography data, this technique has the advantage that the practitioner can also check the mobility and real behaviour of the contact lens to be fitted. However, due to the 3-D printing technology used and the absence of realism in the ocular surface models, the results presented Zhao et al. [2,3] can be considered as rough approximation to this solution.

Alternatively, 3-D light-ltereolitography has demonstrated to achieve good quality results concerning the manufacture of different kind of optical surfaces [4-6]. Trying to take advantage of this, in this work it was researched the use of blue laser stereo-litography to fabricate more realistic ocular surfaces suitable to simulate the fluorogram of RGP contact lens fitting. The work consisted of: 1) Realistic modelling of parametric sclero-corneal surfaces, 2) 3-D printing of sclero-corneal models, 3) Geometric characterization of 3-D printed models, 4) Image acquisition of experimental fluorograms corresponding with real RGP contact lenses and 5) Comparison with numerically simulated fluorograms based on topography data.

Material and methods

The sclero-corneal surfaces were modelled by a combination of two biconic surfaces (Equation 1) for creating both the scleral base and the corneal surfaces.

$$z(x,y) = [Cvx*x^2 + Cvy*y^2] / [1 + (1 - (ccx+1)*Cvx^2*x^2 - (ccy+1)*Cvy^2*y^2)^{0.5}] \quad (1)$$

Where $Cvx=1/Rx$ (Rx is the curvature radius of the x main meridian); $Cvy=1/Ry$ (Ry is the curvature radius of the y main meridian); ccx is the conic constant in the x axis and ccy the conic constant in the y axis. In the scleral surface $ccx=ccy=0$ was set [7].

In the process of printing the SECs, several steps were required. The first step involved creating a stereolithography file in the form of a "Standard Template Library" (stl) file to register the geometry of the sclero-corneal surface. Second, the form of the sclero-corneal model was translated into in G-Code commands by means of Ultimaker Cura 4.13.0 software. In this work, an SLA printer was used (Moai 130, Peopoly). This printer uses blue laser (405 nm) to cause cross-linking of functional groups in specially formulated resin [8]. Finally, a post-washing and curing process was required to remove resin excess and finish the model respectively.

The geometry of the sclero-corneal surface was measured with the Eye surface profiler (ESP, Eaglet-Eye, Netherlands). The ESP employs Fourier domain profilometry to cover up a circular region of 20 mm diameter. This measurement range includes cornea, sclero-corneal limbus, and part of the scleral tissue [9] so it results optimal to characterize the 3-D printed samples of this work. To measure the surfaces with the ESP, a customized holder was fabricated and fitted to the headrest of the instrument.

Finally, to create a real fluorogram Systane® Lubricant Eye Drops (Alcon Laboratories, Fort Worth, TX, USA) was mixed with fluorescein powder and then instilled in the 3D surfaces before the insertion of the contact lens to evaluate. To control the accuracy of the whole process the final fluorogram image was compared with a virtual fluorogram generated based on the nominal contact lens geometry and the measured geometry of the 3-D printed sclero-corneal surface.

Results

A series of 3-D printed sclero-corneal surfaces were manufactured and characterized for fitting purposes using the ESP. Table 1 shows the parameters of one sample example with high astigmatic level measured with the ESP. In this table: Rs is the Steep radius, Rf the Flat radius, Qs is the Conic constant of the steep meridian and Qf is the Conic constant of the steep meridian.

Table 1. Parameters measured with ESP of the SECs.

Nº SEC	Rs (mm)	Rf (mm)	Astigmatism	Qs	Qf	Corneal diameter (mm)	Scleral diameter (mm)
1	7.74	8.52	-4.42D x 4°	-0.39	-0.39	12.00	19.00

Moreover, Figure 1 shows the flow-chart to achieve the fluorogram image of a tricurve spherical RGP-CL with 8.5 mm base curve (9.5 mm diameter) when it is fitted over the sclero-corneal model surface described at Table 1.

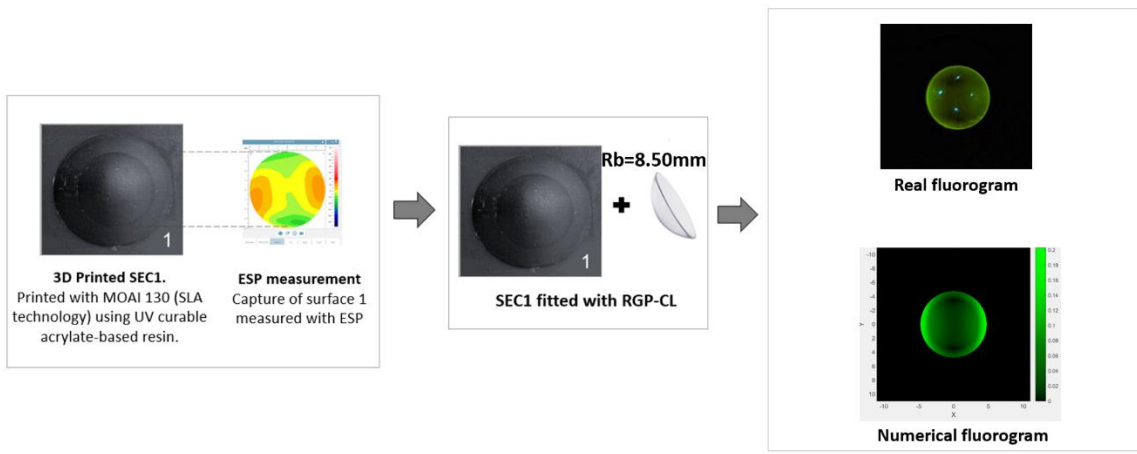


Figure 1. Fitting of RGP- CL on a SEC surface.

Finally, the same figure shows the good agreement between the image corresponding with the real fluorogram and the virtual fluorogram calculated from the nominal geometry of the contact lens and the sclero-corneal topography.

Conclusions

It has been shown how SLA printing technology can be used to make reliable sclero-corneal surface models to simulate clinical contact lens fitting. Considering our results, this kind of technology seems promising as a tool to help the contact lens professional in the fitting of RGP contact lenses. Nevertheless, the real impact of this technology to contact lens fitting is a subject which deserves further researching.

This research was supported by Ministerio de Ciencia, Innovación y Universidades (Grant PID2020-114311RA-I00); Gobierno de Aragón (Grant E44- 20R).

References

- [1] Cardona G, Isern R. Topography-based rgp lens fitting in normal corneas: the relevance of eyelid and tear film attributes. *Eye Contact Lens*. 2011; **37**:359–64.
- [2] Zhao F, Zhao G, Weijie F, Chen L. Application of 3D printing technology in RGPCl simulation fitting. *Med Hypotheses*. 2018; **113**:74–6.
- [3] Zhao F, Wang J, Wang L, Chen L. An approach for simulating the fitting of rigid gas-permeable contact lenses using 3D printing technology. *Contact Lens Anterior Eye*. 2019; **42**(2):165–9.
- [4] Aimar A, Palermo A, Innocenti B. The Role of 3D Printing in Medical Applications: A State of the Art. *J Healthc Eng*. 2019, 5340616
- [5] Vaidya N, Solgaard O. 3D printed optics with nanometer scale surface roughness. *Microsystems Nanoeng*. 2018; **4**:18
- [6] Wang Y, Gawedzinski J, Pawlowski ME, Tkaczyk TS. 3D printed fiber optic faceplates by custom controlled fused deposition modeling. *Opt Express*. 2018; **26**(12):15362.
- [7] W. A. Douthwaite. *CONTACT LENS OPTICS AND LENS DESIGN*. Third ed. ELSEVIER. 2006.
- [8] Silbert SD, Simpson P, Setien R, Holthaus M, La Scala J, Ulven CA, et al. Exploration of Bio-Based Functionalized Sucrose Ester Resins for Additive Manufacturing via Stereolithography. *ACS Appl Polym Mater*. 2020; **2**(7):2910–8.
- [9] Jesus DA, Kedzia R, Iskander DR. Precise measurement of scleral radius using anterior eye profilometry. *Contact Lens Anterior Eye*. 2017; **40**(1):47–52.

A comparison between measurements of actual lens position with two optical biometers: Lenstar LS 900 and Anterion

Diana Gargallo^{1*}, Pilar Mateo¹, Francisco Javier Castro², Laura Remón and Jorge Ares¹

¹ Applied physics, University of Zaragoza, Zaragoza, Spain

² Ophthalmology Department, Hospital de Alcañiz, Alcañiz, Spain.

* dgargallo@unizar.es

A prospective study was conducted to evaluate the inter-device agreement of the measurement of current position of the intraocular lens (ALP) using two optical biometers based on different physical principles. Anterion, based on swept-source optical coherence tomography (SS-OCT), and Lenstar LS900, based on optical low-coherence reflectometry (OLCR). The sample consisted of 25 healthy eyes that underwent cataract surgery by the same surgeon (F.J.C.A), and were implanted with Clareon (Alcon) intraocular lenses. Biometric measurements were performed before and after surgery using both devices. Statistically significant average differences (0.11 mm) between ALP measurements obtained with both instruments were found.

Keywords: Actual Lens Position, Lenstar, Anterion

Introduction

A-scan ultrasound has traditionally been considered the gold standard for assessing ocular parameters such as central corneal thickness, anterior chamber depth, and axial length. However, its use in ophthalmic practice is limited by disadvantages such as direct contact, dependence on expertise, and ocular deformation. To overcome these limitations, technologies such as partial coherence interferometry (PCI), low-coherence optical reflectometry (OLCR), and swept-source optical coherence tomography (SS-OCT) have emerged. PCI technology has been widely used in clinics due to its non-invasive nature, higher accuracy, and reduced dependence on expertise. Subsequently, optical devices based on OLCR, such as the Lenstar LS 900 biometer (Haag-Streit, Köniz, Switzerland), were developed [1]. However, both PCI and OLCR manifest difficulties in measuring patients with dense or posterior cataracts.

Recently, SS-OCT technology has been introduced for ocular biometric measurements, offering improved tissue penetration and higher axial and lateral resolution. The Anterion (Heidelberg Engineering, Germany) is an advanced SS-OCT system designed for high-resolution measurements in the anterior segment and axial length. It utilizes a 1300 nm light source to achieve an axial resolution of less than $10\text{ }\mu\text{m}$, a scanning depth of $14 \pm 0.5\text{ mm}$, and a lateral scanning range of up to 16.5 mm [2].

The use of these advanced technologies and instruments has revolutionized the evaluation and monitoring of the actual lens position (ALP), significantly improving the outcomes of ophthalmic surgeries. ALP is defined as the physical distance measured from the anterior corneal surface to the anterior surface of the intraocular lens. Proper positioning of the intraocular lens is vital for achieving optimal vision as it ensures optimal focusing of light onto the retina. Knowing the final position of the intraocular lens provides valuable information for procedure evaluation, postoperative follow-up, and continuous improvement of surgical techniques. This contributes to ensuring optimal vision and long-term success in cataract surgery [3].

The primary objective of this research was to comprehensively analyse the inter-device agreement in measurements of the ALP using two optical biometers, the Anterion and the Lenstar LS900. This evaluation was conducted on a sample of healthy eyes that had previously undergone cataract surgery with the Clareon lens under the care of the same surgeon.

Methods

The present prospective study was conducted at the Ophthalmology Department of Alcañiz Hospital (Teruel, Aragón) from November 2022 to April 2023. All participants underwent a comprehensive ophthalmological evaluation, which included visual acuity testing, slit lamp examination, non-contact tonometry, and direct examination. Only one eye of each participant was selected for inclusion in the study. Inclusion criteria were decimal visual acuity above 0.5 and proper intraocular lens implantation in the capsular bag. Exclusion criteria included previous refractive surgery, preoperative or postoperative inability to achieve a biometric measurement, capsule rupture during surgery, implantation outside the capsular bag, or a history of vitrectomy. Cases in which the intraocular lens could not be detected with postoperative biometry were also excluded.

A total of 5 measurements were taken preoperatively using the Lenstar optical biometer and 5 measurements with the Anterion prior to the surgical intervention. All surgeries were performed by the same ophthalmologist (F.J.C.A) using the phacoemulsification technique of the crystalline lens through a *2.40 mm* incision, followed by the implantation of a monofocal intraocular lens (IOL) in the posterior chamber. The implanted lens was the Clareon IOL (Alcon Laboratories, Dallas, Texas, USA), a biconvex aspheric lens with a refractive index of 1.55 and nominal fourth-order spherical wavefront aberration *-0.2 microns*.

Four weeks after surgery, 5 postoperative measurements were again conducted using optical biometry with Lenstar in pseudophakic mode and Anterion to measure the postoperative ALP with Anterion (ALP_A) and with Lenstar (ALP_L). Both preoperative and postoperative measurements were performed by the same evaluator (P.M.B).

The normal distribution of data was verified using the Shapiro-Wilk test. A p-value < 0.05 was considered statistically significant. Bland-Altman plots were used to explore potential systematic differences between inter-device results. The limits of agreement were calculated as the mean ± 1.96 standard deviations (SD).

Results

The study involved 25 eyes (16 right eyes and 9 left eyes). The sample were randomly chosen between the right eye and the left eye. The preoperative measurements using Anterion showed the following characteristics of the patients: mean axial length of 23.53 ± 0.96 mm, central corneal thickness of 534 ± 37.85 microns, crystalline lens thickness of 4.65 ± 0.40 mm, anterior chamber depth of 3.12 ± 0.35 mm, white-to-white distance (WTW) of 11.67 ± 0.36 mm, and pupil diameter of 3.81 ± 1.08 mm. Measurements with Lenstar showed a mean axial length of 23.55 ± 0.97 mm, central corneal thickness of 532 ± 38.67 microns, crystalline lens thickness of 4.52 ± 0.38 mm, anterior chamber depth of 3.10 ± 0.36 mm, white-to-white distance (WTW) of 11.84 ± 0.47 mm, and pupil diameter of 4.32 ± 1.07 mm.

From the postoperative means with Anterion and Lenstar, it was found that the mean \pm SD of ALP_A was 4.62 ± 0.27 mm, and ALP_L was 4.51 ± 0.27 mm. Statistical analysis using a t-test showed that the differences between the two measurements were statistically significant ($p < 0.05$). Figure 1 displays the Bland-Altman graphs illustrating the differences between ALP_A and ALP_L . The mean difference

between ALP_A and ALP_L was 0.11 mm with a standard deviation of 0.055 mm . The limits of agreement (LoAs) were calculated as $[0.001, 0.215]\text{ mm}$.

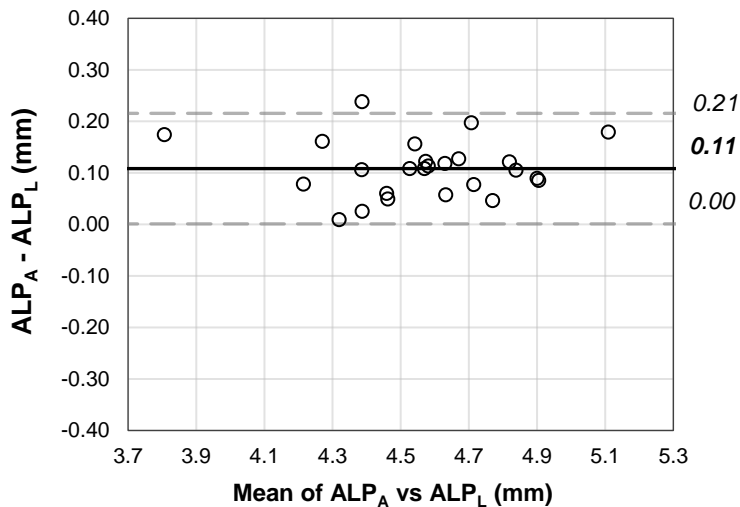


Figure 1: Bland–Altman plot comparing ALP measured with Anterion and Lenstar.

Conclusion

In conclusion, the results of this study reveal statistically significant differences in measurements of the actual lens position (ALP) between the optical biometer Lenstar LS 900 based on OLCR and Anterion based on SS-OCT. A mean discrepancy of 0.11 mm was found between the ALP measurements obtained with both devices, indicating that the measurements of both devices cannot be interchanged. Furthermore, the agreement limits of $[0.001, 0.215]\text{ mm}$ indicate that 95% of the differences between the two devices fall within this range.

It is noticed that the results of this study cannot be directly extrapolated to other populations or clinical situations. The lack of other reference studies to compare with, highlight the need for further research to achieve a deeper understanding of the differences between the Anterion and Lenstar devices in measuring the actual lens position.

Acknowledgement

This research was supported by Ministerio de Ciencia, Innovación y Universidades (Grant PID2020-114311RA-I00); Gobierno de Aragón (Grant E44- 20R).

References

- [1] Cruysberg LP, Doors M, Verbakel F, Berendschot TT, De Brabander J, Nuijts RM. Evaluation of the Lenstar LS 900 non-contact biometer. *Br J Ophthalmol*. 2010;94(1):106-110.
- [2] Ruiz-Mesa R, Aguilar-Córcoles S, Montés-Micó R, Tañá-Rivero P. Ocular biometric repeatability using a new high-resolution swept-source optical coherence tomographer. *Expert Rev Med Devices*. 2020;17(6):591-597.
- [3] Plat J, Hoa D, Mura F, et al. Clinical and biometric determinants of actual lens position after cataract surgery. *J Cataract Refract Surg*. 2017;43(2):195-200.

Effect of rotation and axial shift of toric intraocular lenses analysed by means of numerical ray tracing

Diana Gargallo^{1*}, Francisco J. Castro Alonso², Jorge Ares¹ and Laura Remón¹

¹ Applied physics, University of Zaragoza, Zaragoza, Spain

² Ophthalmology Department, Hospital de Alcañiz, Alcañiz, Spain.

* Corresponding author: dgargallo@unizar.es

Toric intraocular lenses (T-IOLs) are extensively utilized for astigmatism correction in cataract surgery. Precise alignment and rotation are critical for optimizing visual outcomes, as even minor rotations can significantly affect visual acuity. This study employed numerical ray tracing to evaluate the impact of rotation and axial shift on T-IOL performance. Pseudophakic eye models incorporating T-IOLs were generated, and their optical performance was assessed under varying alignment conditions, including rotational angles (2.5° to 40°) and anterior-posterior axial shift (0.10 to 1.00 mm). The study aimed to provide valuable insights into the influence of rotation and axial shift on T-IOL effectiveness attempting to compare with previous researching results.

Keywords: Toric intraocular lens, Rotation, Axial shift, Ray tracing

Introduction

Toric intraocular lenses (T-IOLs) have become a popular and effective solution for correcting astigmatism during cataract surgery. Unlike traditional spherical lenses, T-IOLs require precise rotational alignment to achieve the desired visual outcome. Even small rotations can significantly impact visual acuity. The main sources of error are preoperative corneal measurements, followed by axial displacement and lens tilt. Other factors, such as kappa angle, surgically induced astigmatism, anterior chamber depth, etc., also contribute to the error. Previous studies have demonstrated that each degree of T-IOL rotation reduces its effectiveness by 3.3% with a 30° rotation, eliminating astigmatic correction. However, recent research has questioned these findings. A study by Shimizu et al. [1] in 1994 observed negative effects in two cases due to 30° lens rotations. Based on these observations, the authors concluded that a 30° rotation of the lens was acceptable. Subsequent studies have revealed a more complex relationship between rotation degree and loss of effectiveness, such as the Alpins study [2] with vector analysis or the study by et al. and Tognetto et al. [3], with objective image quality testing for one astigmatic condition (3.75D astigmatic IOL) and an aberration-free cornea.

This work aims to describe the loss of effectiveness of T-IOLs due to rotation and axial shift using numerical ray tracing and extending the analysis to more astigmatic powers and a more physiological cornea model.

Methods

All designs were carried out using the Oslo Edu v22 optical design software. Firstly, a total of 16 T-IOLs were designed with different spherical power (SE) values (16D, 20D, 24D and 28D) and different cylindrical (CYL) powers (1.50D, 3.00D, 4.50D, and 6.00D). The following parameters were kept constant for all T-IOLs: central thickness of 0.663 mm, edge thickness of 0.210 mm, refractive index (for 555 nm)

of 1.55, and anterior and posterior asphericity equal to zero. The posterior curvature radius of the T-IOLs was -20 mm, and the anterior surface was determined based on the astigmatic requirement. Subsequently, 16 pseudophakic eye models were designed based on the Atchison eye model [4], with corneal radii and axial lengths determined for each designed T-IOL. Finally, the lens position measured from the corneal anterior vertex was respectively set to 4.15, 4.47 and 4.85 mm according with the study developed by Castro et al [5].

Once the eyes were designed, the optical performance of the T-IOLs was evaluated using Zernike coefficients (calculated for a pupil diameter of 3.27 mm). Zernike coefficients were converted to regular Fourier terms (M, J_0, J_{45}) to obtain the objective refraction in the form of a negative cylinder [6]. Various conditions were evaluated: 1) T-IOL rotation from 2.5° to 40° in the 16 systems and 2) Axial shift of the T-IOL, describing an anterior-posterior axial shift (E_ALP) from 0.10 to 1.00 mm from the ideal position.

Results

If the T-IOL rotates off its intended axis, an astigmatic change occurs, while the residual M component remains at 0D. Figure 1(a) illustrates the effect of rotation on the remaining amount of astigmatism calculated using ray tracing. The residual cylindrical component (C) arising from rotation shown a clinically noticeable value (> 0.25D) with a rotation error equal to or greater than 5° for all the T-IOLs evaluated in this study. Furthermore, for the T-IOLs of CYL 4.50D and 6.00D, a rotation of 2.5° will be enough to reach a clinically relevant astigmatic error. Nevertheless, it is observed that for systems with T-IOLs having the same CYL value, regardless of the spherical power of the T-IOL, the astigmatic error with rotation is practically the same.

In Figure 1b, it is displayed the comparison of effectiveness loss calculated using the 3.3% rule and the one obtained in this work by means of numerical ray tracing. The greatest differences with the 3.3% rule are found for a rotation of 20°, where there is a difference of 2.37% between this rule (loss of 66.60%)

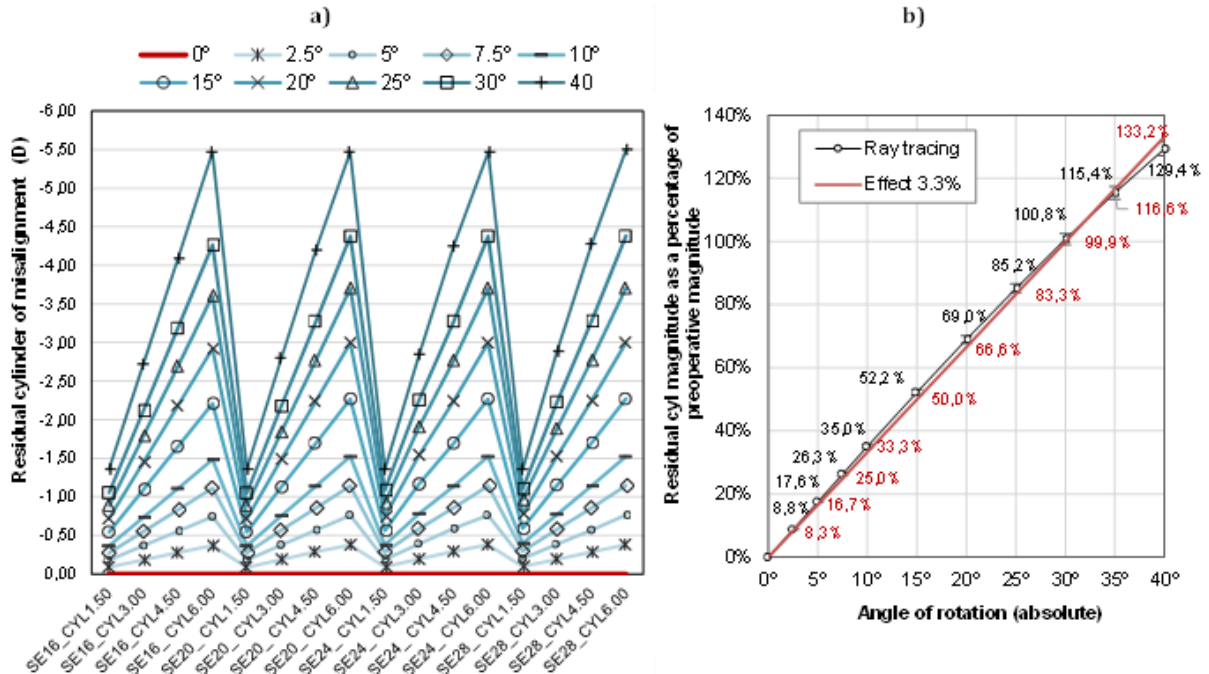


Figure 1a) Residual astigmatism due to rotation of T-IOLs in the 16 systems; Figure 1b): Effect of T-IOL rotation on the magnitude of remaining astigmatism calculated using the 3.3% rule and in the present study in the 16 model eyes.

and the results obtained in this study (loss of 68.97%). Furthermore, effectiveness (100-loss) of the T-IOL reduces to zero for an axis error of 30°.

The calculations performed in this work also have shown that the astigmatic error is not clinically relevant (< 0.25D) when the T-IOL axially shifts from the ideal position without rotation error, this general statement is true except for those with a CYL 6.00D T-IOL. In that case, an astigmatic error > 0.25D (residual C = -0.31D) will be observed only when the T-IOL axially shifts ≥1 mm.

Conclusions

The study showed that a rotation of 5° or more of a toric intraocular lens (T-IOL) results in a clinically noticeable astigmatic error (> 0.25D) for the evaluated T-IOLs. In T-IOLs of CYL 4.50D and 6.00D, a rotation of 2.5° leads to a clinically relevant residual astigmatism. Additionally, regardless of the spherical power of the T-IOL, systems with T-IOLs of the same CYL value exhibit similar residual astigmatism with rotation.

Furthermore, the study found very small discrepancies (< 2.37%) between the effectiveness loss results obtained using the 3.3% rule for T-IOLs and the results obtained through ray tracing. Axial displacement without rotation has minimal impact on residual astigmatism, except for CYL 6.00D T-IOLs with ≥ 1 mm deviation.

Acknowledgement

This research was supported by Ministerio de Ciencia, Innovación y Universidades (Grant PID2020-114311RA-I00); Gobierno de Aragón (Grant E44- 20R).

References

- [1] Shimizu K, Misawa A, Suzuki Y. Toric intraocular lenses: correcting astigmatism while controlling axis shift. *J Cataract Refract Surg.* 1994;**20**(5):523-526.
- [2] Alpins NA. Vector analysis of astigmatism changes by flattening, steepening, and torque. *J Cataract Refract Surg.* 1997;**23**(10):1503-1514.
- [3] Tognetto D, Perrotta AA, Bauci F, et al. Quality of images with toric intraocular lenses [published correction appears in *J Cataract Refract Surg.* 2018 Jun;44(6):794]. *J Cataract Refract Surg.* 2018;**44**(3):376-381.
- [4] Atchison DA. Optical models for human myopic eyes. *Vision Res* 2006; 36: 2236-2250.
- [5] Castro-Alonso FJ, Bordonaba-Bosque D, Piñero DP, Latre-Rebled B. Predictive value of intracystalline interphase point measured by optical low-coherence reflectometry for the estimation of the anatomical position of an intraocular lens after cataract surgery. *J Cataract Refract Surg.* 2019;**45**(9):1294-1304.
- [6] Thibos LN, Horner D. Power vector analysis of the optical outcome of refractive surgery. *J Cataract Refract Surg.* 2001;**27**(1):80-5.

Visual motion perception in a young university population

Pilar Casado, Lucía Cobos, Sofía Otín, and Jorge Ares*

Applied Physics, University of Zaragoza, Zaragoza, Spain

*fatxutxa@unizar.es

The coherent motion discrimination test is an evaluation method for the assessment of global visual motion perception. In this study, this aspect of visual perception was evaluated in 35 young university students. Moreover, the relationship of visual motion perception performance with defocus and stereoscopic visual acuity was also explored. The results showed significant differences between visual motion perception under normal and myopic defocus conditions for the 4 degrees of coherence (10, 20, 30, and 40%) of the pattern tested. Furthermore, no significant differences were found between groups with different stereoscopic visual acuity.

Keywords: motion perception; degree of coherence; coherent motion discrimination

Introduction

The ability to perceive moving objects in the environment around us is one of the numerous skills of the visual system. This ability is essential for hazard detection, spatial orientation, or visual tracking. Although area V5 is the area of the visual cortex specialized in motion detection [1], areas V6, and V3A have been shown to be involved in the analysis of motion-related properties such as direction and speed [2]. These areas are in the extrastriate cortex and are part of the dorsal pathway, which is also known as the *where* pathway, as opposed to the ventral pathway, known as the *what* pathway. An impairment in V5-V6 and V3A could lead to *akinetopsia* or motion blindness [3], in which the subject would be unable to perceive motion through visual function, perceiving scenes of moving objects as frames of a film project at a low frame rate. Discrimination of coherent motion within a random motion noise pattern has been used as a psychophysical measure of global visual motion perception. This test is known as the coherent discrimination motion test (CDM) [4].

The main purpose of this work was to assess global visual motion perception in a university population and to study the influence of defocus and stereoscopic visual acuity (SVA) on this ability. Another aim was to study the repeatability of the CDM test used, incorporated into a commercially available visual assessment device.

Methods

A total of 35 young university optometry students (19.03 ± 2.63 years) participated in the study, which was conducted at the Laboratory of Visual Optics Research of the University of Zaragoza (Spain). Exclusion criteria were a history of ocular pathology or surgery, binocular decimal visual acuity (BVA) with correction for distance vision worse (smaller) than 0.8 on the decimal scale, and stereoscopic visual acuity worse (bigger) than 57".

Measurements were performed in two different sessions on non-consecutive days. Session 1 consisted of measuring binocular VA, measuring SVA, and performing the CDM test, which was repeated 3 times. All measurements were carried out with the subject wearing their prescription for distance vision. Session 2 consisted of measuring binocular VA with a +1.00 D trial lens placed over their habitual prescription and performing the CDM test, 3 repetitions were also carried out under defocused

conditions. All tests were performed using the Optotab^(R) Office Polar (SmarThings4Vision) display.

The CDM test starts with a central fixation cross projected on the screen, which disappears showing a circular pattern of white dots on a black background. During the presentation time of the dot pattern (300 ms), a percentage of the dots move together at the same speed and direction, while the others move at random and independent speeds and directions (distractor dots). When the pattern disappears, the subject is forced to choose the overall direction of the perceived movement between 4 possible answers: up, down, left, or right. The ratio between the number of dots that move together and the number of distractor dots is called the degree of coherence of the pattern. The test consists of 20 trials and randomly presents patterns with four different degrees of coherence: 10, 20, 30, and 40%. As a result of this test, the percentage of correct answers is obtained for each degree of coherence of the pattern.

Statistical analysis was performed using SPSS V.26 (IBM Statistics). To study the repeatability of the CDM test, the coefficient of variation (CV) and the intraclass correlation coefficient (ICC) were calculated. The Kolmogorov - Smirnov test was used to assess the normality of the distribution of the variables collected. Due to the lack of normality, it was necessary to approach the statistical analysis with non-parametric tests. The Mann-Whitney U test for paired samples was used to study the differences in the CDM test under normal and defocused conditions. To study the results of the CDM test as a function of SVA, the sample was divided into two groups. Group 1 consisted of participants with an SVA better (smaller) than 25.2" and group 2 consisted of those with an SVA worse (bigger) than 25.2". The groups represented 77.1 % and 22.9 % of the total sample, respectively.

Results

Table 1 shows the mean and standard deviation of the coefficient of variation obtained from the three CDM test measurements and the intraclass correlation coefficient for each degree of coherence.

Figure 1-a shows the mean and standard deviation of the proportion of correct responses obtained for each degree of coherence, under normal and myopic defocus conditions. The mean binocular decimal VA obtained in each condition was 1.18 ± 0.10 and 0.85 ± 0.29 , respectively. The *p*-values of all Mann-Whitney U-tests were less than 0.05, so a significant difference exists between the two conditions.

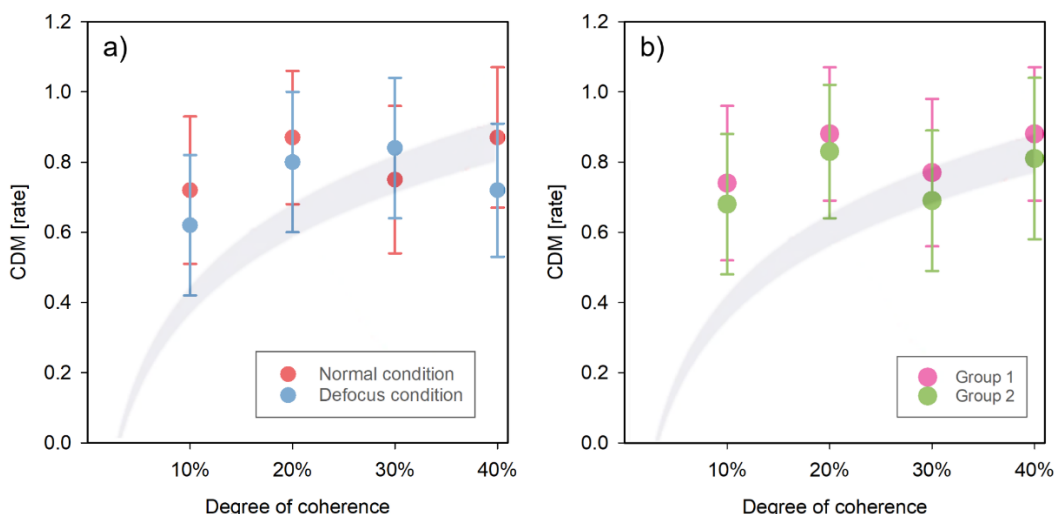


Figure 1. A) Mean and sd of the percentage of correct answers of the CDM test in normal conditions (red) and in myopic defocus conditions (blue). B) Mean and sd of the percentage of correct answers of the CDM test obtained for the high SVA group (pink) and for the low SVA group (green).

Figure 1-b shows that the CDM test results for the high SVA group were higher than for the low SVA group. However, this difference was not significant, as the p-values obtained in the Wilcoxon test were greater than 0.05, for all degrees of coherence. The shaded region in the graphs corresponds to the ranges of normal values obtained in the study by Gori et al [5], for children with normal reading ability.

Table 1. Coefficient of variation and intraclass correlation coefficient

Degree of coherence	CV (%)	ICC
10 %	0.29 ± 0.20	0.70
20 %	0.17 ± 0.21	0.83
30 %	0.15 ± 0.20	0.82
40 %	0.11 ± 0.23	0.91

Conclusions

The CDM test incorporated in Optotab® Office Polar showed high repeatability for the four degrees of coherence evaluated. The results obtained from the CDM test under normal conditions are within the range of normal values obtained by Gori et al [5] for the highest coherence grades. However, for the 10 and 20% degrees of coherence, the values obtained in this study were higher than those obtained in Gori's study. This result suggests an improvement in the perception of movement with age at lower degrees of coherence.

Except for the 30% degree of coherence, the CDM test results under normal conditions resulted statistically higher than those obtained under myopic defocused conditions. Furthermore, after separating the sample into two groups according to their SVA, no significant differences were found between the results obtained for the high SVA group and the low SVA group.

Acknowledgement

This research was supported by Ministerio de Ciencia, Innovación y Universidades (Grant PID2020-114311RA-I00); Gobierno de Aragón (Grant E44- 20R).

References

- [1] Gori S, Cecchini P, Bigoni A, Moteni M and Facoetti A. Magnocellular-dorsal pathway and sub-lexical route in developmental dyslexia. *Front Hum Neurosci*. 2014; Jun 24:8-460.
- [2] Pitzalis S, Fattori P, Galletti C. The functional role of the medial motion area V6. *Front Behav Neurosci*. 2013; Jan 16: 6-91.
- [3] Becker G and Zeki S. The consequences of inactivating areas V1 and V5 on visual motion perception. *Brain*. 1995; 118(1): 49-60.
- [4] Braddick O, O'Brien J, Wattam-Bell J, Atkinson J, Hartley T and Turner R. Brain Areas Sensitive to Coherent Visual Motion. *Perception*. 2001; 30(1):61-72.
- [5] Gori S, Seitz AR, Ronconi L, Franceschini S, Facoetti A. Multiple Causal Links Between Magnocellular-Dorsal Pathway Deficit and Developmental Dyslexia. *Cereb Cortex*. 2016 26(11):4356-4369.

Astigmatic powers of the crystalline lens surfaces derived from ocular biometry (Part 2)

Tanya Evans¹* and Jos J Rozema²

¹ Department of Optometry, University of Johannesburg, Johannesburg, South Africa

² Visual Optics Lab Antwerp (VOLANTIS), Faculty of Medicine and Health Sciences, University of Antwerp, Antwerp Belgium

* Corresponding author: tevans@uj.ac.za

Purpose

Part 1 of this study used linear optics to derive the equivalent power of the crystalline lens, as well as the power of the eye, from available ocular biometry parameters. This second part extends the method to estimate the astigmatic powers of the crystalline lens surfaces.

Methods

Linear optics, a paraxial method, is used to obtain the equivalent power of the crystalline lens (Part 1) [1]. Transferences for the thick lens subsystem and equivalent thin lens subsystem are equated, allowing for the estimation of the surface powers. Four simultaneous linear equations are obtained, two of which provide the astigmatic surface powers. The lens surface powers are $\mathbf{F}_{L1} = -\frac{e_2 n_L}{n_v t} \mathbf{F}_{Eq}$ and $\mathbf{F}_{L2} = \frac{e_1 n_L}{n_q t} \mathbf{F}_{Eq}$, where \mathbf{F} represents a 2×2 power matrix, n the refractive indices, t the lens thickness and e_1 and e_2 the distances from the first and second lens surface vertices to the respective lenticular principal planes. The subscripts Eq , q , L and v refer to equivalent power, anterior chamber, lens, and posterior chamber.

Results

The equations are tested on the Gullstrand-Emsley eye using Bennett's constants [2]. The front- and back-surface powers obtained are $8.28 D$ and $13.79 D$, compared to Bennett's $8.27 D$ and $13.78 D$. An example is given based on biometry measurements taken of the eye of a 63-year-old white European male who had a large proportion of his astigmatism originating from his lens, rather than his cornea. From the ocular biometry parameters of his eye the power of the lens was obtained in Part 1 as $(27.97 \quad -0.55) \quad (-0.55 \quad 21.54) D$ ($\mathbf{f} = (24.76 \quad 3.22 \quad -0.55)^T D$ or $28.02/-6.53 \times 175.1^\circ$). Applying the equations above, we obtain powers of $\mathbf{F}_{L1} = \begin{pmatrix} 11.39 & -0.23 \\ -0.23 & 8.73 \end{pmatrix} D$ ($\mathbf{f}_{L1} = (10.06 \quad 1.33 \quad -0.23)^T D$ or $11.41/-2.70 \times 175.1^\circ$) and $\mathbf{F}_{L2} = \begin{pmatrix} 17.21 & -0.35 \\ -0.35 & 13.18 \end{pmatrix} D$ (or $\mathbf{f}_{L2} = (15.20 \quad 2.01 \quad -0.35)^T D$ or $17.24/-4.08 \times 175.1^\circ$) for the anterior and posterior lens surfaces, respectively.

Conclusion

Linear optics may be used to quickly and accurately estimate the astigmatic power of the lens surfaces based on ocular biometry without the use of phakometry or ray tracing. Since the surface powers of the lens are obtained from its equivalent power, both will always have the same axes, however.

Keywords: Astigmatism; linear optics; crystalline lens powers

- [1] Evans T and Rozema JJ. Astigmatic power of the crystalline lens derived from ocular biometry (Part 1). Visual and Physiological Optics Meeting, Antwerp, Belgium, 2023.
- [2] Bennett AG. A method of determining the equivalent powers of the eye and its crystalline lens without resorting to phakometry. *Ophthal Physiol Opt*. 1988. 8: 53-59.

Objective assessment of the effects of a vision therapy protocol on adults with typical binocular vision

Cristina Rovira-Gay*, Marc Argiles, Clara Mestre and Jaume Pujol

Centre for Sensors, Instruments, and Systems Development (CD6).

Universitat Politècnica de Catalunya (UPC). Terrassa, Spain

* Corresponding author: cristina.rovira@upc.edu

The study aimed to evaluate objectively the change in near fusional vergence amplitudes in adults after performing a vergence/accommodative therapy protocol. 32 adults were randomly divided into an experimental group (EG) and a control group (CG). The EG did 45 minutes/week of vision therapy for 12 weeks, while the CG did 15 minutes/week of eye movement exercises in the frontal plane for 12 weeks. After week 12, the CG followed the same protocol as EG. Before starting the protocols, participants in the two groups exhibited similar positive and negative fusional vergence (PFV and NFV, respectively) amplitudes ($p>0.05$). After week 12, there were no significant differences between groups in PFV and NFV amplitudes. After week 24, NFV and PFV amplitudes were significantly higher ($p<0.001$, and $p=0.022$, respectively) compared to their baseline at week 12. Improvement in PFV and NFV amplitudes was obtained after 24 weeks, but not after the first 12 weeks of the vision therapy protocol.

Keywords: Vision Therapy, Eye-Tracking, Fusional Vergence Amplitudes

Introduction

Vision therapy is a sequence of neurosensory and neuromuscular exercises that are performed to develop, rehabilitate, and improve visual skills and their processing, and is an effective treatment option for some binocular vision dysfunctions such as convergence insufficiency.[1] It could be also used to prevent or relieve vision discomfort in individuals with normal binocular vision who have prolonged use of near work,[2] and to improve visual skills, such as eye-hand coordination, which are important in sports vision.[3] Using conventional clinical methods, it is not possible to quantify objectively the effects of vision therapy over time, but eye tracking systems can be used to measure objectively vergence responses and monitor objectively and accurately the effects of vision therapy protocols.

In the current study, adult participants with normal binocular vision performed a semi-crossover office-based vergence/accommodative therapy (OBVAT) protocol with a control group and an experimental group. The vision therapy protocol of the experimental group was designed to treat convergence insufficiency (CI); as it is the most studied protocol to train vergence. This protocol has been proven to be effective to train both convergence, or positive fusional vergence (PFV), and divergence, or negative fusional vergence (NFV), in patients with CI[1,4] but its effects have not been proved with typical adults.

The aim of this study was to evaluate objectively the change in fusional vergence amplitudes at near in a group of adults with typical binocular and accommodative systems after performing an OBVAT protocol.

Methods

A total of 32 young adults (24 ± 4 years) with normal scores in the Convergence Insufficiency Symptom

Survey [5] were randomly classified into an experimental group (EG) ($N = 16$), who did 45 min/week of OBVAT for 12 weeks; and a control group (CG) ($N = 16$), who did 15 min/week of office-based therapy based on eye movement exercises in the frontal plane for 12 weeks. After week 12, the CG did the same vision therapy protocol as the EG. To measure fusional vergence amplitudes objectively, a column of 0.2 logMAR letters was presented to the two eyes in an haploscopic setup (Figure 1). The stimuli in the two screens moved synchronously every 2 s in steps of 2 PD from 2 PD to 20 PD and steps of 5 PD from 25 PD to 45 PD to stimulate fusional convergence and divergence. Eye movements were recorded using an Eyelink 1000 Plus (SR Research) at 500 Hz. Break points of PFV and NFV were determined offline from the eye movements recordings using a custom algorithm based on an iterative least-squares fitting procedure.[6] A second-degree polynomial function was fitted as it was representative of the change in vergence demand over time. Then, the break point was determined as the vergence demand at the time of the last fit before the coefficient of determination of the fit started to decrease. Participants' PFV and NFV were measured before starting the vision therapy protocol (week 1), and at weeks 6 and 12 for both the EG and CG, and at weeks 18 and 24 for the CG.

Results

NFV and PFV break points averaged across participants in each group at each time point are presented in Table 1 and Figure 2. Before starting the OBVAT protocol, participants in the two groups exhibited similar PFV and NFV ($p = 0.578$, $p = 0.637$, respectively). The results of a mixed ANOVA with Bonferroni post-hoc tests revealed no significant differences in PFV and NFV break points during the first 12 weeks of vision therapy between the CG and the EG ($p = 0.119$, $p = 0.219$, respectively). After completing the OBVAT protocol, at week 24, the CG exhibited a significant increase in PFV and NFV amplitudes compared to their baseline values at week 12 ($p = 0.022$, $p < 0.001$, respectively).

Conclusions

To conclude, this study provided a new insight into the possibility of training fusional vergence amplitudes in participants with typical binocular vision. We observed an improvement in PFV and NFV amplitudes in participants who completed 24 weeks of two different vision therapy protocols, but not after 12 weeks of the OBVAT protocol done by the EG. These results suggest a potential training effect in the measurement of fusional vergence amplitudes. Clinicians may take into account these results in future therapeutic interventions before attempting to train vergence skills of patients without binocular and accommodative dysfunctions.

Acknowledgement

This publication is part of the project PID2020-112527RB-I00 project, funded by MCIN/AEI/10.13039/501100011033.

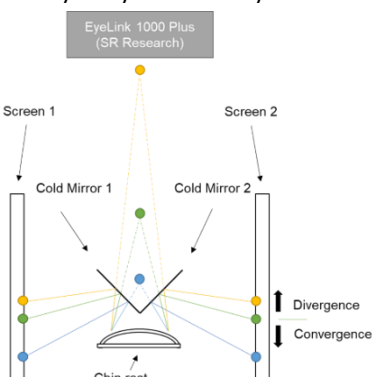


Figure 1: A schematic representation of the haploscopic system used in this study. The three circles in each screen represent three different stimulus positions. The two green stimuli drive the same convergence angle as a real stimulus placed at 40 cm in front of the subject, represented by the light green circle. Thus, this is the stimuli's position at the beginning of the measurements (0 PD). Relative to this position, the yellow and blue stimuli in the two monitors drive fusional divergence and convergence, respectively.

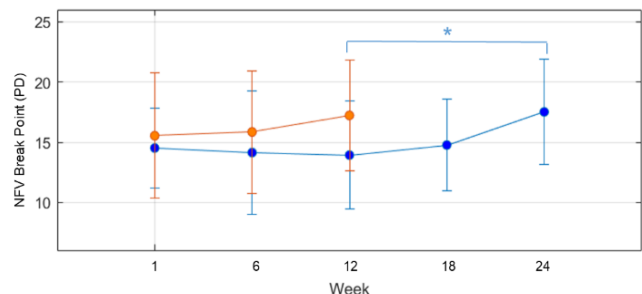


Figure 2: Representation of the negative fusional vergence (NFV) and positive fusional vergence (PFV) tests mean and standard deviation (SD) of control group (in blue) and experimental group (in orange). *indicates statistically significant differences between the tests (corrected p-value < 0.05). Prism diopters: PD. For visualization purposes, axes are not drawn at the same scale.

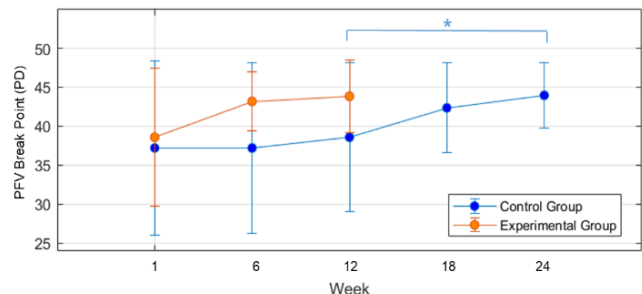


Table 1. Mean ± standard deviation of the negative fusional vergence (NFV) and positive fusional vergence (PFV) break points measured at weeks 1, 6 and 12 for both control and experimental groups, and at weeks 18 and 24 for the control group. PD (Prism Dioptrē).

	PFV break point (PD)		NFV break point (PD)	
	Experimental Group	Control Group	Experimental Group	Control Group
Week 1	38.79±8.05	37.20±11.21	15.54±5.19	14.52±3.31
Week 6	43.22±3.77	37.20±10.89	15.84±5.09	14.14±5.13
Week 12	43.83±4.66	38.58±9.54	17.22±4.63	13.93±4.50
Week 18	-	42.35±5.70	-	14.76±3.83
Week 24	-	43.95±4.16	-	17.51±4.35

References

- [1] Convergence Insufficiency Treatment Trial Investigator Group. The Convergence Insufficiency Treatment Trial: Design, Methods, and Baseline Data. *Ophthalmic Epidemiol.* 2008; **15**:24–36.
- [2] Rosenfield M. Computer Vision Syndrome: A Review of Ocular Causes and Potential Treatments. *Ophthalmic Physiol Opt.* 2011; **31**:502-15.
- [3] Clark JF, Ellis JK, Bench J, Khouri J, Graman P. High-Performance Vision Training Improves Batting Statistics for University of Cincinnati Baseball Players. *PLoS ONE.* 2012; **7**:e29109.
- [4] Scheiman M, Talasan H, Alvarez TL. Objective Assessment of Disparity Vergence after Treatment of Symptomatic Convergence Insufficiency in Children. *Optom Vis Sci.* 2019; **96**:3–16.
- [5] Convergence Insufficiency Treatment Trial (CITT) Study Group. The Convergence Insufficiency Treatment Trial: Design, Methods, and Baseline Data. *Ophthalmic Epidemiol.* 2008; **15**:24–36.
- [6] Rovira-Gay C, Mestre C, Argiles M, Vinuela-Navarro V, Pujol J. Feasibility of Measuring Fusional Vergence Amplitudes Objectively. *PLoS ONE.* 2023; **18**:e0284552.

Immersive virtual reality intervention for post-COVID-19 condition: an eye movement pilot study

Valdeflors Vinuela-Navarro¹, Joan Goset¹, Clara Mestre¹, Mikel Aldaba¹,
Maite Garolera^{2,3}, Neus Cano^{2,4}, Mar Ariza^{2,4}, Bárbara Delàs⁵, Meritxell Vilaseca¹.

¹ Center for Sensors, Instruments and Systems Development,
Universitat Politècnica de Catalunya (UPC), Terrassa (Barcelona), Spain

² Clinical Research Group for Brain, Cognition and Behavior,
Consorci Sanitari de Terrassa (CST), Terrassa, (Barcelona), Spain

³ Neuropsychology Unit, Hospital de Terrassa, Consorci Sanitari de Terrassa (CST),
Terrassa (Barcelona), Spain

⁴ Medical Psychology Unit, Department of Medicine, University of Barcelona, Barcelona, Spain

⁵ Servei d'Oftalmologia. Consorci Sanitari de Terrassa (CST), Terrassa, Spain

* Corresponding author: valldflors.vinuela@upc.edu

Eye movement control and performance is impaired in multiple neurological and neurodegenerative conditions, and current evidence suggests that eye movement alterations may also be present in individuals with Post-COVID-19 condition (PCC) as they often show altered cognitive status. This pilot study aims to provide preliminary data on the impact of an immersive virtual reality intervention designed to enhance cognitive performance on oculomotor function and control in individuals with PCC. Saccadic, smooth pursuit and fixational eye movements were recorded using an EyeLink 1000 Plus eye tracker in a group of participants with PCC who completed the intervention (experimental group) and a control group of participants with PCC who did not receive the intervention. Mild improvements in eye movement performance, especially for smooth pursuit parameters, were observed in both groups of participants.

Keywords: Post-COVID-19 condition; eye movements; cognitive intervention.

Introduction

Post-COVID-19 condition (PCC) refers to a range of symptoms lasting for at least 2 months that occur usually 3 months after the onset of COVID-19, and that cannot be attributed to an alternative diagnosis [1]. Common symptoms of PCC include fatigue, headaches, altered smell and taste, and shortness of breath [2]. Cognitive dysfunction and neuropsychiatric symptoms including brain fog, attention deficits and confusion have also been reported in PCC [2, 3, 4]. Recent research indicates that eye movement control may also be impaired in PCC in a similar way that is impaired in other neurological and neurodegenerative conditions [5, 6, 7].

While there is still no specific treatment for the management of PCC, different interventions are being considered and studied with the objective to recover altered cognitive functions (e.g. memory, attention), functional capacity (i.e. capacity to perform activities of daily living) and well-being in individuals with PCC [8].

This pilot study aims to investigate possible changes in oculomotor function and control in individuals with PCC and cognitive symptoms after conducting an intervention based on immersive virtual reality (immersive VR).

Methods

Participants diagnosed with PCC reporting cognitive symptoms were recruited and randomly allocated to a control ($n = 9$) or an experimental group ($n = 12$). Those in the experimental group conducted an immersive VR intervention designed to enhance cognitive and functional performance by improving attention and concentration. The intervention consisted of 16 one-hour sessions that incorporated mindfulness techniques to improve concentration and attention as well as cognitive and physical exercises.

Eye movements were recorded binocularly twice, before and after the intervention (three months apart), using the EyeLink 1000 Plus eye tracker (SR-Research Ltd., Ottawa-Ontario, Canada) while participants conducted three visually guided pro-saccadic and anti-saccadic tasks (gap, overlap and Posner paradigms), horizontal and vertical smooth pursuit (sinusoidal and rectilinear), and a fixation task. Those in the control group did not receive an intervention and their eye movements were also recorded twice, at the beginning of the study and after a three-month period, following the same procedures as participants in the experimental group.

Latency, amplitude, and peak velocity were obtained for pro-saccades and anti-saccades. For the assessment of smooth pursuit performance, root mean-square (RMS) errors, velocity gains, as well as the number and amplitude of saccades during the pursuit task were calculated. Finally, fixation accuracy and stability were assessed by calculating RMS error, bivariate contour ellipse area (BCEA), as well as the number and amplitude of saccades during the fixation task. Mixed ANOVA statistical analysis was conducted to test main effects on the eye movement performance and interactions between interventions.

Results

Eye movement recordings from three participants were discarded due to the presence of binocular vision anomalies that had an impact on ocular motility (Control $n = 1$; Experimental $n = 2$). Complete successful eye movement *recordings* (before and after the intervention or three months apart for controls) were obtained from 8 control (age 51.07 ± 2.14 years) and 10 experimental (age 51.03 ± 6.93 years) participants.

Preliminary results showed that, in general, eye movement performance and control was very similar between the first (at the beginning of the study) and the second (three months later after intervention

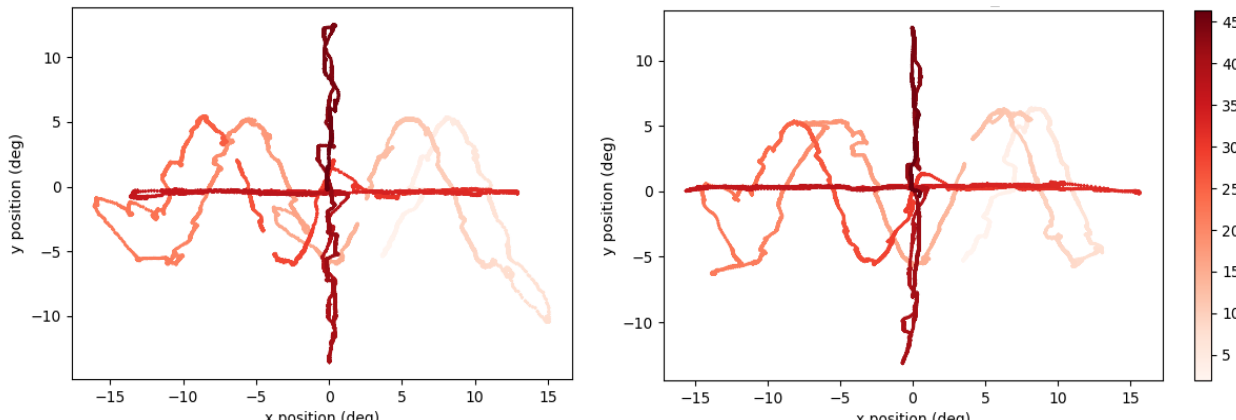


Figure 1. Eye movement (right eye) traces from a participant in the experimental group conducting the smooth pursuit task before (left) and after (right) the immersive VR intervention.

or with no intervention) evaluation. A tendency for reduced saccadic (pro-saccades and anti-saccades) latency, which was not significant, was observed in some participants in the second evaluation, with no differences between those who conducted the intervention and those who did not. Similarly, fixation RMS error and BCEA showed a slight tendency to improve during the study in some participants, but this was not significant. For smooth pursuit eye movements, non-significant mild improvements in RMS error and gains were found during the study. Significantly fewer saccadic intrusions during sinusoidal ($p = 0.048$) and vertical rectilinear ($p = 0.027$) smooth pursuit tasks were observed at the end of the study (Figure 1). While the reduction in the number of saccades seemed slightly larger in the intervention group, there was no significant intervention effect.

Conclusions

A mild improvement in smooth pursuit performance showing fewer saccades during the smooth pursuit was observed. While a non-significant intervention effect was found, the small study sample limits the power of the statistical analysis performed.

These preliminary results suggest that immersive VR designed to improve cognition has limited impact on eye movement function and performance in individuals with PCC. The small improvement found may indicate a learning effect rather than a true improvement from the intervention provided. In order to elucidate all this, ongoing work focuses on increasing the study sample size as well as considering other interventions to improve cognitive function in individuals with PCC.

Acknowledgements

This publication is part of the project TED2021-130409B-C54 and TED2021-130409B-C51, funded by MCIN/AEI/10.13039/501100011033 and the European Union “NextGenerationEU”/PRTR. J.G. thanks the Spanish Government for the predoctoral FPI grant he received. V.V-N is funded by “Ministerio de Universidades” and “European Union - NextGenerationEU”

References

- [1] Soriano JB, Murthy S, Marshall JC, et al. A clinical case definition of post-COVID-19 condition by a Delphi consensus. *Lancet Infect Dis.* 2022;22(4): e102–7.
- [2] Lopez-Leon S, Wegman-Ostrosky T, Perelman C, et al. More than 50 long-term effects of COVID-19: a systematic review and meta-analysis. *Sci Rep.* 2021;11:16144.
- [3] Ariza M, Cano N, Segura B, et al. Neuropsychological impairment in post-COVID condition individuals with and without cognitive complaints. *Front Aging Neurosci.* 2022; 14:1029842.
- [4] Maury A, Lyoubi A, Peiffer-Smadja N, de Broucker T, Meppiel E. Neurological manifestations associated with SARS-CoV-2 and other coronaviruses: A narrative review for clinicians. *Rev. Neurol.* 2020; 177(1):51-64.
- [5] García Cena C, Costa MC, Saltarén Pazmiño R, et al. Eye movement alterations in post-COVID-19 condition: A proof-of-concept study. *Sensors.* 2022;22(4):1481.
- [6] Carbone F, Zamarian L, Rass V, et al. Cognitive dysfunction 1 year after COVID - 19: evidence from eye tracking. *Ann Clin Transl Neurol.* 2022;9(11):1826–31.
- [7] Kelly KM, Anghinah R, Kullmann A, et al. Oculomotor, vestibular, reaction time, and cognitive tests as objective measures of neural deficits in patients post COVID-19 infection. *Front Neurol.* 2022;13:919596.
- [8] Fugazzaro S, Contri A, Esseroukh O, et al. Rehabilitation Interventions for Post-Acute COVID-19 Syndrome: A Systematic Review. *Int J Environ Res Public Health.* 2022;19(9):5185.

A mechanical model of human eye for investigating intraocular pressure effect on geometry of the eye globe

Saeed Zahabi^{1*} Magdalena Asejczyk¹ and Milad Salimibani¹

¹ Department of Optics and Photonics, Wroclaw University of Science and Technology, Wroclaw, Poland

* Corresponding author: saeed.zahabi-amroabadi@pwr.edu.pl

The main purpose of this study was to develop an eye FE model that captures real tissue interactions with acceptable accuracy. Numerical simulations allowed to assess how IOP and boundary conditions affect the mechanical behaviour of the eye components. In addition to determining how IOP changes affect geometry, different types of extraocular tissue modelling were proposed. The effect of extraocular tissues on changes in the geometry of the eye was also clarified.

Keywords: mechanical model of the eye, eye biomechanics, intraocular pressure, eye geometry

Purpose

A comprehensive understanding of eye function requires an integrated approach that combines biomechanical and optical aspects. Previous studies have relied on the optical-mechanical self-regulation hypothesis (OMSA) [1,2], suggesting that the eye has built-in mechanisms that adjust its biomechanical properties to maintain clear vision. On the other hand, simulations and FEM models require appropriate selection of boundary conditions concerning, in the case of the eye, e.g. extraocular tissue parameters (fatty tissue). The goal of these studies is to construct the eye FEM model, including extraocular tissues, and to simulate changes in intraocular pressure (IOP). The main purpose of this study is to determine changes in eye geometry caused by IOP changes and relate them to three different extraocular tissue modelling proposals.

Methods

A three-dimensional symmetric finite element model of the eye globe was created, integrating components such as the sclera, cornea, limbus, zonules, lens, and extraocular tissue (ABAQUS ® FEA Software, 2020) (Fig. 1). Material properties, including elastic and hyperelastic characteristics for these components, were determined based on literature [3-5]. Specifically, hyperelastic properties were assigned to the cornea, limbus, and sclera, while the lens and zonules were assumed to be elastic materials. Furthermore, the viscoelastic properties of fatty tissue around the eye were simulated using a Kelvin-Voigt model. The spring and dash-pot models are parallel, and there is a similar strain on both. According to the Voigt model:

$$\sigma = E_v \varepsilon + \eta_v \dot{\varepsilon} \quad (1)$$

E_v is resists on strain changes and η_v resists on strain rate which can be considered as a spring and a damper, respectively.

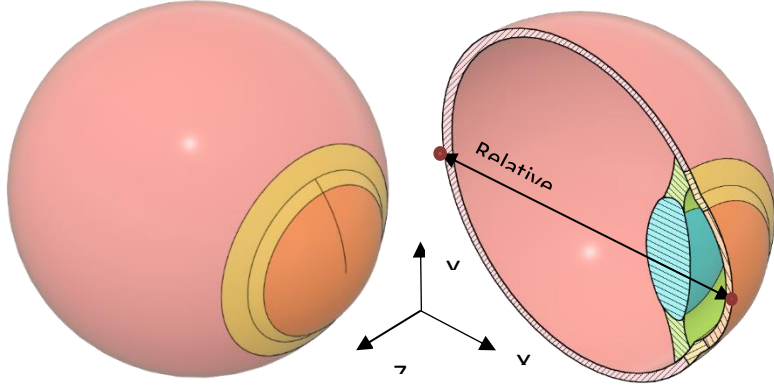


Figure 1: A 3-D model of an eye globe rotated around the x-axis.

Table 1 shows the material parameters of the individual elements of the eye model. Three boundary condition models were applied to the extraocular region. The boundary conditions were divided into spring-only (elastic fatty tissue), spring-dashpot (viscoelastic fatty tissue), and fixed (highly stiff fatty tissue). Furthermore, the relative displacement was calculated based on the difference between the corneal apex and the sclera's end point of the sclera (Fig. 1). An IOP in the range of 12 to 26 mmHg was considered in the vitreous and anterior chambers. In addition, it did not have an external force.

Table 1. Materials used for the different ocular components: k is the bulk modulus, μ is the shear modulus, E and v are the Young modulus and Poisson's ratio, respectively; D is an incompressible parameter used to show volume change.

Component	Material Model	Material properties
Sclera	Hyper elastic, Neo Hookean (1st order)	$C_{neo} = 0.113 \text{ MPa}$, ($\kappa = 100\mu$)
Cornea	Hyper elastic, Ogden (1st order)	$\mu = 0.0541 \text{ MPa}$, $\alpha = 110.4$, $1/D = 10^7 \text{ MPa}$
Limbus	Hyper elastic, Ogden (1st order)	$\mu = 0.270910 \text{ MPa}$, $\alpha = 150$
Lens	Elastic	$E = 1.45 \text{ MPa}$, $v = 0.47$
Zonulas	Elastic	$E = 0.35 \text{ MPa}$, $v = 0.47$
Extraocular Tissue	Visco-elastic, Kelvin-Voigt	Spring stiffness = 0.0831, Dashpot coefficient = 0.3

Results

Figure 2 shows the change in relative displacement as a function of changes in IOP for three different boundary conditions. The results under different boundary conditions differ slightly and the difference between the elastic fatty tissue model and the other two models increases as the IOP increases. It was observed that elastic fatty tissue has a smaller relative displacement than viscoelastic fatty tissue. This indicates that an increase in IOP has less impact on geometry under spring boundary conditions. Additionally, highly stiff fatty tissue has the largest relative displacement compared to viscoelastic fatty tissue. This means that geometry is more affected by changes in IOP.

In general, it can be said that the stiffer the boundary conditions of the tissue around the eye (higher stiffness), the greater the effect of changes in IOP of the eye on geometry and vice versa. Three factors affect the stiffness of extraocular tissue, similar to a truss: Young's modulus, thickness, and equivalent surface area. If Young's modulus is raised, the cross-sectional area of a spring property is increased, or the fatty tissue thickness decreases, the geometry becomes more affected by IOP changes. A part of the tension applied to the viscoelastic fatty tissue is received by the damper. This may explain the greater

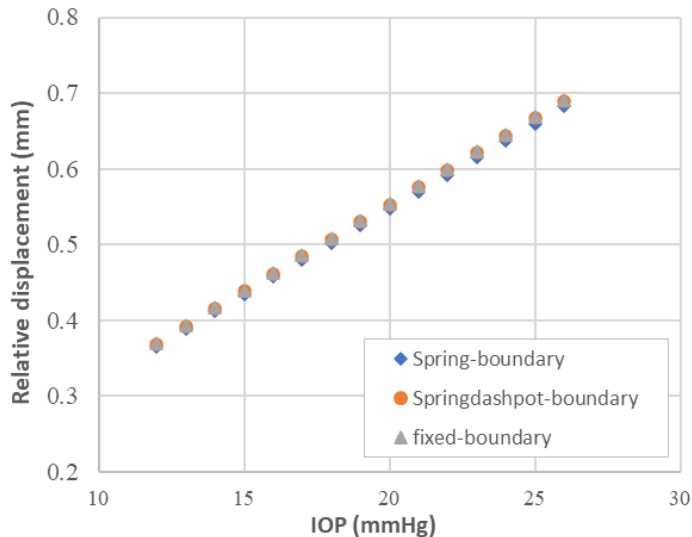


Figure 2: Intraocular pressure vs. Relative displacement.

relative displacement in viscoelastic fatty tissue compared to elastic tissue. Since the damper does not resist displacement, it leads to displacement in other parts. This means that other parts have increased the relative displacement.

Conclusion

The present research was carried out to apply in the future in a model that includes opto-mechanical self-adjustment of the eye. To develop a model that captures real tissue interactions with acceptable accuracy and is suitable for non-invasive techniques to study extraocular tissues. The simulation of fatty tissue around the eye was carried out. To assess the effectiveness of these tissues, we compared Kelvin-Voigt's effective parameters with fixed boundary conditions. A Kelvin-Voigt model can be improved by modifying the parameters. Due to changes in intraocular pressure, relative displacement (geometry) was expected to increase as the stiffness of the tissue around the eye increased. Through numerical simulations, this research assesses how IOP and boundary conditions affect the mechanical behaviour of the eye components. In addition to observing how IOP changes affect geometry, the relationship between IOP changes and fatty tissue types was also clarified. A deeper understanding of the effects on fatty tissue was gained as part of the study.

References

- [1] A. Józwik, M. Asejczyk, P. Kurzynowski, and B. K. Pierscionek, "How a dynamic optical system maintains image quality: self-adjustment of the human eye," *J. Vis.* 21(3), 6 (2021).
- [2] M. Shahiri, A. Józwik, and M. Asejczyk, "Opto-mechanical self-adjustment model of the human eye," *Biomed. Opt. Express* 14, 1923-1944 (2023)
- [3] J. Vroon, J. H. de Jong, A. Aboulatta, A. Elias, F. C. T. van der Helm, J. C. van Meurs, D. Wong, and A. Elsheikh, "Numerical study of the effect of head and eye movement on progression of retinal detachment," *Biomech. Model. Mechanobiol.* 17(4), 975-983 (2018).
- [4] I. Issartel, C. Koppen, and J. J. Rozema, "Influence of the eye globe design on biomechanical analysis," *Comput. Biol. Med.* 135, 104612 (2021).
- [5] A. Karimi, R. Razaghi, C. A. Girkin, and J. C. Downs, "Ocular biomechanics due to ground blast reinforcement," *Comput. Methods Programs Biomed.* 211, 106425 (2021).

Corneal dynamic analysis and its correlation with blood pulsation

Magdalena Asejczyk^{1*}, Mohammadali Shahiri¹, Henryk Kasprzak¹

¹ Department of Optics & Photonics, Wroclaw University of Science and Technology, Poland

* Corresponding author: magdalena.asejczyk@pwr.edu.pl

The present study investigates the dynamic behavior of the cornea by examining the interplay between corneal deformations, fixational eye movements (FEM), and pulsatile ocular blood flow (POBF). An especially custom-designed prototype equipped was used to record video sequences of corneal surface reflections, and simultaneous acquisition of the blood pulsation (BP) signal was performed. The variability of corneal positions and deformations was assessed, and time and frequency domain analyses, including coherence functions, were employed to examine the associations between the acquired signals. The results reveal significant correlations between variations in corneal curvature, selected FEM parameters, and pulsatile blood flow, indicating synchronized expansions of the corneal surfaces with cardiovascular activity. These findings highlight the complex dynamics of both the cornea and FEM, influenced by POBF. Such insights contribute to the development of non-invasive diagnostic techniques and enhance understanding of the optomechanical mechanisms within the eye.

Keywords: Corneal dynamics, Fixational eye movements, Blood pulsation, Eye biomechanics

Purpose

The optical parameters of the cornea are closely related to its geometrical and biomechanical properties, which in depend on its heterogeneous and anisotropic structure, influenced by its physiology. The cornea is often treated as a static element, but in fact it experiences constant and rapid movements. These movements can be influenced by deformations resulting from pulsating fluctuations in intraocular pressure due to blood pulsation variations, which exhibit both slow diurnal changes and rapid fluctuations caused by the heartbeat. The present study investigates the dynamic behaviour of the cornea by examining the interplay between corneal deformations, fixational eye movements (FEM), and pulsatile ocular blood flow.

Methods

An especially custom-designed prototype equipped with a camera and numerical pulse oximeter was utilized to evaluate the right eyeballs of the participants. Video sequences of corneal surface reflections were recorded, and simultaneous acquisition of the blood pulsation (BP) signal was performed (Figure 1). Numerical analysis was conducted to determine the positions and orientations of the reflections, enabling the study of eye movements and corneal deformations. The variability of corneal positions and deformations was assessed, and time and frequency domain analyses, including coherence functions, were employed to examine the associations between the acquired signals.

Results

The presented results display specific parameters that were primarily obtained for two selected images on the cornea, specifically point No. 2 and 4, in each measurement (Figure 1). Nonetheless, numerical

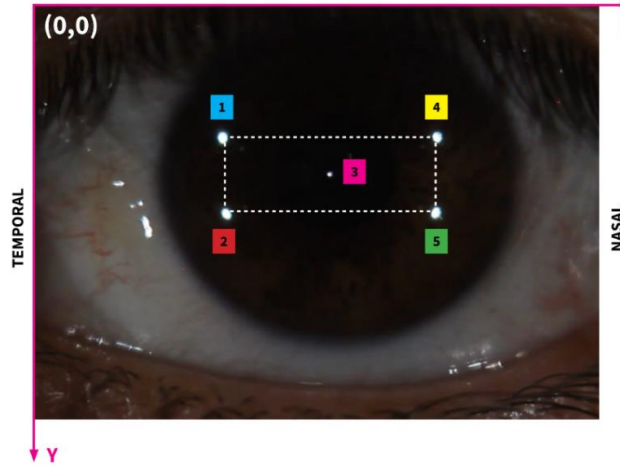


*Figure 1: Identification of the bright reflection spot on the cornea.
Subscripts 1 to 5 illustrate different bright reflection spots. their positions and distances.*

analysis was performed for all five marked points. The achieved subpixel accuracy in determining the position of these points enabled a precise, comprehensive examination of both corneal deformations and eye movements.

Figure 2 illustrates the variability in the linearly detrended distance between points 2 and 4 (d_{24}) and the derivative of the corresponding blood pulsation signal dPu (Fig. 2a), along with their respective Fourier spectra, Fd_{24} and $FdPu$ (Fig. 2b). The Fourier spectra of the blood pulsation derivative were computed to depict the higher harmonics of the blood pulsation more clearly. A significant similarity is observable between the two spectral characteristics.

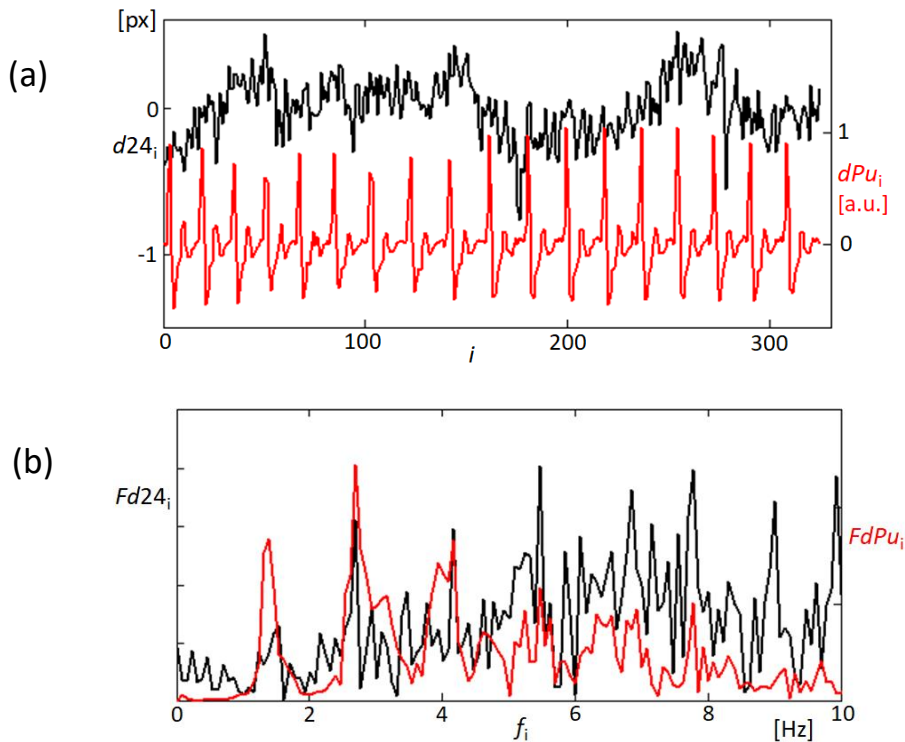


Figure 2. The distance variability between points 2 and 4 after applying a linear detrend, along with the corresponding derivative of the recorded blood pulsation signal. b) The Fourier spectrum of both signals, showcasing the frequency components presented in each signal.

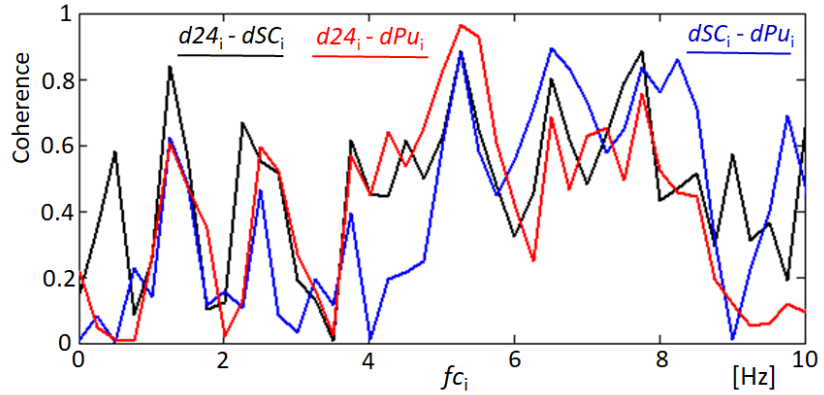


Figure 3: Coherence function between three pairs of respective three signals.

The same analysis was performed for the area of the quadrangle 1254 SC. It was determined and linearly detrended in order to evaluate the dynamics/kinetics of the mutual positions of points 1, 2, 5, and 4 under the assumption of their homogeneous expansion or approach during the measurement. This makes it possible to investigate the signals' frequency components and how they relate to alterations in the quadrangle area.

In order to analyze phase correlations and dependencies among the three signals ($d24$, dSC , and dPu), coherence functions were calculated between each pair of signals. The corresponding coherence functions are presented in Figure 3. Notably, the coherence function values are quite high at specific frequencies (blood harmonics). This indicates that these signals are not independent but exhibit significant correlations. It implies that the relative positions of reflection points from the corneal surface are correlated with blood pulsation, with the correlations being dependent on the harmonic number of the blood pulsation.

Conclusion

These findings highlight the complex dynamics of both the cornea and FEM, influenced by pulsatile ocular blood flow. Such insights contribute to the development of non-invasive diagnostic techniques and enhance understanding of the optomechanical mechanisms within the eye. Further investigation in this field is crucial for a comprehensive understanding of the impact of corneal dynamics on visual processes and for exploring potential diagnostic and treatment approaches.

Computational optics for finite-element corneal modelling

Benedetta Fantaci^{1*}, Miguel-Ángel Ariza-Gracia³, Begoña Calvo^{1,2}

¹ Aragón Institute of Engineering Research, University of Zaragoza, Spain

² Bioengineering, Biomaterials and Nanomedicine Networking Biomedical Research Centre, Zaragoza, Spain

³ ARTORG, University of Bern, Switzerland

* Corresponding author: bfantaci@unizar.es

Finite element models can be employed for reproduction of corneal biomechanical behaviour. To evaluate if a patient-specific model is correctly replicating the vision quality of a subject, its optics must be analysed. This work presents a methodology to compute the optical performance of patient-specific finite-element models, applied to the specific case of Photorefractive Keratectomy (PRK) simulation.

Keywords: cornea; finite element model; optics.

Introduction

In the last two decades, finite element models have been employed in the biomedical field to mimic the mechanical behaviour of biological structures, constituting a tool for the analysis of the mechanical response and prediction of surgical outcomes.

In the optical field, the first models of the cornea and, more in general, of the whole eye were simplified analytical models that did not take into account the biomechanical response of the system [1]. Subsequently, with the advent of numerical methods, more sophisticated models were employed, that allowed to consider multiple biomechanical aspects, without treating the eye tissues as infinite rigid and, thus, providing a more reliable description of the global behaviour of the eye.

To understand if a corneal finite element (FE) model is correctly reproducing the vision quality of a patient, corneal surfaces must be analysed in the same way a topographer (for instance, Pentacam by Oculus or Sirius by CSO) analyses patient's corneas *in vivo*. The optical analysis of FE models is not as straightforward as for analytical models, that usually are constituted by idealized geometries. Moreover, topographers' algorithms are proprietary and are not accessible to the users.

In this work, we developed a methodology that provides a comprehensive evaluation of the optical performance of patient-specific (PS) FE models in the specific application of Photorefractive Keratectomy (PRK) simulation.

Methods

A FE PS corneal model was built, using topographic data of a healthy patient, as described by [2]. A pre-stretch iterative algorithm was used to compute the stress-free configuration and the patient's IOP of 15 mmHg was applied to the corneal posterior surface. A PRK laser surgery was simulated by removing corneal tissue from the anterior surface, whose customised wavefront-guided ablation profile [3] was determined with the intent to correct patient's visual acuity in a personalised fashion.

Pre- and post-surgical FE surfaces of the model, i.e. anterior and posterior point clouds, were compared with topographical data, when available, in order to determine the accuracy of the methodology. The outputs of the topography are two-dimensional maps of the curvature, expressed in terms of refractive

power, of the corneal surfaces.

Before computing curvature maps of a point cloud, it is necessary to perform a polynomial fitting of the surface, given that the point clouds of a FE model are made by a collection of nodes, that constitute the elements of the model, that are not equally spaced as in the point grids created by the topographer, characterized by a constant step between two consecutive points. Moreover, surface fitting is necessary to smooth the surface without changing its optical properties and reduce the noise in the FE point cloud, given the sensibility of curvature maps to micrometric changes. If this step is not performed, too noisy maps will be obtained. Zernike's polynomials are the most used for optical analysis of corneal surfaces:

$$W(r, \theta) = \sum_{n,m} C_n^m \cdot Z_n^m(\rho, \vartheta),$$

where C denotes the Zernike coefficients and Z the polynomials [4]; n describes the order of the radial polynomial and m describes the azimuthal frequency of the sinusoidal component. Zernike's polynomials of order 10 usually perform a reliable fitting, with an error lower than 1 μm with respect to the initial point cloud.

Once the surface fitting is performed, curvature maps were computed on the fitted point cloud. For a complete clinical evaluation, axial, tangential, mean and Gaussian curvature maps must be computed, in order to have a comprehensive view on the health status of patient's corneas. Axial and tangential curvature maps are the most used by clinicians, given their easy computation and interpretation [5]. Axial/sagittal curvature was computed as the inverse of the distance of a point on the anterior surface to the optical axis along its normal. With this map it is possible to determine if refractive defects (myopia, astigmatism, etc.) are present. One limitation is its dependency on the optical axis, making the identification of surface irregularities (like keratoconus) dependent on the location on the surface. Tangential curvature overcomes this limitation, since it does not encounter the optical axis: it was computed as the inverse of the instantaneous radius of curvature, obtained by fitting a sphere at each location of the anterior surface. In this case, the contour map appearance will be influenced by the number of points considered for the sphere fitting.

In this work, mean and Gaussian curvatures were also computed [6], derived from differential geometry. These maps are less sensitive to refractive defects and correctly detect the presence of irregularities. At each point of the surface, it is possible to identify the steepest and the flattest meridians, defined as principal curvatures. Mean curvature (H) and Gaussian curvature (K) are defined as the arithmetic and the geometric means of the principal curvatures, respectively, and they can be calculated as:

$$H = \frac{(1+h_x^2)h_{yy}-2h_xh_yh_{xy}+(1+h_y^2)h_{xx}}{2(1+h_x^2+h_y^2)^{3/2}} \quad (1) \text{ and } K = \frac{h_{xx}h_{yy}-h_{xy}^2}{(1+h_x^2+h_y^2)^2} \quad (2)$$

where $h(x)$ represents the elevation of the corneal anterior surface and $h_x, h_y, h_{xx}, h_{yy}, h_{xy}$ are the first and second partial derivatives, respectively.

Results

Zernike's polynomial fitting error and curvatures contour plots are shown in Figure 1. For the curvature plots, an optical zone of radius $r = 3 \text{ mm}$ was considered. In order to avoid redundancy, Gaussian curvature plots are not reported, given their similar appearance to mean curvature plots. The polynomial fittings in the three cases (topography, pre- and post-surgical meshes) showed a mean error lower than 1 μm , but we can observe some peaks in the error of the post-surgical mesh fitting, due to the customized ablation profile, that induces some surface irregularities. From the comparison between the topographic data and the pre-surgery anterior surface mesh, we can affirm that the methodology

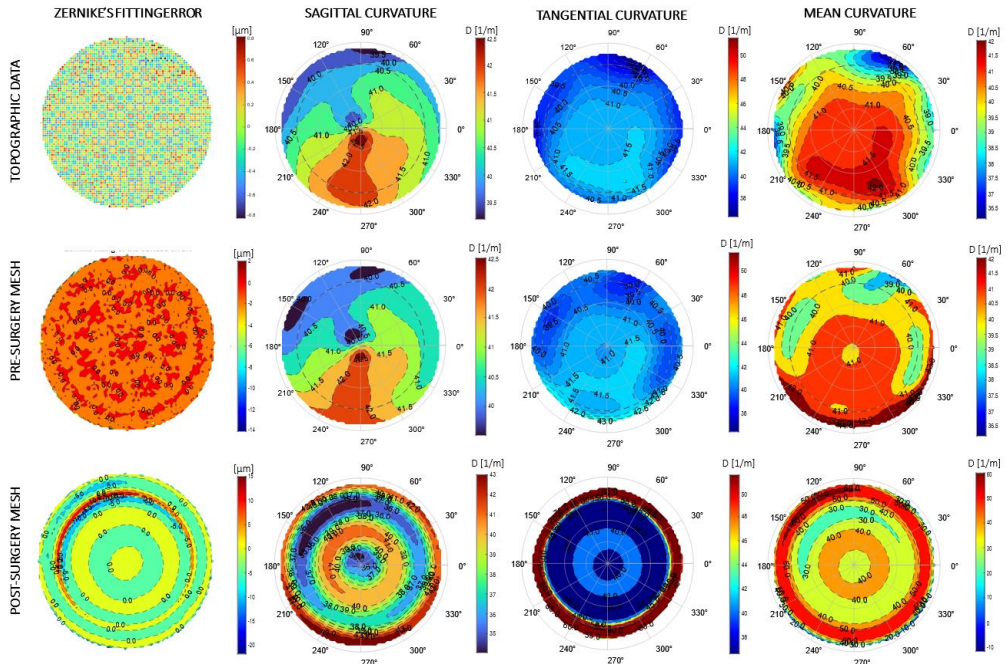


Figure 1: Comparison among initial topographical data, pre- and post-surgery meshes of the patient's corneal anterior surface.

developed in the present work showed high accuracy in reproducing initial optical properties of patient's cornea.

Conclusions

A methodology that computes curvature plots of FE corneal models has been presented, with the specific application to PRK surgery simulation. Accurate results in terms of replicating pre- and post-surgery optical properties of a patient's cornea were achieved. This methodology, that combines FE modelling and optics, could be helpful for surgery planning, given that it allows to obtain a pre-surgical estimation of surgery outcome.

Acknowledgments

This project has received funding from the European Union's Horizon 2020 research and innovation programme under grant agreement No 956720.

References

- [1] Djotyan GP, Kurtz RM, Fernández DC, Juhasz T. An analytically solvable model for biomechanical response of the cornea to refractive surgery. *J Biomech Eng.* 2001 Oct;123(5):440-5.
- [2] Ariza-Gracia MÁ, Zurita J, Piñero DP, Calvo B, Rodríguez-Matas JF. Automatized Patient-Specific Methodology for Numerical Determination of Biomechanical Corneal Response. *Ann Biomed Eng.* 2016 May;44(5):1753-72.
- [3] Carvalho LA. Accuracy of Zernike polynomials in characterizing optical aberrations and the corneal surface of the eye. *Invest Ophthalmol Vis Sci.* 2005 Jun;46(6):1915-26.
- [4] Lakshminarayanan V, Fleck A. Zernike polynomials: A guide. *J MOD OPTIC.* 2011; 58. 1678-1678.
- [5] Tang M, Shekhar R, Huang D. Mean curvature mapping for detection of corneal shape abnormality. *IEEE Trans Med Imaging.* 2005 Mar;24(3):424-8.
- [6] Griffiths GW, Płociniczak Ł, Schiesser WE. Analysis of cornea curvature using radial basis functions - Part I: Methodology. *Comput Biol Med.* 2016 Oct 1;77:274-84

Analysis of the influence of keratoconus mechanical properties, dimension and position on the outputs of Corvis

E Redaelli^{1*}, B Calvo^{1,2}, M. Nana³, J F Rodríguez Matas³, J Rozema⁴, G Luraghi³ and J Grasa^{1,2}

¹ Aragón Institute of Engineering Research (I3A), University of Zaragoza, Zaragoza, Spain

² Centro de Investigación Biomecánica en Red en Bioingeniería, Biomateriales y Nanomedicina, Zaragoza, Spain

³ Department of Chemistry, Materials and Chemical Engineering “Giulio Natta”, Politecnico di Milano, Milan, Italy

⁴ Department of Ophthalmology, Faculty of Medicine & Health Sciences, University of Antwerp, Antwerp, Belgium

* Corresponding author: elena.redaelli@unizar.es

Keratoconus is an eye pathology characterized by a progressive thinning and bulging of the cornea, leading to irregular astigmatism and loss of visual acuity. Non-Contact Tonometry (NCT) is an in-vivo diagnostic test that evaluates intraocular pressure (IOP) by inducing an inward deformation of the corneal tissue through an applied air puff. This work focuses on the use of computational Fluid Structure Interaction simulations to study the impact of pathological material properties, position, and dimension on the output of a commercial NCT (Corvis ST) in diagnosing keratoconus. The deformation parameters are evaluated both on the Nasal-Temporal section and on the perpendicular Superior-Inferior section of the cornea. Some asymmetry indices were proposed to evaluate the severity of the pathology. The results suggest that the proposed double cross-sectional analysis and asymmetry-based approach can enhance the capability of NCT in diagnosing keratoconus.

Keywords: cornea, keratoconus, Corvis ST, Non-Contact Tonometry, FSI simulations

Introduction

Keratoconus is an ocular disorder that manifests in a thinning and a subsequent bulging of the cornea; it results from the loss of the orthogonal architectural organization of the collagen lamellae [1]. Several in-vivo techniques have been developed to investigate the mechanical behaviour of keratoconic corneal tissue. Non-contact tonometry (NCT) is an in-vivo diagnostic procedure aimed to estimate the IOP in response to an air puff. The load applied by the air on the anterior surface of the eye induces an inward deformation of the corneal structure followed by the recovery of its original shape. Corvis ST is a commercially available tonometer that employs an ultra-high-speed camera to capture sectional images of the cornea during the 30 ms procedure. The deformation of the eye in response to the applied air puff depends on four factors: the IOP, the air pressure, the thickness, and the mechanical properties of the structure [2]. Computational simulations are useful to analyse the influence of each component on Corvis ST output. This work aims to assess the capability of the in-use clinical biomarkers of Corvis-ST to detect the presence of keratoconus in its initial stage. In such cases, the ongoing alterations in the internal structure of the tissue are not reflected in its outer appearance, making it challenging to identify the presence of the pathology by topographic analysis. Besides the computation of the biomarkers currently in use, a double-sectional analysis coupled with an asymmetry-based approach is proposed.

Methods

The Fluid Structure Interaction (FSI) simulation detailed in Redaelli *et al* [3] was implemented to simulate the NCT. Three biomarkers of Corvis-ST were selected and evaluated to assess their capability

to detect the presence of pathological tissue. In addition to the Nasal-Temporal (NT) section captured by the device, the Superior-Inferior (SI) section was analysed. At the highest concavity (HC) instant vertical and horizontal asymmetry indexes were defined with the purpose of better characterizing the influence of the diseased tissue on corneal response. Along both sections, the horizontal position of the lowest point of the anterior surface was captured and stored in the *Symh* index, while the difference in height between the positive and negative peaks of the configuration was defined as *Symv*. The work was divided into three sensitivity analyses to investigate the influence of material properties, dimension, and position of the pathological zone. The outputs of each simulation were then compared with the results of the physiological geometry, which was used as a benchmark to evaluate the device's effectiveness in detecting the pathology. The first sensitivity analysis evaluated the influence of the material properties of the designed pathological area on the output data obtained from the simulation. With reference to *Pandolfi et al.* [4], keratoconus was designed as a rounded diseased tissue with a core of 1.5 mm in radius and a transitional area of 1.5 mm in width that was divided into six circular zones. The mechanical properties and the dimension of the corneal pathological tissue are not known a priori. For the sensitivity analysis, we considered a corneal tissue with a decreased influence of the fibres. The central area of the rounded diseased tissue was modelled as an isotropic nearly incompressible hyperelastic material described by a Neo-Hookean formulation with the purpose of reproducing the loss of the architectural organization of the collagen fibres. In the Template material model (TEM) the isotropic constant C_{10} applied in the physiological corneal model was maintained, while in the Increased material model (INC) and Decreased material model (DEC) the parameter was respectively increased and lowered by one-third in order to describe a progressive weakening of the tissue. The second analysis numerically simulated the advancement of the pathology in terms of dimension. The keratoconic area was reduced to 2 mm and 1.5 mm in radius respectively. The last analysis performed examined the accuracy of the proposed asymmetry indexes to locate the position of the affected region. The TEM was named "centred model" and the output data obtained were compared with the "shifted model" obtained by displacing the initial pathological area on the bisector of the Nasal-Inferior dial of the eye. Fluid-structure interaction simulations were performed with Ls-Dyna. Before each simulation, the stress-free geometry was pressurized with the aim of attaining the in-vivo geometry reconstructed from topographical data.

Results and discussion

A trend of increasing values of downward displacement is evident from the material sensitivity analysis consistent with the material weakening. The asymmetry indices underline a non-symmetrical downward displacement induced by the degeneration of the tissue. The values of *Symh* show how the lowest point of each pathological configuration is shifted towards the positive values of x along the NT and the negative values of z on SI consistent with the position of the pathological tissue. The analysis of the *Symv* index indicates how all the models exhibit a difference in height between the peaks of the HC configuration, with the lowest peak captured in the positive values of the x along NT and on the negative value of the z along SI. To assess the detectability of the variations computed by the indexes, their magnitude should be compared with the resolution of the clinical images characterized by squared pixels of 14 μm . The progressive reduction performed on the diameter of the rounded disease results in a progressive reduction of corneal deformation. The unaltered deformation behaviour of the 1.5 mm model captured is given by the combination of two separate factors. The acquired data resulted from both the halving of the initial size of the diseased tissue and the increased distance of the tissue from the area subjected to the applied pressure load. This increased distance was due to the fixed position of the centre of the rounded diseased tissue. In both geometries tested in the last analysis, the clinical

biomarkers were significantly apart from the physiological ones, emphasizing how these variations could lead to the detection of the pathology but without providing suitable details regarding the location of the affected area. Instead, the data obtained from the asymmetry-based analysis can be integrated for deriving position information on the direction of maximum displacement of the anterior surface of the cornea. In each model, combining the values of the *Symh* parameter computed along the two sections of analysis a point on the outer surface of the tissue can be derived and assumed as a guide to identifying the affected region. The values computed in both models are in fact directed toward the centre of the designed rounded diseased tissue.

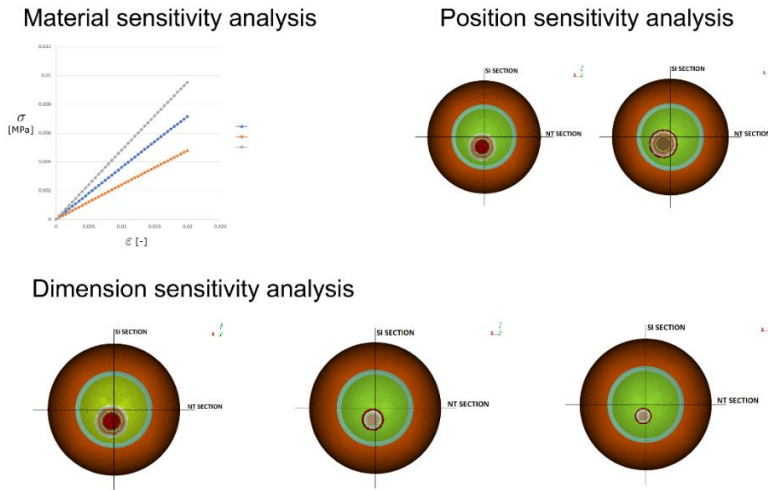


Figure 2: Material used for the pathological area in the material sensitivity analysis. Position and dimension of the keratoconic area.

Conclusion

The data obtained from the simulations highlight the potential improvements that can be achieved by making adjustments to the operation of the device, which can help in the detection of keratoconus, even in the most challenging cases where no indications are found through topographic analysis. The double-section analysis can be performed by rotating the ultra-high-speed camera of the device, while the asymmetry-based approach can be implemented on the already segmented images. Since the work presented was based solely on numerical analysis, it is necessary to test the index's ability to detect pathological tissue in an experimental environment.

Acknowledgment

This project has received funding from: the European Union's Horizon 2020 research and innovation programme under the Marie Skłodowska-Curie grant agreement No 956720.

References

- [1] Morishige, N et al. Second-harmonic imaging microscopy of normal human and keratoconus cornea. *Investigative ophthalmology & visual science*, 2007, 48(3), 1087-1094.
- [2] Ariza-Gracia, M et al. Coupled biomechanical response of the cornea assessed by non-contact tonometry. A simulation study. *PloS one*, 2015, 10(3), e0121486.
- [3] Redaelli, E et al. A detailed methodology to model the Non Contact Tonometry: a Fluid Structure Interaction study. *Frontiers in Bioengineering and Biotechnology*, 2022, 10, 1826.
- [4] Pandolfi, A., & Manganiello, F. A model for the human cornea: constitutive formulation and numerical analysis. *Biomechanics and modeling in mechanobiology*, 2006, 5(4), 237-246.

Opto-mechanical simulations of crystalline lens wobbling during gaze change in accommodated eyes

Ali Dahaghin^{1*}, Milad Salimibani, Agnieszka Boszczyk and Damian Siedlecki

¹ Department of Optics and Photonics, Wroclaw University of Science and Technology, Wroclaw, Poland

* Corresponding author: ali.dahaghin@pwr.edu.pl

The goal of the study was to evaluate the wobbling movement of the crystalline lens, associated to the inertial force resulting from the rotation of the accommodated eyeball, with the aim of finding the wobbling magnitude and stabilization time by means of finite elements simulations on a 2D mechanical model. The output of mechanical simulations was used as an input to optical simulations in order to visualize the Purkinje images performance. The results of combined mechanical and optical simulations were compared to in-vivo bibliographical data. The results of simulations are reasonable extent consistent with the experimental data. After a sudden stopping, the lens manifests some initial magnitude of wobbling; after that, it stabilizes gradually. The decay of wobbling amplitude over time is caused by the damping behaviours of mechanical structures of the eye, as a kind of energy dissipation.

Keywords: crystalline lens; wobbling; eye model; FEM

Introduction

One of the most interesting dynamical phenomena that can be observed in the anterior part of the eye is the so-called lens wobbling – the oscillatory inertial movement of the crystalline lens, resulting from a rapid saccadic movement of the whole eyeball while changing the direction of sight. After the first qualitative observation of the lens wobbling in the 30's of the XXth Century [1] and then in 1970 [2], its real quantitative description was presented by Jacobi and Jagger in 1981 [3] while investigating the intraocular lens (IOL) wobbling in pseudophakic eyes. From the anterior part of the eye, Purkinje images (PI) can be seen as a representation of eyeball movement [4]. To evaluate the oscillations of crystalline lenses, a computer modelling seems to be a convenient tool/approach aimed for better understanding the nature of the wobbling phenomenon.

The general objective of the project is to understand the nature of the dynamical behaviour of the crystalline lens induced by rapid changes of gaze direction. While changing the gaze, the eye undergoes rapid rotational movement around its centre of rotation. When the eye stops immediately after this sudden rotation, the crystalline lens manifests an inertial motion. This motion of the lens – so-called lens wobbling – is likely to be a superposition of two movements induced by the rapid eye's rotation: an inclination of the lens with regard to the axis of the eye and its lateral dislocation that is tangential to the angular direction of the eye's rotation. It has been proved that the wobbling has a nature of damped oscillations, which can be described by the damping factor and its frequency (or period)[5].

Methods

In order to analyse the hypothesis on the inertial movement of the crystalline lens, a 2D numerical model of an accommodated human eye was developed in COMSOL Multiphysics undergoing intraocular pressure as a fluid. Even though, 3D models seem to be more accurate for some research, in this case 2D

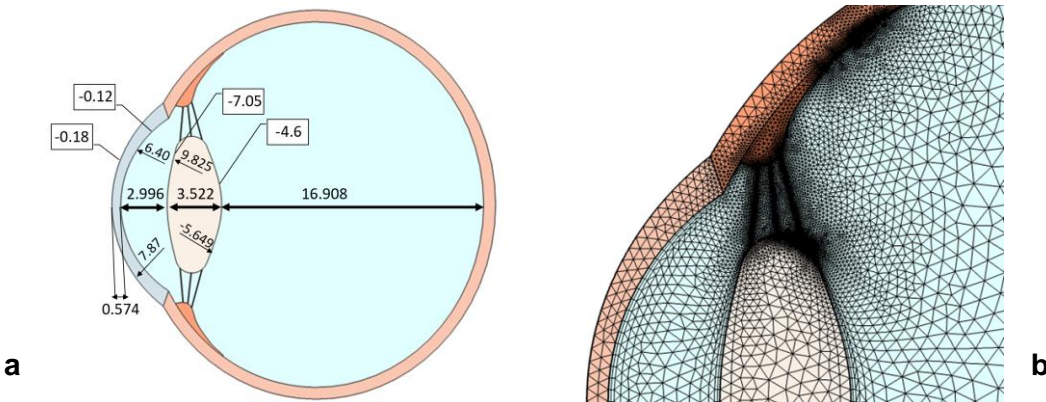


Figure 1. a) Geometry of the model. All distances and radii of curvature are in mm and respective asphericity (conic constants) are shown in the rectangles. b) Mesh representation of the zonular region of the eye globe.

model is simpler and precise enough. The reason is that, the movements of eye in this direction followed by lens rotation is in 2 dimensions and third dimension can be neglected [5]. This model contains the main and influential components in eye biomechanics: lens, zonular fibres, cornea, sclera, and ciliary body. The calculation model was built using the accommodated 20-year-old eye [6]. In Figures 1 and 2, the geometry data and quality of the mesh are displayed, respectively.

It was assumed that the model's components were all homogeneous, isotropic, and linear elastic. The values of the mechanical constants for the various eye structures that are mentioned in the literature are presented in Table 1. Both vitreous body and aqueous humour were modelled as viscous Newtonian incompressible fluid with constant pressure. Dynamic viscosity and density are respectively $0.00074 \text{ Pa}\cdot\text{s}$ and $1000 \text{ kg}/\text{m}^3$ [7]. Also applying an initial pressure of 15 mmHg corresponds to the physiological magnitude of intraocular pressure (IOP). In the mechanical simulations, the whole eyeball was rotated around the vertical axis by 9 degrees.

Table 1. Material properties of the human eye [8, 9].

Modelled structure	Young's modulus [MPa]	Poisson's ratio [-]	Density [kg/m ³]
Ciliary Muscle	11	0.4	1600
Lens	1.45	0.47	1225
Sclera	10	0.4	1400
Cornea	2	0.42	1400
Zonular Fibers	1.5	0.4	1000

Results and conclusions

After a sudden stopping, the lens manifests an initial wobbling, and then it undergoes a gradual stabilization. As the Fig 3 (a) shows this movements are similar to the classical pattern of a harmonic oscillator. Simulation results are reasonable in line with *in vivo* experimental data (Fig 3 (b)), captured by measuring the optical reflections from the posterior surface of the lens (4th Purkinje images) [4]. It seems that zonules, the ciliary body and the lens work as a kind of energy dissipater using damping properties. In order to improve the convergence of the numerical results with the *in vivo* experimental data, a further detailed investigation on the role of the force absorption systems of the eye needs to be conducted.

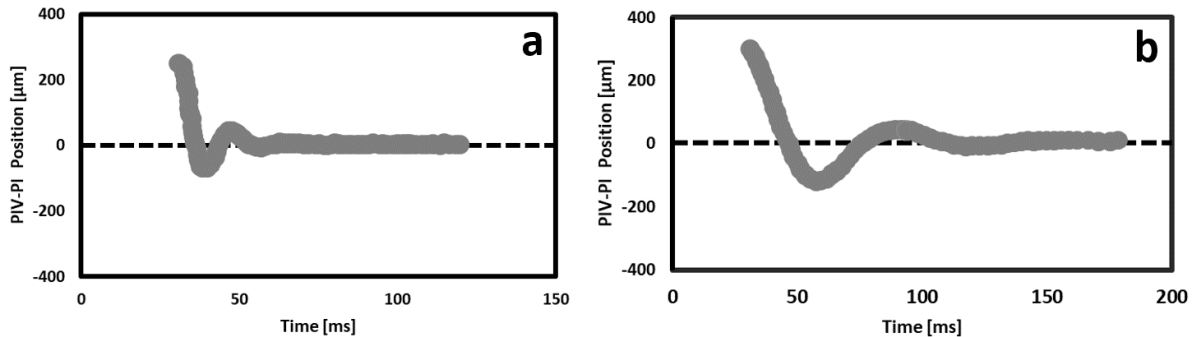


Figure 2. (a) The simulated wobbling of the lens and (b) in vivo measurement of the human eye [4].

In order to obtain the most compatible results, in addition to studying the effect of geometry (based on the accommodation stage), the specific arrangement of the attachment points of zonules to the lens were also chosen in order to achieve the most compatible results. However, there is a wide range of mechanical properties that can be found in the literature, especially for zonular fibres, in the next stage of this research, we will have the sensitivity analysis for mechanical properties.

Acknowledgement

This project has received funding from: the European Union's Horizon 2020 research and innovation programme under the Marie Skłodowska-Curie grant agreement No 956720 and the National Science Centre, grant agreement No 2019/35/B/ST7/03998. FEM simulations have been carried out using resources provided by Wroclaw Centre for Networking and Supercomputing (<http://wcss.pl>), grant No. 556.

References

- [1] A. D'Ombrain, "TREMULOUS LENS," *The British Journal of Ophthalmology*, vol. 20, no. 1, p. 22, 1936.
- [2] R. Bartholomew, "Phakodonesis. A sign of incipient lens displacement," *The British Journal of Ophthalmology*, vol. 54, no. 10, p. 663, 1970.
- [3] K. W. Jacobi and W. S. Jagger, "Physical forces involved in pseudophacodonesis and iridodonesis," *Albrecht von Graefes Archiv für klinische und experimentelle Ophthalmologie*, vol. 216, pp. 49-53, 1981.
- [4] J. Tabernero and P. Artal, "Lens oscillations in the human eye. Implications for post-saccadic suppression of vision," *PloS one*, vol. 9, no. 4, p. e95764, 2014.
- [5] A. Boszczyk, F. Dębowy, A. Jóźwik, A. Dahagin, and D. Siedlecki, "Complexity of crystalline lens wobbling investigated by means of combined mechanical and optical simulations," *Biomedical Optics Express*, vol. 14, no. 6, pp. 2465-2477, 2023.
- [6] J. F. Zapata-Díaz, H. Radhakrishnan, W. N. Charman, and N. López-Gil, "Accommodation and age-dependent eye model based on in vivo measurements," *Journal of Optometry*, vol. 12, no. 1, pp. 3-13, 2019.
- [7] D. Singh, K. Firouzbakhsh, and M. T. Ahmadian, "Human intraocular thermal field in action with different boundary conditions considering aqueous humor and vitreous humor fluid flow," *International Journal of Mechanical and Mechatronics Engineering*, vol. 11, no. 4, pp. 717-725, 2017.
- [8] Z. Bocskai and I. Bojtár, "Biomechanical modelling of the accommodation problem of human eye," *Periodica Polytechnica. Civil Engineering*, vol. 57, no. 1, p. 3, 2013.
- [9] I. Issarti, C. Koppen, and J. J. Rozema, "Influence of the eye globe design on biomechanical analysis," *Computers in Biology and Medicine*, vol. 135, p. 104612, 2021.

Modelling the sensitivity of the accommodative amplitude to the orientation of zonular fibres

Liying Feng^{1,2*}, Henk Weeber¹, Carmen Canovas Vidal¹, Barbara Krystyna Pierscionek³

Bram Koopman¹, Shima Bahramizadeh Sajadi¹ and Jos Rozema^{2,4}

¹ Johnson & Johnson Vision, Groningen, The Netherlands.

² Visual Optics Lab Antwerp (VOLANTIS), Faculty of Medicine and Health Sciences,
University of Antwerp, Antwerp, Belgium

³ Faculty of Health, Education, Medicine and Social Care, Medical Technology Research Centre,
Anglia Ruskin University, Chelmsford, United Kingdom

⁴ Department of Ophthalmology, Antwerp University Hospital, Edegem, Belgium

* Corresponding author: Lfeng13@its.jnj.com

To assess the effect of zonular fibres' orientation on crystalline lens accommodation, finite element models with different orientations of zonular fibres were developed. Three zonular sections were modelled with multiple anterior and posterior zonular angles combinations. Crystalline lens deformation was processed to get the accommodative amplitude. The link between the accommodative amplitude and zonular angles was investigated and quantified by the sensitivity of dioptric change with anterior and posterior zonular angles' shifts. The modelling shows that small anterior angles (~2°) and larger posterior angles (14 – 16°) contribute the greatest sensitivity.

Keywords: Finite element modelling; Eyes accommodation; Zonular fibres

Purpose

Ocular accommodation decreases with age as a result of multiple factors. While increasing lens stiffness plays a role, also other factors are considered. One of these factors is the orientation of the zonular fibres. In this study, we investigate the sensitivity of the accommodative amplitude to the orientation of the zonular fibres.

Methods

A finite element mechanical model of the accommodative apparatus was made in COMSOL [1], consisting of the crystalline lens and zonular fibres. The shape of the crystalline lens and stiffness of the cortex and nucleus represented the 45-year-old lens as previously described by Burd 2002[2]. The model included zonular fibres as annular sheets surrounding the lens and extended to an outer diameter

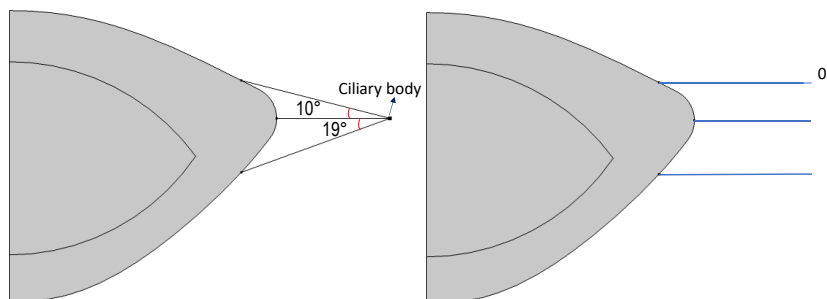


Figure 1: Largest and smallest zonular angles modeled by moving zonules connected to the ciliary body.

of 6.33 mm, representing the diameter of the ciliary body in the accommodated state. The orientation of the anterior and posterior zonular fibres was varied between 0 - 10° and 0 - 19°, respectively as shown in Figure 1, in 2° increments. In each case the outer ends of the zonular fibres were stretched by 0.4 mm in four steps to model accommodative change. Material properties were according to Krag et al [3] and Fisher [4]. Accommodation was determined as the difference between the initial and the stretched state of the lens. The accommodative amplitude, or the change of optical power before and after accommodation, was calculated using the thick lens equation applied to the coordinates of the anterior and posterior lens surfaces in the central 1.6 mm region.

Results

The lenticular shape changes due to accommodation are shown in Figure 2. Sixty-six (66) combinations of orientations of anterior and posterior angles were evaluated. Under the different orientations of zonular fibres, the accommodative amplitude ranges from 5.0 to 6.2 D, indicating that zonular fibre orientation can have an effect on the accommodative amplitude as large as 1.2 D. To quantify the sensitivity of accommodative amplitude (AA) to the orientation of zonular fibres, the maximum dioptric change by a change in angular change in each direction (+ and -) of anterior and posterior fibres was calculated, for example at 4° for anterior and 8° for posterior zonules as shown in Table 1. The maximum dioptric change in accommodative amplitude (AA) as a function of fibre orientation was expressed as $d(AA)/d(\theta)$ and indicates the sensitivity of the accommodative amplitude to the orientation of the zonular fibres. $d(AA)/d(\theta)$ ranged from 0.10 to 0.53 D/degree, as shown in Table 2. For small anterior angles (~2°) and larger posterior angles (14 - 16°), AA showed the greatest sensitivity to the orientation of zonular fibres.

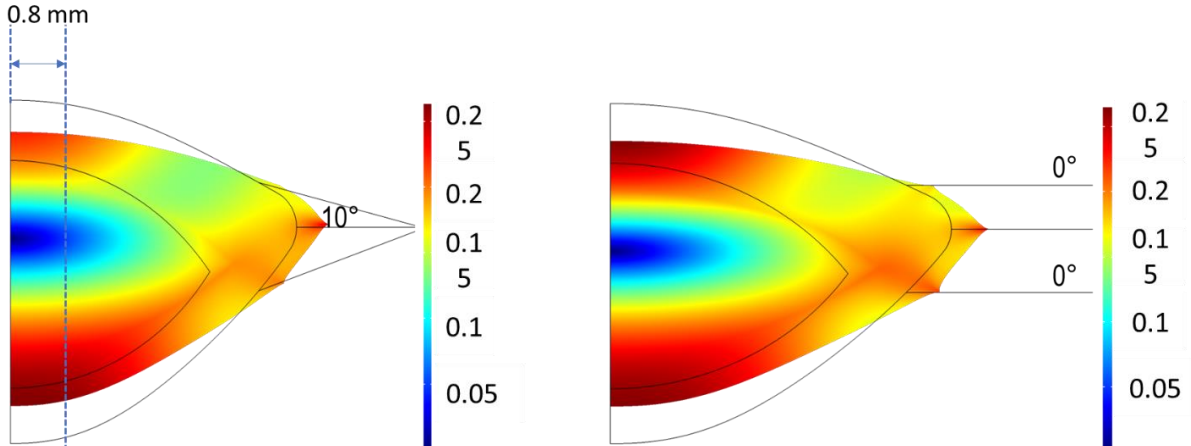


Figure 2: Deformed lens after the (dis)accommodation in the two extreme configurations (maximum and minimum angles of the zonular fibres). The colour bars depict the displacement amplitude in the crystalline lens(mm).

Table 1: Maximum dioptric change $d(AA) = AA_{Max} - AA_{Min}$

		Anterior		
Posterior	2°	4°	6°	
6°	AA_{26}	AA_{46}	AA_{66}	
8°	AA_{28}	AA_{48}	AA_{68}	
10°	$AA_{2\ 10}$	$AA_{4\ 10}$	$AA_{6\ 10}$	

Table 2: The sensitivity of AA as follows $d(\text{AA})/d(\theta)$

	0°	2°	4°	6°	8°	10°
0°	0.11	0.05	0.05	0.06	0.18	0.18
2°	0.18	0.10	0.10	0.18	0.22	0.22
4°	0.18	0.21	0.21	0.19	0.24	0.23
6°	0.23	0.24	0.24	0.22	0.24	0.23
8°	0.23	0.26	0.26	0.22	0.27	0.24
10°	0.16	0.19	0.19	0.23	0.21	0.21
12°	0.23	0.22	0.22	0.25	0.25	0.25
14°	0.53	0.51	0.51	0.24	0.25	0.20
16°	0.53	0.49	0.49	0.27	0.29	0.23
18°	0.46	0.40	0.40	0.23	0.24	0.24
19°	0.20	0.18	0.18	0.20	0.22	0.22

Conclusion

The orientation of the zonular fibres has a significant influence on the accommodative amplitude. In specific angle ranges, the accommodative amplitude can change by 1 D with only a few degrees of variation of the orientation of zonular fibres. Therefore, changing the orientation of zonular fibres with age could contribute to the development of presbyopia.

Acknowledgement

This project has received funding from the European Union's Horizon 2020 research and innovation programme under the Marie Skłodowska-Curie grant agreement No 956720

References

- [1] COMSOL Multiphysics® v. 5.6. www.comsol.com. COMSOL AB, Stockholm, Sweden
- [2] Burd, H., S. Judge, and J. Cross, Numerical modelling of the accommodating lens. *Vision Res*, 2002. 42(18): p. 2235-2251.
- [3] Krag, S., Andreassen, T. T., & Olsen, T. (1996, February). Elastic properties of the lens capsule in relation to accommodation and presbyopia. In *Investigative Ophthalmology & Visual Science* (Vol. 37, No. 3, pp. 774-774)
- [4] Fisher, R. F. "Elastic constants of the human lens capsule." *The Journal of physiology* 201.1 (1969): 1-19.

Influence of zonular fibres on lens accommodation assessed by a pre-stressed eye model

Kehao Wang^{1*}, Yutian Pu¹, Lin Ye², Barbara K Pierscionek²

¹Key Laboratory for Biomechanics and Mechanobiology of Ministry for Education, Beijing Advanced Innovation Center for Biomedical Engineering, School of Engineering Medicine, Beihang University, Beijing, China

²Faculty of Health, Education, Medicine and Social Care, Medical Technology Research Centre, Anglia Ruskin University, Chelmsford, United Kingdom

* Corresponding author: kehaowang@buaa.edu.cn

To investigate the individual roles of different groups of zonular fibres during visual accommodation, a 3D Finite Element model containing the major accommodative components and the eyeball were developed in ANSYS. Five groups of zonular fibres were considered to connect the lens equatorial region to the ciliary body. The far-to-near accommodation was simulated using the developed pre-stress approach to mimic the lens deformation from a flattened shape to a more spherical shape. The five groups of zonules were then cut off in sequence creating five additional zonular-cut model to assess their individual function. In the model with all five zonules, the anterior and equatorial zonules carry the highest tensions; in the anterior and the equatorial zonular-cut model, there is an increase and a decrease in the central optical power, respectively; models cut off with other zonules did not show significant change in optical power.

Keywords: Zonular fibres; accommodation; Finite Element model

Introduction

The zonular system in the eye serves to maintain the physiological position of the lens [1]. It consists of different groups of ligaments that originate from various locations of the ciliary body and connect to the lens equatorial region. During accommodation, tensions in different groups of zonular fibres change in response to the contraction/relaxation of the ciliary muscle and as a result the lens changes its central surface curvature and thickness. The coupled function of different zonules is directly related to the dynamic accommodative change and guarantees the proper function of this opto-biomechanical process. The zonular fibres mainly consist of anterior and posterior fibre bundles that originate from the posterior end of the ciliary body, the equatorial fibre bundles that originate from the anterior end of the ciliary body. These three groups of zonular fibres are inserted into the equatorial region of the lens capsule [2]. In addition, the vitreous zonule and anterior hyaloid membrane also form the part of the zonular system and have recently been postulated to contribute to accommodation [3,4].

Current theories describing visual accommodation differ in how different groups of zonular fibres function during accommodation. The classical theory by Helmholtz suggests that different groups of zonular fibres change tensions synchronously in altering the lens shape [5]. An opponent theory by Schachar postulated that the anterior and posterior zonular fibres have the opposite tensional behaviour to the equatorial zonular fibres [5]. Contributions by the vitreous support during accommodative process was suggested by Coleman [5]. Due to the limitations of current imaging techniques, it is not possible to examine the exact mechanism of accommodation *in vivo* or *in vitro*. Computational simulations, under such condition, have been widely used to explore the accommodative mechanism and to assess the possible reasons that contribute to presbyopia.

Methods

A three-dimensional whole eye model was developed using ANSYS Mechanical APDL (Ansys Parametric Design Language). The model contains the cornea, the sclera, the choroid, the vitreous as well as the accommodative structures including the lens, ciliary body and five groups zonular fibres (Figure 1a). Geometries of the lens nucleus and lens cortex were according to a 35-year-old human sample [6] while geometries of other structures were taken from the literature [7,8]. The cornea and the sclera were modelled using a neo-Hookean hyperelastic material [7], the vitreous were modelled using incompressible hydrostatic fluid model, other components were considered as isotropic, linear elastic materials [6]. The lens capsule and the anterior hyaloid membrane were meshed using 4-node membrane elements, the anterior, equatorial, posterior vitreous and pars plana zonules were discretized using 2-node link elements, other structures were modelled using 8-node brick elements, totalling in 119,050 elements and 121,829 nodes of the developed model.

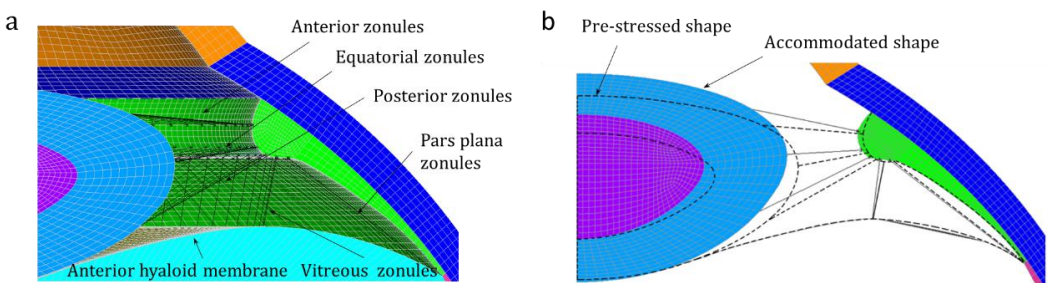


Figure 1. Developed Finite Element eye model showing (a) five groups of zonules connecting the lens to the ciliary body, (b) the pre-stressed lens shape and the deformed accommodated lens shape.

The present study simulates the lens deformation from a stressed unaccommodated state to accommodated state. To do this, a pre-stress modelling approach was developed. The lens model using geometry taken from its fully isolated state, was initially stretched to a stressed and flattened shape, from where the stresses at each node as well as the coordinates of each node were extracted to build the pre-stress file, which served as an input for formal analysis. During formal analysis, the lens released its pre added stresses and gradually returned to a more spherical shape until an equilibrium state was reached (figure 1b). Simulations were performed for five additional models with one group of zonular fibres cut off in sequence. Changes in surface curvature and optical power were analysed.

Results

During simulated accommodation, the lens anterior/posterior surface radii of curvatures decrease while the sagittal thickness increase (figure 2a-c). The trends of these parameters in response to the change in central optical power were compared with those reported in previously *in vivo* study [9] and a good fit were found for the anterior surface ($p>0.05$). Changes in the length and thickness of the ciliary body during simulation also fit well to those measured in an *in vivo* study [10].

Among all six models, the one with anterior zonules cut off show the highest change in central optical power, the one with equatorial zonules cut off show the lowest change in central optical power. Models with the vitreous zonules or pars plana zonules cut off show identical change in optical power to that of the model with all five zonules (Figure 2d). In the model with all five zonules, the anterior and equatorial zonules carry most of the tension. In contrast, tensions in the posterior zonules and pars plana zonules are the lowest (figure 2e). When the anterior zonules were removed, the equatorial zonular tension increases while the posterior zonular tension decreases (figure 2f). However, when other set of zonules were removed, the distributions of tensions and strain show little change.

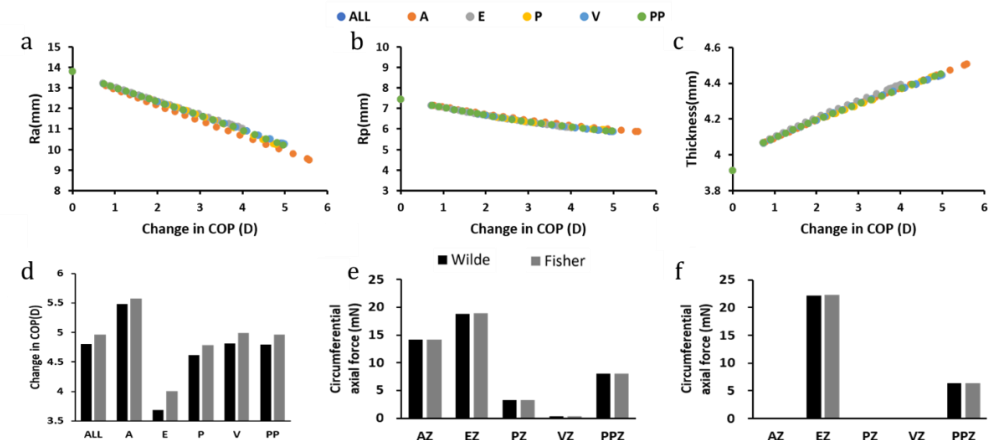


Figure 2. During simulated accommodation the changes in lens (a) anterior, (b) posterior radii curvature, (c) thickness, using two different sets of materials [5] the (d) comparison in changes in optical power among six models, (e) distribution of zonular tensions in model with all zonules and (f) in model without the anterior zonules. (COP: Central Optical Power; ALL, A, E, P, V, PP: models with all (ALL) or without anterior (A), equatorial (E), posterior (P), vitreous (V) or pars plana (PP) set of zonules; AZ: anterior zonule, EZ: equatorial zonule, PZ: posterior zonule, VZ: vitreous zonule, PPZ: pars plana zonule)

Conclusions

This study compares the functional differences between different zonules during far-to-near accommodation. Results suggested that the anterior and equatorial zonules have major influences on lens deformation and distribution of zonular tensions among different sets. The anterior zonules have a positive effect while the equatorial zonules have negative effect on the change in optical power. The vitreous and pars plana zonules have little impact on lens deformation.

Acknowledgements

Lin Ye is funded by the European Union's Horizon 2020 research and innovation program under the Marie Skłodowska-Curie grant agreement No 956720.

References

- [1] Bassnett S. Zinn's zonule. *Prog Retin Eye Res*. 2021; **82**:100902.
- [2] Raviola G. The fine structure of the ciliary zonule and ciliary epithelium. With special regard to the organization and insertion of the zonular fibrils. *Invest Ophthalmol*. 1971; **10**(11):851-869.
- [3] Croft MA, Nork MT, McDonald JP, Katz A, Lütjen-Drecoll E, Kaufman PL. Accommodative movements of the vitreous membrane, choroid, and sclera in young and presbyopic human and nonhuman primate eyes. *Invest Ophthalmol Vis Sci*. 2013; **54**(7):5049-5058.
- [4] Croft MA, Heatley G, McDonald JP, Katz A, Kaufman PL. Accommodative movements of the lens/capsule and the strand that extends between the posterior vitreous zonule insertion zone & the lens equator, in relation to the vitreous face and aging. *Ophthalmic Physiol Opt*. 2016; **36**(1):21-32.
- [5] Wang K, Pierscionek BK. Biomechanics of the human lens and accommodative system: Functional relevance to physiological states. *Prog Retin Eye Res*. 2019; **71**:114-131.
- [6] Wang K, Venetsanos DT, Hoshino M, Uesugi K, Yagi N, Pierscionek BK. A Modeling Approach for Investigating Opto-Mechanical Relationships in the Human Eye Lens. *IEEE Trans Biomed Eng*. 2020; **67**(4):999-1006.
- [7] Cabeza-Gil I, Grasa J, Calvo B. A validated finite element model to reproduce Helmholtz's theory of accommodation: a powerful tool to investigate presbyopia. *Ophthalmic Physiol Opt*. 2021; **41**(6):1241-1253.
- [8] Knaus KR, Hipsley AM, Blemker SS. The action of ciliary muscle contraction on accommodation of the lens explored with a 3D model. *Biomech Model Mechanobiol*. 2021; **20**(3):879-894.
- [9] Martinez-Enriquez E, Pérez-Merino P, Velasco-Ocana M, Marcos S. OCT-based full crystalline lens shape change during accommodation in vivo. *Biomed Opt Express*. 2017; **8**(2):918.
- [10] Sheppard AL, Davies LN. In vivo analysis of ciliary muscle morphologic changes with accommodation and axial ametropia. *Invest Ophthalmol Vis Sci*. 2010; **51**(12):6882-6889.

The effect of zonular insertion and finite element model on simulated stretching of the lens

Lin Ye¹, Kehao Wang², Barbara K. Pierscioneck^{1*}

¹ Faculty of Health Education Medicine and Social Care, Medical Technology Research Centre, Anglia Ruskin University, Chelmsford Campus, UK

² Beijing Advanced Innovation Centre for Biomedical Engineering, Key Laboratory for Biomechanics and Mechanobiology of Ministry of Education, School of Engineering Medicine, Beihang University, Beijing, China

* Barbara K. Pierscioneck: barbara.piersonek@aru.ac.uk

The process of accommodation is still not fully understood. Modelling approaches have been used to complement experimental findings to determine how constituents in the accommodative process influence lens shape change. An unexplored factor in modelling is the role of the software on the results of simulated shape change. Finite element models were constructed in both Abaqus and Ansys software with biological parameters taken from measurements of shape and refractive index on two 35-year-old lenses. The effect of zonular insertion on simulated shape change was tested on both lens models with both software types. Comparative analysis of shape change and stress distributions showed that lens shape and zonular insertion positions affect the results of simulated shape change; Abaqus and Ansys show considerable differences in their respective models. The effect of the software package used needs to be taken into account when constructing finite element models and deriving conclusions.

Keywords: eye lens, finite element modelling, zonular insertion, refractive index

Introduction

The human eye lens has been studied from biological, optical, and more recently biomechanical aspects to try and understand structure and function relationships that can explain the process of accommodation and its gradual loss with age, namely, presbyopia. Finite element modelling has been applied to complement experimental studies and learn more about the process of lens shape change. However, no models to date can claim to be truly representative of the accommodative system let alone to understand individual variations in the component structures that mediate and control the forces of accommodation. The zonular insertion positions are not known and could vary between individuals. Recent modelling work has indicated that the insertion positions of the zonule have a significant impact on the forces mediated to the lens and on shape changes induced [1-2]. Variations in results, with regard to material properties, have been reviewed and shown to be dependent on experimental methods [2]. Yet to date, there have not been any studies that have compared models created by different software to elucidate whether variations in software principles and algorithms can have a discernible effect on results of modelling lens shape change. Any differences in modelling arising from software used need to be known so that there is no over reliance on any single software model type in trying to improve understanding of accommodation, presbyopia and/or for aiding design of intraocular implants.

Methods

1. Three-dimensional quarter lens geometric models were developed using 3D CAD software

SolidWorks (ver. 2021), which were then imported into Finite Element Analysis software Abaqus (ver. 2022) and Ansys workbench (ver. 2021R2) for discretization and FE model development. The geometries of developed models were based on the images obtained from measurements of human lens refractive index contour profiles [3]. Two 35-year-old lenses with different shapes, symmetric and asymmetric, were selected to construct 3D models.

2. The lens cortical sections were divided into several layers according to the respective refractive index profiles [3]. Each layer was assigned a different Young's modulus based on the data from Fisher for 35-year-old lenses [4]. Each zonule was 1.5 mm in length and 0.025 mm in radius [1]. The capsule has a constant thickness of $6\text{ }\mu\text{m}$ [5]. Young's modulus was 0.35 MPa and 1.5 MPa for the zonule and capsule respectively [6,7]. Poisson's ratio was 0.49 for the entire lens and 0.47 for the capsule and zonule [4,8].
3. The lens was meshed using 8-node solid element (ANSYS element type: Solid185, ABAQUS element type: C3D8RH). The capsule was discretized using 4-node membrane element (ANSYS element type: Shell181, ABAQUS element type: M3D4R). In both Abaqus and Ansys, the capsule was set as a skin (face-coating) during meshing. Zonule was modelled as 2-node beam element.
4. To test how zonular anchorage position influences shape change and biomechanics, two different locations of insertion points were selected for each lens model. In the symmetric model zonular combinations were called *A* and *B*; in the asymmetric model these were called *C* and *D*.

Results

The stress distributions of the asymmetric and symmetric models after simulated stretching, with two zonular combinations, in Ansys and Abaqus software are shown in Figures 1 and 2, respectively. The stress distributions vary between models constructed in Ansys and in Abaqus.

For the asymmetric lens (Figure 1), the maximum stress in the Abaqus model ($6.5\text{e-}4\text{ MPa}$) is greater than the maximum stress in the Ansys model ($5.7\text{e-}4\text{ MPa}$) for zonular combination *A*. Conversely, the maximum stress in the Ansys model is greater for zonular combination *B* ($6.8\text{e-}4\text{ MPa}$ compared to $5.8\text{e-}4\text{ MPa}$ in the Abaqus model). The effect of varying posterior zonular insertion points is seen when comparing figures 1a with 1c or 1b with 1d. With the insertion position of the posterior zonule placed further from the equator (figures 1c and d), the stresses are more distributed than for models in which the posterior zonule is closer to the equator (figures 1a and b). The contours of stress are less widely distributed in the symmetric (Figure 2) than the asymmetric models (Figure 1). The maximum stress magnitudes are higher in models constructed with Abaqus than the same models constructed in Ansys.

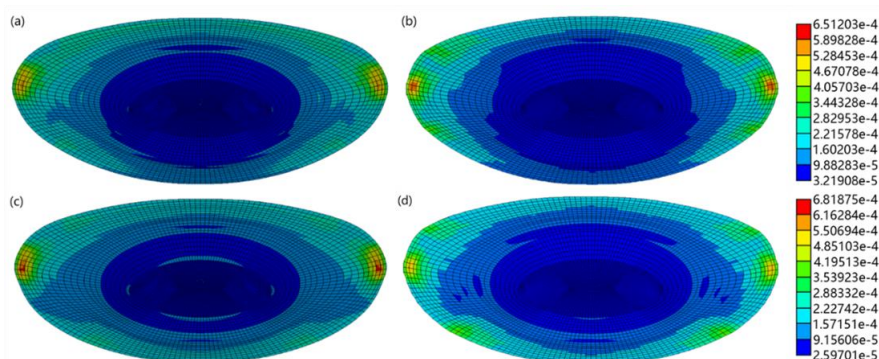


Figure 1: Stress distribution results of the asymmetric lens models showing two zonular combinations for the models in Ansys and Abaqus, where (a) shows the model using combination *A*, calculated in Ansys, (b) shows the model using combination *A*, calculated in Abaqus, (c) shows the model using combination *B*, calculated in Ansys, (d) shows the model using combination *B*, calculated in Abaqus.

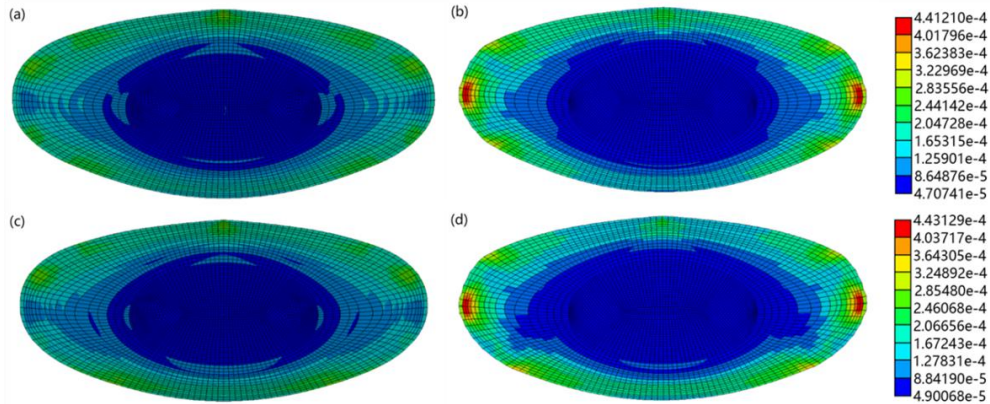


Figure 2: Stress distribution results of the symmetric lens models each used two zonular combinations in the two software. where (a) shows the model using combination C, calculated in Ansys, (b) shows the model using combination C, calculated in Abaqus, (c) shows the model using combination D, calculated in Ansys, (d) shows the model using combination D, calculated in Abaqus.

There are several localized stress concentrations around the cortico-nuclear region in the models constructed with Ansys (Figures 2a and c); these are not seen in the models constructed with Abaqus (Figures 2b and d). Elevated localized stresses are seen around the areas of the anterior and, to a lesser extent, posterior zonular insertions in the Ansys models (Figures 2a and c). These are of a much higher magnitude in the Abaqus models, which also show particularly high stress concentrations around the equatorial zonular insertion (Figures 2b and d).

Conclusions

This study shows that lens shape, which is not necessarily indicative of lens age, has a significant effect on results of modelling simulated shape change. The findings of this study show that even with identical input parameters, differences in lens shape and zonular insertions can produce differences in biomechanical results depending on the Finite Element modelling software package used.

Acknowledgment

This project has received funding from: the European Union's Horizon 2020 research and innovation programme under the Marie Skłodowska-Curie grant agreement No 956720.

References

- [1] Wang K, Venetsanos DT, Hoshino M, Uesugi K, Yagi N, Pierscionek BK. A Modeling Approach for Investigating Opto-Mechanical Relationships in the Human Eye Lens. *IEEE Trans Biomed Eng.* 2020;67(4):999-1006.
- [2] Wang K, Pierscionek BK. Biomechanics of the human lens and accommodative system: Functional relevance to physiological states. *Prog Retin Eye Res.* 2019; 71:114-131.
- [3] Pierscionek B, Bahrami M, Hoshino M, Uesugi K, Regini J, Yagi N. The eye lens: age-related trends and individual variations in refractive index and shape parameters. *Oncotarget.* 2015;6(31):30532-30544.
- [4] Fisher RF. The elastic constants of the human lens. *J Physiol.* 1971;212(1):147-180.
- [5] Barraquer RI, Michael R, Abreu R, Lamarca J, Tresserra F. Human lens capsule thickness as a function of age and location along the sagittal lens perimeter. *Invest Ophthalmol Vis Sci.* 2006;47(5):2053-2060.
- [6] Fisher RF. The ciliary body in accommodation. *Trans. Ophthalmol. Soc. UK* 1986;105(2):208-219.
- [7] Krag S, Andreassen TT. Mechanical properties of the human posterior lens capsule. *Invest Ophthalmol Vis Sci.* 2003;44(2):691-696.
- [8] van Alphen GW, Graebel WP. Elasticity of tissues involved in accommodation. *Vision Res.* 1991;31(7-8):1417

Linear fitting of biconic surfaces for corneal modelling

Iñaki Blanco-Martínez*, José M. González-Méijome and Miguel Faria-Ribeiro

Clinical & Experimental Optometry Research Lab (CEORLab), Physics Center of Minho and Porto Universities,
University of Minho, Braga, Portugal

* Corresponding author: Iblanco@fisica.uminho.pt

This paper presents a novel method for reconstructing the corneal surface with precision and efficiency. The proposed method has been tested on two groups: one consisting of 56 healthy eyes, and the other of 15 post-orthokeratology eyes. The Medmont E300 Corneal Topographer was used to carry out this analysis, and MATLAB was employed for data analysis, adjustments, and other computational processes. Results were compared with the fitting to an ellipsoid and a biconic using another method, and were similar between the different methods, with comparable goodness of fit values. Notably, the proposed method exhibited lower standard deviation in the first group, indicating higher robustness with regular corneas. In conclusion, the proposed method provides a precise and robust approach to reconstructing corneal surfaces, with potential applications.

Keywords: Corneal modelling; Corneal topography; Biconic surface; Zernike polynomials.

Introduction

The cornea, the clear, outermost layer of the eye, plays a crucial role in the refractive power of the human eye. In fact, the anterior surface of the cornea has the highest refractive power in the eye, and due to its importance in ocular refraction, accurate measurement and modeling of its surface is critical.

Different approaches have been used depending on the number of parameters employed to model the corneal surface. In ascending order of complexity, these approaches included a sphere (1 parameter, radius of curvature, R), a conic surface (2 parameters, R and its conic constant, Q), a 3-axis non-revolution ellipsoid (3 parameters, the three semi-axes, a, b, c), and finally, a biconic surface (4 parameters, R_x, Q_x, R_y, Q_y) [2]. Typically, increasing the complexity of the surface allows for a more precise mathematical representation of the corneal surface, and then, a more realistic description of its fundamental optical properties.

This manuscript introduces a novel method for fitting the corneal surface by employing a linear formulation for a biconic surface. Leveraging the orthogonality properties of Zernike polynomials, this method eliminates tilts, decentering, and rotations, being of great importance for the accurate estimation of the corneal surface's geometrical parameters [3]. In this context, we consider it a promising method for corneal modeling, as it allows for a precise and numerical efficient approximation of the corneal surface and the calculation of its optical properties.

Methods

Anterior corneal elevation maps were acquired with the Placido based system Medmont E300 (Medmont, Australia) from two groups of patients: one consisting of 56 healthy eyes and another one with 15 post-orthokeratology eyes, to allow to test the method on topographically altered corneal shapes. Custom made software developed in Matlab (The MathWorks Inc., USA) was employed for data analysis, fitting, and other computational processes.

To deal with the potential alignment problem between the cornea and the axis of the topographer, that affects the correct estimation of its geometrical parameters [3], we made use of the orthogonality properties of Zernike polynomials to extract the contribution of non-astigmatic and non-spherical modes from the raw elevation data. Hence, possible decentrations and/or tilts and all other modes except for spherical and astigmatic ones were removed, which results in a centered and aligned surface. The rotation angle around the z-axis (astigmatism axis) was obtained from the orientation of the low-order astigmatic modes and subsequently applied to the coordinate system. Thus, with the centered, aligned, and rotated system, the corneal surface was fitted to the linear equation of a biconic surface:

$$x^4 + y^4 + 2x^2y^2 + p_x x^2z^2 + p_y y^2z^2 - 2R_x zx^2 - 2R_y zy^2 = 0 \quad (1)$$

where R_x and R_y are the radius of curvature of the horizontal and vertical meridians of the surface, while $p_x = Q_x + 1$ and $p_y = Q_y + 1$ are the correspondent shape factors, and Q_x and Q_y the conic constants ($Q = 0$ is a sphere). These coefficients can be obtained by linear least squares methods, and the surface sagitta can be reconstructed from the same expression solved for z .

$$z(x, y) = \frac{c_x x^2 + c_y y^2}{1 + \sqrt{1 - (1 + Q_x)c_x^2 x^2 - (1 + Q_y)c_y^2 y^2}} \quad (2)$$

Finally, the curvature radii (R_x, R_y), the conic constants (Q_x, Q_y) and the rotation angle with respect to the z axis, obtained with the new method were compared to the ones obtained with the ellipsoid and biconic methods proposed by Navarro *et al.* [4]. The goodness of the fit was calculated as the Root Mean Square error (RMSe). All the analyses were conducted for an 8 mm corneal diameter.

Results

The resulting average parameters for the 56 normal corneas are shown in Table 1 for the different fitting methods following the procedures explained above.

In addition to the fits for normal corneas, the same methods were applied to corneas with a less common shape, to demonstrate the robustness of the method. Table 2 shows the fitting results for 15 post-orthokeratology corneas.

Table 1. Corneal fitting from 56 healthy eyes, showing the mean of the curvature radii (R_1, R_2), axis angle, conicities (Q_1, Q_2), Root Mean Square error (RMSe), and standard deviation.

Fit Method	R_1 (mm)	$\pm\sigma_{R_1}$	R_2 (mm)	$\pm\sigma_{R_2}$	Axis (°)	$\pm\sigma_{Axis}$
Navarro Ellipsoid	7.77	0.23	7.59	0.22	83.96	79.34
Ellipsoid→Biconic	7.77	0.24	7.59	0.21	83.96	79.34
Zernike→Linear Biconic	7.77	0.20	7.61	0.21	83.02	80.67
Fit Method	Q_1	$\pm\sigma_{Q_1}$	Q_2	$\pm\sigma_{Q_2}$	RMSe (μm)	$\pm\sigma_{RMSe}$
Navarro Ellipsoid	-0.21	0.10	-0.22	0.09	4.22	4.28
Ellipsoid→Biconic	-0.21	0.10	-0.22	0.11	4.21	4.20
Zernike→Linear Biconic	-0.23	0.10	-0.20	0.11	3.59	1.91

Table 2. Corneal fitting from 15 post-orthokeratology treated eyes, showing the mean of the curvature radii (R_1 , R_2), axis angle, conicities (Q_1 , Q_2), Root Mean Square error ($RMSe$), and standard deviation.

Fit Method	R_1 (mm)	$\pm\sigma_{R_1}$	R_2 (mm)	$\pm\sigma_{R_2}$	Axis (°)	$\pm\sigma_{Axis}$
Navarro Ellipsoid	8.28	0.15	8.08	0.16	83.45	85.88
Ellipsoid→Biconic	8.24	0.15	8.10	0.16	83.45	85.88
Zernike→Linear Biconic	8.23	0.15	8.08	0.15	83.10	85.60
Fit Method	Q_1	$\pm\sigma_{Q_1}$	Q_2	$\pm\sigma_{Q_2}$	$RMSe$ (μm)	$\pm\sigma_{RMSe}$
Navarro Ellipsoid	0.59	0.28	0.55	0.27	4.82	2.01
Ellipsoid→Biconic	0.49	0.30	0.61	0.27	4.76	2.04
Zernike→Linear Biconic	0.45	0.30	0.58	0.27	4.77	2.05

Conclusions

In both cases of normal and post-orthokeratology corneas, the results for the curvature radii, conic constants and astigmatism axis were similar among the different methods, with similar values for the goodness of the fit. An interesting result is the case shown in Table 1, where the mean $RMSe$ and standard deviation for the method presented in this manuscript is slightly lower than the other two, suggesting that the new method might be more robust.

Acknowledgment

This project has received funding from: the European Union's Horizon 2020 research and innovation programme under the Marie Skłodowska-Curie grant agreement No 956720.

References

- [1] Smith, G., Atchison, D. A. Optics of the human eye. Butterworth-Heinemann. 2000.
- [2] Schwiegerling, J., Snyder, R. W. Custom photorefractive keratectomy ablations for the correction of spherical and cylindrical refractive error and higher-order aberration J Opt Soc Am A. 1998; **9**: 2572–2579.
<https://doi.org/10.1364/josaa.15.002572>
- [3] Navarro, R., González, L., Hernández, J. L. Optics of the average normal cornea from general and canonical representations of its surface topography. J Opt Soc Am A. 2006; **2**: 219–232.
<https://doi.org/10.1364/josaa.23.000219>
- [4] Navarro, R., Rozema, J. J., Tassignon, M. J. Optical changes of the human cornea as a function of age. Optom Vis Sci. 2013; **6**: 587–598. <https://doi.org/10.1097/OPX.0b013e3182928bc6>

Measuring contact lens base curve radius using a clinical OCT: an in-vitro study

Diana Gargallo*, Sofía Otín, Nerea Tolón, Oscar del Barco and Jorge Ares

Applied physics, University of Zaragoza, Zaragoza, Spain

* dgargallo@unizar.es

The purpose of this study was to evaluate the potential use of a clinical Optical Coherence Tomography device to measure the Base Curve Radius (BCR) of Rigid Gas-Permeable Contact Lenses (RGP CL) in vitro. In order to do that, an optomechanical adapter and imaging processing techniques were developed to measure contact lenses with a commercial OCT (Topcon 3D OCT-1000). The statistical analysis of our experiments demonstrated that the OCT measurements were accurate and repeatable meeting the standards of accuracy and repeatability proposed by ISO norm 18369-2:2018-3.

Keywords: OCT, Contact Lenses, Base Curve Radius.

Introduction

Optical Coherence Tomography (OCT) devices are mainly used in optometry and ophthalmology clinical environment to diagnose and study eye health integrity [1] and secondarily to evaluate Contact Lens (CL) fitting [2] and to measure in-vivo the geometric surface shape and position of the main refractive surfaces of the eye [3,4]. On a more technical domain, specific spectral domain OCT devices have been used to measure the topographic surface and central thickness of intraocular lenses [5]. In particular, an OCT device marketed to measure intraocular and contact lenses (CLs) [6] has shown consistent results within the ISO 18369-2:2018 tolerance ranges for curvature radius and central thickness measurements [7,8]. Therefore, it can be argued that this technology could help CL professionals to monitor and control the geometry of the contact lenses. Unfortunately, the adaptation of clinical OCT devices to measure contact lenses is not available to their users.

In order to overcome this limitation, we developed: (1) a specific opto-mechanical to ease the measurement of contact lenses with an OCT device marketed for clinical application (Topcon 3-D OCT-1000), and (2) a linear calibration model and image processing methods to recover accurate geometric contact lens measurements from B-scan image data. Finally, the performance of this methodology was evaluated over a set of spherical rigid contact lenses. As far as we know this is the first time that a clinical OCT has used to determine the base curve of a contact lens.

Methods

The experiment consisted of measuring 18 monofocal rigid gas-permeable spherical CLs (Lenticon Pharmaceutical SA, Madrid, Spain) with a central base curve radius (BCR) from 7.30 mm to 8.40 mm using of a clinical spectral domain OCT (3D OCT-1000, Topcon Co.) in combination with a custom optomechanical OCT CL Adaptor fabricated via a commercial Fused Deposition Modelling 3D printer.

The B-Scan measurement of the CL involved placing the CL in a stabilized horizontal position with the concave side facing up on the OCT CL adapter. The transversal and axial OCT position was adjusted to position the image profile within the reference axial interval displayed on the B-scan live video display.

Image processing algorithm were used to estimate the posterior curvature radius from CL B-scan image profiles. A program code was written (Matlab R2019b, Mathworks Inc) to carry out: colour to intensity conversion, noise filtering to increase the B-scan signal-to-noise image ratio, automatic intensity thresholding to avoid background noise, and image segmentation to pre-process the B-scan exported data before the analysis. Once the region corresponding with the posterior curve was segmented, local centroid calculations, were performed to estimate the axial position of each scattering point of the posterior CL curve. Finally, the pairs of XZ centroid coordinates were fitted using least squares to a general circle profile to estimate the BCR.

Statistical analyses were performed using IBM SPSS V.20 to assess the precision and accuracy of the OCT BCR measurements. The absolute maximum differences between OCT and Micro-Spherometer BCR measurements were evaluated along with the SD of the difference. Inter-observer and inter-session repeatability were assessed using t-tests for paired samples between measurements taken by different operators and the same operator in two different sessions. Furthermore, Bland-Altman plots were used to explore any systematic differences between measurements taken by different operators and sessions. Finally, to evaluate the accuracy of OCT-based BCR measurements (BCR operator1-session1, BCR operator2-session1) in comparison with the Micro-Spherometer, the t-student test for paired samples and the intra-class correlation coefficient were used.

Results

A total of 162 B-scan image profiles were acquired and processed to estimate the BCR for all the samples of the CL set. The results of the paired t-test and intra-class correlation coefficient analysis performed to assess intra-operator and intra-session repeatability. On the one hand, the measurements taken by different OCT operators did not show any significant statistical differences between them. On the other hand, testing BCROperator1-session1 vs BCROperator1-session2 resulted in a p-value = 0.666 so it can be noticed that a good intra-operator repeatability has also been achieved.

The results of the comparison between BCR with Micro-Spherometer and BCR OCT-based measurements were also shown. There, it can be seen t-student results for BCROperator1-session1 vs

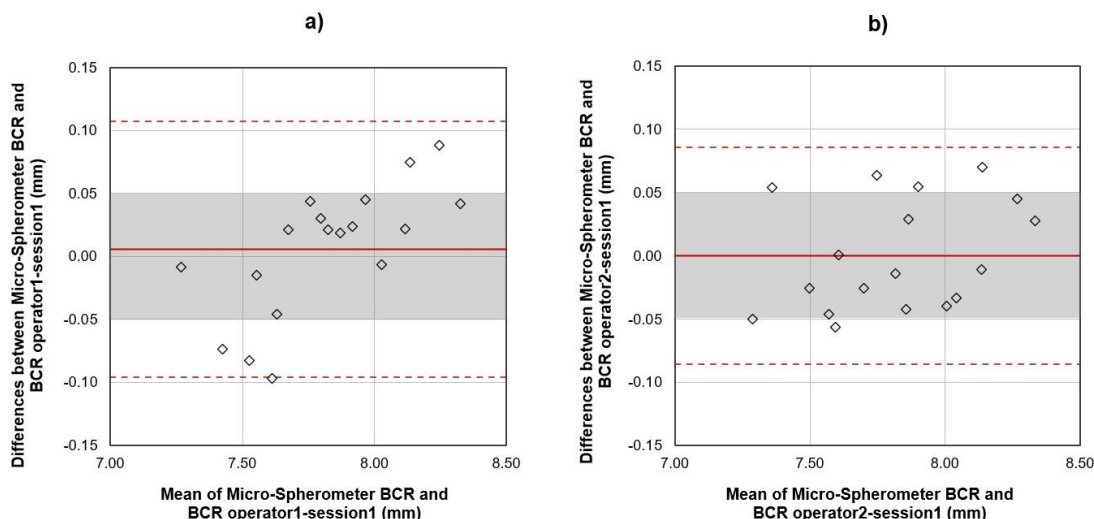


Figure 1: Bland-Altman plots for BCR measurement differences between Micro-Spherometer measurements and two different operators. (a) Differences between Micro-Spherometer BCR values and the measurements taken by operator1-session1 (BCROperator1-session1). (b) Differences between Micro-Spherometer BCR values and the measurements taken by operator2 (BCROperator2-session1).

Micro-Spherometer BCR, $p = 0.661$ and BCROperator2-session1 vs Micro-Spherometer BCR, $p = 0.996$, and intra-class correlation coefficients between the Micro-Spherometer measurement and BCR obtained for operator 1 ($0.992; p < 0.001$) and operator 2 ($0.991; p < 0.001$).

The mean difference differences between Micro-Spherometer measurements and OCT-based between two different operators was represented by a solid red line (Figure 1) since dashed red lines symbolized the 95% confidence intervals for the mean difference. Gray filled regions inform about ISO 18369-2:2018-3 tolerance limits ($\pm 0.05 \text{ mm}$) [8].

Conclusions

First, the statistical analysis of the BCR measurements demonstrated that the CLs BCR measurements present good accuracy and reproducibility. Second, it has been demonstrated for this clinical OCT that with our purposed methods, it is possible to obtain Base Curve Radius measurements of RGP CLs that nearly meet the standards of accuracy and repeatability proposed by proposed by ISO 18369-2:2018-3 with a clinical OCT. The success of this pioneering study should encourage to clinical OCT manufacturers to offer the necessary optomechanical adapters, methods, and software to perform measurements like those presented here.

Acknowledgement

This research was supported by Ministerio de Ciencia, Innovación y Universidades (Grant PID2020-114311RA-I00); Gobierno de Aragón (Grant E44- 20R).

References

- [1] Jaffe J., and Caprioli J. Optical coherence tomography to detect and manage retinal disease and glaucoma. *Am. J. Ophthalmol.* 2004; 137(1): 156-169.
- [2] M. Shen, L. Cui, C. Riley, M. R. Wang, J. Wang, "Characterization of soft contact lens edge fitting using ultra-high resolution and ultra-long scan depth optical coherence tomography," *Invest. Ophthalmol. Vis. Sci.* 2011 52(7): 4091-7.
- [3] Venkateswaran N., Galor A., Wang J., and Karp C. L. Optical coherence tomography for ocular surface and corneal diseases: a review. *Eye and Vis.* 2018; 5: 13.
- [4] Sun M., Birkenfeld J., de Castro A., Ortiz S., and Marcos S. OCT 3-D surface topography of isolated human crystalline lenses. *Biomed. Opt. Express* 2014; 5: 3547-3561.
- [5] Huang Y., Zhang K., Kang JU, et al. Noncontact common-path Fourier domain optical coherence tomography method for in vitro intraocular lens power measurement. *J. Biomed. Opt.* 16(12), 126005 (2011).
- [6] Optimec Systems (England). Optimec is 830. <https://www.optimecsystems.com/solutions/optimec-is830/> (accessed 20-05-2023).
- [7] Ophthalmic Optics. Contact lenses. Part 3: Measurement Methods. ISO-18369-3 I. 2018.
- [8] Coldrick B. J., Richards C., Sugden K., Wolffsohn J. S., and Drew T. E. Developments in contact lens measurement: A comparative study of industry standard geometric inspection and optical coherence tomography. *Cont. Lens. Anterior Eye.* 2016; 39(4): 270-276.

Contact lens mask to block the most aberrated pupillary regions in keratoconic eyes

Sharon Marina Francis¹, Raymond Applegate² and Jos J. Rozema^{1,3*}

¹ Visual Optics Lab Antwerp (VOLANTIS), Faculty of Medicine, University of Antwerp, Antwerp, Belgium

² College of Optometry, University of Houston, Houston TX, USA

³ Department of Ophthalmology, Antwerp University Hospital, Edegem, Belgium

* Corresponding author: jos.rozema@uantwerp.be

Keywords: Keratoconus; linear optics; aberration correction

Purpose

The work investigates the selective blocking of light in severely aberrated areas of the visual field to reduce their effect of optical distortion in the eye, which should enhance the visual image quality in highly aberrated eyes. Similar work by González et al. [1] focused on designing a customised pupil shape to improve visual acuity in best spectacle corrected eyes. This numerical analysis seeks to extend the work of González for a mask applied to the best contact lens correction in keratoconic eyes.

Methods

This work uses linear optics, which describes the behaviour of a parallel ray grid transmitted through an eye and provides the coordinate changes of each optical ray at any interface of the eye [2]. An equally spaced square grid of incident rays parallel to the optical axis of the eye is constructed as an input beam.

Keratoconus was simulated by taking the corneal curvature and thickness maps of real patients, imported from the Pentacam data, and using those to replace the cornea in the Navarro eye model [3]. Next, a rigid contact lens is placed in front of the eye and the incident rays are traced repeatedly for different anterior contact lens curvatures to determine the best spherical correction with a through-focus series. Once the best retinal focus is found, the rays in the retinal point spread function are weighed according to their distance from the ideal position at the origin. Using this retinal distance, various blocking masks can be defined based on a trade-off between amount of allowable aberrations and retinal illumination.

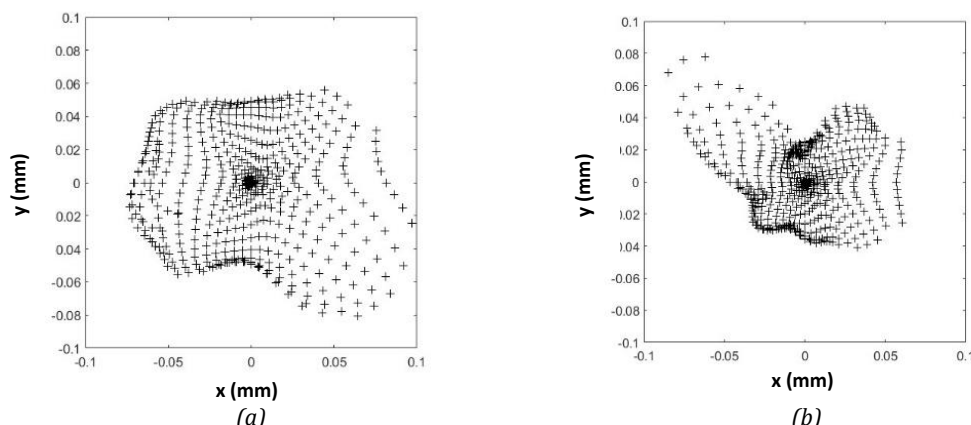


Figure 1: Point spread function at the retinal plane with best spherical correction of contact lens for two keratoconic eyes of two different patients. Patient b has a more advanced case than patient a.

Results

The retinal point spread function of keratoconic eyes is rather large and irregular (Figure 1). Based on the radial distance from the origins, the area of the contact lens that needs to be blocked to improve retinal image quality is shown in Figure 2, where the darkest areas correspond with the worst levels of aberrations.

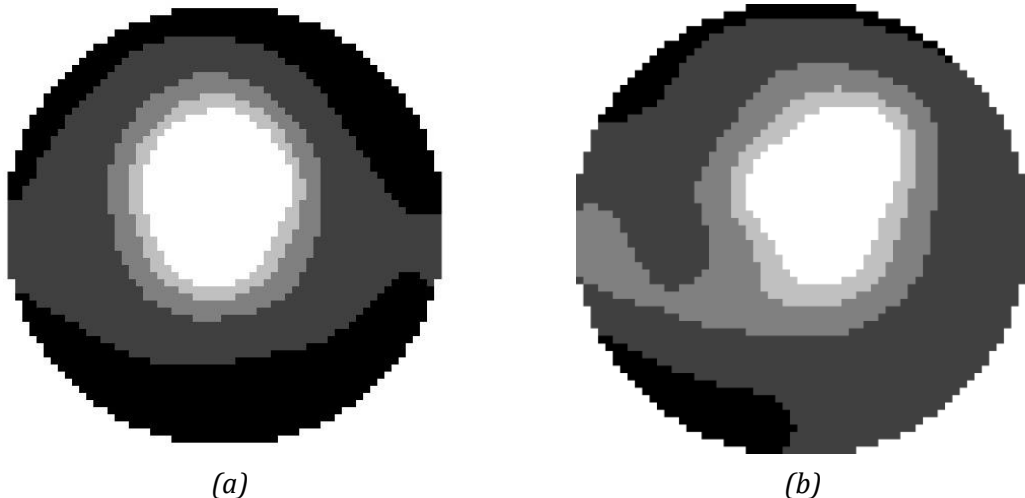


Figure 2: Masks of the cases (a) and (b) given in Figure 1. at pupil plane for a keratoconic eye based on radial distance from the origin on the retina. The white region corresponds with clear areas, and increasingly dark grey shades with more aberrated regions that are to be blocked to improve retinal image quality.

Conclusion

We developed an algorithm to determine a mask that can be printed on a rigid contact lens to block highly aberrated regions of the pupil that are insufficiently corrected by the lens. This method is based on ray tracing and uses the retinal coordinates with respect to the origin. The mask, shown in Figure 2, can either be made completely opaque as an attenuating filter. Alternatively, a slightly adjusted version of the mask could be printed on a phakic intraocular lens for a more permanent solution.

References

- [1] Bonaque-González S., Ríos-Rodríguez, S., & López-Gil, N. (2016). Improving vision by pupil masking. *Biomed Opt Express*, **7**(7), 2538-50.
- [2] Evans T, Rubin A. Linear optics of the eye and optical systems: a review of methods and applications. *BMJ Open Ophthalmology*. 2022;7(1):e000932.
- [3] Navarro R, González L, Hernández-Matamoros JL. On the prediction of optical aberrations by personalized eye models. *Optom Vis Sci*. 2006;83(6):371-81.

Automatic segmentation of corneal cuts in OCT images

Masoud Mehrjoo^{1*}, Alexander Pacuraru¹, Luise Krüger¹, Florian Beck²,
Konrad Doll², Samuel Arba Mosquera¹

¹ Biomedical Engineering Office, SCHWIND eye-tech-solutions, Kleinostheim, Germany

² Laboratory for the design of digital circuits and systems, University of Applied Sciences Aschaffenburg, Aschaffenburg, Germany

*Corresponding author: Masoud.Mehrjoo@eye-tech.net

We propose and preliminary evaluate an image processing routine empowered with optimisation to automatically characterise 3-dimensional confluent cuts through the cornea (in particular, volumes for lenticule extraction or surfaces for flap lift on corneal refractive surgery). The algorithm precisely traces the cut and determines the macroscopic parameters such as thickness, width, angles, inherited axes of rotations. We report on the algorithm concept and the primary results, on porcine eyes using images obtained from a commercially available OCT.

Keywords: OCT imaging system; Corneal segmentation; Refractive eye surgery

Introduction

Evaluation of refractive correction techniques, whether SMILE or LASIK procedure can effectively help diagnostics and monitor the treatment performance, as well as explaining probable post-operative issues originating from imperfect residuals. Technologically, Optical Coherent Tomography (OCT) has been established as a non-invasive, micro-resolution method to capture high-resolution volumetric images of biological tissues; however, the presence of strong speckle noises and the small contrast between adjacent faults aggravate an accurate segmentation (characteristics inference) of images.

The aim of this work is to segment and analyse corneal cuts produced in the cornea (in particular, either tissue volumes for lenticule extraction or surfaces for flap lift on corneal refractive surgery) before corneal manipulation took place (i.e., prior to extraction or lift). Beyond the segmentation, the aim of this work is to universally determine the macroscopic distances and angles of the segmented geometries. Our technique may serve for e.g., in-situ segmentation and evaluation of the cuts measured by an integrated OCT channel into a therapeutic medical device (e.g., SCHWIND ATOS or Ziemer Z8 Neo). The routine envisioned here has been orchestrated under the premise of universal applicability to OCT images obtained from “any” OCT device (provided a minimum quality requirement).

Methods

OCT images were obtained with a Thorlabs GAN111 OCT consisting of a Ganymede GAN111 as the base unit and an OCTG9 (with OCT-LK4-BB scan lens) as the scan head unit. With a wet lab handling, the epithelium of each eye was first removed, and the eyes were placed under the laser for further processing. The porcine eyes were treated with the SCHWIND ATOS femtosecond laser system (SCHWIND eye-tech-solutions, Germany). The eye was docked with the disposable patient interface and held with a vacuum level of 250 mmHg. The treatment specifications were set before each treatment to minimise the handling time for treatment and image acquisition. The porcine eyes were treated and, immediately after the treatment, placed under the OCT instrument to capture inter-tissue images at

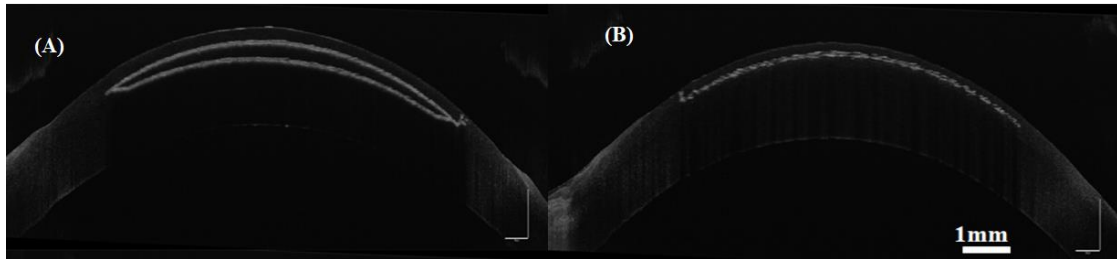


Figure 1. OCT images of treated porcine eyes. Shown of lenticule (A) and flap (B) cuts.

specific azimuthal angles (4 full meridians). Emphasis was put in providing a fast systematic and routine process, to ensure the homogeneity of the tissue throughout the experiment (from preparation to OCT scans). The OCT acquisition parameters and an example captured image from each category of treatments are given in Table 1 and Figure 1.

Table 1. OCT GAN111 acquisition parameters

	Lateral	Axial
#Pixel	10000	1024
Pixel Size (μm)	1.2	2.46
FOV (mm)	12	2.52
Scan averaging	A-Scan of (6)	A-Scan of (5)

The localisation of the cuts (as well as the corneal anterior layer) is explained in Figure 2. The algorithm first positions the peaks of interest determining the desired layers. In this work, we utilised the Sobel gradient analysis [1] to accurately localise the domain of cuts with a (quasi) Bayesian optimisation [2] to regulate hyperparameters of polynomial fits (e.g., Zernike) describing the shape structures. Numerically, we use a two-pass method Rosenfeld-Pfaltz augmented with the Union-Find and a decision tree based on the 2D 8-connected work of Wu et.al.[3]. Ultimately, Taylor polynomials were fitted on the point of interest (POI; the maxima of the vertical peak scans) to obtain the cap thickness (at different radial positions), diameter, incision angles and the tilt angle respect to the reference axis. The optimisation routine sets the hyperparameter of signal processing such that the boundaries fall off when POI density (with a Gaussian convolution) drops.

Results

Figure 3 summarises the algorithm performance on identifying lenticule/flap cuts. Through a statistical analysis over more than 50 porcine eyes (more than 200 OCT scans), the automatic measurement of caps/diameters was in good agreement with manual measurements of $\sim 1\text{ mm}$ separated markers directly using the OCT software with less than 3% deviation. Computationally, each processing unit took approximately 15 sec for flap and 55 second for lenticule cuts on a single CPU (compared to several minutes for the manual measurements). The reason for longer processing of lenticule originates from the complexity in shape detections of 3 layers. Preliminary success was also obtained at determining the entry angle of the edge cut into the cornea. Also, a computational layer of “Fast Mean Denoising” [4] was used to reduce the noise effect. The automation accelerates the post-processing and enhances data density and resolution without loss of accuracy that is needed for moving towards digitalised medicine.

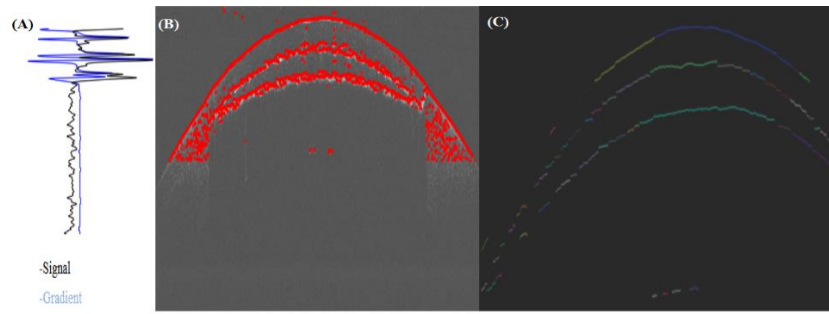


Figure 2. Image processing pipeline. The peaks of vertical signal scan are determined by Sobel gradient search (A-B) and the 2D connected components algorithm specifies pronounced (as top 64 closed sections) boundaries (C)

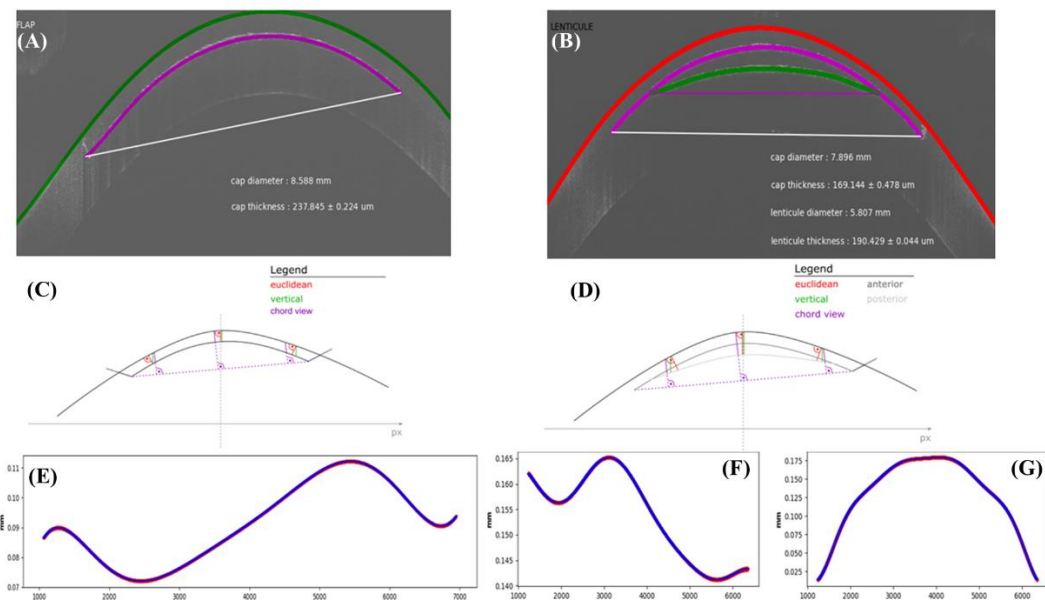


Figure 3. (A,B) Characterising flap and lenticule cuts. (C-H) Inner distance measurements between the layers form the chord view (as the precise reference for measurements).

Conclusion

In this work, we propose a segmentation model for the auto-segmentation of flap/lenticule profile from (generic) noisy OCT images. No manual effort is required to either annotate the segments or identifies the points of boundaries. This work can aid further analysis of optical/geometrical characteristics of treated eyes under different types of refractive surgery.

References

- [1] Ren X., Lai S., Medical Image Enhancement Based on Laplace Transform, Sobel Operator and Histogram Equalisation, Academic Journal of Computing & Information Science. 2022; 4:48-57.
- [2] Joy T., et. al. Fast hyperparameter tuning using Bayesian optimisation with directional derivative. Knowledge-Based Systems. 2020; 205:106247.
- [3] Wu K., et. al. Optimising two-pass connected component labelling algorithm. PAA. 2009; 12:117-135.
- [4] Nagoor M., et. al. Denoising Speckle Noise in Optical Coherence Tomography Images. EJMCM. 2022; 07.

Algorithm-assisted refraction: preliminary perspectives from different clinical application paradigms

José M. González-Méijome, Rute J. Macedo-de-Araújo, Sofia C. Peixoto-de-Matos,
Rafaela Carvalho, Ana I. Amorim-de-Sousa, Iñaki Blanco, Paulo RB Fernandes

Clinical & Experimental Optometry Research Lab (CEORLab),
Physics Center of Minho and Porto Universities, University of Minho, Braga, Portugal

* jgmeijome@fisica.uminho.pt

Algorithm-assisted semiautomatic refraction methods aim to improve the repeatability of refraction determination decreasing inter-examiner variability and eventually saving chair and clinician time in clinical context. Studies show increasingly positive agreement when compared with gold standard clinical refraction. However, questions still remain on the performance of such methodologies for other clinical applications as contact lens over-refraction. Refraction in the specialty contact lens fitting clinical practice can be time consuming and provide variable results. This is related with the poorer sensitivity of the patient to resolution tests due to poorer optical quality. The purpose of the present work is to report on different experiments conducted in non-presbyopic and presbyopic patients, using algorithm-based refraction by specialists and non-specialists as well as in other challenging conditions as refraction in eyes with irregular corneas, scleral contact lens over-refraction in regular and irregular corneas using subjective refraction through conventional methods as gold standard comparator. Results shows that algorithm-assisted subjective refraction from Hartmann-Shack aberrometry in the hands of a vision specialist is a useful method to arrive to a final prescription with similar levels of reliability to conventional subjective refraction.

Keywords: physiological optics; algorithm-based refraction; subjective refraction; objective refraction; subjective refraction.

Introduction

Refraction is an essential procedure in eye care. It provides the adequate combination of optical power in corrective lenses at a given distance from the eye to provide a focused image in the retina while the accommodation is relaxed under physiological conditions. The procedure can be negatively impacted by internal and external factors that the optometrist should rule out as much as possible such as involuntary accommodation, instrument bias and environmental conditions. In an attempt to reduce variability, automatization of refractive procedure has been an aspiration by the ophthalmic instrumentation developers [1-5]. The aim of the present study was to evaluate the reliability of refraction conducted with an algorithm-assisted subjective refraction system operated by trained optometrist and a non-specialist in determining refractive error from objective refraction followed by subjective refraction assisted by semi-automatic phoropters, compared to standard clinical refraction.

Methods

In a sequence of 3 different trials, 81 subjects without contact lens or surgical history, 20 scleral contact lens wearers with regular cornea and 10 scleral contact lens wearers were recruited in this non-dispensing cross-sectional comparative trial. Considering the sensitivity to refraction changes and blur [6], the sample size was estimated to detect a mean difference of 0.12 D between two refractions and

standard deviation of 0.15 D in refraction for a level of statistical significance alpha = 0.05 and statistical power = 80% (beta = 0.80). Protocols have been reviewed and approved by the Ethics Subcommittee for Research in Life and Health Sciences of the University of Minho (CEICVS 081/2020).

The Vision-R 700, Vision-S 700 and Vision-R 800 algorithm-based refraction units were used to obtain subjective refraction from the measurements of the Hartman-Shack WAM 800 wavefront aberrometer (Essilor, France). All three devices use optoelectronic lenses to generate spherical and cylindrical power at a resolution of 0.01 diopters and use proprietary algorithms (Smart Refraction, Semi Auto, Smart Check) to guide the operator (visual specialist or non-specialist) to derive final prescription based on the patient answers. Measurements were compared to the subjective refraction obtained by conventional subjective refraction from retinoscopy measurements using as endpoint the maximum plus power to obtain the maximum visual acuity. Two experienced optometrists (bachelor and master degree with over five years of clinical experience), one optometrist with minimal clinical experience (recent bachelor degree) and one non-specialist participated as examiners in these set of trials. Only the right or left eye of each subject was included for statistical analysis using SPSS version 28 (IBM, IL, USA). Pairwise comparisons were performed using T-test or Wilcoxon test, and Bland-Altman plots were used to assess the agreement between refraction methods. Statistical significance was set at alpha = 0.05 .

Results

Vision-R 700 was tested in a final study group of 40 subjects (40 eyes) of whom 12 (28%) were male and 31 (78%) were female, with an average age of 36.3 years (range 20 to 65 years); 16 (40%) were presbyopes, 30 (75%) wear spectacles. Of those who wore specs, five were progressive lens wearers and 25 of them use monofocal lens. Table 1 present the descriptive analysis and repeated measures analysis for spherical equivalent (M), horizontal component of astigmatism (J_0) and oblique component of astigmatism (J_{45}).

N= 41 M (D)	vs	Mean diff	SE	p	R
SR1_M_D1	GS1_M_D1	-0.04	0.05	>0.05	0.991
	GS1_M_D2	-0.09	0.05	>0.05	0.989
SR1_M_D2	GS1_M_D1	-0.03	0.04	>0.05	0.991
	GS1_M_D2	-0.08	0.04	>0.05	0.991
N= 41 J0 (D)	vs	Mean diff	SE	p	R
SR1_J0_D1	GS1_J0_D1	-0.03	0.02	>0.05	0.954
	GS1_J0_D2	-0.03	0.02	>0.05	0.944
SR1_J0_D2	GS1_J0_D1	-0.03	0.02	>0.05	0.965
	GS1_J0_D2	-0.03	0.02	>0.05	0.951
N= 41 J0 (D)	vs	Mean diff	SE	p	R
SR1_J45_D1	GS1_J45_D1	-0.01	0.01	>0.05	0.830
	GS1_J45_D2	-0.02	0.02	>0.05	0.585
SR1_J45_D2	GS1_J45_D1	0.01	0.02	>0.05	0.654
	GS1_J45_D2	0.00	0.02	>0.05	0.720

Table 1. Repeated measures ANOVA - Pairwise comparisons for measurements measured on day 1 (D1) and day two (D2) with Bonferroni Post-hoc correction (SE: standard error, R: Pearson correlation coefficient; SR1: semi-automatic subjective refraction; GS1: gold standard conventional refraction)

Vision-S 700 was tested in a final study group of 41 subjects (41 eyes) of whom 14 (33%) were male and 29 (67%) were female (Table 1), with an average age of 38.0 years (range 20 to 65 years); 59% are spectacles wearers and 26% of them uses correction for near vision. According to the age, the subjects were divided in 2 groups: Group 1 (Young with age < 45 years) and Group 2 (Presbyopes with age > 45 years with add). Table 2 present the agreement analysis between the non-specialist and specialist for the M component of refraction. Vision-R 800 was used in the contact lens experiments. Results are reported for 20 eyes from 20 patients with regular cornea fitted with scleral contact lenses and 19 eyes from 10 habitual scleral contact lens wearers with irregular cornea.

Table 2. Agreement between all the parameters measured for M component. p: statistical significance, LoA: limits of agreement, R: Pearson coefficient of correlation

M	Mean diff (95% CI)	p	LoA Inferior (95% CI)	LoA Superior (95% CI)	R
Non-Specialist R#2 vs Specialist 1 R#1	0.30 (0.19 to 0.41)	<.001	-0.40 (-0.59 to -0.20)	1.00 (0.80 to 1.19)	0.98
Non-Specialist R#2 vs Specialist 1 P#1	0.31 (0.19 to 0.41)	<.001	-0.40 (-0.59 to -0.20)	1.00 (0.80 to 1.19)	0.98
Non-Specialist R#2 vs Specialist 2 P#2	0.22 (0.11 to 0.32)	<.001	-0.45 (-0.64 to -0.26)	0.88 (0.70 to 1.07)	0.98
Specialist 1 R#1 vs Specialist 1 P#1	0.01 (-0.01 to 0.03)	0.53	-0.12 (-0.15 to -0.08)	0.13 (0.09 to 0.16)	0.99
Specialist 1 R#1 vs Specialist 2 P#2	-0.08 (-0.16 to -0.01)	0.05	-0.57 (-0.71 to -0.43)	0.40 (0.26 to 0.54)	0.99
Specialist 1 P#1 vs Specialist 2 P#2	-0.09 (-0.16 to -0.02)	0.03	-0.54 (-0.67 to -0.42)	0.36 (0.24 to 0.49)	0.99

	WAM 800	Retinoscopy	Conventional subjective Rx	V-R 800 Subjective Rx	p
M (D)	0.67 ± 2.53	0.64 ± 2.66	0.81 ± 2.39	0.73 ± 2.38	0.996
J0 (D)	-0.23 ± 0.17	-0.15 ± 0.22	-0.22 ± 0.17	-0.26 ± 0.18	0.306
J45 (D)	0.01 ± 0.13	-0.01 ± 0.12	0.00 ± 0.10	0.01 ± 0.14	0.946

Table 3. Descriptive values of M, Jo and J45 of the over-refraction obtained in scleral contact lens wearers with different methods (aberrometry WAM800, retinoscopy, conventional and algorithm-assisted subjective refraction VR800)

Conclusions

For the M component, the mean values for both between measurements taken on the same day for each measurement and those taken on different days is less than 0.25D with 95% confidence intervals of less than 0.5D most cases. While the algorithm-assisted semi-automatic subjective refraction performed by a non-specialist can be a good starting point for the specialist to arrive faster to a final prescription, both outcomes are not directly interchangeable. In scleral contact lens wearers, conventional over-refraction provides less negative refractive values with equal or comparable high and low contrast VA values. However, operated by a trained optometrist, algorithm-assisted subjective refraction provides an alternative reliable method to assist in the specialty contact lens clinic. Similar results were obtained in the irregular cornea scleral contact lens wearers.

Disclosure

The study has been funded by Essilor (France) that also made the instruments available to the researchers during the study duration. Authors have no conflicts of interest to disclose.

References

- [1] Venkataraman AP, Sirak D, Brautaset R, Dominguez-Vicent A. Evaluation of the Performance of Algorithm-Based Methods for Subjective Refraction. Journal of Clinical Medicine. 2020; 9(10):3144.
- [2] Pujol J, Ondategui-Parra JC, Badiella L, Otero C, Vilaseca M, Aldaba M. Spherical subjective refraction with a novel 3D virtual reality based system. J Optom. 2017;10(1):43-51. doi:10.1016/j.joptom.2015.12.005
- [3] Perches S, Collados MV, Ares J. Repeatability and Reproducibility of Virtual Subjective Refraction. Optom Vis Sci. 2016;93(10):1243-1253. doi:10.1097/OPX.0000000000000923
- [4] Guo H, Atchison DA. Subjective blur limits for cylinder. Optom Vis Sci. 2010;87(8):E549-E559. doi:10.1097/OPX.0b013e3181e61b8f
- [5] Pesudovs K, Parker KE, Cheng H, Applegate RA. The precision of wavefront refraction compared to subjective refraction and autorefraction. Optom Vis Sci. 2007;84(5):387-392. doi:10.1097/OPX.0b013e31804f81a9
- [6] Guo H, Atchison DA. Subjective blur limits for cylinder. Optom Vis Sci. 2010;87(8):E549-E559. doi:10.1097/OPX.0b013e3181e61b8f

Mobile app for tele-monitoring potential changes in myopia and presbyopia

Mateusz Jaskulski^{1,2*}, Rosa María Salmerón-Campillo¹,
Ginés Martínez-Ros¹, Norberto López-Gil¹

¹Universidad de Murcia, Murcia, Spain

²Indiana University, Bloomington, IN, USA

* Corresponding author: mateusz.jaskulski@gmail.com

Purpose

To evaluate the precision and repeatability a new app for detecting potential increase in a user's myopia or presbyopic addition.

Methods

Standard clinical spherocylindrical refraction (SCR) and addition (ADD) was obtained in two groups of subjects: 30 young between 18 and 40 years (22 ± 5 years), and 20 presbyopes older than 52 years (56 ± 3 years) in one eye per subject. Trial lenses were used to correct the clinical SCR in young subjects and the SCR+ADD in the presbyopic subjects. On top of their correction several levels of myopia or presbyopia were induced using trial lens in both groups. A mobile app was used to subjectively find far points (FP) in the young group and the near points (NP) in the presbyopic group. The app-displayed on-screen stimulus consisted of a group of blue lines on a black background. Due to the longitudinal chromatic aberration (LCA) of blue light, this allowed most subjects to find the subjective FP at a distance no greater than 1.4 m. The NP could always be found at a handheld distance. The on-screen stimuli for the FP and NP measurements were configured with a visual acuity (VA) measure obtained by the app with devices placed within the subjects' interval of clear vision. Three measurements were obtained per each subject for each value of induced myopia or presbyopia.

Results

In the young group the mean inter-subject standard deviation (SD) for all induced myopia levels was 0.23 D. Using a calibration method based in a Leave-One-Out Cross-Validation procedure (LOOCV) a linear fit between induced and measured myopia was $y = 1.00x + 0.00$ with $R^2 = 0.8$ ($p < 0.0001$) and limits of agreement (LOA) ± 0.5 D. In case of the presbyopic group, the SD was 0.4 D, and the linear fit yielded $y = 0.95x + 0.07$ with $R^2 = 0.98$ ($p < 0.001$) and $LOA \pm 0.8$ D.

Conclusion

The app was able to correctly find induced changes in FP and NP in young and presbyopic subjects. The app could be used as tool for over-refraction and "over-presbyopia" measurements, advising users to visit an eye care specialist in case the values changed.

Keywords: telehealth; smartphone; myopia; presbyopia

Mobile app for detecting early cataract

Norberto López-Gil ^{1*}, Ibtissam Oujelloul¹, Ginés Martínez-Ros², Mateusz Jaskulski^{2,3}

¹Clinica Universitaria de Vision Integral (CUVI), Universidad de Murcia, Murcia, Spain

²Universidad de Murcia, Murcia, Sapin

³ CORL. Indiana University. Bloomington, IN, USA

* Corresponding author: norberto@um.es

Purpose

To test a new app for detecting the potential presence of an early cataract.

Methods

Two groups of subjects were recruited for the study: a control group with 15 subjects (25 ± 9 years old) without cataract, and a cataract group with 15 subjects (53 ± 7 years old) with an early cataract (ranged 1 out 4). A standard cataract test using a slit lamp was performed in the subjects' right eyes in addition to obtaining a measure of straylight using C-Quant (Oculus™, Germany) followed by a CSV-1000 contrast sensitivity (CS) test (VectorVision, USA). An app was used to measure the CS of a blue target on a black background with a spatial frequency of 9 c/g. A forced 4-choice procedure was used in each measurement. The measurements were obtained under three conditions with the device handheld by the subjects: a) the device screen facing the subject and flash off (natural condition NC), b) screen facing the subject and flash on, illuminating the subject's face after being reflected in a flat mirror (flash reflected FR), c) screen facing a flat mirror in front of (and viewed by) the subject and flash on, illuminating the subject's face directly (direct flash FD). All subjects performed four repeated measurements for each condition.

Results

Significant differences were found between the cataract and control groups in the straylight measurements ($p < 0.01$) and CSV-1000 test measurements for 3, 6, 12 and 18 c/g ($p < 0.012$). The CS measurements obtained with the app usually took between 60 and 120 seconds in all conditions. When using the app, all conditions also showed significant difference between the two groups: $p = 0.00020$ (NC); 0.01000 (FR); and 0.00004 (FD). Maximum statistical accuracy of the test corresponded to 0.83 and was found for a sensitivity contrast of 26 under the FD condition.

Conclusions

This initial test indicates that the app was able to discriminate most subjects with an early cataract from those belonging to the control group (no cataract). The greatest differences between the cataract and control group were found when the device's flash was directly illuminating the face (FD). The methodology could be of interest as a tele-health tool for a self-screening with a smartphone to detect early cataract.

Keywords: smartphone; cataract; contrast sensitivity

Prediction of the spherical subjective refraction from accommodation data

Aina Turull-Mallofré, Mikel Aldaba, Meritxell Vilaseca, Jaume Pujol, Carlos E. García-Guerra

Centre for Sensors, Instruments and Systems Development (CD6),
Universitat Politècnica de Catalunya, Terrassa, Spain

* Corresponding author: aina.turull@upc.edu

The uncorrected refractive error is the leading cause of visual impairment, particularly in developing countries. This has increased the interest in developing objective methods for assessing refraction. Furthermore, some works have used machine learning with various input data for the prediction of the subjective refraction. However, none of the studies have considered data from accommodation in their input variables. This study aimed to evaluate the performance of machine learning regression models to predict the spherical component of subjective refraction using information from an accommodative response as an input variable. Three models were used: Gradient Descent (GD), Normal Equation (NE), and Extreme Gradient Boosting (XGB). The results showed that machine learning models improved the estimation of subjective refraction compared to the objective refraction obtained with a commercial autorefractor, in particular GD and NE models.

Keywords: subjective refraction; accommodation; machine learning

Introduction

The first cause of visual impairment is the uncorrected refractive error, with an importance incidence in developing countries [1]. With this scenario the need and interest to develop new devices and methodologies for assessing refraction in an objective and accurate way has increased. The gold standard currently used to assess refraction is the subjective refraction. This technique is the only that considers the patients' response and has been proven as a technique especially good in controlling accommodation. The growing interest in deep learning and machine learning, has contributed to develop new studies to predict the subjective refraction using different input data [2–5]. However, none of the previous studies consider accommodation data in their input variables. Therefore, the aim of this work was to assess the performance of machine learning (ML) regression models for predicting the spherical component of the subjective refraction by using information from the accommodative response as input variable.

Methods

The objective refraction of the participants was measured with the commercial autorefractor Grand-Seiko WAM-5500. After, the accommodative data was obtained by measuring changes in the spherical component of the refractive state of the eye when inducing accommodation with a sweep of lenses of gradual decreasing powers from +1.00 D to -1.00 D in 0.25 D steps relative to the objective refraction. This sweep generated a response from a relaxed to activated accommodation state. The measuring set-up was a custom-developed Hartmann-Shack aberrometer coupled to a phoropter [6]. Data of the subjective refraction was determined following the conventional procedure [7] and its spherical component was used for training the models as target value.

Three models were trained and tested for the spherical component of the subjective refraction (M_{SR}): Normal Equation (NE), Gradient Descent (GD), and Extreme Gradient Boosting (XGB). The input variables were the measured spherical equivalent (M) during the sweep of lenses, the spherical component of the objective refraction (OR) and age. The total data was divided randomly into two sets: 132 eyes (75%) in the train set and 44 eyes (25%) in the test set.

Performance of the models in comparison to the real value of M_{SR} was evaluated with the Bland Altman analysis, Mean Absolute Error (MAE), Root Mean Square Error (RMSE) and the percentage of agreement for thresholds of 0.25 D and 0.50 D . Same parameters were analyzed for the OR with comparing purposes. Moreover, the weight of the input features for the three models was analyzed.

Results

A total of 176 eyes were included in the study. Participants' mean age \pm standard deviation (SD) was 32.60 ± 15.25 years in a range from 19 to 73 years and the mean spherical equivalent error \pm SD was $-0.86 \pm 1.67\text{ D}$ ranging from -5.38 D to $+2.75\text{ D}$. The results for the performance of the OR as an estimator of M_{SR} are summarized in Table 1.

Table 1. Performance of the OR as an estimator of M_{SR}

Agreement (%)		Bland-Altman (D)		MAE (D)	RMSE (D)	Min (D)	Max (D)
0.25 D	0.50 D	Mean Difference \pm SD	95% LOA				
56.82	78.89	-0.160 ± 0.413	$-0.97, +0.65$	0.34	0.44	-5.13	+3.00

For the analysis of the results achieved with the different models it is worth noting that the comparison is between the predicted value of M_{SR} obtained for the 44 eyes in the test set and their actual value of M_{SR} . The range of real M_{SR} in this group went from -5.38 D to $+1.50\text{ D}$. The performance parameters for the three models are shown in Table 2.

Table 2. Performance of the three tested models for estimating M_{SR}

Model	Agreement (%)		Bland-Altman (D)		MAE (D)	RMSE (D)	Min (D)	Max (D)
	0.25 D	0.50 D	Mean Difference \pm SD	95% LOA				
NE	70.45	93.18	-0.103 ± 0.269	$-0.42, +0.63$	0.21	0.29	-5.35	+1.00
GD	70.45	93.18	-0.098 ± 0.264	$-0.42, +0.62$	0.20	0.28	-5.35	+0.98
XGB	65.90	90.90	$+0.089 \pm 0.342$	$-0.58, +0.76$	0.24	0.35	-4.93	+1.03

The three models outperformed the OR as an estimator of M_{SR} . The performance of NE and GD was similar in all parameters whereas that of XGB was slightly worse. The three models improved the percentage of agreement for threshold of 0.25 D and 0.50 D , reaching a maximum agreement between the real and predicted value of M_{SR} with GD and NE of 93.18% for the 0.50 D threshold. Moreover, MAE and RMSE values were reduced with all three models with respect to OR a 38% and 36%, respectively, with NE and GD and a 30% and 20% with XGB.

In Figure 1 the weight for each input variable is shown for the studied models. For the GD and NE models, the features with higher weights were the measured spherical equivalent with the lenses of $+0.75\text{ D}$ and -0.50 D and the OR. Similarly, in the case of the XGB model, the three input variables that stand out are the measured equivalent with the lenses of $+0.75\text{ D}$ and -0.25 D and the OR.

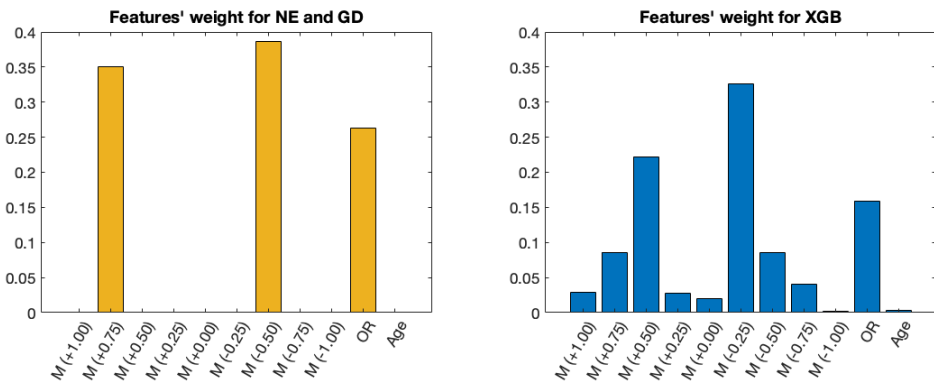


Figure 1: Left: Feature weights for the GD and NE models. Right: Feature weights for XGB model.

Conclusions

To sum up, ML models that considered accommodation data seem to provide better estimations of the M_{SR} than the OR. The performance of NE and GD were similar while weaker results were obtained with XGB. The results of the features' weight suggest that having data from accommodation is relevant, such as the relaxed state of accommodation, the point with the accommodation slightly activated or the transition point between relaxed and activated accommodation, which can contribute to improve the estimation of M_{SR} . However, future work should be done to improve these results. On the one hand, the train and test sets used in the current study are significantly small compared to other studies with similar purposes [2–5] and should be increased. On the other hand, considering the features' weights, new input variables or approaches should be studied, as non-linear fits that can give information about the behavior of the accommodative response when it is relaxed or activated.

Funding

This publication is part of the project PID2020-112527RB-I00, funded by MCIN/AEI/10.13039/501100011033; Aina Turull-Mallofré gratefully acknowledges the Universitat Politècnica de Catalunya and Banco Santander for the financial support of her predoctoral grant FPI-UPC. The author Mikel Aldaba is a Serra Húnter Fellow.

References

- [1] Alswailmi FK. Global prevalence and causes of visual impairment with special reference to the general population of Saudi Arabia. *Pak J Med Sci*. 2018;34:751–756.
- [2] Hernández CS, Gil A, Casares I, et al. Prediction of manifest refraction using machine learning ensemble models on wavefront aberrometry data. *Artif Intell Data Sci E-Health Vis Res Clin Act*. 2022;15:S22–S31.
- [3] Rampat R, Debellemière G, Malet J, et al. Using Artificial Intelligence and Novel Polynomials to Predict Subjective Refraction. *Sci Rep*. 2020;10:1–9.
- [4] Chun J, Kim Y, Shin KY, et al. Deep learning-based prediction of refractive error using photorefraction images captured by a smartphone: Model development and validation study. *JMIR Med Inform*. 2020;8:1–12.
- [5] Espinosa J, Pérez J, Villanueva A. Prediction of Subjective Refraction From Anterior Corneal Surface, Eye Lengths, and Age Using Machine Learning Algorithms. *Transl Vis Sci Technol*. 2022;11:1–11.
- [6] García-Guerra CE, Martínez-Roda J, Ondategui Parra JC, et al. System for objective assessment of the accommodation response during subjective refraction. *Transl Vis Sci Technol*. (to be published)
- [7] Benjamin WJ. *Borish's Clinical Refraction*. 2nd ed. Borishs Clin. Refract. Elsevier; 2006.

The effect of stimulus background luminance on temporal contrast sensitivity

Pilar Casado^{1*}, Victoria Collados, Francisco Ávila, and Jorge Ares

¹ Applied Physics, University of Zaragoza, Zaragoza, Spain

* Corresponding author: pilarcasado@unizar.es

Temporal contrast sensitivity is highly dependent on the characteristics of the stimulus used for its measurement. In this study, we evaluated the influence of background luminance on temporal contrast sensitivity for two temporal frequencies of the stimulus, 4 Hz and 20 Hz. Temporal contrast sensitivity proved to be higher as background luminance increased and, in addition, the functional relationship between the two variables depended on the stimulus frequency.

Keywords: temporal contrast sensitivity; temporal frequency; background luminance

Introduction

The human capacity to perceive information from the environment through the visual function is based on the ability to distinguish luminance variations in objects, that is the ability to perceive contrast. Contrast sensitivity, defined as the inverse of threshold contrast, is usually measured as a function of spatial frequency. However, measuring contrast sensitivity as a function of temporal frequency is useful for characterizing a subject's temporal vision.

Temporal contrast sensitivity (TCS) has been found to reach its maximum in the frequency range of 8 – 12 Hz [1]. Temporal contrast sensitivity is influenced by individual factors such as age [2] or degenerative diseases [3]. Nevertheless, it also depends on the characteristics of the stimulus used for its measurement. Stimulus parameters affecting temporal contrast sensitivity include angular size, eccentricity, and mean luminance. Evidence has shown that as each of these parameters increases, so does the TCS [4-6]. However, little is known about the relationship between TCS and the luminance surrounding the flickering stimulus (named in this work as background luminance). This work aims to evaluate the influence of background luminance on temporal contrast sensitivity when the mean luminance of the stimulus remains constant.

Methods

The study was carried out at the Laboratory of Visual Optics Research of the University of Zaragoza. The sample was composed of 10 subjects with an average age of 28 ± 6 years. Measurements were performed monocularly with the subjects wearing their refractive correction for distance vision.

A variation of a system developed for the study of disability glare vision was used [7]. Only the visualization channel of this system was employed, which consists of a collimating lens and an afocal system composed of two achromatic doublets. The monitor where the stimulus is presented, with a refresh rate of 120 Hz, is placed on the object focal plane of the collimating lens. The subject's eye is positioned, using a chinrest, at the image focal plane of the second achromatic doublet.

The stimulus consists of two adjacent semicircles that subtend a visual field of 3° through the optical

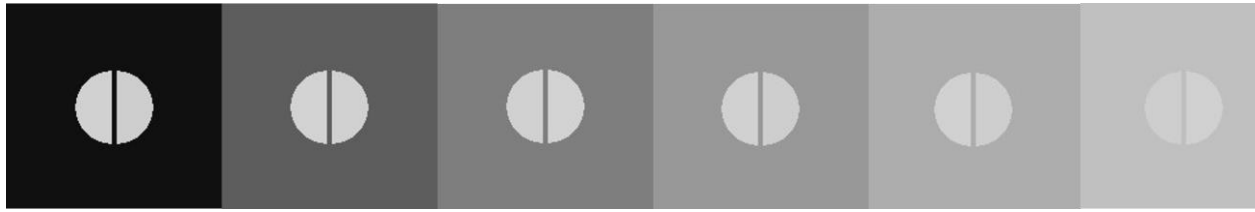


Figure 1. Stimulus appearance with increasing background luminance. Mean luminance of the stimulus is 150 nt in all cases, and background luminance is: 0, 25, 50, 75, 100, and 150 nt

system (see Figure 1). One of the semicircles flickers between two different luminance levels following a waveform with a square profile. Both the average luminance of the flickering semicircle and the static semicircle are 150 nt.

TCS was measured using a 2 Alternative Forced Choice task and a QUEST algorithm [8] programmed in Matlab R2017a with the Psychtoolbox package (PTB-3). QUEST is an adaptive psychophysical method used for threshold estimation. Forty trials were used for each QUEST procedure. The stimulus presentation time per trial was 1 second.

TCS was measured for stimulus frequencies of 4 and 20 Hz in combination with 6 different levels of background luminance: 0, 25, 50, 75, 100, and 125 nt. Two additional measurements were taken for frequencies of 8.57 and 12 Hz only for 0 nt background luminance. Overall, 14 different stimulus conditions were presented in random order resulting in a total of 560 responses per participant.

Results

Figure 2 shows the TCS values obtained with a background luminance of 0 nt for the four temporal frequencies evaluated (4, 8.57, 12, and 20 Hz). Among these four frequencies, the highest TCS was found for the 12 Hz temporal frequency.

In Figure 3, the TCS is shown as a function of background luminance for the 4 Hz frequency and the 20 Hz frequency. In the case of the 4 Hz frequency, it shows that there is a linear relationship between TCS and background luminance. The fitted line takes the form: $TCS(4 \text{ Hz}) = 0.546 L_{back} + 15.116$ ($R^2 = 0.998, p < 0.001$). On the right, the TCS obtained with a temporal frequency of 20 Hz is displayed. The relationship between the TCS and the background luminance for this frequency does not follow a linear relationship. However, there is a quadratic relationship as follows: $TCS(20 \text{ Hz}) = -0.003 \cdot L_{back}^2 + 0.753 \cdot L_{back} + 17.736$ (p -value for all coefficients was lower than 0.05).

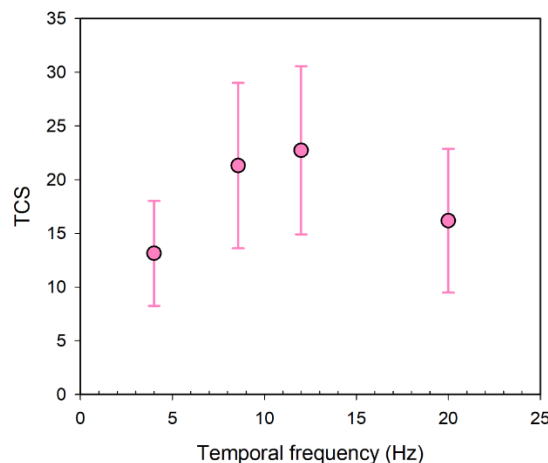


Figure 2. TCS as a function of temporal frequency measured with a background luminance of 0 nt.

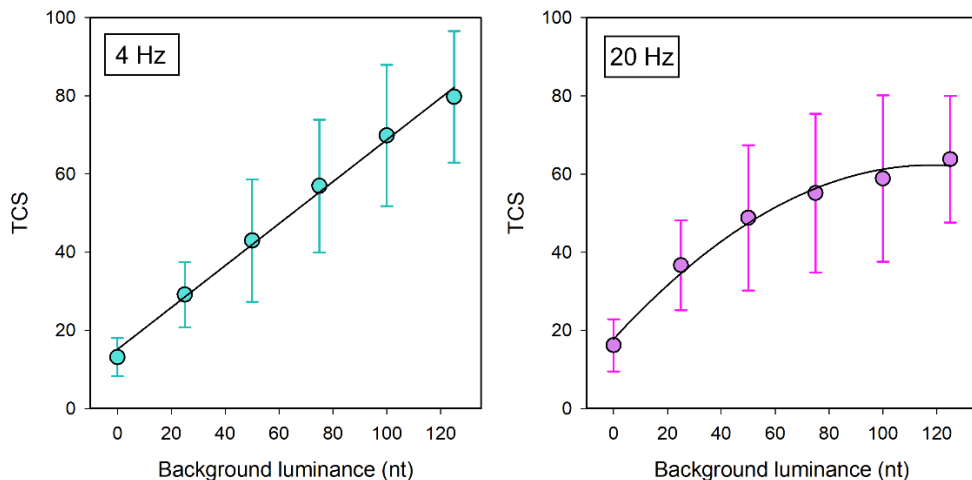


Figure 3. TCS as a function of background luminance for a stimulus flicker frequency of 4 Hz (left) and 20 Hz (right).

Conclusions

A study was conducted to reveal the relationship between TCS and background luminance. Consistent with previous research [1, 5], a pass-band behavior was found for the TCS as a function of the temporal frequency. Among the frequencies studied, the highest contrast sensitivity was found for the temporal frequency of 12 Hz. However, to accurately find the peak of the temporal contrast sensitivity curve, more temporal frequencies should have been evaluated. Different linear and quadratic behaviors in relation to background luminance were found for 4 and 20 Hz frequencies, respectively. To our knowledge, this behavior has not been previously described in the literature. Further research should be conducted to clarify the relationship between temporal contrast sensitivity and the characteristics of the environment surrounding the flickering stimulus.

Acknowledgement

This research was supported by Ministerio de Ciencia, Innovación y Universidades (Grant PID2020-114311RA-I00); Gobierno de Aragón (Grant E44- 20R).

References

- [1] Kelly D. Flickering Patterns and Lateral Inhibition. *J. Opt. Soc. Am.* 1969; 59: 1361-1370
- [2] Mayer M, Kim C, Syringos A and Glucs A. Foveal flicker sensitivity in healthy aging eyes. I. Compensating for pupil variation. *J. Opt Soc. Am. A.* 1988; 5(12): 2201-2209.
- [3] Seiple W, Greenstein V, and Carr R. Losses of temporal modulation sensitivity in retinal degenerations. *Br. J. Ophthalmol.* 1989; 73(6):440-447
- [4] Keesey U. Variables determining flicker sensitivity in small fields. *J. Opt. Soc. Am.* 1970; 60(3):390-398.
- [5] Wooten B, Renzi L, Moore R and Hammond B. A practical method of measuring the human temporal contrast sensitivity function. *Biomed. Opt. Express.* 2010; 1: 47-58.
- [6] De Lange H. Research into the dynamic nature of the human fovea-cortex systems with intermittent and modulated light. I. Attenuation characteristics with white and colored light, *J. Opt. Soc. Am.* 1958; 48:777-784
- [7] Casado P, Avila F, Collados V and Ares J. A study on disability glare vision in young adult subjects. *Sci Rep.* 2023; 13.
- [8] Watson AB, Pelli DG. QUEST: a Bayesian adaptive psychometric method. *Percept Psychophys.* 1983;33(2):113-120.

Design of a holographic stereoacuity test

Jorge Lasarte Sanz *^{1,2,3}, Eduardo Iglesias Mayayo ¹, Jorge Ares García ¹,
Mª Victoria Collados Collados ¹, and Jesús Atencia Carrizo ¹

¹ Research Institute of Aragon (I3A), Applied Physics Department,
University of Zaragoza, Pedro Cerbuna 12, 50009 Zaragoza, Spain

² Centre for Industrial and Engineering Optics, School of Physics, Clinical and Optometric Sciences,
TU Dublin, Grangegorman, D07 ADY7 Dublin, Ireland

³ FOCAS Research Institute, TU Dublin, 13 Camden Row, D08 CKP1 Dublin, Ireland

* Corresponding author: jorge.lasarte@tudublin.ie

Purpose

To develop a novel stereoacuity test based on holographic techniques presented as a potential alternative to current tests relying on stereograms and real-depth. The aim is also to compare it with the three widely used ones: Titmus, TNO and Frisby.

Methods

A series of reflection holograms from a flat diffusing object are recorded on a Bayfol HX photopolymer using a 532 nm laser in a Denisyuk (one beam) set-up. The recording geometry is selected to illuminate the hologram using a LED source at approximately 150 mm in order to reconstruct a real image. The distance between the object and the photosensitive material during recording is varied to obtain 10 holograms with images corresponding to specific stereoacuity values, namely $800'', 400'', 200'', 140'', 100'', 80'', 60'', 50'', 40'',$ and $25''$ of arc. The developed test comprises a discriminatory assessment, necessitating an ordered arrangement in either an ascending or descending manner. This test does not rely on glasses or any external device to perceive the image, since it's based on a real-depth image.

Results

A set of 10 functional reflection holograms providing images with varying seconds of arc was generated and utilized to assess the stereoacuity of 21 individuals, alongside conventional tests, namely TNO, Titmus and Frisby tests. Comparative analyses were conducted between the outcomes obtained from this novel test and those obtained from conventional stereoacuity tests. The obtained results show an average stereoacuity of $48.6'', 28.4'', 41.9''$ and $53.8''$ for TNO, Titmus, Frisby and the holographic test respectively, which initially would lead to believe that the holographic test was showing similar results as TNO, but when calculated the correlation coefficients between the holographic test and the other was 0.41 for TNO, 0.53 Titmus and 0.71 for Frisby, being that one the one showing most correlation.

Conclusion

The present study aimed to develop and evaluate an alternative stereoacuity measurement test utilizing holographic techniques. The findings revealed a discernible trend in the results, indicating the potential efficacy and suitability of the proposed holographic-based test as an alternative method for assessing stereoacuity.

Keywords: Stereoacuity; Holography; HOE; LED

Cognitive impairment in patients with post-COVID condition: correlations between eye movements metrics and the Stroop Colour and Word neuropsychological test

Joan Goset¹, Valldeflors Vinuela-Navarro¹, Clara Mestre¹, Mikel Aldaba¹, Neus Cano^{2,3}, Mar Ariza², Bàrbara Delàs⁴ and Maite Garolera^{2,5}, Meritxell Vilaseca¹

¹Center for Sensors, Instruments and Systems Development,
Universitat Politècnica de Catalunya, Terrassa (Barcelona), Spain

²Clinical Research Group for Brain, Cognition and Behavior,
Consorci Sanitari de Terrassa (CST), Terrassa (Barcelona), Spain

³Departament de Ciències Bàsiques, Universitat Internacional de Catalunya (UIC),
Sant Cugat del Vallès (Barcelona), Spain.

⁴Servei d'Oftalmologia. Consorci Sanitari de Terrassa (CST), Terrassa (Barcelona), Spain

⁵Neuropsychology Unit, Hospital de Terrassa, Consorci Sanitari de Terrassa (CST), Terrassa (Barcelona), Spain

* Corresponding author: joan.goset@upc.edu

This study investigates the cognitive dysfunction experienced by patients with post-COVID condition (PCC) exploring correlations between eye movement metrics and scores from the neuropsychological tests Stroop Colour and Word Test (SCWT). The results of the study suggest that patients with PCC have an impaired ability to inhibit cognitive interference, as evidenced by correlations found in the visual tasks of anti-saccades and fixation. Correlations found in terms of prosaccades and smooth pursuit seem to be related to other altered cognitive functions, such as reduced processing speed.

Keywords: eye tracker, eye movements, cognition, Stroop Colour and Word Test (SCWT)

Purpose

Although COVID-19 patients present primarily with symptoms of respiratory disease, a prevalent symptom of post-COVID condition (PCC) is cognitive dysfunction. It is well established that eye movement control is affected in neurodegenerative conditions [1,2], and a few recent studies suggest that COVID-19 disease may have a similar impact, in particular when patients show cognitive impairment [3]. This study aims to explore correlations between oculomotor performance and scores from the Stroop Color and Word Test (SCWT), which is extensively used in neuropsychology for experimental purposes to measure multiple cognitive functions, in patients with PCC.

Methods

Preliminary data from a sub-group of participants who were taking part in the Nautilus study, a large multi-center study that aims to evaluate and characterize cognition, mental health, and functional capacity of people who recovered from COVID-19, were analyzed. The sample consisted of 65 participants with PCC and 20 control participants. Eye movements were measured using an eye tracker (EyeLink 1000 Plus, SR-Research Ltd., Canada), with the head supported on a chinrest. Participants were seated 60 cm away from a computer monitor where visual stimuli for pro/anti-saccades, smooth pursuit, and fixation tasks were displayed. Eye movement metrics (e.g., saccade latency, amplitude, peak velocity, etc.) were computed and correlated with the direct scores from the SCWT test. Figure 1 depicts

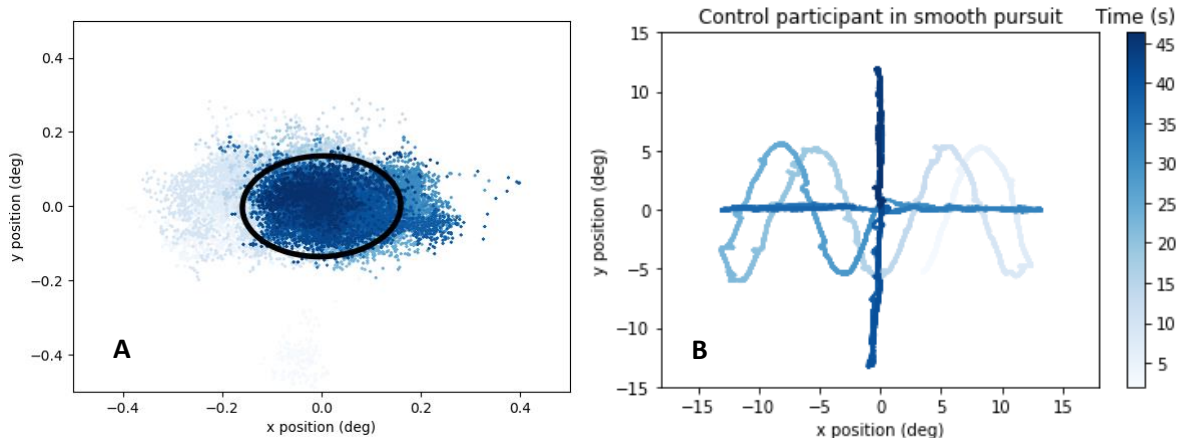


Figure 1. (A) Cloud of points recorded during the fixation task for one participant and the Bivariate Contour Ellipse Area (BCEA) around the central 68% of the fitted distribution of gaze positions. (B) Smooth pursuit test data divided by sinusoidal, horizontal, and vertical trajectories.

an example of the recorded data during the fixation and the smooth pursuit tests.

The SCWT is a widely used neuropsychological test that measures a range of cognitive functions, including attention, cognitive processing speed, and inhibitory control. The test consists of several conditions, including the congruous condition, in which participants are required to read color words that are printed in black ink (W) and name different color patches (C), which is a relatively easy task that requires minimal cognitive effort. However, in the incongruent condition of the SCWT, the task becomes more challenging. In this condition, color-words are printed in an inconsistent color ink, and participants are required to name the color of the ink instead of reading the word (CW). This task involves inhibitory control, as participants need to suppress the automatic response of reading the word and instead focus on naming the color of the ink. Correlations of variables (i.e. eye movements metrics and SCWT scores) were assessed using Pearson's correlation coefficients.

Results

Significant correlations between oculomotor performance and SCWT scores were found for the following metrics: W: antisaccades peak velocity ($r = 0.301; p = 0.018$), mean amplitude of saccades during smooth pursuit ($r = -0.294; p = 0.012$); C: prosaccades latency ($r = -0.239; p = 0.045$), antisaccades peak velocity ($r = 0.253; p = 0.048$), mean amplitude of saccades during smooth pursuit ($r = -0.251; p = 0.033$); fixation BCEA ($r = -0.238; p = 0.043$); CW: prosaccades peak velocity ($r = 0.250; p = 0.036$), antisaccades duration ($r = -0.257; p = 0.049$), antisaccades amplitude ($r = -0.321; p = 0.012$), mean amplitude of saccades during smooth pursuit ($r = -0.403; p < 0.001$), mean amplitude of saccades during smooth pursuit ($r = -0.403; p < 0.001$), fixation BCEA ($r = -0.288; p = 0.014$) .

Discussion

The visual task of antisaccades involves inhibition since participants were asked to fixate a central fixation target and look at the opposite side relative to the peripheral target as fast as possible when it appeared. Similarly, fixation also accounts for inhibition because in this task, participants' eye movements were recorded while they were fixating a central cross and peripheral distractors appeared. Therefore, correlations found in terms of these visual tasks could be attributed to the inability to inhibit cognitive interference in patients with PCC. The other correlations reported in terms of prosaccades and smooth pursuit could be related to other altered cognitive functions such as reduced processing speed.

Acknowledgement

This publication is part of the project TED2021-130409B-C54 and TED2021-130409B-C51, funded by MCIN/AEI/10.13039/501100011033 and the European Union “NextGenerationEU”/PRTR, and La Marató de TV3 Foundation (202111-30-31-32). J.G. thanks the Spanish Government for the predoctoral FPI grant he received.

References

- [1] Tao L, Wang Q, Liu D, Wang J, Zhu Z, Feng L. Eye tracking metrics to screen and assess cognitive impairment in patients with neurological disorders. *Neurol Sci.* julio de 2020;41(7):1697-704.
- [2] Opwonya J, Doan DNT, Kim SG, Kim JI, Ku B, Kim S, et al. Saccadic Eye Movement in Mild Cognitive Impairment and Alzheimer's Disease: A Systematic Review and Meta-Analysis. *Neuropsychol Rev.* junio de 2022;32(2):193-227.
- [3] Carbone F, Zamarian L, Rass V, Bair S, Ritter M, Beer R, et al. Cognitive dysfunction 1 year after COVID -19: evidence from eye tracking. *Ann Clin Transl Neurol.* noviembre de 2022;9(11):1826-31.

A study about the relation between virtual subjective refraction, objective refraction, and real subjective refraction

Jorge Ares¹, Victoria Collados*¹, Sara Perchés¹, Nuria Tomás¹, Esther García¹, Diana Gargallo¹, Pilar Casado¹, Laura Remón¹ and Francisco Ávila¹

¹ Applied physics, University of Zaragoza, Zaragoza, Spain

² CD6. Universitat Politècnica de Catalunya, Terrassa, Spain

* Corresponding author: vcollado@unizar.es

Subjective refraction is a technique used to determine the combination of spherical and cylindrical lenses required to achieve the best visual acuity considering the individual's subjective response. In this study is evaluated an alternative method to carry out a subjective refraction using retinal image simulation called virtual subjective refraction (VSR). In order to do that, comparisons were made between the results of real and virtual subjective refraction a couple of objective refraction methods taken over a sample of real patients. The results show that, in contrast with the objective refraction methods, virtual subjective refraction did not show statistically significant differences in its refractive components compared to real subjective refraction. However, objective metric-guided refraction and objective refraction based on Zernike coefficients received higher acceptance scores.

Keywords: subjective refraction; aberrometry; visual simulation, virtual refraction.

Introduction

The standard protocol for monocular subjective refraction seeks the most positive lens spherocylindrical lens that provides the maximum visual acuity value based on the subject's subjective response. Although it is considered the "gold standard," it has drawbacks as: the need of interaction between examiner and subject, the control of accommodation and perceptual inter-subject differences. In support of the "gold standard," automatic refraction techniques are often used as a starting point, where the subject's response is not necessary. The most commonly used automatic techniques are autorefractometry and other based on wavefront aberration measurements.

This study examined the validity of an alternative method called virtual subjective refraction (VSR) for obtaining the values of the spherocylindrical correction. The method relies on evaluating retinal simulated images to carry out a subjective virtual refraction without the need of patient's cooperation.

Methods

Thirty-four subjects were enrolled in the study, ranging in age from 23 to 55 years. The subjects were free of ocular pathology or refractive surgery and had a decimal visual acuity of ≥ 0.8 with their best refractive correction. Before the experiment, each subject underwent three measurements of wavefront aberrometry using the iTrace wavefront sensor (Tracey Technologies, Houston, TX) under low-light conditions. The mean spherical equivalent of the sample was $-1.91 \pm 2.34D$, with a maximum cylindrical component value of $3.25D$.

Monocular subjective refraction

Conventional monocular subjective refraction was performed on both eyes using five-letter optotypes

with logarithm of the minimum angle of resolution (logMAR) steps of *0.10*. The starting point was obtained by adding *+2D* of myopia to the spherical correction value (*S*) given by the aberrometer.

Finally, the effectiveness of cylindrical correction (*C*) was tested by adding *+0.25D* of cylindrical correction and measuring visual acuity. Finally, the Jackson refraction components (*M*, *J0*, and *J45*) were calculated from the *S*, *C*, and the cylinder axis orientation α values obtained by means of conventional subjective refraction.

Virtual subjective refraction

Virtual subjective refraction was performed taking advantage of the wavefront aberration data obtained from each eye and the simulation software described elsewhere [1,2]. The protocol used in the subjective virtual refraction process was identical to that used during the conventional subjective refraction.

Objective refraction calculated with Zernike coefficients.

M, *J0*, and *J45* were directly obtained from the Zernike coefficients in the sense of minimum root mean square as it is described in [3].

Refraction based on Visual Strehl OTF.

A computer program was developed in Matlab to perform an automatic refraction process based on aberrometry data and Visual Strehl OTF (VSOTF) metrics [3].

Acceptance of each prescription.

Once the results of the four refraction methods were obtained, the subjects evaluated the comfort obtained with each one. Using a line of letters with a *0.10* lower visual acuity value than the maximum obtained, the patient was first forced to choose between the four refractive corrections obtained. Then, they were also asked to rate the visual comfort of each refraction on a scale of 0 (worst) to 5 (best). The order in which the corrections were presented was randomly selected by a third person, so neither the examiner nor the subject knew which technique was used for the tested refraction.

Results

The results of the comparisons between refractive components for virtual and subjective refraction are shown in Figure 1. The mean differences and the limits of agreement (calculated as 1.96 times the

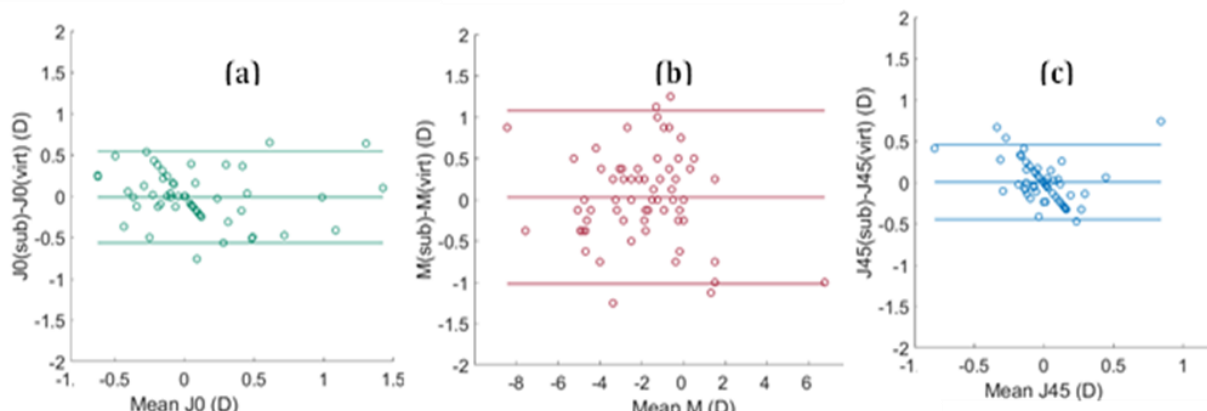


Figure 1. Bland-Altman plots for the *M*, *J0*, and *J45* components comparing the results of virtual refraction with conventional subjective refraction.

standard deviation) are displayed as horizontal lines.

The results of the refractive comparisons indicate that virtual refraction is the only method that does not exhibit statistically significant differences in any of its components (M , $J0$, and $J45$) compared to conventional subjective refraction. In terms of acceptance of the different refraction methods, the highest mean score is obtained for metric-guided refraction, followed by objective refraction based on Zernike coefficients, with both methods outperforming subjective refraction or virtual refraction.

Conclusions

It is concluded that, despite the lack of statistically significant differences between virtual refraction and subjective refraction, virtual refraction cannot replace subjective refraction in monocular prescription based on the acceptance of the results by the sample of subjects used in this study. Further research is required to explore the potential and limitations of subjective virtual refraction in clinical practice.

Acknowledgement

This research was supported by Ministerio de Ciencia, Innovación y Universidades (Grant PID2020-114311RA-I00); Gobierno de Aragón (Grant E44- 20R).

References

- [1] Perches S, Collados MV, Ares J. Retinal Image Simulation of Subjective Refraction Techniques. PLoS One. 2016;11(3).
- [2] Perches S, Collados MV, Ares J. Repeatability and Reproducibility of Virtual Subjective Refraction. Optom Vis Sci. 2016;93(10):1243-1253.
- [3] Thibos LN, Hong X, Bradley A, Applegate RA. Accuracy and precision of objective refraction from wavefront aberrations. J Vis. 2004;4(4):329-351.

ZOSPy, a Python package for optical simulations

Jan-Willem Beenakker^{1,2,3*}, Corne Haasjes^{1,2,3}, Luc van Vught^{1,2}

¹ Department of Ophthalmology, Leiden University Medical Center, Leiden, The Netherlands

² Department of Radiology, Leiden University Medical Center, Leiden, The Netherlands

³ Department of Radiation Oncology, Leiden University Medical Center, Leiden, The Netherlands

* Corresponding author: j.w.m.beenakker@lumc.nl

ZOSPy is an open-source Python package that facilitates optical simulation in OpticStudio. It provides an easy method to define and analyse optical (eye) models. Furthermore, it facilitates sharing analysis results outside the OpticStudio environment. In this presentation its main features, together with three different applications in the fields of refractive surgery and ocular oncology, will be shared.

Keywords: OpticStudio; eye modelling; Python; radiotherapy; negative dysphotopsia

Purpose

OpticStudio (Ansys/Zemax) is one of the main software platforms for optical simulations. Within ophthalmology it has a wide range of applications ranging from intra-ocular lens (IOL) design to assessing the origin of pseudophakic dysphotopsia [1] or even evaluating the accuracy of marker surgery for the treatment of eye tumours.[2] OpticStudio has a large and powerful set of analysis tools to offer, but it largely relies on manual user interaction. As a result, it has a steep learning curve and applications in large cohort of subjects are few. While OpticStudio has an Application Programming Interface (the ZOS-API), using this API requires in-depth programming knowledge which limits its use in ophthalmic vision science.

We therefore developed ZOSPy [3], an open science platform that allows the user to focus on optics modelling and analysis by providing an accessible interface to the OpticStudio API. In this presentation we will share the main features of ZOSPy together with some real-world ophthalmic examples.

Methods

ZOSPy is a python-based wrapper around the official ZOS-API, which connects to OpticStudio using a .NET connection. In addition to enabling full access to all the OpticStudio functions available through the API, it provides the following features:

- Simplified initiation of the connection between Python and OpticStudio
- Object-oriented methods to define surfaces
- A uniform method to perform and parse analyses
- Easy access to solvers and constants (e.g. through zospy.solvers)
- Auto-completion
- Unit tests (results have been validated across different OpticStudio versions ranging from 20.3 to 23.0)

Results

The basic principles of using ZOSPy are shown below by building the Escudero-Sanz eye model and assessing its peripheral point spread function (full code is available on GitHub).

```

import zospy as zp
# initiation connection to OpticStudio
zos = zp.ZOS()
zos.connect_as_extension()
oss = zos.get_primary_system()
oss.make_sequential()

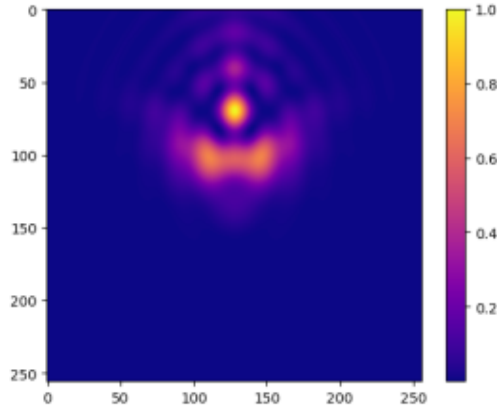
# set wavelength
wl_1 = oss.SystemData.Wavelengths.GetWavelength(1)
wl_1.Wavelength = .543

...
# Example of defining the lens front
lensF_surf = oss.LDE.InsertNewSurfaceAt(n_surf)
lensF.Comment = "Lens Front"
lensF.Radius = 10.2
lensF.Conic = -3.1316
lensF.Thickness = 4.00
solvers.material_model(lensF.MaterialCell, 1.3374)

...
# Set field eccentricity to 15 degrees
field1 = oss.SystemData.Fields.GetField(1)
field1.Y = 15

# Perform and plot analysis
psf = zp.analyses.psf.huygens_psf(oss, "256x256")
plt.imshow(psf.Data, cmap="plasma")

```



Three examples of studies that have been performed using ZOSPy:

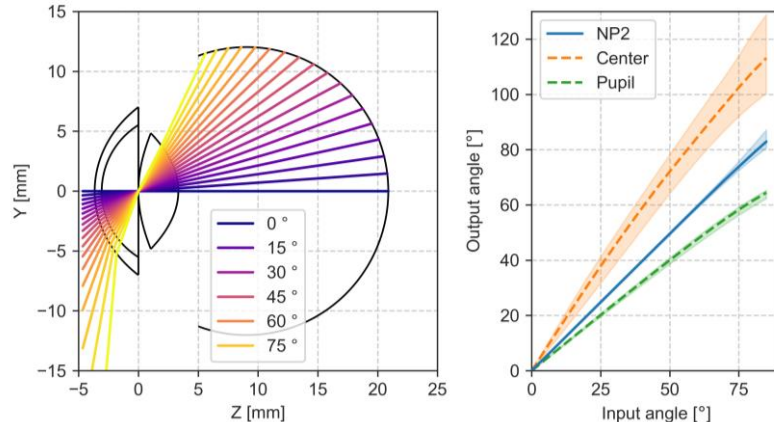


Figure 1: Assessment of the relation between visual field eccentricity and retinal location in personalized eye models of 30 subjects, used to incorporate fundus imaging in radiotherapy planning.

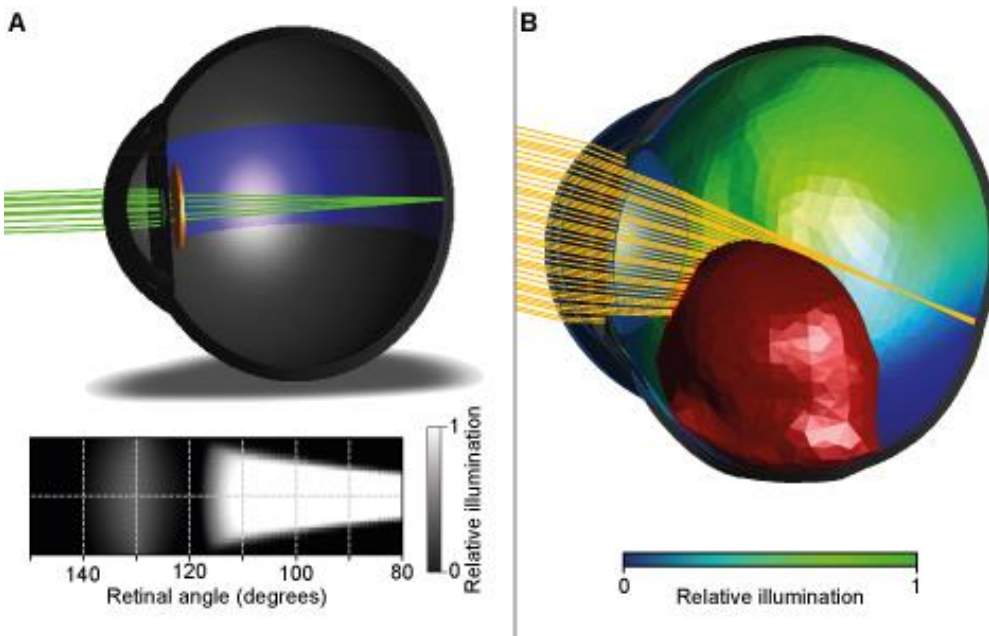


Figure 2: Clinical studies performed with ZOSPy. A) Determining the retinal illumination profile to assess the relation between the eye's anatomy and negative dysphotopsia [1]. Here ZOSPy was used to iterate through a large set of ocular geometries. B) Retinal illumination of MRI-based eye-model with an intra-ocular tumor (red), showing that during transillumination the tumor extent can be erroneously overestimated. [2].

Conclusions

ZOSPy allows the user to focus on the optic modelling and analysis rather than on complex coding, therewith enabling the use of ray tracing simulations in (ophthalmic) research.

References

- [1] van Vught L, Que I, Luyten GPM, Beenakker JM. Effect of anatomical differences and intraocular lens design on negative dysphotopsia. *J Cataract Refract Surg*. 2022 Dec 1;48(12):1446-1452
- [2] Jaarsma-Coes MG, Ferreira TA, Marinkovic M, Vu THK, van Vught L, van Haren GR, Rodrigues MF, Klaver YLB, Verbist BM, Luyten GPM, Rasch CRN, Beenakker JM. Comparison of Magnetic Resonance Imaging-Based and Conventional Measurements for Proton Beam Therapy of Uveal Melanoma. *Ophthalmol Retina*. 2023 Feb;7(2):178-188.
- [3] van Vught L, Haasjes C, Beenakker JWM. ZOSPy [Computer software]. <https://github.com/MREYE-LUMC/ZOSPy>

A study about Jackson cross cylinder test reliability by means of retinal image simulation

Diana Gargallo^{1*}, Esther García¹, Sara Perchés¹, Victoria Collados¹,
Laura Remón¹, Walter Furlam² and Jorge Ares¹

¹ Applied physics, University of Zaragoza, Zaragoza, Spain

² Departamento de Óptica y Optometría y Ciencias de la Visión, Universitat de València, Burjassot, Spain

*Corresponding author: dgargallo@unizar.es

The present work studied the influence of higher-order aberrations, the magnitude of astigmatism and the type of optotype in the Jackson Cross Cylinder Test (JCCT). To accomplish this, retinal images were numerically generated under various conditions during the JCC. These images were presented to the participants, who were required to compare pairs of retinal image simulations in a sequential time-based sequence following the JCC procedure. The results demonstrate that the accuracy depends on the aberration profile. In presence of higher-order aberrations, there is a decrease in the percentage of hits compared to systems without higher-order aberrations.

Keywords: Jackson Cross Cylinder; high-order aberrations; simulated images

Introduction

Monocular subjective refraction is a technique used to determine the combination of spherical and cylindrical lenses required to achieve the best visual acuity considering the individual's subjective response. The Jackson Cross Cylinder Test (JCCT) is a widely used technique in subjective refraction to accurately determine the axis and power of regular astigmatism [1]. Various factors [2] can influence the JCCT and should be considered during the procedure, including the type of optotype, accommodative dynamics or the magnitude of astigmatism. Additionally, the presence of significant high-order aberrations (HOA) also can introduce errors in the final spherocylindrical result, which may vary depending on the patient's pupil size [3].

In this study, the influence of higher-order aberrations, the magnitude of astigmatism, and the optotype used in the JCCT was researched. To accomplish this, a retinal image simulation was done to reveal the relation of these conditions with the precision accuracy of this popular test.

Methods

This study involved 40 healthy volunteers with an average of 21.21 ± 3.49 years. The research followed the tenets of the Declaration of Helsinki, and all participants provided written informed consent. Inclusion criteria were no current ocular pathology, no history of ocular surgery, strabismus, nystagmus or amblyopia, and refractive astigmatism less than 0.50 dioptres (D). All participants were best spectacle-corrected binocular visual acuity (VA) of at least 0.1 logMAR.

Retinal Image Simulation

Convolved retinal images corresponding with a single line of optotypes, and a dot pattern were numerically simulated for different situations of a Jackson cross cylinder test (JCCT). A detailed description of the method to compute the simulated images can be found elsewhere [2].

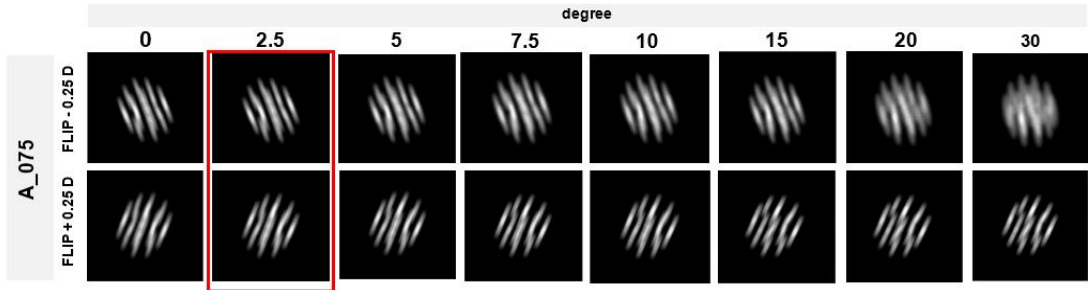


Figure 1. Convolved retinal image simulation of system A_075 for 0, 2.5, 5, 7.5, 10, 15, 20, 30° off-axis. Red square represents flipped pair of images obtained for 2.5° off-axis position.

Six different synthetic aberrometry data for a pupil diameter of 6 mm (A_075, A_125, B_075, B_125, C_075, C_125) were used in this study. A_075 and A_125 represented two aberrometric profiles free of higher-order aberrations (HOA) with different levels of horizontal astigmatism: -0.75D ($Z_2^2 = -0.686 \mu\text{m}$) and -1.25 D ($Z_2^2 = -1.270 \mu\text{m}$), respectively. B_075 and B_125 presented typical fourth-order spherical aberration ($Z_4^0 = -0.200 \mu\text{m}$), while C_075 and C_125 had higher fourth ($Z_4^0 = -0.395 \mu\text{m}$) and sixth-order spherical aberration ($Z_6^0 = -0.081 \mu\text{m}$). Moreover, B and C profiles had -0.75D and -1.25D of horizontal astigmatism added to the existing spherical aberration.

Eight JCC axis positions (0, 2.5, 5, 7.5, 10, 15, 20, 30°) together with their corresponding flipped positions were generated for each object, so a total of 96 pairs of retinal images were simulated (48 pairs for the single line of optotypes and 48 pairs for the dot pattern). Figure 1 shows the retinal image simulations flipping pairs for A_075 with all axis position for the JCC lens.

Examination Protocol

The experiment consisted of presenting retinal image simulations in pairs to the participants on a computer (2560- by-1600-pixel resolution at 227 dpi) at a viewing distance of 0.40 cm with display brightness of 500 nits. Each pair of images were presented to the observers who were always wearing their individual refractive correction. The protocol was carried out by 1 experienced optometrist and in a quiet environment exclusively used for research activities with constant ambient lighting conditions. The measurements were carried in one session (45 minutes long). The observer compares a retinal image simulations pair following the procedure of JCC and being forced to choose between 3 possible answers: a) Image 1 looks better than Image 2, b) Image 2 looks better than Image 1 or c) There is no preference between them. A random sequence was used in each trial to avoid learning effect.

Data Analysis

Data Analysis was performed using the software SPSS for Windows version 19.0. The variable to study is the percentage of correct answers (hits), and the confidence interval was calculated using the Wilson

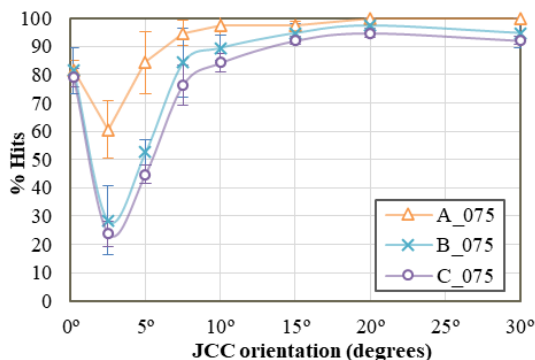


Figure 2. Percentage of hits depending on the turning orientation of the JCC for the three systems: A_075, B_075 and C_075, using the pattern of dots optotype

score interval method for $p < 0.05$. The percentage of hits was studied for different factors such as the aberrometry profile, the magnitude of astigmatism and the type of optotype.

Results

Considering both optotypes and magnitudes of astigmatism together, the system A achieved a hit percentage of $88.41 \pm 16.54\%$. In contrast, system B and system C achieved hit percentages of $76.48 \pm 24.69\%$ and $73.27 \pm 26.05\%$, respectively. Figure 2 illustrates the hit percentages based on the turning orientation of the JCC for the three systems: A_075, B_075, and C_075. The figure shows the results for a single cylindrical lens power (-0.75D) and a specific optotype (pattern of dots). Similar results were obtained with the other cylindrical lens power and optotype. It is shown that when the cross-cylinder axes were placed parallel to the axis of compensation, all systems demonstrated hit percentages around 80%. However, when a rotation of 2.5° off-axis was introduced, a decrease in the percentage of hits was observed across all systems. This decrease was more prominent in systems with higher-order aberrations (B_075 and C_075) compared to system A_075. Interestingly, when the cross-cylinder axes were placed at orientations more than 2.5° off-axis from the compensation axis, the percentage of hits increased. Specifically, as the rotation increased from 5° off-axis to 15° off-axis, systems B_075 and C_075 exhibited a lower percentage of hits compared to system A_075. However, for a rotation of 20° off-axis, the percentage of hits for all three systems was very similar.

Conclusions

The obtained results show that the aberrometric profile influences the performance of the Jackson Cross Cylinder test. As far as we know this is the first time than this result has been reported. In systems with HOA, the decrease in accuracy is lower for a rotation of 2.5 degrees compared to systems without HOA. Our results may suggest that the Jackson Cross Cylinder technique should be initiated by deviating from the subject's astigmatism axis by more than 7.5 degrees if there are no higher-order aberrations (HOAs), and more than 15 degrees if HOAs are present. These results might be useful for clinicians who are using this popular test during the subjective refraction procedure. Nevertheless, further researching must be conducted with different refractive profiles.

Acknowledgement

This research was supported by Ministerio de Ciencia, Innovación y Universidades (Grant PID2020-114311RA-I00); Gobierno de Aragón (Grant E44- 20R).

References

- [1] Del Priore et al. The Jackson cross cylinder. A reappraisal. Ophthalmology. 1986; 93:1461-1465.
- [2] Perches S et al. Retinal image simulation of subjective refraction techniques. PLoS One. 2016; 11: e0150204.
- [3] Collins MJ et al. The effect of pupil size on subjective refraction with irregular cornea. IOVS 2002; 43: 2058.

Bridging physiological optics and visual physiology in myopia control research

José M. González-Méijome, Ana I. Amorim-de-Sousa, António Queirós, Paulo RB Fernandes.

CEORLab, Physics Center of Minho and Porto Universities, University of Minho, Braga, Portugal

* Corresponding author: jgmeijome@fisica.uminho.pt

The mathematical description and recent computational model of the image formation in the human eye allow to determine objectively the visual performance of the eye in several clinical applications. The use of quality metrics based on the optical assessment of the eye allows to predict the visual performance, incorporating neural contributions that are key in the visual process. Contrary to the optical component, accurately measured with wavefront sensors and/or anatomical model based on advanced imaging of the anterior segment of the eye, the neural component uses to be an average factor that does not account for the interindividual variability. Visual electrophysiology has the capability to objectively measure the neural activity at different parts of the retina and visual cortex. The combination of objective characterization of the optical properties of the eye and the retinal and cortical neural activity has the potential to better understand the visual mechanisms and how they can be modulated by changes in the image quality of the eye.

Keywords: visual electrophysiology; electroretinography; visual evoked potentials.

Introduction

Previous studies have shown that visual evoked potentials are an objective tool to evaluate the perceptual image quality with the electrical signal detected in the occipital area being weaker as the level of defocus increases [1]. However, there is a growing interest in understanding how the retinal image quality is reflected in the activity of the retinal cells. In previous studies the research of this group showed that electrophysiology can detect statistically significant differences in the retinal electrophysiological response in eyes fitted with multifocal contact lenses, and after an initial delay in the amplitude and increase in latency, the results tend to return to baseline values after fifteen days of adaptation [2]. During 1 month of orthokeratology treatment to neophyte myopic patients, the electroretinogram showed an initial response of delay in the activity and a reduction in amplitude that progressively returns to baseline values [3]. These results suggest that electroretinogram can reflect changes in the physiological activity at the retinal level to demonstrate adaptation effects that were supposed to be exclusive of the central nervous system with particular interest to understand simultaneous image presbyopic correction adaptation. It also opens an opportunity to better understand the cascade of mechanisms that signal the eye to guide its growth when different light stimulation is provided with special interest in emmetropization and myopia control strategies.

The present lecture aims to show the potential of electrophysiology to objectively evaluate the effect of visual and non-visual stimulation using different optical medical devices for the management of myopia.

Methods

Ten eyes of ten myopes used a peripheral gradient contact lens (Amiopik, Paune Vision, Spain) and seventeen eyes wore dual focus contact lens (MiSight, CooperVision, NY, USA) and an extended depth of

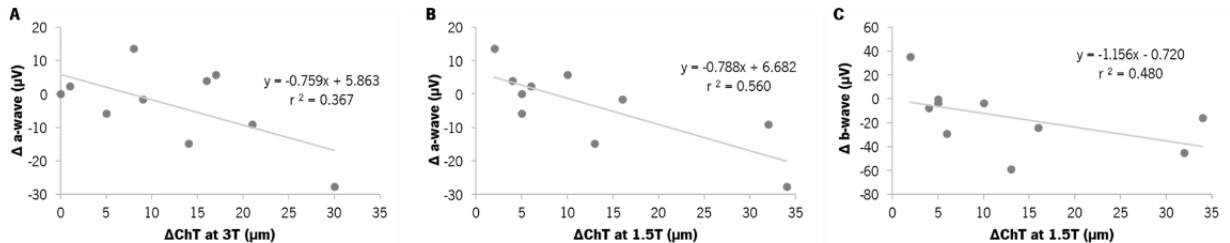


Figure 1: Scatter plots of the differences between PG and SV in choroidal thickness with the difference in ffERG a- and b-wave amplitudes. (A,B) shows the relationship between the changes in a-wave amplitude and the increase in ChT at 3.0 mm and 1.5 mm temporal side, respectively. (C) shows the relationship between the changes in b-wave amplitude with the increase in ChT at 1.5 mm on the temporal side. Regression lines and the coefficients of determination (r^2) are displayed.

focus (MYLO, markennovy, Madrid, Spain) contact lens all intended for myopia control were evaluated in three different experiments. Single vision contact lenses made of the same material were used as controls in all experiments. a-wave and b-wave component of the Full field electroretinogram (ffERG), pattern electroretinography (PERG) and multifocal electroretinograms (mfERGs) and global-flash multifocal electroretinogram (gf-mf-ERG) were recorded with the RETI-port/scan21 (Roland Consult, Wiesbaden, Germany), following the Standards of the International Society for Clinical Electro-physiology of Vision (ISCEV). Simultaneous choroidal thickness (ChT) changes across the central 6 mm of the posterior pole were evaluated during the exposure to one of the contact lenses (peripheral gradient) while in the group of dual focus and extended depth of focus wearers the peripheral refraction was also measured along 8 different semi-meridians along the visual field. Protocols have been reviewed and approved by the Ethics Subcommittee for Research in Life and Health Sciences of the University of Minho (CEICVS 038/2019). Considering the small sample size and the non-normal distribution of several variables, non-parametric statistics were used for comparison. Statistical significance was set at $\alpha = 0.05$.

Results

Peripheral gradient contact lenses showed a statistically significant decrease in amplitude in the a-wave and b-wave of the ffERG as well as in the PERG results. a-wave and b-wave amplitude changes were moderately correlated (Coefficient of correlation > 0.500) with changes in the choroidal thickness with the peripheral gradient contact lens (Figure 1). The dual focus (DF) and extended depth of focus (EDoF) myopia control contact lenses a significant myopic shift in the relative peripheral refraction, being more consistent for the DF lens in all meridians (Figure 2). Both lenses showed changes in different

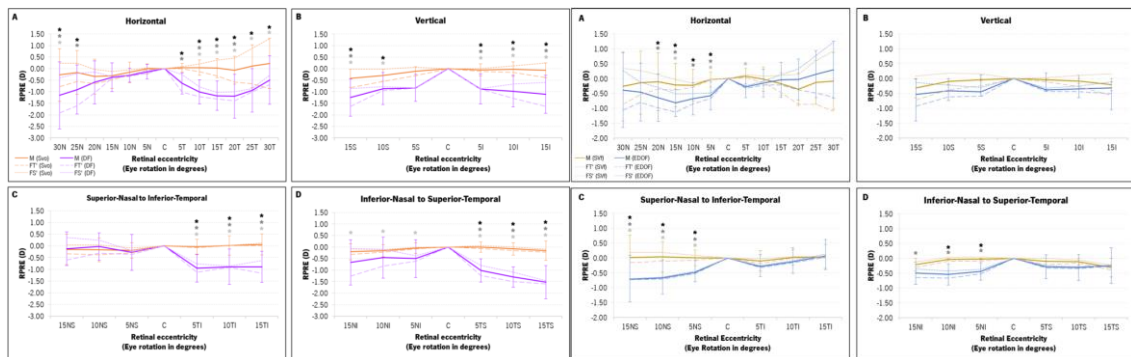


Figure 2: (Left) Mean relative peripheral refractive error (RPRE) profile, in diopters (D), of the three components of refraction (M, FT' and FS') with: Left: single vision (SVo, in orange) and the dual-focus (DF, in purple) contact lenses and Right: single vision (SVf, in yellow) and the dual-focus (EDoF, in blue) contact lenses. Four retinal meridians are presented: horizontal (A), vertical (B), nasal-superior to temporal-inferior (C) and nasal-inferior to temporal-superior (D).

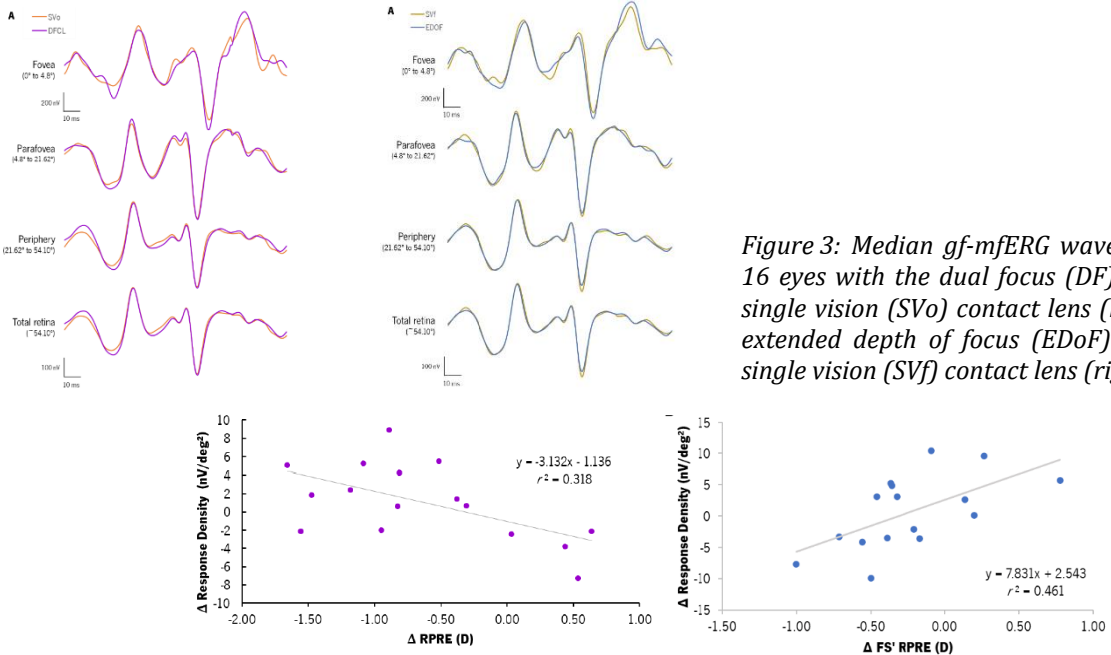


Figure 3: Median gf-mfERG wave response of 16 eyes with the dual focus (DF) and control single vision (SVo) contact lens (left side) and extended depth of focus (EDoF) and control single vision (SVf) contact lens (right side)

Figure 4: Scatterplots of the differences in the response density of the induced component (IC, in nV/deg^2) at Parafovea and the median value of the differences in RPRE of the Tangential foci (RPRE FT) for dual focus lens (A) and between differences in the response density of the induced component (IC, in nV/deg^2) at Parafovea and the median value of the differences in RPRE of the Sagittal foci (FS') for extended depth of focus lens (B)

components of gf-mfERG wave response (Figure 3). Figure 4 illustrates the potential connection between the changes in relative peripheral refractive error RPRE) and the changes in the retinal response density in the parafovea with myopia control contact lenses. However, to establish a potential causality between both, further researcher is needed.

Conclusions

Myopia control contact lenses show an impact on the electrophysiological activity of the retina that might be related with the peripheral relative defocus effect induced. These potential connections between the optical effect and the retinal activity, along with the simultaneous evaluation of the choroidal thickness changes induced by such devices provide a path for shedding light into the mechanisms of action of optical myopia control devices. Future research will be directed to link the changes of the retinal image quality at different retinal sites with the impact in the electrical signal amplitude and potential changes overtime.

Disclosure

Part of these results have been accepted for publication or are in process of submission. Authors have no conflicts of interest to disclose regarding materials and methods mentioned in this work.

References

- [1] Plainis S, Petratou D, Giannakopoulou T, Atchison DA, Tsilimbaris MK. Binocular summation improves performance to defocus-induced blur. Invest Ophthalmol Vis Sci. 2011;52:2784-2789.
- [2] Fernandes P et al. Short-term delay in neural response with multifocal contact lens might start at the retinal level. Doc Ophthalmol. 2022;145:37-51.
- [3] Queirós A, et al. Retinal Response of Low Myopes during Orthokeratology Treatment. J Clin Med. 2020;9:2649.
- [4] Amorim-de-Sousa, A et al. Changes in Choroidal Thickness and Retinal Activity with a Myopia Control Contact Lens. J Clin Med. 2023;12: (accepted for publication).

Optical characterisation of two novel myopia control spectacle lenses

Matt Jaskulski,¹ Javier Gantes-Nuñez,¹ Norberto López-Gil,² Pete S Kollbaum¹

1. Indiana University School of Optometry, Bloomington, Indiana, USA.

2. CiViUM Research Group, Universidad de Murcia, Murcia, Spain.

* Corresponding author: majask@iu.edu

Purpose

To quantify the amount of myopic defocus, contrast modulation and other optical characteristics of two novel spectacle lenses (MiYOSMART by Hoya and Stellest by Essilor) with the inclusion of lenslets in their designs were investigated computationally and experimentally. This paper examined the hypothesis that despite the non-coaxial nature of the optics, image degradation will exist due to the fragmented nature of the base optic when imaging through the lens regions populated by lenslets.

Methods

Optical power was evaluated by computing wavefront vergence and curvature from wavefront slope measured with the Optocraft aberrometer within 1.0- and 6.0-mm apertures across MiYOSMART hexagons and Stellest rings. Point-spread functions (PSFs) were computed using physical (wave) optics and geometrical ray optics principles, and compared with experimental measurements using a 4f optical system. Simulated retinal images and modulation transfer functions (MTFs) were computed from PSF-derived optical transfer functions (OTFs).

Results

Mean lenslet power in MiYOSMART was $+3.95 \pm 0.10$ D through the hexagons and $+6.00 \pm 0.15$ D in Stellest in rings 1-5 and decreased by 0.42 D/ring reaching 3.50 D in the final one. Stellest lenslets included up to -0.015 microns of primary spherical aberration. PSFs and retinal images revealed simultaneous contributions of the base optic and lenslets. MTFs showed a decrease in contrast at low (1-10 c/deg) spatial frequencies (SFs) comparable to 0.25 D of defocus, and retention of diminished levels of contrast at higher SFs.

Conclusions

Varying sagittal power and consistent curvature power across the lenslets is an identifying signature of the novel non-coaxial lens design included in both spectacle lenses. Lenslet array structure itself plays a significant role in determining image characteristics. For both lenses, the blur created by the fragmented base optic contributes to the image quality. The reduced MTFs over a wide range of spatial frequencies result in lowered image contrast.

Keywords: DIMS; H.A.L.T.; image quality; myopia control; optical aberration; spectacles.

How the source of the refractive error can influence image quality

Fabian Debowy¹* and Barbara Pierscionek¹

¹ Faculty of Health, Education, Medicine and Social Care, Medical Technology Research Centre, Chelmsford Campus, Bishops Hall Lane, Chelmsford CM1 1SQ, UK

* Corresponding author: fkd100@pgr.aru.ac.uk

Refractive errors are considered to be largely caused by an optical mismatch between curvature of the cornea and axial length of the eye. This study shows how the source of refractive error can influence the image quality. We simulated the refractive errors in two ways by changing the corneal radius and by changing the axial length. Both methods simulated refractive errors from -2D to +2D with increments of +0.25D for different pupil diameters from 3mm to 6mm and different incident light angles of -5° and +5° in sagittal and meridional planes and 0° as the geometrical axis using the root mean square as the main criterion. The findings show that the source of the refractive error can influence the simulation of image quality. The conic constant has a significant influence on the results.

Keywords: simulation; refractive errors; human eye; optical modelling

Introduction

The human eye has been studied from a variety of perspectives: biological, optical, and biomechanical, in an attempt to understand different aspects of the eye. Studies have been conducted on the behaviour of the eye, but there has been a lack of research on refractive errors, despite the fact that refractive errors are a worldwide problem [1]. Although refractive error can be corrected with glasses, contact lenses, or surgery, the contribution of optical components on the quality of the image requires further investigation. A biologically relevant representative numerical model to simulate refractive errors is required. There are two primary sources of refractive error: corneal radius and axial length [2], and when their mismatch the refractive error occurs [3,4]. Knowledge about how this mismatch affects image quality and ultimately vision is limited. This study applies modelling to investigate and shows how the source of refractive error influences image quality and the influence of the conic constant.

Methods

Zemax OpticStudio® was used to simulate the eye models. The basis model was the Navarro eye model [5]. Refractive errors were simulated from -2D to +2D with step of +0.25D for different pupil diameters from 3 mm to 6 mm and different incident light angles of -5° and +5° sagittal and tangential planes and 0° geometrical axis. The z-axis was the light propagation axis. The root mean square (RMS) of spot diagram was used to determine the image quality for every light ray, for the x component and for the y component of the rays. Refractive errors were simulated in two ways: by changes in axial length from those in the initial emmetropic eye or by changes in the power of the cornea from that in the initial emmetropic eye. Axial length changes were simulated by altering the depth of the posterior chamber and corneal refractive power was altered by changing the radii of curvature of the corneal surface. Every axial length simulation commenced from the model of the emmetropic eye with the object placed at infinity (Figure 1a). After that the object plane was changed to the specific finite length that represents

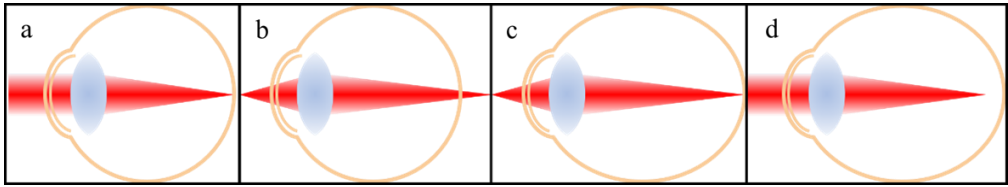


Figure 1: Axial length induced refractive errors.

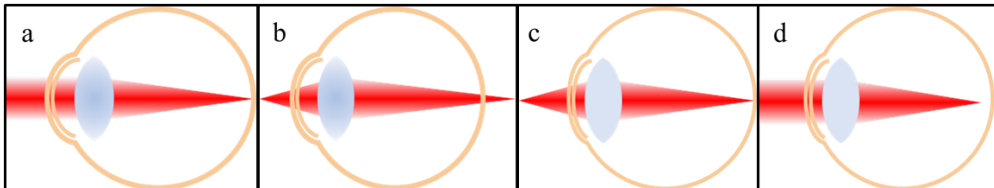


Figure 2: Corneal shape induced refractive errors.

the far point for every respective refractive error length (Figure 1b). The image plane was then altered by changing the posterior chamber depth to find the smallest geometrical root mean square value (Figure 1c). After altering the axial length change, the object plane was changed back to infinity to create the optical mismatch of the particular refractive error (Figure 1d).

The same method, as described above, was used to create models with refractive error induced by altering corneal curvature (Figure 2).

Different sources of refractive error were simulated: corneal radius induced, vitreous thickness induced and combined (corneal radius and vitreous induced). Corneal induced refractive errors were split into two categories: first, where only the anterior surface of cornea changed during simulations and second, where the initial anterior and posterior surface ratio was preserved. Additionally, all corneal models were optimized with or without the conic constant.

Results

All 3 mm pupil diameter simulations had the smallest *RMS* for 0D. This minima at 0D did not change for any method used and any angle.

For the 6 mm pupil, the minima position was dependent on the source of refractive error. All simulations have a shift toward hyperopic values ($-0.25D$ or $-0.50D$). For axial length induced refractive errors the shift minima were between $-0.25D$ and $-0.50D$. The smallest *RMS* value shift was at $-0.25D$ for -5° x-axis, -5° y-axis, and for 0° . The $-0.50D$ shift was observed for 5° x-axis and 5° y-axis. The simulations with aspheric cornea gave a shift of $-0.25D$ for all angles, even when combined with the axial length induced refractive errors. Cornea without conic constant induced refractive errors shift was $-0.25D$ for -5° x-axis and $-0.50D$ for the rest of the angles. The combined axial length induced refractive errors and corneal radius without conic constant induced refractive error shift was, similarly to the axial length minima, between $-0.25D$ and $-0.50D$. The $-0.25D$ shift was observed at -5° x-axis, 0° and 5° y-axis. The remaining 5° sagittal and -5° tangential angles shifts were $-0.50D$.

The axial length induced refractive errors gave *RMS* values from $7.5\mu m$ to $10\mu m$ for the pupil diameter of 3 mm and values from $38\mu m$ to $44.5\mu m$ for the 6 mm pupil diameter. Corneal radius induced refractive errors gave similar *RMS* values for 3 mm pupil in simulations with conic constant (from $17.5\mu m$ to $23\mu m$) and without conic constant (from $18\mu m$ to $23.5\mu m$) but for the 6mm pupil diameter

the values were more distinct, respectively from $27\mu m$ to $40.5\mu m$ for simulations with conic constant and from $34.5\mu m$ to $42\mu m$ for simulations without conic constant. The smallest *RMS* values for the 3 mm pupil diameter were observed in combined models with a range from $3.5\mu m$ to $7.5\mu m$ for models with conic and from $3.8\mu m$ to $7.5\mu m$ for models without conic. For the 6 mm pupil diameter, the two model types showed more diverse *RMS* values starting from $27\mu m$ to $40.5\mu m$ for aspherical simulations and from $34.8\mu m$ to $41.3\mu m$ for the combined model without the conic constant.

Corneal radius induced refractive errors with the preserved ratio of surface curvatures gave similar results to the corneal radius induced refractive errors without the preserved ratio of surface curvatures (difference of $\sim 0.01\mu m$ for pupil diameter of **3 mm** and difference of $\sim 0.15\mu m$ for pupil diameter of **6 mm**).

The incident light angle influences the *RMS* values of different models. Depending on the angle and the induced method of refractive errors, different combinations gave the best *RMS* value. The axial length induced refractive error for the 3 mm pupil gives a minimum *RMS* value for an angle of 5° horizontal axis whereas for the corneal radius with conic constant induced refractive errors, the minimum *RMS* value occurs for an angle of -5° horizontal axis. Similarly, for the 6mm pupil diameter, the minimum *RMS* value is found for a different angle than for the 3mm diameter pupil.

Conclusions

The source of the refractive error can influence the image quality and the conic constant has a significant influence on the results. The combined models (axial length and corneal radius changes) give smaller *RMS* values than the non-combined models. The conic constant helps to improve the image quality. The light angle of incidence influences the *RMS* values, and its values depend on the simulation method used.

Acknowledgement

This project is funded by the European Union's Horizon 2020 research and innovation program under the Marie Skłodowska-Curie grant agreement No 956720.

References

- [1] Haarman AEG, Enthoven CA, Tideman JWJL, Tedja MS, Verhoeven VJM, Klaver CCW. The complications of myopia: a review and meta-analysis. *Invest Ophthalmol Vis Sci*. 2020;61(4):49.
- [2] Flitcroft DI, He M, Jonas JB, et al. IMI – Defining and classifying myopia: a proposed set of standards for clinical and epidemiologic studies. *Invest Ophthalmol Vis Sci*. 2019;60:M20–M30.
- [3] Hashemi H, Khabazkhoob M, Mirafatab M, Emamian MH, Shariati M, Abdolahi-Nia T, Fotouhi A. Axial length to corneal radius of curvature ratio and refractive errors. *J Ophthalmic Vis Res*. 2013 Jul;8(3):220-6.
- [4] Pan CW, Wong TY, Chang L, Lin XY, Lavanya R, Zheng YF, Kok YO, Wu RY, Aung T, Saw SM. Ocular biometry in an urban Indian population: the Singapore Indian Eye Study (SINDI). *Invest Ophthalmol Vis Sci*. 2011 Aug 22;52(9):6636-42.
- [5] Navarro R; Adaptive model of the aging emmetropic eye and its changes with accommodation. *Journal of Vision* 2014;14(13):21.

Estimating the biometric contributions to variations in refractive error in premature and full-term children

Arezoo Farzanfar,^{1,2} Veronica Lockett,³ Rafael Navarro,³ Jos J Rozema^{1,2}

¹ Visual Optics Lab Antwerp (VOLANTIS), Faculty of Medicine and Health Sciences, Antwerp University, Wilrijk, Belgium

² Department of Ophthalmology, Antwerp University Hospital, Edegem, Belgium

³ INMA, Consejo Superior de Investigaciones Científicas & Universidad de Zaragoza, Spain

Corresponding author: jos.rozema@uantwerpen.be

Keywords: *Ocular biometry, Refractive error, Error propagation, Premature infants*

This paper applied error propagation to two methods, referred to as the simple and the matrix methods, to evaluate the importance of eye components on the variations in spherical equivalent refractive error (SE). The simple method defines SE as the difference between axial power and whole-eye power, while the matrix method uses more accurate ray transfer matrices. Both methods were applied to the biometry data for premature infants without retinopathy, newborn, and children taken from the literature. The results show that axial length makes the most important contribution to refractive error variations, followed by the lenticular and corneal power. Myopization considerably increases the contribution of axial length, increasing it from 54.7% to 73.6%.

Introduction

It is well known that the source of refractive errors in an eye lies in its components. The newborn eye undergoes many biometric changes during eye growth, as observed in many clinical studies [1], and these changes are interconnected in a complex way that has to be just right to reach emmetropia. It is known that axial length provides the largest contribution to the refractive error by far [2], but accurate estimates of the contributions of individual refractive components are as yet unavailable. This paper takes an approach by looking at the well-known analytical relationships between the biometric components of the eye and determine how their influences interact to form the refractive distribution using the principles of error propagation. This analysis is applied to the Navarro eye model [3], implemented as either a set of two lenses or as ray transfer matrices [4].

Method

Error propagation

This is a well-known method in engineering to estimate the compounded uncertainty on a parameter f (here SE) that is calculated from several other parameters x_1, \dots, x_N (e.g. axial length, corneal power, etc.), each with an uncertainty $\Delta x_1, \dots, \Delta x_N$. So, the error propagation is calculated as [5]:

$$\Delta f(x_1, \dots, x_N) = \sqrt{\sum_{k=1}^N \left(\frac{\partial f}{\partial x_k} \right)^2 (\Delta x_k)^2} \quad (1)$$

The relative contributions of each x_k and Δx_k to Δf is given by:

$$100 \times \left(\frac{\partial f}{\partial x_i} \right)^2 (\Delta x_i)^2 / \sum_{k=1}^N \left(\frac{\partial f}{\partial x_k} \right)^2 (\Delta x_k)^2 \quad (2)$$

All partial derivatives were calculated manually and validated using the Matlab symbolic toolbox (R2022a, The Mathworks, Natick, MA, USA).

Eye models

The simple method starts from the observation that SE is the difference between the axial power P_{ax} and whole eye power P_{eye} . Both powers can be expanded as follows:

$$SE = P_{ax} - P_{eye} = \left(\frac{n}{L - pp_{eye2}} \right) - \left(K + P_L - K \cdot P_L \cdot \frac{pp_{c2} + ACD_{tot} + pp_{l1}}{n} \right) \quad (3)$$

for which the parameter's definition are provided in Navarro eye model [3] and age-based regressions. These include parameters that are clinically available (axial length L , keratometry K , and total anterior chamber depth ACD_{tot}), lens power P_L and the estimated refractive index of the humours n .

The matrix method is more accurate than the simple method but requires more parameters, such as the anterior and posterior corneal and lenticular radii of curvature (r_{ca} , r_{cp} , r_{la} , r_{lp} , respectively), the gradient index power of the lens (P_G), lens thickness LT and refractive index of the lens surface (n_s). It creates a 2-by-2 matrix \mathbf{M}_{eye} consisting of elements $ABCD$ that describe how the position and inclination of a light ray is altered by the optical system [4]. Using matrix elements A and C in \mathbf{M}_{eye} , the position of the principal plane with respect to the anterior corneal apex can be estimated by:

$$pp_{eye2} = CCT + ACD + LT + (A - 1)/C \quad (4)$$

Meanwhile, the power of the entire eye is given by:

$$P_{eye} = \frac{n}{f_{eye2}} = n \cdot C \quad (5)$$

From this, the refractive error used for the error propagation analysis can be calculated as:

$$SE = P_{ax} - P_{eye} = \frac{n}{L - pp_{eye2}} - n \cdot C = \frac{n}{L - CCT - ACD - LT + (A - 1)/C} - n \cdot C \quad (6)$$

The contribution of the gradient index to the lens power (P_G) is calculated as the difference between the total lens power P_L and the lens surface power P_S .

Results

The simple method was applied average data from newborns, premature infants without retinopathy of prematurity, and children taken from the literature [6-9]. The matrix method was only applied to the children's data by Mutti et al. [6], which contained measured lens biometry (Figure 1).

For the children's data by Mutti et al., the largest contributions for the Mutti dataset were given by the axial length, lenticular, and corneal power for the simple method (68%, 23%, and 9%, respectively), and by the axial length, gradient lens power and the anterior corneal curvature for the matrix method (55%, 21%, and 14%, respectively). In the children's data by Twelker et al., myopization caused the contribution of axial length to increase from 54.7% to 73.6%, and that of the corneal power decreased from 10% to 6.3%. This demonstrates that during normal refractive development the percentage contributions to the variation in SE are generally stable for each eye component, but that this is disrupted by myopization. More chaotic behavior was seen in premature and full-term infants, where the contributions of the axial length and lens power were about equal due to the large standard deviations for the lens power, which was calculated for the data by Cook et al. and Rozema et al, but measured for the dataset by Mutti et al, leading to a smaller uncertainty.

Discussion

The error propagation analysis allows quantifying the size of the relative contributions of the different optical components to the variations in refractive error, and demonstrated that variations in axial length are responsible for about 2/3 of the variations in refractive error, followed by the contribution by the

lens power and anterior corneal power, respectively. Both methods seem to be in agreement. As expected, myopization will disturb this proportion as axial length becomes even more dominant. Note, however, that the method strongly depends on the quality of the data, as indicated by the differences found between the lens powers calculated for the Cook et al. and Rozema et al. datasets and the measured lens power by Mutti et al.

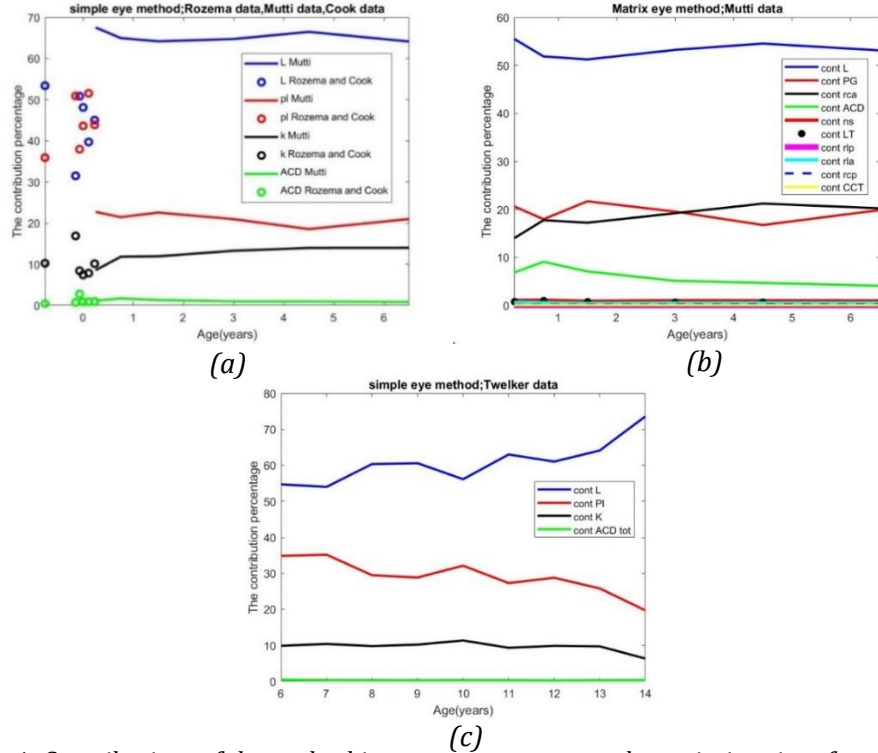


Figure 1: Contributions of the ocular biometry parameters to the variations in refractive error for data by (a) Mutti, Rozema and Cook (b) Mutti, and (c) Twelker.

Acknowledgement

This project has received funding from: the European Union's Horizon 2020 research and innovation programme under the Marie Skłodowska-Curie grant agreement No 956720.

References

- [1] Rozema J, Dankert S, Iribarren R. Emmetropization and non-myopic eye growth. *Surv Ophthalmol*. 2023.
- [2] Hou W, Norton TT, Hyman L, Gwiazda J, Group C. Axial elongation in myopic children and its association with myopia progression in the Correction of Myopia Evaluation Trial (COMET). *Eye Cont lens*. 2018;**44**(4):248-59.
- [3] Navarro R, Santamaría J, Bescós J. Accommodation-dependent model of the human eye with aspheric. *J Opt Soc Am A*. 1985;**2**(8):1273-80.
- [4] Navarro R, Lockett-Ruiz V, López JL. Analytical ray transfer matrix for the crystalline lens. *Biomed Opt Express*. 2022;**13**(11):5836-48.
- [5] Gertsbakh I, Gertsbakh I. Measurement Uncertainty: Error Propagation Formula. *Measurement Theory for Engineers*. 2003;87-94.
- [6] Mutti, D.O., et al., Ocular component development during infancy and early childhood. *Optom Vis Sci*. 2018;**95**(11):976-85.
- [7] Twelker, J.D., et al., Children's ocular components and age, gender, and ethnicity. *Optom Vis Sci*. 2009;**86**(8): 918-35.
- [8] Rozema JJ, Herscovici Z, Snir M, Axer-Siegel R. Analysing the ocular biometry of newborn infants. *Ophthal Physiol Opt*. 2018;**38**(2):119-28.
- [9] Cook A, White S, Batterbury M, Clark D. Ocular growth and refractive error development in premature infants without retinopathy of prematurity. *Invest Ophthalmol Vis Sci*. 2003;**44**(3):953-60.

SyntEyes OBM: higher order statistical model for biomechanical analyses

Hosna Ghaderi^{1*} and Jos Rozema^{1,2}

¹ Visual Optics Lab Antwerp (VOLANTIS), Faculty of Medicine and Health Sciences, Antwerp University, Wilrijk, Belgium

² Dept. of Ophthalmology, Antwerp University Hospital, Edegem, Belgium

* Corresponding author: jos.rozema@uantwerpen.be

Current models of the human eye typically describe either its optical or its mechanical properties, but thus far models combining both have been lacking. The work expands the existing SyntEyes model to allow biomechanical analysis on a realistic range of ocular biometry values, e.g. to test the viability of new ophthalmological treatment modalities.

Keywords: Eye modelling; Biomechanics; SyntEyes

Introduction

Currently, researchers have access to various optical and mechanical eye models that aid in simulating and predicting the optical and mechanical characteristics of the eye. These models have evolved from simplified representations of ocular refractive surfaces [1,2] to more advanced descriptions that include biometric variability. One such description is SyntEyes, a stochastic algorithm, able to generate synthetic biometry data sets with statistical properties similar to that of real data, without the need to perform additional biometry measurements [3,4]. This makes SyntEyes a valuable tool for scientists, e.g. to simulate clinical procedures before applying them in real patients.

Until now, the SyntEyes model only describes the optical aspects of the eye, rather than the ocular biomechanics. Hence, this work aims to provide researchers with a platform that simultaneously describes both the optical and biomechanical properties of the eye, enabling a more comprehensive analyses of the eye's behaviour under various circumstances.

Methods

A 3D geometric model of the eye was created that includes the cornea, sclera, lens, and ciliary body and zonular fibres. The cornea was represented by the anterior and posterior corneal surfaces, each described by 45 Zernike coefficients provided by the SyntEyes model, extended to an 11 mm diameter. The crystalline lens was described by two aspherical surfaces generated based on the provided anterior and posterior radii and conic constant taken from SyntEyes using the aspheric equation:

$$Z(s) = \frac{Cs^2}{1 + \sqrt{1 - (1+k)C^2s^2}}$$

with Z the surface sag, s the radial distance from the optical axis, C the curvature, and k the conic constant.

The sclera is a thick spherical shell with a uniform thickness of 0.83 mm that connects the corneal limbus with the retina fovea. The modelling of the ciliary body was taken from previous work [5], but adjusted to each individual SyntEye, while zonular fibres were modelled as beam elements connecting the ciliary body and lens. All biomechanical modelling was done in Ansys (Ansys Inc, Southpointe, PA, USA) using

the biomechanical properties proposed by Burd [6].

As an initial validation, the model was made to accommodate from distance to near vision. The lenticular surface shape was then extracted to calculate the optical power changes using the thick lens equation:

$$\text{Optical power} = \frac{n_l - n_a}{r_a} + \frac{n_a - n_l}{r_p} - \frac{n_l - n_a}{r_a} \cdot \frac{n_a - n_l}{r_p} \cdot \frac{LT}{n_l}$$

with r_a and r_p the lens surface radii of curvature, LT , the lens thickness, $n_l = 1.43$, the equivalent lens refractive index and $n_a = 1.336$, the refractive index of the aqueous and vitreous humours.

Results

The biomechanical algorithm developed in this study is able to successfully generates a mesh based on the input from the SyntEyes database (Figure 1a). This model allows for an accommodative change in lens power of 9D from far to near vision, leading to a lens thickness increase of 75 μm . These values are well within range of young adults.

Conclusion

This study presented a biomechanical expansion of the SyntEyes model. By incorporating biomechanical considerations into the existing optical model, this platform allows to comprehensively and accurately assess both the optical and biomechanical properties of the eye simultaneously, which could potentially become a valuable tool for optical and clinical simulations.

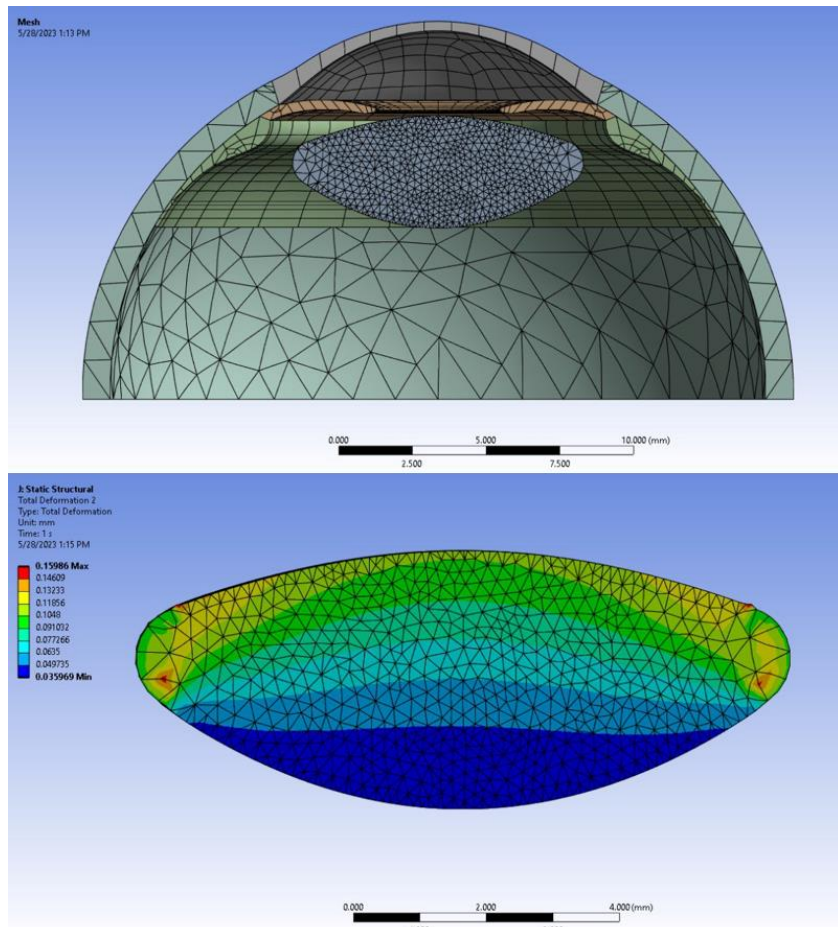


Figure 3: top: Mesh of the eye with lens in non-accommodated state (far focus); bottom: Lens in accommodated state (near focus). Colours represent lens deformation due to accommodation.

Acknowledgement

This project has received funding from: the European Union's Horizon 2020 research and innovation programme under the Marie Skłodowska-Curie grant agreement No 956720.

References

- [1] Gullstrand A. Appendix II and IV. von Helmholtz' Handbuch der Physiologischen Optik. 3rd ed. Vol. 1. Hamburg, Germany: Voss; 1909:301–358, 382–415.
- [2] Lotmar W. Theoretical eye model with aspherics. J Opt Soc Am. 1971;**61**:1522–9.
- [3] Rozema JJ, Rodriguez P, Navarro R, Tassignon MJ. SyntEyes: A higher-order statistical eye model for healthy eyes. Invest Ophthalmol Vis Sci 2016;**57**:683–91.
- [4] Rozema JJ, Rodriguez P, Ruiz Hidalgo I, Navarro R, Tassignon MJ, Koppen C. SyntEyes KTC: higher order statistical eye model for developing keratoconus. Ophthal Physiol Opt 2017;**37**:358–65.
- [5] Ghaderi H, ní Dhubhghaill S, Tassignon MJ, Rozema JJ. The potential influence of the ligament of Wieger on the crystalline lens shape: A modelling study. (*in review*)
- [6] Burd HJ, Judge SJ, Cross JA. Numerical modelling of the accommodating lens. Vision Res 2002;**42**:2235–51.

How similar are male and female eyes?

Jos Rozema^{1,2*} and Larry Thibos³ for EVICR.net, Project Gullstrand Study Group

¹ Visual Optics Lab Antwerp (VOLANTIS), Faculty of Medicine, University of Antwerp, Antwerp, Belgium

² Department of Ophthalmology, Antwerp University Hospital, Edegem, Belgium

³ School of Optometry, Indiana University, Bloomington Indiana, USA

* Corresponding author: jos.rozema@uantwerp.be

Women generally have smaller eyes than men and therefore require more powerful optics to reach emmetropia. Through isotropic scaling individual eyes can be brought to a common reference for direct comparison, which was used to demonstrate significant differences in relative corneal and lenticular power in male and female eyes. These differences cannot be attributed to sex, however, but rather the axial length of the eyes themselves.

Keywords: Ocular biometry; sex-based difference; scaling

Introduction

Ever since the early studies on ocular biometry it has been known that the eyes of women are smaller than those of men [1], which is typically attributed to their shorter stature. Shorter eyes require more refractive power to emmetropize, suggesting that there may be sex-based differences in refractive development. These differences are reflected in the observation that girls tend to develop myopia earlier [2], but much remains unclear about the underlying processes. This work extends the existing sex-based comparisons of ocular biometry using a novel scaling method that brings the intraocular distances and surfaces powers into a common framework.

Methods

To test for sex-based differences in human eyes, we adopt a null hypothesis that optical models of male and female eyes are identical when scaled isotropically (i.e., all spatial proportions remain the same) to achieve a common overall length. Our rationale is based on the inverse relationship between the power P_1 of a refractive surface and its radius of curvature r_1 given by $P_1 = (n_2 - n_1)/r_1$, with n_1 and n_2 the refractive indices of the first and second optical medium, respectively. Hence, if r_1 changes by a factor ω , P_1 becomes:

$$\frac{P_1}{\omega} = \frac{n_2 - n_1}{\omega r_1} \quad (1)$$

So, if the surface radius of curvature r_1 increases by a factor of 2, its power is halved. This principle also applies to the thick lens equation under isotropic scaling (i.e., all proportions remain the same):

$$\frac{P}{\omega} = \frac{P_1}{\omega} + \frac{P_2}{\omega} + \frac{P_1 P_2 \omega T}{\omega^2 n_2} \quad (2)$$

where P_2 is the posterior surface power and T the lens thickness. Since the relationship in (1) applies to all surface powers, the positions of the lens' cardinal points are scaled in exactly the same way as the lens dimensions. Scaling a refractive optical system isotropically is therefore simply multiplying all distances by scale factor ω , while dividing all power values by the same amount.

Applying this to the eye, one has to find the scale factor ω that resizes the eye in such a way that some aspect of it would match a chosen reference value C . In this study we scaled eyes based on their axial

length L , which would work well for emmetropic eyes, so that $\omega = C/L$. It is possible that, for ametropic eyes, the distance between the anterior cornea and the back focal point might be a better choice. This work tests the null hypothesis that sex differences vanish when eye models are scaled isotropically to achieve an axial length of $C = 24\text{ mm}$, corresponding to the axial lengths of the Navarro model [3].

These methods are applied to a subset of 876 eyes (412 males, 464 females; age 20 – 82 years; refractive error range [-9.88D, +6.50D]) from the previously published Project Gullstrand study [4], consisting of uncyclopleged refractive error, ocular biometry (Haag-Streit Lenstar) and lens power estimated using the Bennett equation [5]. Eyes with cataract were excluded, and only one randomly selected eye was used per participant.

Results

Direct comparison

A direct comparison of the biometry according to sex shows that axial length is significantly longer by 0.59 mm in men than in women for the same mean refractive error (Table 1). This is accomplished through significantly lower corneal and lenticular powers in men by $-0.38D$ and $-1.43D$, respectively. This results in an overall power of the eye that is $-1.60D$ lower in men.

Scaled comparison

Scaling each eye isotropically to an axial length of 24 mm , appears to preserve the significantly lower lens power in men ($-0.86D$), but the scaled corneal power is on average $0.66D$ higher in men than in women. Meanwhile, the refractive error and whole eye power of both groups are not significantly different (Table 1), indicating that male and female eyes must produce their overall refractive power through a different balance of their components. On this basis we reject our null hypothesis: male and female eyes are not isotropically similar and can therefore not be scaled into one another.

Influence of sex

The lack of isotropic similarity leads to the question whether this is due to the participants' sex, or rather something that may be expected in groups with different axial lengths. To test this hypothesis, as well as to exclude the possible influence of refractive error, a subgroup of 138 emmetropes (62 males, 76 females; refractive error $|SE| \leq \pm 0.5D$) was analysed. The axial lengths of these eyes ranged between 21.40 mm and 25.29 mm , while their overall ocular powers ranged between $57.60D$ and $69.99D$, roughly

Table 1: Comparison of the ocular biometry of men and women [mean ± StDev (N)]

	SE (D)	K_m (D)	$P_{l,b}$ (D)	P_{eye} (D)	AL (mm)
Direct comparison of biometry					
Male	-0.93 ± 2.25 (412)	42.01 ± 1.36 (412)	24.19 ± 1.89 (198)	61.68 ± 2.00 (198)	24.12 ± 1.10 (412)
Female	-0.78 ± 2.15 (464)	42.39 ± 1.37 (464)	25.62 ± 2.04 (210)	63.28 ± 1.99 (210)	23.53 ± 1.04 (464)
t-test*	0.315	< 0.001	< 0.001	< 0.001	< 0.001
Comparison of isotropically scaled biometry, so for each eye AL = 24 mm					
Male	-1.01 ± 2.35 (412)	42.20 ± 2.02 (412)	24.10 ± 1.56 (198)	61.53 ± 2.00 (198)	24.00 (412)
Female	-0.83 ± 2.19 (464)	41.54 ± 1.89 (464)	24.97 ± 1.61 (210)	61.75 ± 2.03 (210)	24.00 (464)
t-test*	0.248	< 0.001	< 0.001	0.283	---

SE: spherical equivalent; K_m : corneal power; $P_{l,b}$: Bennett lens power; P_{eye} : overall power of the eye; AL: Axial length.

* Unpaired t-test, $p < 0.05$ is significant.

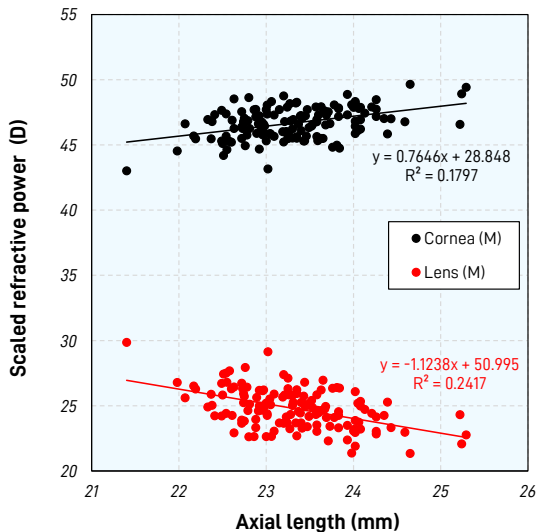


Figure 1. Corneal and lenticular powers of emmetropic eyes each scaled to an axial length of 24 mm.

corresponding with what may be expected from the literature [6].

After isotropic scaling of these eyes, it is seen that the scaled corneal power clearly increases as a function of the unscaled axial length, while the scaled lenticular power shows a similar decrease (Figure 1). This mirrors the observations in Table 1 for the shorter female eyes and longer male eyes.

Finally, stepwise linear regression and a mediation analysis were performed to determine the relative importance of axial length, refractive error, sex and age for the values of the scaled corneal and lenticular powers. In both cases, and for both methods, the influences of axial length and age were significant ($p < 0.001$), while sex showed no significant influence.

Conclusion

The optical systems of male and female eyes differ both in their internal dimensions as well as the refractive power of their components. These differences cannot be compensated through isotropic scaling, demonstrating that each group accomplishes their overall refractive power through a different balance of their components. Sex does not seem to play a determining role, however, since very similar processes are seen in emmetropes with short and long eyes, which is confirmed by statistical analysis.

References

- [1] Stenström S. Variations and correlations of the optical components of the eye. In: Modern Trends in ophthalmology, Vol II. Sorsby A (ed.), Butterworth, London, 1948.
- [2] Pärssinen O, Lyyra AL. Myopia and myopic progression among schoolchildren: a three-year follow-up study. Invest Ophthalmol Vis Sci. 1993 Aug 1;34(9):2794-802.
- [3] Navarro R. Adaptive model of the aging emmetropic eye and its changes with accommodation. J Vision. 2014; 14(13):21-21.
- [4] Rozema JJ, Tassignon MJ. The Bigaussian nature of ocular biometry. Optom Vis Sci. 2014;91:713-22.
- [5] Bennett AG. A method of determining the equivalent powers of the eye and its crystalline lens without resort to phakometry. Ophthalmic and Physiological Optics. 1988;8:53-9.
- [6] Kuzmanović Elabjer B, Petrinović-Dorešić J, Đurić M, Bušić M, Elabjer E. Cross-sectional study of ocular optical components interactions in emmetropes. Coll. Antropol. 2007;31:743-9.